



UNIVERSITÀ
DEGLI STUDI
DI PADOVA

Sede Amministrativa: Università degli Studi di Padova

Dipartimento di Processi Chimici dell'Ingegneria

SCUOLA DI DOTTORATO DI RICERCA IN INGEGNERIA INDUSTRIALE

INDIRIZZO INGEGNERIA CHIMICA

XXIV° CICLO

**SYNTHESIS AND CHARACTERIZATION OF POLYMER
NANOCOMPOSITES FOR HIGH PERFORMANCE
APPLICATIONS**

Direttore della Scuola: Ch.mo Prof. Paolo Bariani

Coordinatore d'indirizzo: Ch.mo Prof. Alberto Bertucco

Supervisore: Ch.mo Prof. Michele Modesti

Dottorando: Stefano Donadi

Table of contents

Riassunto	I
Summary	VII
Introduction	1
Chapter 1	
Polymer nanocomposites	5
1.1 Introduction	5
1.2 Background	6
1.3 Polymer/layered silicates nanocomposites	8
1.3.1 Structure of layered silicates	9
1.3.2 Structures of nanocomposites	10
1.3.3 Preparative methods of nanocomposites	13
1.3.4 Properties of nanocomposites	14
1.4 Polymer/particles nanocomposites	17
1.4.1 Kinds of particles	17
1.4.2 Preparative methods of nanocomposites	18
1.4.3 Properties of nanocomposites	18
1.5 Polymer/POSS nanocomposites	20
1.5.1 Definition of POSS	20
1.5.2 History of POSS	21
1.5.3 Synthesis of POSS	21
1.5.4 Properties of nanocomposites	22
References	25
Chapter 2	
Reinforcement of thermoplastic polymer based nanocomposites	33
2.1 Nanoplatelets-reinforced nanocomposites	33
2.2 Nanoparticles-reinforced nanocomposites	45
References	51
Chapter 3	
PET, PMMA, PC based nanocomposites	53
3.1 PET based nanocomposites	53
3.1.1 PET/layered silicates nanocomposites	53
3.1.2 PET/particles nanocomposites	55
3.1.2 PET/POSS nanocomposites	56

3.2 PMMA based nanocomposites	57
3.2.1 PMMA/layered silicates nanocomposites	57
3.2.2 PMMA/particles nanocomposites	59
3.2.3 PMMA/POSS nanocomposites	60
3.3 PC based nanocomposites.....	61
3.3.1 PC/layered silicates nanocomposites.....	61
3.3.2 PC/particles nanocomposites.....	62
3.3.3 PC/POSS nanocomposites	63
References.....	64

Chapter 4

Processing and characterization of polymers..... 71

4.1 Processing of polymers	71
4.1.1 Melt blending: extruder.....	71
4.1.2 Melt blending: Brabender® plastograph	74
4.1.3 Compression molding	75
4.1.4 Injection molding	75
4.1.5 Blow molding	76
4.2 Characterization of polymers	77
4.2.1 Tensile test	77
4.2.2 Flexural test	79
4.2.3 Thermogravimetric analysis (TGA).....	79
4.2.4 Differential scanning calorimetry (DSC)	81
4.2.5 Dynamic mechanical analysis (DMA)	82
4.2.6 X ray diffraction (XRD)	84
4.2.7 Transmission electron microscopy (TEM)	86
4.2.8 Melt flow index (MFI).....	87
4.2.9 Intrinsic viscosity	88
4.2.10 Oxygen permeability	89
4.2.11 Fourier transform infrared spectroscopy (FTIR).....	90
4.2.12 Prediction of partial solubility parameters	90
References.....	93

Chapter 5

PET/MXD6/oMMT nanocomposites for packaging application 95

5.1 Introduction	95
5.2 Raw materials	95
5.3 Preparation of samples.....	96
5.4 Main results.....	96

5.5 Conclusion	100
References.....	100

Chapter 6

The effect of processing on PET properties..... 101

6.1 Introduction	101
6.2 Raw materials	102
6.3 Preparation of samples.....	102
6.4 Characterization	102
6.5 Results and discussion.....	103
6.5.1 Mechanical properties	103
6.5.2 DSC	104
6.5.3 Intrinsic viscosity	105
6.6 Conclusion	107
References.....	107

Chapter 7

PET/POSS nanocomposites: effect of POSS functionalization 109

7.1 Introduction	109
7.2 Raw materials	110
7.3 Preparation of samples.....	110
7.4 Characterization	111
7.5 Results and discussion.....	112
7.5.1 Mechanical properties	112
7.5.2 DSC	113
7.5.3 TGA	115
7.5.4 MFI	117
7.5.5 XRD	119
7.5.6 Oxygen permeability	121
7.5.7 TEM.....	122
7.6 Conclusion	127
References.....	129

Chapter 8

PET/POSS nanocomposites: a screening of different POSS 131

8.1 Introduction	131
8.2 Raw materials	132
8.3 Preparation of samples.....	132
8.4 Characterization	133
8.5 Results and discussion.....	133

8.5.1 DSC	133
8.5.2 TGA	138
8.5.3 Solubility	141
8.6 Conclusion	144
References.....	144

Chapter 9

PET/tspPOSS nanocomposites 145

9.1 Introduction	145
9.2 Raw materials	146
9.3 Preparation of samples.....	147
8.4 Characterization	147
9.5 Results and discussion.....	148
9.5.1 Mechanical properties	148
9.5.2 DSC	150
9.5.3 TGA	152
9.5.4 XRD	153
9.5.5 Oxygen permeability	156
9.5.6 TEM	158
9.5.7 Polarized light	165
9.5.8 Heating test.....	167
9.6 Conclusion	169
References.....	170

Chapter 10

PET/MA-g-EVA/oMMT nanocomposites for flexible packaging

application 173

10.1 Introduction	173
10.2 Raw materials.....	175
10.3 Preparation of samples.....	175
10.4 Characterization	177
10.5 Results and discussion.....	178
10.5.1 Mechanical properties	178
10.5.2 TGA	183
10.5.3 DSC	187
10.5.4 TEM	190
10.5.5 XRD	194
10.6 Conclusion	196
References.....	197

Chapter 11

PMMA/oMMT and PC/oMMT nanocomposites: effects of processing parameters	201
11.1 Introduction	201
11.2 Raw materials.....	203
11.3 Preparation of samples.....	203
11.4 Characterization	204
11.5 Results	204
11.5.1 MFI	204
11.5.2 Flexural test	205
11.6 Discussion.....	206
11.7 Conclusion	208
References.....	208

Chapter 12

PMMA and PC based nanocomposites: a screening of different fillers.....	211
12.1 Introduction	211
12.2 Raw materials.....	212
12.3 Preparation of samples.....	212
12.4 Characterization	213
12.5 Results and discussion.....	214
12.5.1 Solubility	214
12.5.2 Tensile test	216
12.5.3 DMA.....	217
12.5.4 Optical clarity	218
12.6 Conclusion	224
References.....	224

Chapter 13

PMMA/functionalized SiO₂ nanocomposites	227
13.1 Introduction	227
13.2 Raw materials.....	228
13.3 Preparation of samples.....	228
13.4 Characterization	231
13.5 Results and discussion.....	232
13.5.1 FTIR.....	232
13.5.2 TGA	233
13.5.3 Optical clarity	234

13.5.4 Mechanical tests	236
13.6 Conclusion	237
References.....	237
Chapter 14	
Gas transport in nanocomposites.....	239
14.1 Gas permeation in polymers.....	239
14.1.1 Steady state approach	240
14.1.2 Time-lag method	240
14.2 Gas permeation in rubbery and glassy polymers	241
14.2.1 Free volume.....	242
14.2.2 Gas permeation in rubbery polymers	243
14.2.3 Gas permeation in glassy polymers	243
14.2.4 Gas permeation in semicrystalline polymers	244
14.3 Gas permeation in nanocomposites	245
14.3.1 Models for permeability of nanocomposites	246
14.3.2 PET/tspPOSS nanocomposites: prediction of permeability	258
References.....	266
Conclusion.....	269

Riassunto

Il progetto in esame si svilupperà attraverso un'attività atta all'individuazione delle tipologie di additivi, allo studio formulativo e all'ottimizzazione delle fasi di processo che consentano l'ottenimento di nanocompositi polimerici aventi migliori prestazioni meccaniche rispetto alla matrice polimerica. Data l'interesse e la collaborazione di alcune aziende operanti nel settore packaging ed automotive, le matrici di interesse sono il polietilene tereftalato (PET), il polimetil metacrilato (PMMA) ed il policarbonato (PC). Un miglioramento delle prestazioni di questi materiali consente un minore utilizzo, in termini di peso, dei medesimi, ne consegue un notevole risparmio economico, specialmente in settori in cui il costo del materiale è notevole (packaging). Nel settore automotive, un vantaggio che ne deriva dalla riduzione del peso che si ottiene sostituendo i componenti metallici con quelli nanocompositi polimerici, è la riduzione dei consumi del veicolo.

Per via dell'elevata trasparenza dei polimeri di interesse in questa attività (PET, PMMA, PC) sono state tenute d'occhio le proprietà ottiche dei nanocompositi ottenuti, nonché le proprietà barriera dei materiali a base PET, dato il loro utilizzo nel settore del packaging di bevande.

Fa seguito una breve sintesi dei contenuti dei capitoli di questa tesi.

Capitolo 1. Riassume i concetti fondamentali relativi ai nanocompositi polimerici, focalizzandosi sulla tipologia delle nanocariche utilizzate nelle attività descritte in questa tesi (silicati lamellari, particelle isodimensionali, POSS) e sui principali effetti che hanno sulle proprietà delle matrici in cui sono disperse.

Capitolo 2. Approfondisce l'azione di rinforzo delle nanocariche nei confronti di matrici termoplastiche, suddivise in base alla loro forma (piastrine e particelle). Essendo l'obiettivo principale di questo studio quello di migliorare le prestazioni meccaniche, è stato ritenuto opportuno dedicare un capitolo a parte a questo argomento.

Capitolo 3. Tratta dello stato dell'arte relativo ai nanocompositi a base PET, PMMA e PC. Viene fatta una distinzione in base alla tipologia di nanocarica usata (silicati lamellari, particelle, POSS) mettendo maggiormente in risalto gli studi relativi a nanocompositi ottenuti per miscelazione allo stato fuso e gli studi che valutano le loro proprietà meccaniche.

Capitolo 4. Vengono descritte le macchine e i metodi adottati per produrre i nanocompositi preparati nelle diverse attività. Inoltre, per quanto riguarda la loro caratterizzazione, vengono fornite informazioni teoriche di base e le descrizioni degli strumenti usati. Un po' al di fuori degli argomenti trattati in questo capitolo, vengono descritti i metodi usati per il calcolo dei parametri parziali di solubilità delle nanocariche e dei polimeri utilizzati nel capitolo 8 e 12.

Capitolo 5. Viene descritta brevemente un'attività che è stata svolta precedentemente al dottorato e riguarda lo studio di nanocompositi polimerici aventi come matrice un blend di PET e nylon (MXD6) e come nanocarica una montmorillonite organo modificata (oMMT). La prima fase dell'attività ha previsto lo studio di come diverse metodologie di miscelazione influiscono sulle proprietà meccaniche, termiche, morfologiche e barriera dei nanocompositi. Questa fase è stata oggetto di una pubblicazione scientifica, perciò è stata solamente accennata in questa tesi. La seconda fase ha condotto allo sviluppo di bottiglie in materiale nanocomposito ed ha offerto gli spunti dai quali sono nate delle attività discusse in questa tesi (capitolo 7 e 10). In particolare, i problemi riscontrati nello sviluppo di bottiglie contenenti oMMT (delaminazione, perdita di trasparenza, colorazione indesiderata) in seguito all'operazione di soffiaggio della preforma, hanno volto il nostro interesse verso nanocariche alternative (capitolo 7). Inoltre è stata osservata la localizzazione preferenziale della oMMT nella fase dispersa (MXD6), piuttosto che nella matrice (PET), a causa di fattori termodinamici. Questo aspetto ci ha indotto a svolgere un'attività relativa a blend nanocompositi in cui si vuole avere il controllo sulla localizzazione della oMMT all'interno del materiale (capitolo 10). E' su questi aspetti che questo capitolo si focalizza, senza entrare nel dettaglio, trattandosi di un'attività che non rientra nello scopo di questa tesi, ma che comunque si è dimostrata di estrema importanza.

Capitolo 6. Si tratta di un confronto tra PET tal quale e lo stesso ottenuto in seguito ad un processo di estrusione. Il PET è un polimero molto sensibile alla lavorazione, a causa della sua igroscopicità e dell'alta temperatura necessaria alla sua fusione. Inoltre l'estrusore bivate, principale macchina usata per la preparazione dei nanocompositi, esercita alti sforzi di taglio in fase di miscelazione, che possono parzialmente danneggiare i componenti organici. Per questo motivo, come attività iniziale, è stata verificata la qualità delle metodologie di processing adottate (essiccazione, estrusione) affinché non vengano compromesse le proprietà del PET. Questa verifica è stata condotta principalmente tramite misure reologiche e meccaniche. Ne risulta una piccola diminuzione di peso molecolare del PET in seguito all'estrusione, ma di entità tale da non compromettere le sue proprietà meccaniche.

Comunque il PET estruso verrà assunto come riferimento nei successivi capitoli che trattano nanocompositi a base PET (capitolo 7, 8 e 9) in modo da annullare, nei confronti tra polimero puro e polimero caricato, l'effetto del processing.

Capitolo 7. Preso atto dei risultati descritti nel capitolo 5, come rinforzo del PET sono state utilizzate delle nanocariche alternative alle montmorilloniti, i silsesquiossani poliedrici oligomerici (POSS). Questi hanno un nucleo inorganico circondato da gruppi organici col compito di compatibilizzare o farli reagire col polimero. In particolare sono stati utilizzati due tipi di POSS, uno apolare, non reattivo (POSSo), ed uno avente una catena contenente due gruppi ossidrilici (POSSp). In questa attività sono stati confrontate le proprietà meccaniche, termiche, morfologiche, barriera e reologiche di nanocompositi a base PET contenenti i due diversi POSS. La seconda fase ha previsto lo sviluppo di bottiglie nanocomposite per verificare se il avviene la delaminazione durante lo stampaggio per soffiaggio e se la trasparenza viene compromessa. Si è visto che le bottiglie caricate con POSSo, analogamente a quanto visto nel capitolo 5, si delaminano perdendo la trasparenza. Quelle caricate con POSSp si delaminano anch'esse ma la larghezza delle fessure è tale da non incidere sulla qualità ottica del manufatto.

Capitolo 8. Verificata l'enorme influenza della componente organica dei POSS nelle proprietà dei nanocompositi ottenuti, si è deciso di effettuare uno screening di diversi POSS, scelti ad hoc per essere dispersi in una matrice poliestere o per reagire con essa creando forti interazioni polimero-nanocarica. Questi POSS si differenziano per i gruppi reattivi e per quelli compatibilizzanti di cui sono superficialmente circondati. Di questi ne è stata valutata la stabilità termica, dato che il PET richiede alte temperature di lavorazione, e sono stati calcolati i parametri parziali di solubilità per ognuno di questi e confrontati con quelli del PET per valutare l'affinità termodinamica tra i due componenti. Ne è risultato che il trisilanol fenil POSS (tspPOSS) presenta ottime proprietà in termini di stabilità termica e di solubilità nel PET. Inoltre la qualità ottica dei nanocompositi PET/tspPOSS risulta superiore rispetto ai materiali contenenti altri tipi di POSS.

Capitolo 9. In seguito ai risultati descritti nel capitolo 8, è stato approfondito lo studio di nanocompositi PET/tspPOSS variando il contenuto di POSS nella matrice. In seguito ad un'ampia caratterizzazione meccanica, termica e morfologica sono state sviluppate delle bottiglie, analogamente a quanto descritto nel capitolo 5 e 7. Queste non presentano fessurazioni, a differenza di quelle precedentemente sviluppate, e i manufatti mantengono una elevata qualità ottica.

Capitolo 10. L'attività descritta in questo capitolo è nata dall'interessante osservazione riportata nel capitolo 5, ossia la dispersione preferenziale della oMMT nella fase dispersa del blend PET/MXD6. Si intende migliorare la tenacità del PET (per applicazioni di tipo packaging flessibile) disperdendo una fase duttile quale l'etilen vinil acetato (EVA). La dimensione dei domini di EVA influenza enormemente le proprietà meccaniche del blend. Si vuole aggiungere della oMMT nella fase dispersa affinché porti ad un'affinazione dei domini, grazie a fattori cinetici che intervengono in fase di processing, migliorando la duttilità del PET. Ne è risultata una notevole influenza degli aspetti formulativi sulle proprietà meccaniche del materiale, la morfologia ottenuta differisce però da quella desiderata.

Capitolo 11. Grazie alle attività precedentemente descritte, è stata raggiunta una buona esperienza relativamente al processing di nanocompositi a base PET. Volendo analizzare materiali analoghi a base PMMA e PC è stato effettuato un breve studio dei parametri di processing, in maniera tale da evitare fenomeni degradativi e da ottenere una buona dispersione delle nanocariche nelle due matrici. Come è noto, i parametri di miscelazione incidono su entrambi questi aspetti a seconda dei componenti usati.

Capitolo 12. Analogamente a quanto svolto nel capitolo 8, sono stati preparati nanocompositi a base PMMA e PC contenenti diverse tipologie di POSS ed altre nanoparticelle (a base silice), e calcolati i parametri parziali di solubilità dei componenti. Se, dal punto di vista teorico, una migliore solubilità significa interazioni più favorevoli tra polimero e carica e una minore dimensione delle particelle disperse, questa dovrebbe essere strettamente legata alla trasparenza e resistenza meccanica del nanocomposito. In questa attività si è voluto verificare in modo qualitativo la presenza di questa relazione tra questi tre aspetti: solubilità, qualità ottica, proprietà meccaniche. Questa si è visto esserci ma la sua entità dipende dal sistema nanocomposito in esame. Un buon compromesso degli aspetti indagati è stato riscontrato in nanocompositi PMMA/silice.

Capitolo 13. Dagli interessanti risultati ottenuti nel capitolo 12, si è voluto ottenere un ulteriore aumento delle proprietà meccaniche dei nanocompositi PMMA/silice modificando la superficie delle particelle di silice con un silano (MPS), in modo da renderle più compatibili col polimero. Un'ulteriore miglioramento si è cercato di ottenerlo modificando la superficie della silice, tramite il silano, con delle catene di PMMA. Questo processo richiede solitamente una sintesi in soluzione, in più passaggi, più complessa e meno produttiva della miscelazione allo stato fuso. Per rendere il processo più industrialmente interessante, riducendo l'uso di

solventi, la preparazione dei nanocompositi è stata effettuata con metodi alternativi rispetto a quanto riportato in letteratura.

Capitolo 14. Vengono approfondite le proprietà di trasporto dei gas nei polimeri e nei nanocompositi polimerici, e vengono descritti e confrontati i principali modelli di permeabilità esistenti. Questa trattazione teorica introduce la formulazione di un modello, sviluppato in questo lavoro, relativo alla permeabilità di nanocompositi PET/tspPOSS (trattati nel capitolo 9). Trattandosi di nanocariche particolari, i modelli convenzionali non predicono l'aumento di permeabilità all'ossigeno riscontrato in questi nanocompositi, perciò ne è stato formulato uno appositamente.

Summary

This work has been performed through an activity aimed to the individuation of suitable fillers, to a formulative investigation and to the optimization of processing, that lead to obtain polymer nanocomposites with improved mechanical properties compared to the unfilled matrix. Due to the interest and collaboration of some companies working on the packaging and automotive fields, the matrixes, involved in this work are poly(ethylene terephthalate) (PET), poly(methyl methacrilate) (PMMA) and polycarbonate (PC). The enhancement of the performances of these polymers allows a lower weigh, reducing the overall cost, especially in applications in which the cost of the raw materials is relevant (packaging). In automotive applications, an advantage coming from a lower weight obtained substituting metal components with polymer nanocomposites, is the reduction of the fuel consumed by the vehicle.

Due to the high transparency of the polymer studied in this work (PET, PMMA, PC), the optical properties of the obtained nanocomposites have been evaluated, as well as the barrier properties of PET based materials, since they are used mainly for beverage packaging applications.

Subsequently, a summary of the contents dealt in this work is reported.

Chapter 1. It provides a basic background concerning polymer nanocomposites, focusing on the typology of fillers used in this work (layered silicates, particles, POSS) and on the main effects they lead on the properties of the matrix in which they are dispersed.

Chapter 2. It delves into the reinforcement activity exercised by the filler towards thermoplastic matrixes, distinguishing them on the basis of their shape (platelets and particles). Since the main purpose of this work is the enhancement of the material properties, it has been considered opportune to dedicate a chapter exclusively to this topic.

Chapter 3. It deals the state of the art concerning PET, PMMA and PC based nanocomposites. A classification on the basis of the kind of used fillers is done (layered silicates, particles, POSS) highlighting the studies on nanocomposites prepared by melt blending and that investigate their mechanical properties.

Chapter 4. The devices and methods used to prepare the nanocomposites in this activities are described. Moreover, concerning the characterization, basic theoretical concepts and description of instruments are provided. A little out topic, the methods to predict the partial solubility parameters of fillers and polymers used in chapter 8 and 12.

Chapter 5. It shortly describes an activity carried out earlier than this work and it studied polymer nanocomposites with a PET/nylon (MXD6) blend as matrix, and a organomodified montmorillonite (oMMT) as filler. In the first phase of this activity, the effects of different mixing methods on the mechanical, thermal, morphological and barrier properties of nanocomposites have been studied. This phase has been already discussed in a scientific publication, thus it has been only mentioned in this thesis. The second phase involved the development of nanocomposite bottles and provided the cues for some activities approached in this work (chapter 7 and 10). In particular, the troubles found during the development of bottles filled with oMMT (delamination, transparency loss, unwanted color), occurring after the blowing of the preform, turned our interest toward alternative fillers (chapter 7). Moreover, preferential localization of oMMT into the dispersed phase (MXD6), rather than in the matrix (PET), has been observed, due to thermodynamic factors. This aspect induced us to carry out an activity on nanocomposite blends with controlled localization of oMMT into the material. The chapter is focused to these aspects, without go in detail, since it is an activity out from the purpose of this thesis, but it is essential to introduce the next chapter.

Chapter 6. It compare the neat PET with the extruded PET. This polymer is very sensitive to the processing due to its high hygroscopy and to the high temperatures required to melt it. Moreover the twin screw extruder, the main device used to prepare the nanocomposites, provide high shear stress during the mixing, that may partially degrade the organic components. For this reason, as starting activity, the quality of the processing methods (drying, extrusion) has been verified in order to do not compromise the PET properties. It is performed mainly through rheological and mechanical measurements. It results in a slight loss in molecular weight after the extrusion, but in such an extent to do not compromise the mechanical properties. However the extruded PET will be assumed as control in the following chapter dealing PET base nanocomposites (chapter 7, 8 and 9) so that to remove, comparing filled and unfilled PET, the effect of the processing.

Chapter 7. Subsequently to the results described in chapter 5, we chose alternative fillers to the conventional montmorillonite as reinforcement of PET, the polyhedral oligomeric silsesquioxanes (POSS). They are constituted by an inorganic cage surrounded by organic

groups that act as compatibilizer or they may react with the polymer. In particular two kinds of POSS have been used, a non-polar and un-reactive one (POSSo) and the other has a chain with two hydroxyl groups (POSSp). In this activity the mechanical, thermal, morphological, barrier and rheological properties of nanocomposites filled with these two different POSS have been investigated. The second phase involved the development of nanocomposite bottles in order to verify the occurring of delamination during the blow molding and if the transparency is prejudiced. It has been observed that the POSSo filled bottles, similarly to what has been seen in chapter 5, undergo to delamination losing the transparency. The POSSp filled bottles undergo to delamination as well but the width of slits is not so high to affect the optical clarity.

Chapter 8. The strong influence of the organic part of POSS to the nanocomposites properties induced us to perform a screening of different POSS. We chose suitable kind to disperse them into polyester matrixes or to make react them, forming strong interaction polymer-filler. These POSS differ in the reactive groups and in the compatibilizer groups. We studied their thermal stability, since PET require high temperature of processing, and we calculated their partial solubility parameters comparing to the one of PET in order to evaluate the thermodynamic affinity between the two components. It has been seen that the trisilanol phenyl POSS (tspPOSS) exhibited good thermal stability and solubility in PET. Moreover the optical clarity of PET7tspPOSS nanocomposites is better than nanocomposites containing different POSS.

Chapter 9. Subsequently to the results described in chapter 8, a detailed study of PET/tspPOSS nanocomposites has been performed varying the content of filler. After a wide mechanical, thermal and morphological characterization, nanocomposite bottles have been developed, similarly to chapter 5 and 7. In this case there are no evidence of slits and the good optical clarity is maintained.

Chapter 10. As previously mentioned, this activity arises from the observation of preferential localization of oMMT, described in chapter 5. The aim is to enhance the toughness of PET (for flexible packaging applications) dispersing a ductile phase, i.e. ethylene vinyl acetate (EVA). The EVA domain size strongly affect the mechanical properties of blend. The addition of oMMT in EVA may refine the ductile domains, due to kinetic factors that act during the processing, leading a better toughness maintain a good stiffness as well. The mechanical properties of the material are shown very dependent by the formulative aspects, but the obtained morphology differ from the expected one.

Chapter 11. Thanks to the previously described activities, a good experience about the processing of PET based nanocomposites has been achieved. Since there is the intent to prepare similar materials based on PMMA and PC, a quick study on the processing parameters has been carried out, in order to avoid degradation phenomena and to obtain a good dispersion of fillers into the two matrixes. As it is well known, the mixing parameters affect both these two aspects, depending to the involved components.

Chapter 12. Similarly to the activity describe in chapter 8, PMMA and PC based nanocomposites filled with different POSS and particles (silica based) have been prepared, and the partial solubility parameters have been calculated. If, from a theoretical point of view, a good solubility leads more favorable interactions between polymer and filler and a lower size of dispersed particles, it should be strongly correlated to the transparency and mechanical resistance of the nanocomposite. In this activity we verified the presence of the relation between these three aspects: solubility, optical quality, mechanical properties. We found that there is this relation but its extent depends by the nanocomposite system under exam. A good compromise of the studied aspects has been reported in PMMA/silica nanocomposites.

Chapter 13. After the interesting results described in chapter 12, we tried to obtain a further improvement of the mechanical properties of PMMA/silica nanocomposites superficially modifying the silica particles using a silane (MPS), in order to make them more compatible with the polymer. This process usually involves a multi-steps synthesis in solution, more complex and lesser productive than the melt blending. In order to make the process more interesting from a industrial point of view, reducing the use of solvent, the preparation of the nanocomposites has been done using alternative methods compared to the which ones reported in literature.

Chapter 14. It delves into the gas transport in polymers and polymer nanocomposites and the main existing permeability models have been described and compared. These theoretical concepts introduce the formulation of a model, developed in this work, relative to the permeability of PET/tspPOSS nanocomposites (discussed in chapter 9). Since this filler is particular, the conventional models doesn't predict the increase of the oxygen permeability observed in these nanocomposites, thus a model has been ideated appositely.

Introduction

The field of nanotechnologies is one of the most interesting area concerning the research and development in many technical and applicative disciplines. One of them is the polymer materials science and engineering, which finds application in many specific disciplines, i.e. nanoelectronic, biomaterials, biomedical materials for a controlled release of drugs and active principles, combustible cells, catalysis, membranes, nanofibers, polymer nanocomposites.

The latter involve different branches aimed to introduce nanofillers into the polymer to study the mechanical, gas barrier, thermal, fire resistance and optical properties.

Essentially, the nanoscale represents the transition zone between the microscale and the molecular level. The interest toward polymer nanocomposites, born in the early 90', involved the study of polymers filled with clay and layered silicates. In the last years many studies successfully resulted in a dispersion of fillers at the nanometer level leading to a relevant improvement of the performances, without compromising the processability, weight, resilience, ductility, etc.

The addition of microsized filler as reinforcement of polymers is a common way to obtain composite materials with balanced properties, resulting in an enhancement of the performances of the unfilled matrix. These composites lead an improvement of some features, such as mechanical and gas barrier properties, at the expense of others, such as transparency, that is indispensable in specific applications like packaging. One of the main advantages provided by polymer nanocomposites, compared to the traditional microcomposites, is the capability to obtain the same enhancement of the physic-mechanical properties by adding a lower filler content (one order of magnitude). The enhancement of the performances of these polymers allows a lower weight, reducing the overall cost. In automotive application, an advantage coming from a lower weight obtained substituting metal components with polymer nanocomposites, is the reduction of the fuel consumed by the vehicle. Polymer nanocomposites generally exhibit relevant improvements to the mechanical properties, in terms of elastic modulus and tensile strength, scratch resistance and dimensional shrinkage of the final products. They exhibit better gas barrier and self-extinguishing properties than the

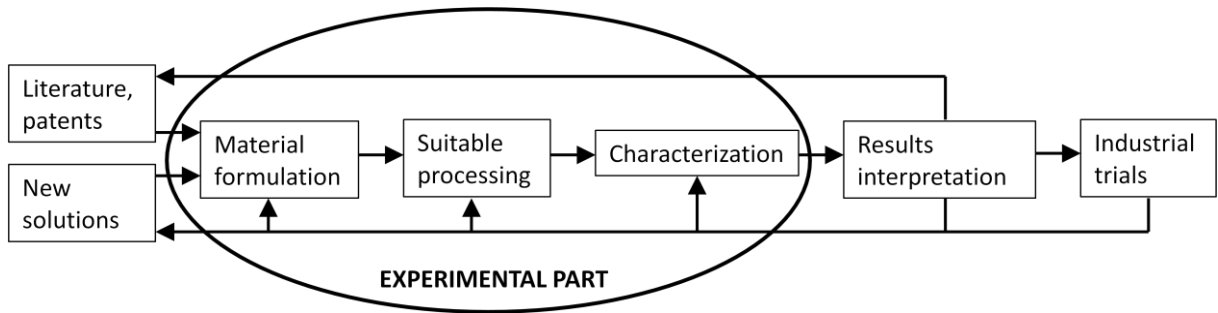
traditional composites. Moreover, the impossibility to obtain completely transparent materials by adding microsized fillers, can be solved.

Several studies showed some critical aspects related to the dispersion of the layered silicates at the nanometer level. The difficulty and sometimes, the impossibility, to achieve this level of dispersion is detrimental for the final properties of the material. In these cases the addition of filler does not significantly affect the material due to its low concentration. Thus, it is necessary to improve the miscibility between the components by increasing their reciprocal affinity. Layered silicates are organically modified by using suitable compatibilizing agents, typically based on quaternary ammonium salts, that affect the hydrophilic character of the silicates, making them more compatible, even with the highly non-polar polymers (g.e. polyolefins). Another important role of these compatibilizers is to increase the spacing between the clay layers, through steric effect, and to promote the penetration of the polymer (intercalation). In this case, due to the high aspect ratio of these filler, a great extent of specific surface is available to interact favorably with the polymer matrix.

In this thesis some limitations concerning the use of organically modified layered silicates will be shown, turning our interest toward alternative fillers; i.e. inorganic particles, polyhedral oligomeric silsesquioxanes (POSS). The latter are inorganic-organic hybrid molecules that have a lower specific surface than the clay platelets but offer some advantages. In particular, the POSS filler has a molecular size, that can be commercially available with a wide range of compatibilizing and reactive groups, has a colorless appearance and leads no, or slightly, embrittlement effects in the nanocomposite.

The dispersion of inorganic fillers by melt blending has the advantage to be carried out by using a traditional technology, well known in the field of transformation of plastic materials, despite the processing optimization is complex, since it depends upon many factors, such the structure and properties of the polymer, kind of filler, mixing conditions (temperatures, residence time). It is very important to carefully characterize these materials, not only physically and mechanically, but rheologically, morphologically and thermally as well.

A simple scheme that describes a general activity of this work is shown in the following Figure.



This work is focused on the improvement of the mechanical properties of poly(ethylene terephthalate) (PET), poly(methyl methacrylate) (PMMA) and polycarbonate (PC) for packaging and automotive applications. The aim is to develop interesting polymer nanocomposites from an industrially point of view, thus, other properties have been evaluated, such as the optical clarity, processability and the gas barrier properties (for PET based materials). Another important aspect that has taken into account is the processing of these nanocomposites, that should not be too much complex and expensive in terms of money and time. This work involves different activities, depending to the polymer/filler system under exam and to the aspects that we want to study, generally aimed to understand the correlation between the formulative and processing parameters and the structure of the material, which strongly affect its final properties.

A previous study on PET based nanocomposites provided the cues for some studies, described in this thesis, on PET filled POSS and organomodified montmorillonite (oMMT). Interesting results have been obtained, inducing us to carry out similar studies on PMMA and PC based nanocomposites. Finally, a gas permeability model for a particular nanocomposites material has been presented, since conventional models do not predict a worsening of the barrier properties of the nanocomposite compared with the matrix

Chapter 1

Polymer nanocomposites

1.1 Introduction

The recent interest aimed to produce nanostructured materials with novel properties, induced the research to create multi-functional engineering materials by designing their structures at the nanometer scale. It has been allowed by recent progresses in nanotechnology, that has been defined as “the creation, processing, characterization, and utilization of materials, devices, and systems with dimensions on the order of 0.1–100 nm, exhibiting novel and significantly enhanced physical, chemical, and biological properties, functions, phenomena, and processes due to their nanoscale size” [1]. Thanks to nanotechnology, it is increasingly easy to develop nanostructured materials using a bottom-up rather than a top-down approach [2]. The first involves their building from atoms, molecules, and the nanoscale powders, fibers and other small structural components made from them, while in the second, raw materials are pressed, cut, molded and otherwise coerced into parts and products.

In the nanostructured materials field it is required to understand the material behavior from an atomistic to a macroscopic point of view. In particular it is fundamental to know the relation between the nanoscale structure of the materials and their bulk properties.

The focus of this chapter is to give a wide overview on the state of knowledge in processing, typologies and material properties for the commonest polymer nanocomposites. They will be discussed nanocomposites based upon two categories of reinforcement materials: layered nanofillers (in particular layered silicates) and nanoparticles, while fibrous materials are out from the purpose of this chapter. Polyhedral oligomeric silsesquioxanes (POSS) will be discuss separately despite their structure has nanometric size in three dimensions, like the nanoparticles.

1.2 Background

The transition from a microparticles to nanoparticles leads dramatic changes in its physical properties. Nanoscale materials have a large surface area for a given volume [3]. Since many important chemical and physical interactions are governed by surfaces and surface properties [4], a nanostructured material can have substantially different properties from a larger-dimensional material of the same composition. In the case of particles and fibers, the surface area per unit volume is inversely proportional to the material's diameter, thus, the smaller the diameter, the greater the surface area per unit volume [3].

Common particle geometries and their respective surface area/volume ratios are shown in Figure 1.1. For the fiber and layered material, the surface area/volume is dominated, especially for nanomaterials, by the first term in the equation. Therefore, logically, a change in particle diameter, layer thickness, or fibrous material diameter from the micrometer to nanometer range, will affect the surface area-to-volume ratio by three orders of magnitude [5]. In general, nanomaterials provide reinforcing efficiency because of their high aspect ratios [3]. The properties of a nanocomposite are greatly influenced by the size scale of its component phases and the degree of mixing between the two phases. Depending on the nature of the components used (layered silicate or nanofiber, cation exchange capacity, and polymer matrix) and the method of preparation, significant differences in composite properties may be obtained [6].

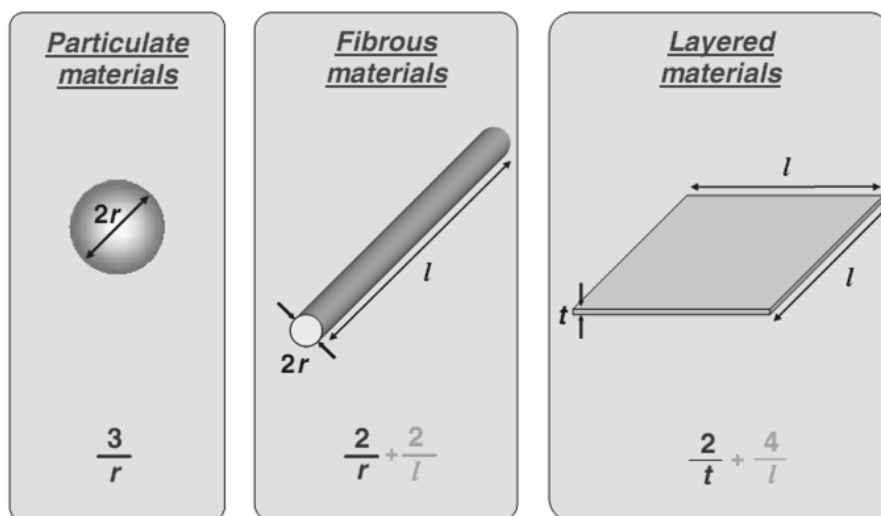


Figure 1.1 Common particle reinforcements/geometries and their respective surface area/volume ratios (reprinted from [5]).

Concerning layered silicate materials, Figure 1.2 represents three main types of composites. When the polymer is unable to intercalate between the silicate sheets, a phase-separated composite is obtained, and the properties stay in the same range as those for traditional microcomposites [7]. In an intercalated structure, where a single extended polymer chain can penetrate between the silicate layers, a well-ordered multilayer morphology results with alternating polymeric and inorganic layers. When the silicate layers are completely and uniformly dispersed in a continuous polymer matrix, an exfoliated or delaminated structure is obtained [7]. In each case, the physical properties of the resultant composite are significantly different, as it will be subsequently discussed.

Analogously, in fibrous or particle-reinforced polymer nanocomposites, dispersion of the nanoparticle and adhesion at the particle–matrix interface play crucial roles in determining the mechanical properties of the nanocomposite. Without proper dispersion, the nanomaterial will not offer improved mechanical properties over that of conventional composites, in fact, a poorly dispersed nanomaterial may degrade the mechanical properties [8].

Additionally, optimizing the interfacial bond between the particle and the matrix, one can tailor the properties of the overall composite, similar to what is done in macrocomposites. For example, good adhesion at the interface will improve properties such as interlaminar shear strength, delamination resistance, fatigue, and corrosion resistance.

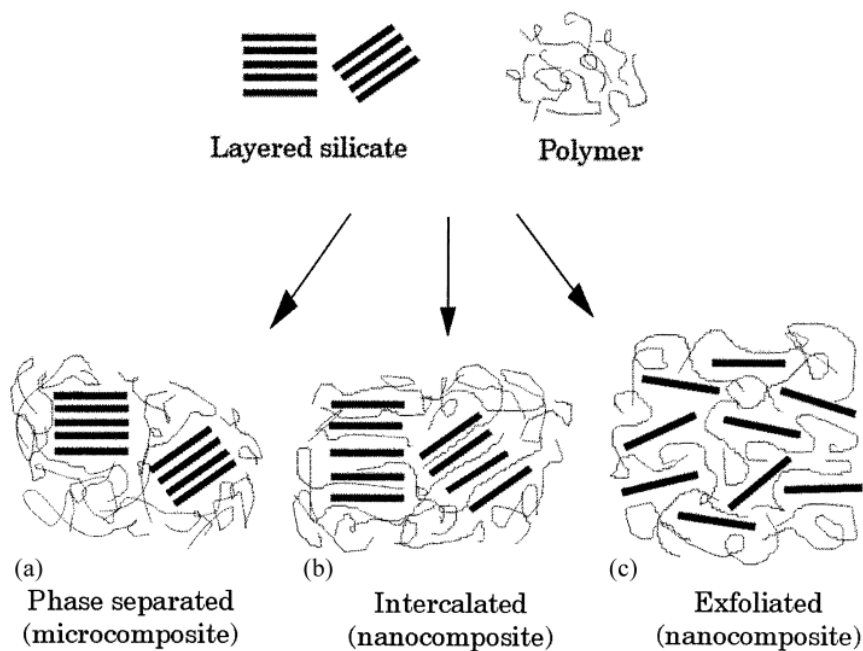


Figure 1.2 Scheme of three main type of layered silicates in polymer matrix (reprinted from [6]).

1.3 Polymer/layered silicates nanocomposites

There is a wide variety of both synthetic and natural crystalline fillers that are able, under specific conditions, to intercalate a polymer. Possible layered host crystals are: graphite [9], metal chalcogenides [10,11], carbon oxides [12,13], metal phosphates [14], layered silicates and layered double hydroxides [15,16].

Amongst all the potential nanocomposite precursors, those based on clay and layered silicates have been more widely investigated probably because the starting clay materials are easily available and because their intercalation chemistry has been studied for a long time [17,18]. Owing to the nanometer-size particles obtained by dispersion, these nanocomposites exhibit markedly improved mechanical, thermal, optical and physic-chemical properties when compared with the pure polymer or conventional (microscale) composites as firstly demonstrated by Kojima et al. [19] for nylon/clay nanocomposites. Improvements can include, for example, increased moduli, strength and heat resistance, decreased gas permeability and flammability.

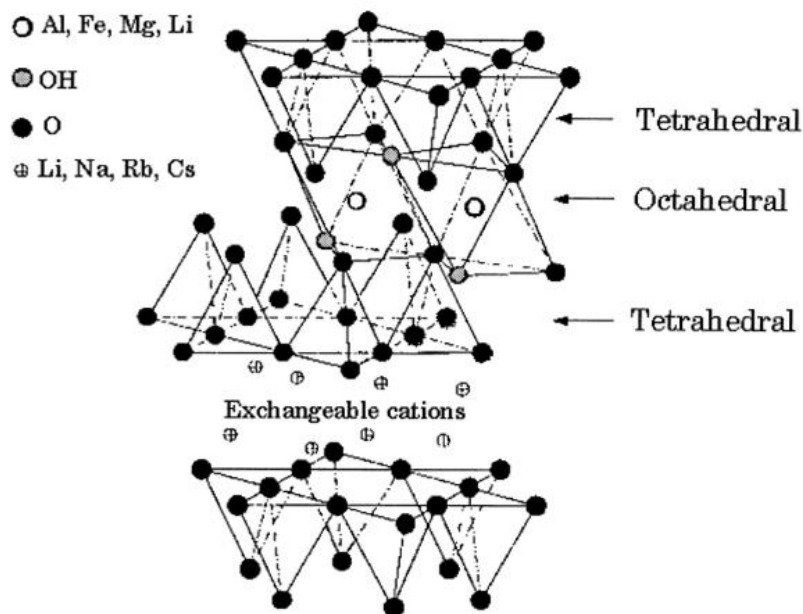


Figure 1.3 Structure of 2:1 phyllosilicates (reprinted from [20]).

1.3.1 Structure of layered silicates

The layered silicates commonly used in nanocomposites belong to the structural family known as the 2:1 phyllosilicates. Their crystal lattice consists of two-dimensional layers where a central octahedral sheet of alumina or magnesia is fused to two external silica tetrahedron by the tip so that the oxygen ions of the octahedral sheet do also belong to the tetrahedral sheets. The layer thickness is around 1 nm and the lateral dimensions of these layers may vary from 300 Å to several microns and even larger depending on the particular silicate. These layers organize themselves to form stacks with a regular van der Waals gap in between them called the interlayer or the gallery. Isomorphic substitution within the layers (for example, Al^{3+} replaced by Mg^{2+} or by Fe^{2+} , or Mg^{2+} replaced by Li^+) generates negative charges that are counterbalanced by alkali or alkaline earth cations situated in the interlayer. As the forces that hold the stacks together are relatively weak, the intercalation of small molecules between the layers is easy [17]. In order to render these hydrophilic phyllosilicates more organophilic, the hydrated cations of the interlayer can be exchanged with cationic surfactants such as alkylammonium or alkylphosphonium (onium). The modified clay (or organoclay) being organophilic, its surface energy is lowered and is more compatible with organic polymers. These polymers may be able to intercalate within the galleries, under well defined experimental conditions.

Montmorillonite (MMT), hectorite and saponite are the most commonly used layered silicates. Their chemical formula is $\text{M}_x(\text{Al}_{4-x}\text{Mg}_x)\text{Si}_8\text{O}_{20}(\text{OH})_4$, $\text{M}_x(\text{Mg}_{6-x}\text{Li}_x)\text{Si}_8\text{O}_{20}(\text{OH})_4$ and $\text{M}_x\text{Mg}_6(\text{Si}_{8-x}\text{Al}_x)\text{O}_{20}(\text{OH})_4$ respectively, where M is the monovalent cation and x is the degree of isomorphous substitution (between 0.5 and 1.3). Their structure is given in Figure 1.3 [20]. This type of clay is characterized by a moderate negative surface charge (known as the cation exchange capacity, CEC and expressed in meq/100 g). The charge of the layer is not locally constant as it varies from layer to layer and must rather be considered as an average value over the whole crystal. Proportionally, even if a small part of the charge balancing cations is located on the external crystallite surface, the majority of these exchangeable cations is located inside the galleries. When the hydrated cations are ion-exchanged with organic cations such as more bulky alkylammoniums, it usually results in a larger interlayer spacing.

In order to describe the structure of the interlayer in organoclays, one has to know that, as the negative charge originates in the silicate layer, the cationic head group of the alkylammonium molecule preferentially resides at the layer surface, leaving the organic tail radiating away from the surface. In a given temperature range, two parameters then define the equilibrium layer spacing: the cation exchange capacity of the layered silicate, driving the packing of the chains, and the chain length of organic tail(s). According to X ray diffraction (XRD) data, the organic chains have been long thought to lie either parallel to the silicate layer, forming mono or bilayers or, depending on the packing density and the chain length, to radiate away from the surface, forming mono or even bimolecular tilted paraffinic arrangement [21] as shown in Figure 1.4.

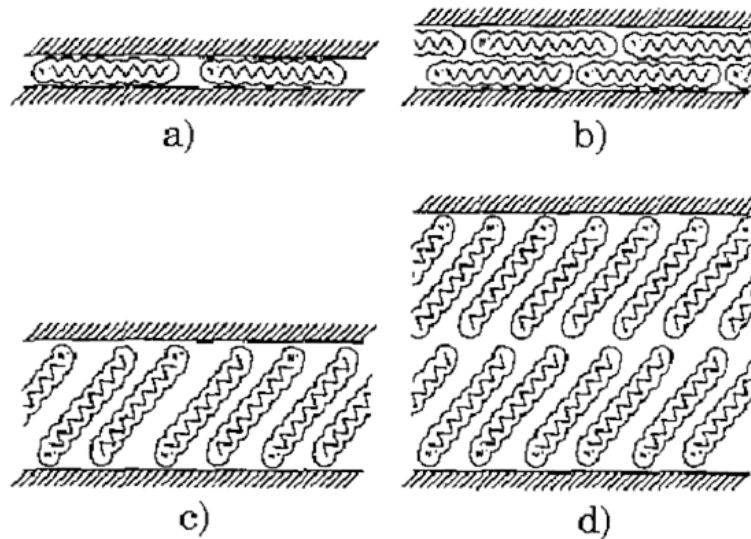


Figure 1.4 Alkyl chain aggregation in layered silicates: lateral monolayer (a), lateral bilayer (b), paraffin-type monolayer (c), paraffin-type bilayer (d) (reprinted from [22]).

1.3.2 Structures of nanocomposites

Depending on the nature of the components used (layered silicate, organic cation and polymer matrix) and the method of preparation, three main types of composites may be obtained when a layered clay is associated with a polymer (Fig. 1.2).

When the polymer is unable to intercalate between the silicate sheets, a phase separated composite (Figure 1.2a) is obtained, whose properties stay in the same range as traditional microcomposites. Beyond this classical family of composites, two types of nanocomposites can be recovered. *Intercalated* structure (Figure 1.2b) in which a single (and sometimes more than one) extended polymer chain is intercalated between the silicate layers resulting in a well ordered multilayer morphology built up with alternating polymeric and inorganic layers. When the silicate layers are completely and uniformly dispersed in a continuous polymer matrix, an *exfoliated* or *delaminated* structure is obtained (Figure 1.2c). Two complementary techniques are used in order to characterize those structures. XRD is used to identify intercalated structures. In such nanocomposites, the repetitive multilayer structure is well preserved, allowing the interlayer spacing to be determined. The intercalation of the polymer chains usually increases the interlayer spacing, in comparison with the spacing of the organoclay used (Fig. 1.5), leading to a shift of the diffraction peak towards lower angle values (angle and layer spacing values being related through the Bragg's relation).

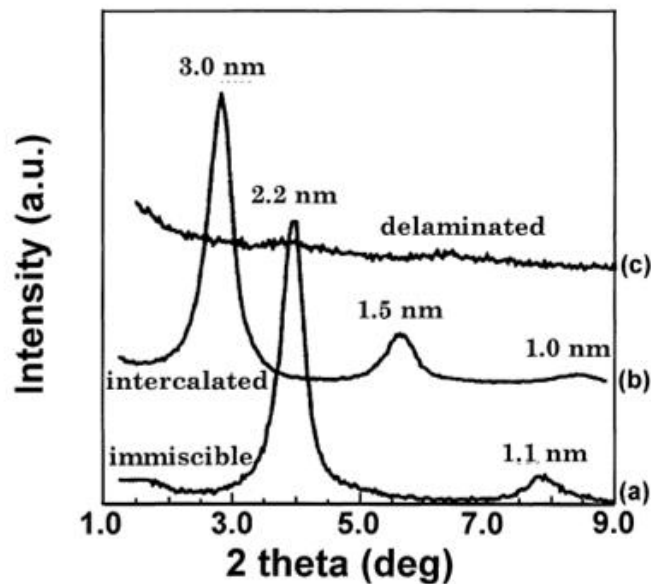


Figure 1.5 XRD patterns of: phase separated microcomposite (organomodified fluorohectorite in a HDPE matrix (a)), intercalated nanocomposite (same organomodified fluorohectorite in a PS matrix) (b), exfoliated nanocomposite (the same organomodified fluorohectorite in a silicone rubber matrix) (reprinted from [20]).

As far as exfoliated structure is concerned, no more diffraction peaks are visible in the XRD diffractograms either because of a much too large spacing between the layers (i.e. exceeding 8 nm in the case of ordered exfoliated structure) or because the nanocomposite does not present ordering anymore. In the latter case, transmission electronic spectroscopy (TEM) is used to characterize the nanocomposite morphology. Fig. 1.6 shows the TEM micrographs obtained for an intercalated and an exfoliated nanocomposite. Besides these two well defined structures, other intermediate organizations can exist presenting both intercalation and exfoliation. In this case, a broadening of the diffraction peak is often observed and one must rely on TEM observation to define the overall structure.

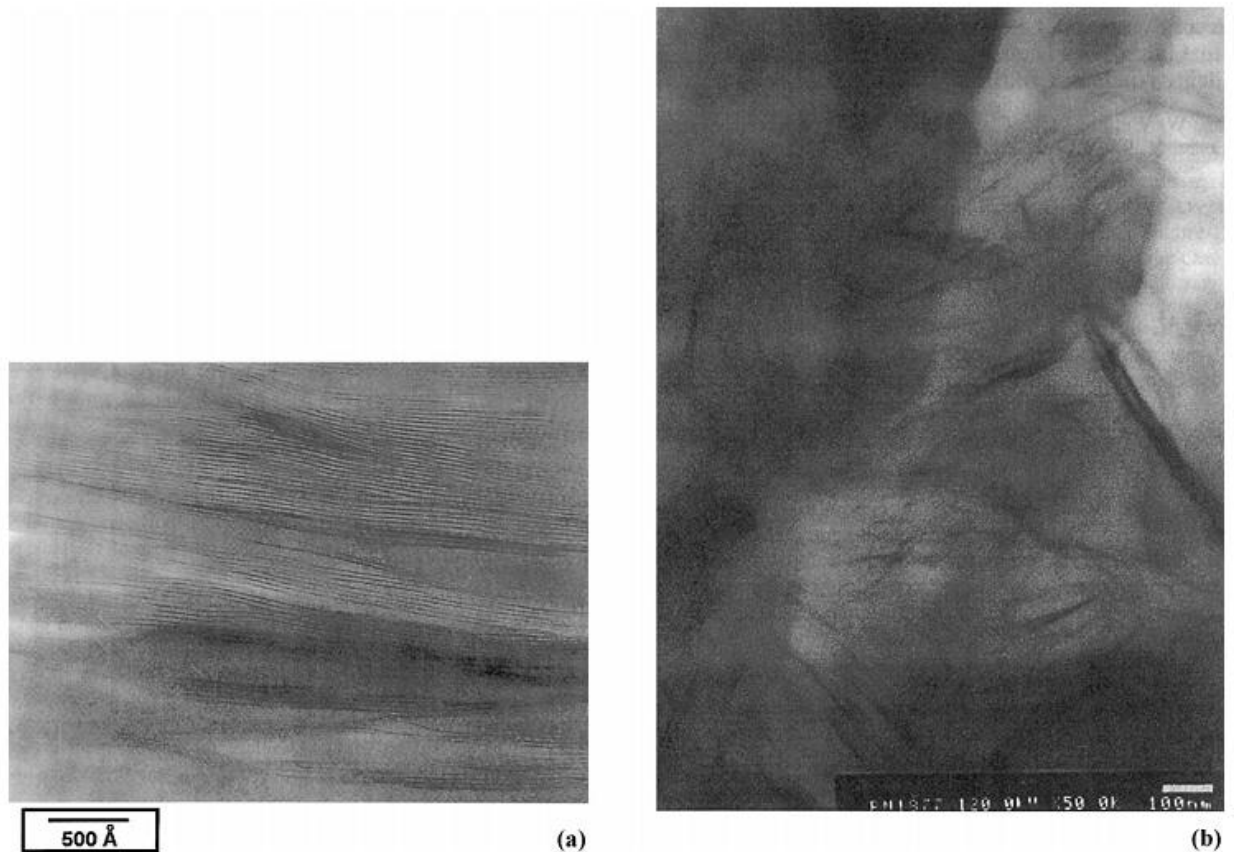


Figure 1.6 TEM micrographs of PS based nanocomposites: intercalated nanocomposite (a) (reprinted from [23]), exfoliated nanocomposite (b) (reprinted from [24]).

1.3.3 Preparative methods of nanocomposites

Several strategies have been considered to prepare polymer/layered silicate nanocomposites. They include four main processes [25]:

- *Exfoliation-adsorption.* The layered silicate is exfoliated into single layers using a solvent in which the polymer (or a prepolymer in case of insoluble polymers such as polyimide) is soluble. It is well known that such layered silicates, owing to the weak forces that stack the layers together can be easily dispersed in an adequate solvent. The polymer then adsorbs onto the delaminated sheets and when the solvent is evaporated (or the mixture precipitated), the sheets reassemble, sandwiching the polymer to form, in the best case, an ordered multilayer structure. Under this process are also gathered the nanocomposites obtained through emulsion polymerization where the layered silicate is dispersed in the aqueous phase.
- *In situ intercalative polymerization.* In this technique, the layered silicate is swollen within the liquid monomer (or a monomer solution) so as the polymer formation can occur in between the intercalated sheets. Polymerization can be initiated either by heat or radiation, by the diffusion of a suitable initiator or by an organic initiator or catalyst fixed through cationic exchange inside the interlayer before the swelling step by the monomer.
- *Melt intercalation.* The layered silicate is mixed with the polymer matrix in the molten state. Under these conditions and if the layer surfaces are sufficiently compatible with the chosen polymer, the polymer can crawl into the interlayer space and form either an intercalated or an exfoliated nanocomposite. In this technique, no solvent is required.
- *Template synthesis.* This technique, where the silicates are formed in situ in an aqueous solution containing the polymer and the silicate building blocks has been widely used for the synthesis of double-layer hydroxide-based nanocomposites [15,16] but is far less developed for layered silicates. In this technique, based on self-assembly forces, the polymer aids the nucleation and growth of the inorganic host crystals and gets trapped within the layers as they grow. The following sections review the four aforementioned preparation techniques, that will be illustrated with representative examples.

1.3.4 Properties of nanocomposites

Nanocomposites consisting of a polymer and layered silicate (modified or not) frequently exhibit remarkably improved mechanical and materials properties when compared to those of pristine polymers containing a small amount (≤ 5 wt%) of layered silicate. Improvements include a higher modulus, increased strength and heat resistance decreased gas permeability and flammability, and increased biodegradability of biodegradable polymers. The main reason for these improved properties in nanocomposites is the stronger interfacial interaction between the matrix and layered silicate, compared with conventional filler-reinforced systems. Subsequently, the main enhanced properties by addition of clay are described.

Tensile properties

The Young's modulus (or tensile modulus), expressing the stiffness of a material at the start of a tensile test, has shown to be strongly improved when nanocomposites are formed. Polyamide 6 (PA6) based nanocomposites obtained through the intercalative ring opening polymerization of ϵ -caprolactam, leading to the formation of exfoliated nanocomposites, show a drastic increase in the Young's modulus at rather low filler content [19,26,27]. In these studies it has been seen a clear dependence between the ability of dispersed silicate layers to increase the Young's modulus of PA6 based nanocomposites and the average length of the layers, hence to the aspect ratio of the dispersed nanoparticles.

A similar behavior was exhibited by partially intercalated-exfoliated ethylene vinyl acetate (EVA) based nanocomposites [28]. The non-linear increase in the relative tensile modulus as function of the clay content may be explained by a decrease in exfoliated particle fraction at higher filler content. Another possible explanation would take into account a continuous variation of the mean aspect ratio of the primary particles, decreasing when the filler content is increased [29].

The inefficiency of intercalated structures to improve the stiffness of the has been showed in studies on intercalated PMMA and PS nanocomposites [30,31]. A large increase in the tensile modulus for an exfoliated structure is also observed for thermoset matrices [32,33].

In thermoplastic-based (intercalated or exfoliated) nanocomposites, the stress at break, which expresses the ultimate strength that the material can bear before break, may vary strongly depending on the nature of the interactions between the matrix and the filler [19,26,27,30].

Polypropylene (PP) based nanocomposites [28] exhibited no or only very slight tensile stress, unless maleic anhydride is added to promote favorable interactions between matrix and fillers. Epoxy resins-based nanocomposites display a totally different behavior depending upon their glass transition temperature, located above or below room temperature. In high T_g epoxy thermosets [33,34], neither intercalated nor exfoliated nanosilicates lead to an improvement of the tensile stress at break, they rather make the materials more brittle. In contrast, nanocomposites based on both epoxy [32,35] and polyurethane [36] elastomeric matrices exhibit a sizeable increase in tensile stress at break upon the addition of small quantities of nanofillers.

The effect of nanocomposite formation on the elongation at break has not been widely investigated. When dispersed in thermoplastics such as for intercalated poly(methyl methacrylate) (PMMA) [30] and polystyrene (PS) [31] or intercalated-exfoliated PP, the elongation at break is reduced. In the last case, the decrease is very important, dropping from 150 and 105% for a pure PP matrix and a 6.9 wt.% non-intercalated clay microcomposite, respectively, down to 7.5% in the better case for a PP-based nanocomposite filled with 5 wt.% silicate layers.

Deviations from this behavior have been seen only in a few of studies (in elastomeric epoxy [35], polyurethane [36], polyimide [37] based nanocomposites) in which an increase of the elongation at break has been observed.

Dynamic mechanical properties

Dynamic mechanical analysis (DMA) measures the response of a given material to an oscillatory deformation (here in tension–torsion mode) as a function of temperature. DMA results are expressed by three main parameters: the storage modulus E' , corresponding to the elastic response to the deformation, the loss modulus E'' , corresponding to the plastic response to the deformation and $\tan \delta = E''/E'$, useful for determining the occurrence of molecular mobility transitions such as the glass transition temperature T_g . By using this technique on nanocomposites, an increase of the E' is generally observed [38–43]. In some studies no relevant deviations in E' have been observed [31]. This behavior is associated to the intercalation of polymer chains between the layers of high aspect ratio fillers, which leads to the suppression of the mobility of the polymer segments near the interface. This enhancement generally occurs below T_g but some exceptions have been observed

[28,40,42,44,45]. E' appears to be substantially enhanced at temperatures above T_g for exfoliated nanocomposites filled with layered silicates of high aspect ratio. A possible explanation for such an improvement could be the creation of a three-dimensional network of interconnected long silicate layers, strengthening the material through mechanical percolation.

Thermal stability

The thermal stability of polymeric materials is usually studied by thermogravimetric analysis (TGA). The weight loss due to the formation of volatile products after degradation at high temperature is monitored as a function of temperature. When the heating occurs under an inert gas flow, a non-oxidative degradation occurs, while the use of air or oxygen allows oxidative degradation of the samples.

Generally, the incorporation of clay into the polymer matrix was found to enhance thermal stability by acting as a superior insulator and mass transport barrier to the volatile products generated during decomposition.

Blumstein [46] first reported the improved thermal stability of a intercalated PMMA nanocomposites filled with organomodified montmorillonite (oMMT). He argues that the stability of the PMMA nanocomposite is due not only to its different structure, but also to the restricted thermal motion of the PMMA in the gallery.

Recently, there have been many reports concerned with the improved thermal stability of nanocomposites prepared with various types of clay and polymer matrices [47–55]. In air, the nanocomposite exhibits a significant delay in weight loss that may derive from the barrier effect caused by diffusion of both the volatile thermo-oxidation products to the gas and oxygen from the gas phase to the polymer. In some studies an improvement of thermal stability is followed by a higher degradation rate [55–57]. In these systems the clay acts as a heat barrier, which enhances the overall thermal stability of the system, as well as assist in the formation of char after thermal decomposition. In the early stages of thermal decomposition, the clay would shift the decomposition to higher temperature. After that, this heat barrier effect would result in a reverse thermal stability. In other words, the stacked silicate layers could hold accumulated heat that could be used as a heat source to accelerate the decomposition process, in conjunction with the heat flow supplied by the outside heat source.

Flame retardancy

The Cone calorimeter is one of the most effective bench-scale methods for studying the fire retardant properties of polymeric materials. Fire-relevant properties such as the heat release rate (HRR), heat peak HRR, smoke production, and CO₂ yield, are vital to the evaluation of the fire safety of materials. The reduction of the peak HRR is the most clear-cut evidence for the efficiency of a flame retardant.

The oMMT must be nanodispersed for it to affect the flammability of the nanocomposites [59]. However, the clay need not be completely delaminated. In general, the nanocomposites flame retardant mechanism involves a high-performance carbonaceous-silicate char, which builds up on the surface during burning. This insulates the underlying material and slows the mass loss rate of decomposition products.

Gas barrier properties

Clays are believed to increase the barrier properties by creating a maze or tortuous path that retards the progress of the gas molecules through the matrix resin. This enhancement has been observed in many studies [60-66] and is strongly affected by the aspect ratio and orientation of the clay.

The gas barrier properties of nanocomposites will be discussed more in detail in Chapter 14, since it is an important aspect of this work.

Optical clarity

Although layered silicates are microns in lateral size, they are just 1 nm thick. Thus, when single layers are dispersed in a polymer matrix, the resulting nanocomposite is optically clear in visible light [50,67-68].

1.4 Polymer/particles nanocomposites

1.4.1 Kinds of particles

Nanoparticles are often defined as particles of less than 100 nm in diameter [69]. Nanometer-sized particles have been made from different organic–inorganic particles and impart composite materials improved properties [70]. Different particles have been used to prepare

polymer/inorganic particle nanocomposites, including: metal (Al, Fe, Au, Ag, etc.), metal oxide (ZnO, Al₂O₃, CaCO₃, TiO₂ etc.), non-metal oxide (SiO₂), other (SiC).

The selection of nanoparticles depends on the desired thermal, mechanical, and electrical properties of the nanocomposites. For example, Al nanoparticles are often selected due to their high conductivity; CaCO₃ particles are chosen because of the relative low cost of the material, and SiC nanoparticles are used because of their high hardness, corrosion resistance, and strength [71].

1.4.2 Preparative methods of nanocomposites

In the case of organic–inorganic nanocomposites, the strength or level of interaction between the organic and inorganic phases is an important issue. Physical or simple mechanical mixing causes a weak phase interaction, e.g., hydrogen bonding, van der Waals forces. On the other hand, a strong chemical covalent or ionic–covalent bond between the organic and inorganic phases or sol gel technique is the typical preparation method for the organic–inorganic nanocomposites. Surface chemistry has been studied for understanding the effect of nanoparticles on a polymer matrix, particle–matrix adhesion etc. in different studies [69,72-74]. Yong and Hahn used a dispersant and coupling agent in a vinyl ester/SiC nanocomposite system to improve the dispersion quality and strength [75].

Different methods have been used to prepare polymer/inorganic particle nanocomposites, including: in situ polymerization [73], melt compounding by twin-screw extrusion [76-78], high shear mixing [79] with three roll milling [80,81], etc. Tang et al. [69] used two traditional polymer-processing techniques (free cast and spinning) to prepare polyacrylonitrile (PAN) matrix and nano-ZnO composites.

1.4.3 Properties of nanocomposites

Micron-scale particles typically scatter light making otherwise transparent matrix materials appear opaque. In PMMA/SiO₂ nanocomposites it has been observed no reduction in transparency even reinforced at relatively high loadings unlike the micrometer-sized filled systems [82,83].

Polymer/inorganic particle-based nanocomposites have shown significant improvement in mechanical, thermal and electrical properties. For example, in polyamide 6 (PA6) filled with

5wt% 50 nm SiO₂ nanoparticles, an increase in tensile strength by 15%, strain at failure by 150%, Young's modulus by 23%, and impact strength by 78% were reported [84]. Jiang et al. [85] investigated acrylonitrile butadiene styrene (ABS) reinforced with both microsized and nanosized calcium carbonate particles through melt compounding.

It was found that the ABS/micron-sized particle composites had higher modulus but lower tensile and impact strength than neat ABS. However, the ABS/nano-sized particle composites increased the modulus as well as impact strength. Chen et al. [86] found that different particle sizes influence the glass transition temperature (T_g) of the nanocomposites. Ma et al. [72] showed an improvement in electrical properties of polyethylene nanocomposites by introducing functional groups at TiO₂ nanoparticles. Zhang and Singh [74] improved the fracture toughness of nominally brittle polyester resin systems by incorporating Al₂O₃ (15 nm). An Al₂O₃ particle has been found to be effective in improving the dielectric constant of polymer in other studies [87] also. Koo et al. [79-81] used fumed silica nanoparticles (7–40 nm) to process different nanocomposites with different resin systems (phenolic, epoxy, cyanate ester) for high temperature application. Recently creep tests were performed on TiO₂/PA66 nanocomposites by Zhang and Yang [78]. Poor creep resistance and dimensional stability have been improved by adding TiO₂ in PA66 based composites. Chisholm et al. [88] investigated micro- and nano-sized SiC in an epoxy matrix system. In their study, an equal amount of loading, nanoparticle infusion brings superior thermal and mechanical properties than microsized particle-based composites. Li et al. [89] performed a low velocity impact test with improved impact strength using TiO₂ and nanoclay in an epoxy system. They also showed a linear relationship with impact energy and corresponding initial velocity.

Polymeric foams are extensively used in different applications such as aerospace, marine, automotive, packaging, and cushioning due to their energy absorption capabilities especially in the event of impact loading [90], good moisture resistance, dampening characteristics (sound, vibration, and oscillation). Mahfuz et al. [91,92] modified polyurethane foam by infusing 3% TiO₂ nanoparticles (spherical shape, diameter: 29 nm) through ultrasonic cavitation process. They found that nanophased foams are thermally stable and their strength and stiffness are greatly improved. It also showed higher absorbed energy [92]. On the basis of research results, it can be said that nanocomposite foam plays an important role in packaging industries and also for short-term disposal applications.

Sandwich composites have been used in the aerospace industry and as load bearing members in naval structures. As the core plays an important role in enhancing the flexural rigidity, Mahfuz et al. [93] studied about strengthening the core materials by using nanophased polyurethane foam (infused TiO₂) for a better performance of the structural sandwich.

1.5 Polymer/POSS nanocomposites

1.5.1 Definition of POSS

The Polyhedral Oligomeric Silsesquioxanes (POSS) are an interesting class of three-dimensional inorganic/organic hybrids with the generic formula of (RSiO_{3/2})_n, as shown in Figure 1.7 [94-97]. POSS molecules with well-defined shapes and sizes ranging from 1–3 nm have been described as the smallest version of colloidal silica. However, unlike silica, silicones, or fillers, each POSS molecule contains organic substituents on its outer surface that make the POSS nanostructure compatible with polymers, biological systems, or surfaces. Furthermore, these groups can be specially designed to be non-reactive or reactive.

R can be inert organic groups used to enhance miscibility with polymeric host materials [98,99]. Making one or more of the R groups reactive permits bonding of the cages to polymers by copolymerization [100] or grafting [101] onto backbone chain.

Incorporating such POSS cages into polymeric materials has already provided useful property enhancements, such as increased glass transition temperature, decomposition temperature, and mechanical strength. Because of the tailorability of POSS molecules, they can also be designed to probe the molecular basis of reinforcement, and to establish structure–property relationships that can then be exploited to optimize properties for particular applications. These POSS reagents have a number of desirable physical properties. For example, they are soluble in common organic solvents such as tetrahydrofuran (THF), toluene, chloroform, and hexane [102,103].

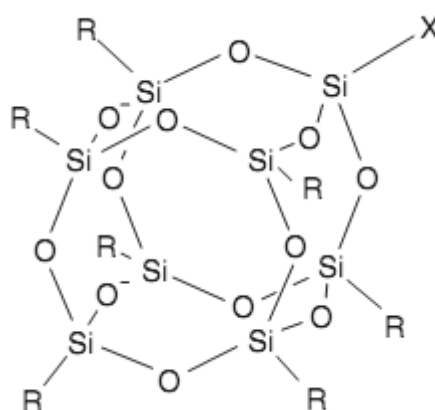


Figure 1.7 Schematic structure of POSS (*R* = compatibilizing groups, *X* = reactive group).

1.5.2 History of POSS

POSS was discovered in 1946 by Scott [104]. After 1990 the field developed rapidly due to the work of two groups: the Feher group at the University of California-Irvine and the Lichtenhan group at the Air Force Research Laboratory. The Feher group devised many methods for synthesizing and chemically modifying structurally well-defined Si/O frameworks [96,97,105–122]. The Lichtenhan group, on the other hand, pioneered the use of discrete POSS in polymer-related applications [100,112,123–125].

The University-Government collaboration between Lichtenhan and Feher rapidly expanded to include more academic collaborators including Laine and Sellinger [126], Mather et al. [127] and others who were all intrigued by the physical and mechanical property improvements imparted by incorporation of these nanostructured materials into polymer systems. In the late nineties not only was government and academic interest growing, but also that of the industrial sector which desired lower costs and larger quantities of the material.

The fall of 1998 marked the start-up of Hybrid Plastics in Fountain Valley, CA, which transitioned the government scale-up facilities to the commercial sector through a cooperative research and development agreement.

1.5.3 Synthesis of POSS

The synthesis of fully condensed POSS frameworks starts with the controlled hydrolysis and condensation of tri-functional organosilicon monomers [106,109,128]. The functionalization

of the POSS framework is then easily accomplished by corner capping of the POSS-trisilanols with silane coupling agents containing organic groups suitable for polymerization [94,106,19]. This methodology provides access to a family of cycloalkyl-substituted POSS monomers, each containing one polymerizable group, as shown in Figure 1.8 [94]. In cases where the appropriate functionality is not directly available by the corner capping sequence, subsequent functional group transformation of the reactive group on a unique silicon atom is possible [94]. Multi-functional POSS derivatives can be made by the condensation of $\text{RSi}(\text{OEt})_3$, as described above, where R is a reactive group [95,129]. Another approach involves functionalizing POSS cages that have been formed [130–132].

The detailed methods of POSS synthesis have been reviewed by Voronkov et al. in 1982 [95] and Feher and et a. in 2000 [121]. It is now possible to prepare range of useful Si/O frameworks from relatively inexpensive feedstocks. A variety of POSS reagents with one or more covalently bonded reactive functionalities has become commercially available from the Hybrid Plastics Company (<http://www.hybridplastics.com>).

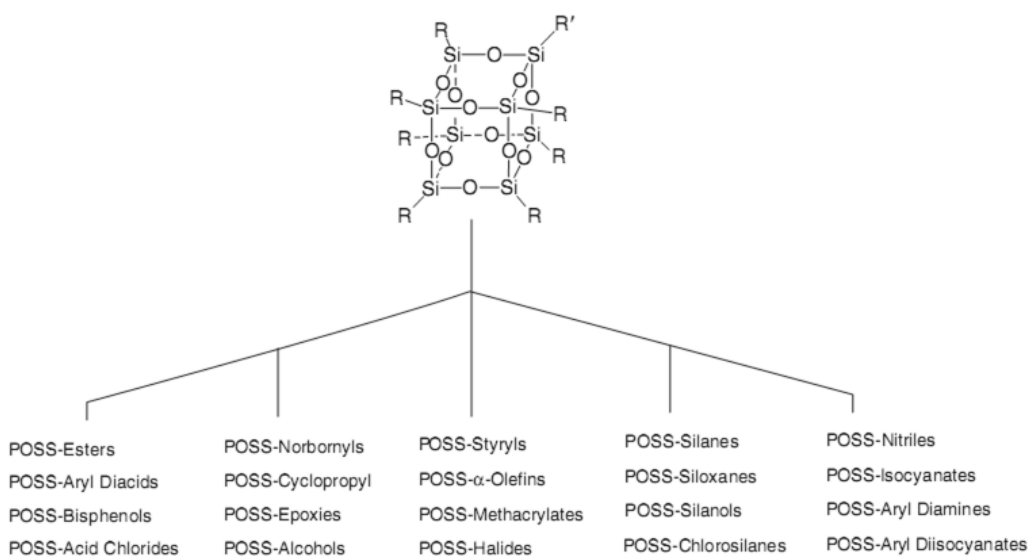


Figure 1.8 Some of functionalities that can be prepared from POSS-trisilanol precursors [94].

1.5.4 Properties of nanocomposites

Because of its chemical nature, POSS is easily incorporated into common plastics via copolymerization or blending. The incorporation of POSS in thermoplastic or thermoset

polymers can affect the thermal, oxidative, and dimensional stability of many polymeric resins, resulting in improvements in properties, including increased glass transition temperature, decomposition temperature and modulus, reduced flammability, and increased gas permeability. Depending on the number of POSS functional groups, different architectures of POSS/polymer composite can be obtained, as shown in Figure 1.9.

A variety of copolymers with POSS units attached as dangling blocks to the polymer backbone have been synthesized [133–144] by using mono-functional and di-functional POSS. The resulting materials represent a new category of polymers characterized by the presence of bulky POSS nanoparticles. The commonest features of these materials is an increase of T_g and thermal stability as the POSS content increases.

Incorporation of multi-functional POSS into polymer systems has been investigated with different polymers [99,145–149]. In these cases, single-phase polymer networks with POSS molecularly dispersed are often formed. POSS acts as a polyhedral crosslink. But no definite effect of POSS on network properties has been established. Both a decrease [147,148] and no change in T_g [99] were reported. The rubbery modulus increases due to a high crosslink density, and thermal stability increases with POSS content.

A more convenient method of incorporating POSS into organic polymers is physical blending. Since each POSS molecule has a Si_8O_{12} core covered with alterable organic side groups, it is believed that better dispersion may result from increased interaction of compatible side groups and polymer [150–152].

Blanski et al. [152] studied the dispersion of POSS in polystyrene (PS). They found that by altering the organic side groups to more compatible phenethyl groups, POSS molecules can be fully dispersed into PS. The surface hardness of the PS/styrenyl POSS film increased 30%. Molecularly dispersed POSS behave as a weak crosslinker in polymer melts and accelerate the crystallization rate of the host polymer [153]. Matejka et al. [147,148] studied the effect of POSS with various topological locations in a network on its structure and properties. These authors incorporated mono-functional, multi-functional, and non-functional POSS into epoxy networks and observe that that POSS pendant on a network chain showed a strong tendency toward aggregation and crystallization. The crystalline domains thus act as physical crosslinks, leading to very strong reinforcement. The mechanical properties are affected mainly by POSS–POSS interactions while the POSS–network chain interactions are of minor importance.

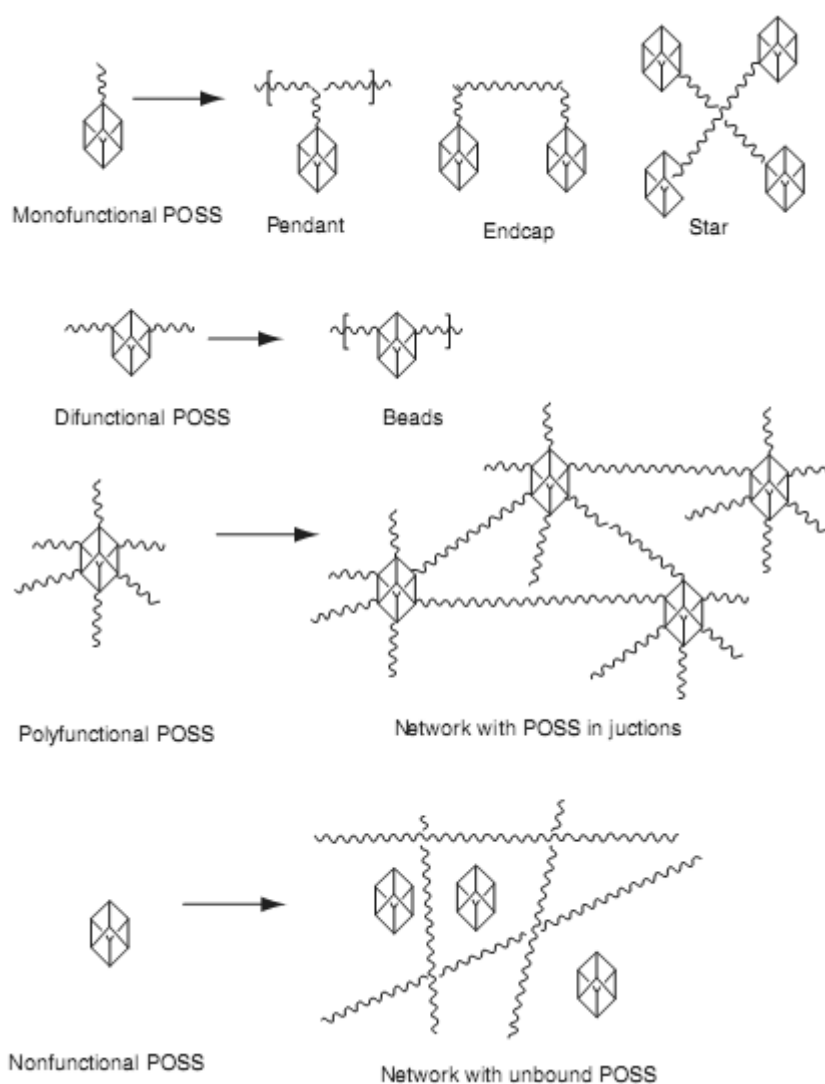


Figure 1.9 *POSS/polymer architectures.*

POSS have dimensions comparable with the size of segments of polymer chains and can restrict their mobility at the molecular level. Restraining the mobility of polymer chains leads to elevation of the glass transition temperatures and to an enhancement of stress–strain characteristics. In addition, POSS molecules have shells of a nearly spherical shape and are able to effectively reduce the viscosity of polymer systems; i.e., their action is similar to that of plasticizers.

The introduction of POSS into the side units of polymer chains can suppress the ability of POSS molecules to aggregate and to form nanocrystals [99,154,155]. The aggregation of POSS is prevented by long organic spacers that link the POSS molecules to polymer chains,

as well by the size of the POSS molecules themselves, which impedes the formation of crystalline regions.

In the case of differences in the reactivity of functional groups of the POSS and the organic monomer, the aggregates formed in the polymer matrix can contain a considerable amount of unreacted POSS molecules [156]. As a result, the majority of POSS molecules that aggregate into nanocrystals in this polymer are not bound to the polymer and do not exert a significant effect on the thermo-mechanical characteristics of the samples .

The incorporation of POSS molecules has an effect on the structural organization of polymer chains. A change in the relative amount of POSS units in poly- ϵ -caproamide leads to alteration in the structure of polymer crystals with prevalence of the α - or γ forms [157]. DSC studies showed that the crystallinity of PEO is reduced with an increase in the amount of POSS units. At M_n values of 1000 and 2000 for PEG, the DSC curves do not exhibit the PEO melting endotherm [158].

It has been observed that the presence of POSS facilitates a considerable depression of the melting point of the crystalline phase of the organic constituent [159] and leads to T_g elevation for the amorphous phase [160]. In the case of POSS with bulky peripheral groups, the complete suppression of the segmental mobility of organic moieties can take place. Along with the glass transition temperature, the onset temperature for the degradation of the polymers is increased as a result of incorporation of POSS [123,161]. The incorporation of POSS molecules substantially enhances the thermo-oxidative stability of polyolefins owing to the formation on the polymer melt surface of a layer of POSS nanoparticles preventing the underlying polymer layers from degrading [162].

References

- [1] American Ceramic Society (2004).
- [2] Nanotechnology: Shaping the World Atom by Atom. National Science and Technology Council Interagency Working Group on Nanoscience, Engineering and Technology (1999).
- [4] RTO Lecture Series, EN-AVT-129, May 2005.
- [3] J.J. Luo, I.M. Daniel. *Compos Sci Technol* 2003, 63, 1607.
- [5] E. Thostenson, C. Li, T. Chou. *J Compos Sci Technol* 2005, 65, 491.
- [7] M. Alexandre, P. Dubois. *Mater Sci Eng Rep* 2000, 28, 1.

- [6] C. Park, O. Park, J. Lim, H. Kim. *Polymer* 2001, 42, 7465.
- [8] R.E. Gorga, R.E. Cohen. *J Polym Sci Part B: Polym Phys* 2004, 42, 2690.
- [9] H. Shioyama. *Carbon* 1997, 35, 1664.
- [10] L. Hernan, J. Morales, J. Santos. *J Solid State Chem* 1998, 141, 327.
- [11] D.J. Harris, T.J. Bonagamba, K. Schmidt-Rohr. *Macromolecules* 1999, 32, 6718.
- [12] Y. Matsuo, K. Tahara, Y. Sugie. *Carbon* 1996, 34, 672.
- [13] Y. Matsuo, K. Tahara, Y. Sugie. *Carbon* 1997, 35, 113.
- [14] Y. Ding, D.J. Jones, P. Maireles-Torres. *Chem Mater* 1995, 7, 562.
- [15] O.C. Wilson Jr., T. Olorunyolemi, A. Jaworski, L. Borum, D. Young, A. Siriwat, E. Dickens, C. Oriakhi, M. Lerner. *Appl Clay Sci* 1999, 15, 265.
- [16] C.O. Oriakhi, I.V. Farr, M.M. Lerner. *Clays Clay Miner* 1997, 45, 194.
- [17] B.K.G. Theng. *The chemistry of clay-organic reactions*. Wiley, New York (1974).
- [18] M. Ogawa, K. Kuroda. *Bull Chem Soc Jpn* 1997, 70, 2593.
- [19] Y. Kojima, A. Usuki, M. Kawasumi, A. Okada, Y. Fukushima, T. Kurauchi, O. Kamigaito. *J Mater Res* 1993, 6, 1185.
- [20] E.P. Giannelis, R. Krishnamoorti, E. Manias. *Adv Polym Sci* 1999, 118, 108.
- [21] G. Lagaly. *Solid State Ionics* 1986, 22, 43.
- [22] R.A. Vaia, R.K. Teukolsky, E.P. Giannelis. *Chem Mater* 1994, 6, 1017.
- [23] J.G. Doh, I. Cho. *Polym Bull.* 1998, 41, 511.
- [24] M.W. Weimer, H. Chen, E.P. Giannelis, D.Y. Sogah. *J Am Chem Soc* 1999, 121, 1615.
- [25] C. Oriakhi. *Chem Br* 1998, 34, 59.
- [26] Y. Kojima, A. Usuki, M. Kawasumi, A. Okada, T. Kurauchi, O. Kamigaito. *J Polym Sci Part A Polym Chem* 1993, 31, 983.
- [27] Y. Kojima, A. Usuki, M. Kawasumi, A. Okada, T. Kurauchi, O. Kamigaito. *J Polym Sci Part A Polym Chem* 1993, 31, 1755.
- [28] N. Hasegawa, M. Kawasumi, M. Kato, A. Usuki, A. Okada. *J Appl Polym Sci* 1998, 67, 87.
- [29] L. Mullins, N.R. Tobin. *J Appl Polym Sci* 1965, 9, 2993.
- [30] D.C. Lee, L.W. Jang. *J Appl Polym Sci* 1996, 61, 1117.
- [31] M.W. Noh, D.C. Lee. *Polym Bull* 1999, 42, 619.
- [32] T. Lan, T.J. Pinnavaia. *Chem Mater* 1994, 6, 2216.
- [33] T. Lan, P.D. Kaviratna, T.J. Pinnavaia. *Chem Mater* 1995, 7, 2144.

- [34] C. Zilg, R. Mu Elhaupt, J. Finter. *Macromol Chem Phys* 1999, 200, 661.
- [35] Z. Wang, T.J. Pinnavaia. *Chem Mater* 1998, 10, 1820.
- [36] Z. Wang, T.J. Pinnavaia. *Chem Mater* 1998, 10, 3769.
- [37] Y. Yang, Z.K. Zhu, J. Yin, X.Y. Wang, Z.E. Qi. *Polymer* 1999, 40, 4407.
- [38] P.H. Nam, P. Maiti, M. Okamoto, T. Kotaka, N. Hasegawa, A. Usuki. *Polymer* 2001, 42, 9633.
- [39] X. Liu, Q. Wu. *Polymer* 2001, 42, 10013.
- [40] P. Maiti, P.H. Nam, M. Okamoto, T. Kotaka, N. Hasegawa, A. Usuki. *Macromolecules* 2002, 35, 2042.
- [41] S.S. Ray, P. Maiti, M. Okamoto, K. Yamada, K. Ueda. *Macromolecules* 2002, 35, 3104.
- [42] A. Usuki, Y. Kojima, M. Kawasumi, A. Okada, Y. Fukushima, T. Kurauchi, O. Kamigaito. *J Mater Res* 1993, 8, 1179.
- [43] M. Laus, O. Francesangeli, F. Sandrolini. *J Mater Res* 1997, 12, 3134.
- [44] P.B. Messersmith, E.P. Giannelis. *Chem Mater* 1994, 6, 1719.
- [45] A. Okada, A. Usuki. *Mater Sci Eng* 1995, C3, 109.
- [46] A. Blumstein. *J Polym Sci A* 1965, 3, 2665.
- [47] M. Biswas, S.S. Ray. *Adv Polym Sci* 2001, 155, 167.
- [48] E.P. Giannelis. *Appl Organomet Chem* 1998, 12, 675.
- [49] J.W. Gilman. *Appl Clay Sci* 1999, 15, 31.
- [50] M. Alexandre, P. Dubois. *Mater Sci Eng* 2000, 28, 1.
- [51] B. Lepoittevin, M. Devalckenaere, N. Pantoustier, M. Alexandre, D. Kubies, C. Calberg, R. Jerome, P. Dubois. *Polymer* 2002, 43, 4017.
- [52] G. Camino, R. Sgobbi, S. Colombier, C. Scelza. *Fire Mater* 2000, 24, 85.
- [53] J.W. Gilman, T. Ksahiwagi, E.P. Giannelis, E. Manias, S. Lomakin, J.D. Lichtenhan, P. Jones. Flammability properties of polymer/layered silicate nanocomposites. In *Chemistry and technology of polymer additives*. S. Al-Malaika, A. Golovoy, C.A. Wilkie editors. Oxford: Blackwell Science (1999) Chapter 14.
- [54] G.S. Sur, H.L. Sun, S.G. Lyu, J.E. Mark. *Polymer* 2001, 42, 9783.
- [55] J. Zhu, A.B. Morgan, F.J. Lamelas, C.A. Wilkie. *Chem Mater* 2001, 13, 3774.
- [56] J.T. Yoon, W.H. Jo, M.S. Lee, M.B. Ko. *Polymer* 2001, 42, 329.
- [57] S.T. Lim, Y.H. Hyun, H.J. Choi, M.S. Jhon. *Chem Mater* 2002, 14, 1839.
- [58] S.T. Lim, Y.H. Hyun, H.J. Choi, M.S. Jhon. *Chem Mater* 2002, 14, 1839.

- [59] J.W. Gilman, C.L. Jackson, A.B. Morgan, R. Harris Jr, E. Manias, E.P. Giannelis, M. Wuthenow, D. Hilton, S.H. Phillips. *Chem Mater* 2000, 12, 1866.
- [60] R. Xu, E. Manias, A.J. Snyder, J. Runt. *Macromolecules* 2001, 34, 337.
- [61] K. Yano, A. Usuki, A. Okada, T. Kurauchi, O. Kamigaito. *J Polym Sci Part A: Polym Chem* 1993, 31, 2493.
- [62] K. Yano, A. Usuki, A. Okada, T. Kurauchi, O. Kamigaito. *Polym Prepr Jpn* 1991, 32, 65.
- [63] K. Yano, A. Usuki, A. Okada A. *J Polym Sci Part A: Polym Chem* 1997, 35, 2289.
- [64] T. Lan, P.D. Kaviratna, T.J. Pinnavaia. *Chem Mater* 1994, 6, 573.
- [65] P.B. Messersmith, E.P. Giannelis. *J Polym Sci Part A: Polym Chem* 1995, 33, 1047.
- [66] C. Scherer. PA film grade with improved barrier properties for flexible food packaging applications. In *Proceedings of the New plastics'99*, London, February 1999.
- [67] K.E. Strawhecker, E. Manias E. *Chem Mater* 2000, 12, 2943.
- [68] P.H. Nam, P. Maiti, M. Okamaoto, T. Kotaka. *Proceeding nanocomposites*. June 25–27, 2001, Chicago, Illinois, USA: ECM Publication (2001).
- [69] *Nanoscience and Nanotechnologies*, July 2004, The Royal Society & the Royal Academy of Engineering.
- [70] J. Tang, Y. Wang, H. Liu, Y. Xia, B. Schneider. *J Appl Polym Sci* 2003, 90, 1053.
- [71] Private Communication with Dr Jihua Chen, at AMTC/NRC, Montreal 2005.
- [72] D. Ma, T.A. Hugener, R.W. Siegel, A. Christerson, E. Martensson, C. Onneby, L. Schadler, L. *Nanotech* 2005, 16, 724.
- [73] Y.C. Chen, S.X. Zhou, H.H. Yang, L.M. Wu. *J Appl Polym Sci* 2005, 95, 1032.
- [74] M. Zhang, R. Singh *Mater Lett* 2004, 58, 408.
- [75] V. Yong, H.T. Hahn. *Nanotech* 2004, 15, 1338.
- [76] S. Lao, W. Ho, K. Ngyuen, J.H. Koo. Microstructural analyses of nylon 11 nanocomposites. 37th International SAMPE Technical Conference, Seattle, WA, October 2005.
- [77] C.L. Wu, M.Q. Zhang, M.Z. Rong, K. Friedrich. *Compos Sci Technol* 2002, 62, 1327.
- [78] Z. Zhang, J.L. Yang. *Polymer* 2004, 45, 3481.
- [79] J.H. Koo, L.A. Pilato, G.E. Wissler. Polymer nanostructured materials for propulsion system. 41st AIAA/ASME/SAE/ASEE Joint Propulsion Conference & Exhibit, Tucson, AZ, July 2005.

- [80] J.H. Koo, J. Stretz, Z. Weispfenning, P. Luo, W. Wootan. Nanocomposite rocket ablative materials: subscale ablation test. SAMPE Conference, Long Beach, CA, May 2004.
- [81] J.H. Koo, L.A. Pilato, G. Wissler, A. Lee, A. Abusafieh, J. Weispfenning. Epoxy nanocomposites for carbon fiber reinforced polymer matrix composites. SAMPE Conference, Long Beach, CA, May 2005.
- [82] Y.Y. Yu, C.Y. Chen, W.C. Chen. *Polymer* 2003, 44, 593.
- [83] Y.L. Liu, C.Y. Hsu, K.Y. Hsu. *Polymer* 2005, 46, 1851.
- [84] Y. Ou, F. Yang, Z. Yu. *J Polym Sci Part B Polym Phys* 1998, 36, 789.
- [85] L. Jiang, Y.C. Lam, K.C. Tam, T.H. Chua, G.W. Sim, L.S. Ang. *Polymer* 2005, 46, 243.
- [86] Y. Chen, S. Zhou, H. Yang, G. Gu, L. Wu. *J Colloid Interf Sci* 2004, 276, 370.
- [87] L. Lopez, B.M.K.. Song, H.T. Hahn. The effect of particles size in alumina nanocomposites. ICCM 14th Conference, San Diego, CA, July 2003.
- [88] N. Chisholm, H. Mahfuz, V.K. Rangari, S. Jeelani. *Compos Struct* 2005, 67, 115.
- [89] J.C. Lin, L.C. Chang, M.H. Nien, H.L. Ho. *Compos Struct* 2006, 74, 30.
- [90] M. Avalle, G. Belingardi, R. Montanini. *Int J Impact Eng* 2001, 25, 455.
- [91] H. Mahfuz, M.S. Islam, V.K. Rangari, S. Jeelani. *Compos Part A* 2004, 35, 453.
- [92] M. Uddin, H. Mahfuz, M. Saha, V.K. Ragari, S. Jeelani. Strain rate effects on nanophased polyurethane foams. SAMPE Conference Proceedings (2004) pp. 2291–2304.
- [93] H. Mahfuz, M. Islam, M.C. Saha, S. Jeelani. *Composites Part B* 2004, 35, 543.
- [94] J.J. Schwab, J.D. Lichtenhan. *Appl Organometal Chem* 1998, 12, 707.
- [95] M.G. Voronkov, V. Lavrentev. *Top Curr Chem* 1982, 102, 199.
- [96] F.J. Feher, T.A. Budzichowski. *J Organometal Chem* 1989, 379, 33.
- [97] F.J. Feher, T.A. Budzichowski. *J Organometal Chem* 1989, 373, 153.
- [98] J.D. Lichtenhan, C.J. Noel, A.G. Bolf, P.N. Ruth. *Mat Res Soc Symp Proc* 1996, 435, 3.
- [99] G.Z. Li, L.C. Wang, H. Toghiani, T.L. Daulton, K. Koyama, C.U. Pittman. *Macromolecules* 2001, 34, 8686.
- [100] T.S. Haddad, J.D. Lichtenhan. *Macromolecules* 1996, 29, 7302.
- [101] S.B. Chun, P.T. Mather. *Mat Res Soc Symp Proc* 2001, 661, KK10.18.11.
- [102] J.D. Lichtenhan, N.Q. Vu, J.A. Carter. *Macromolecules* 1993, 26, 2141.
- [103] J.J. Schwab, W.A. Reinert Sr, J.D. Lichtenhan. *Polym Prepr* 2001, 42, 48.
- [104] D.W. Scott. *J Am Chem Soc* 1946, 68, 356.
- [105] F.J. Feher, T.A. Budzichowski, K.J. Weller. *J Am Chem Soc* 1989, 111, 7288.

- [106] F.J. Feher, D.A. Newman, J.F. Walzer. *J Am Chem Soc* 1989, 111, 1741.
- [107] F.J. Feher, R.L. Blanski. *J Chem Soc Chem Commun* 1990, 1614.
- [108] F.J. Feher, D.A. Newman. *J Am Chem Soc* 1990, 112, 1931.
- [109] F.J. Feher, T.A. Budzichowski, R.L. Blanski, K. Weller. *J Organometallics* 1991, 10, 2526.
- [110] F.J. Feher, S.H. Phillips, J.W. Ziller. *J Am Chem Soc* 1997, 119, 3397.
- [111] F.J. Feher, K.D. Wyndham, D.J. Knauer. *J Chem Commun* 1998, 2393.
- [112] F.J. Feher, D. Soulivong, F. Nguyen, J.W. Ziller. *Angew Chem-Int Edit* 1998, 37, 2663.
- [113] F.J. Feher, K.D. Wyndham, M.A. Scialdone, Y. Hamuro. *Chem Commun* 1998, 1469.
- [114] F.J. Feher, D. Soulivong, F. Nguyen. *Chem Commun* 1998, 1279.
- [115] F.J. Feher, K.D. Wyndham. *Chem Commun* 1998, 323.
- [116] F.J. Feher, D. Soulivong, A.G. Eklund. *Chem Commun* 1998, 399.
- [117] F.J. Feher, R. Terroba, J.W. Ziller. *Chem Commun* 1999, 2309.
- [118] F.J. Feher, R. Terroba, J.W. Ziller. *Chem Commun* 1999, 2153.
- [119] F.J. Feher, F. Nguyen, D. Soulivong, J.W. Ziller. *Chem Commun* 1999, 1705.
- [120] F.J. Feher, K.D. Wyndham, D. Soulivong, F.J. Nguyen. *Chem Soc-Dalton Trans.* 1999, 1491.
- [121] F.J. Feher, R. Terroba, R. Jin, K.D. Wyndham, S. Lucke. *Polym Mater Sci Eng* 2000, 82, 301.
- [122] R. Bakhtiar, F.J. Feher. *Rapid Commun Mass Spectrom* 1999, 13, 687.
- [123] J.D. Lichtenhan, Y.A. Otonari, M.J. Carr. *Macromolecules* 1995, 28, 8435.
- [124] J.D. Lichtenhan. *Comments Inorg Chem* 1995, 17, 115.
- [125] J.D. Lichtenhan, C.J. Noel, A.G. Bolf, P.N. Ruth. *Mat Res Soc Symp Proc.* 1996, 435, 3.
- [126] R.M. Laine, A. Sellinger. *Macromolecules* 1996, 29, 2327.
- [127] P.T. Mather, T.S. Haddad, H.W. Oviatt, J.J. Schwab, K.P. Chaffee, J.D. Lichtenhan. *Polym Prepr* 1998, 39, 611.
- [128] J.F. Brown, L.H. Vogt. *J Am Chem Soc* 1965, 87, 4313.
- [129] C.L. Frye, W.T. Collins. *J Am Chem Soc* 1970, 92, 5586.
- [130] A. Sellinger, R.M. Laine. *Chem Mater* 1996, 8, 1592.
- [131] A. Sellinger, R.M. Laine. *Macromolecules* 1996, 29, 2327.
- [132] C. Zhang, R.M. Laine. *J Am Chem Soc* 2000, 122, 6979.

- [133] J. Pyun, K. Matyjaszewski. *Macromolecules* 2000, 33, 217.
- [134] A. Lee, J.D. Lichtenhan. *Macromolecules* 1998, 31, 4970.
- [135] R.A. Manze, P.F. Jones, K.P. Chaffee, J.D. Lichtenhan. *Chem Mater* 1996, 8, 1250.
- [136] T.S. Haddad, B.D. Viers, S.H. Phillips. *J Inorg Organomet Polym* 2002, 11, 155.
- [137] A. Romo-Uribe, P.T. Mather, T.S. Haddad, J.D. Lichtenhan. *J Polym Sci Part B: Polym Phys* 1998, 36, 1857.
- [138] H.Y. Xu, S.W. Kuo, J.S. Lee, F.C. Chang. *Macromolecules* 2002, 35, 8788.
- [139] A. Lee, J.D. Lichtenhan, W.A. Reinert Sr. *Polym Mater Sci Eng* 2000, 82, 235.
- [140] P.T. Mather, H.G. Jeon, A. Romo-Uribe, T.S. Haddad, J.D. Lichtenhan. *Macromolecules* 1999, 32, 1194.
- [141] H.G. Jeon, P.T. Mather, T.S. Haddad. *Polym Inter* 2000, 49, 453.
- [142] B.K. Bharadwaj, R.J. Berry, B.L. Farmer. *Polymer* 2000, 41, 7209.
- [143] B.X. Fu, B.S. Hsiao, H. White. *Polym Inter* 2000, 49, 437.
- [144] B.X. Fu, B. Hsiao, S. Pagola, P. Stephens. *Polymer* 2001, 42, 599.
- [145] G.Z. Li, L. Wang, H. Toghiani, C.U. Pittman Jr. *Polymer* 2002, 43, 4167.
- [146] G.Z. Li, H. Cho, L.C. Wang, H. Toghiani, C.U. Pittman. *J Polym Sci Pol Chem* 2005, 43, 355.
- [147] L. Matejka, A. Strachota, J. Plestil, P. Whelan, M. Steinhart, M. Slouf. *Macromolecules* 2004, 37, 9449.
- [148] A. Strachota, I. Kroutilova, J. Kovarova, L. Matejka. *Macromolecules* 2004, 37, 9457.
- [149] Y.J. Lee, J.M. Huang, S.W. Kuo, J.S. Lu, F.C. Chang. *Polymer* 2005, 46, 173.
- [150] K.M. Kim, K. Adachi, Y. Chujo. *Polymer* 2002, 43, 1171.
- [151] K.H. Yoon, M.B. Polk, J.H. Park, B.G. Min, D.A. Schiraldi. *Polym Inter* 2005, 54, 47.
- [152] R.L. Blanski, S.H. Phillips, K. Chaffee, J.D. Lichtenhan. *Mat Res Soc Sym Proc* 2000, 628.
- [153] B.X. Fu, L. Yang, R.H. Somani, S.X. Zong, B. Hsiao. *J Polym Sci Part B: Polym Phys* 2001, 39, 2727.
- [154] B. X. Fu, B. S. Hsiao, S. Pagola, P. Stephens, H. White, M. Rafailovich, J. Sokolov, P. T. Mather, H. G. Jeon, S. Phillips. *Polymer* 2001, 42, 599.
- [155] G. M. Kim, H. Qin, X. Fang, F.C. Sun, P.T. Mather. *J Polym Sci Part B: Polym Phys* 2003, 41, 3299.
- [156] S. Bizet, J. Galy, J.F. Gerard. *Macromolecules* 2006, 39, 2574.

- [157] B. X. Fu, B. S. Hsiao, M. Rafailovich, j. Sokolov, G. Johansson, B.B. Sauer, S. Phillips, R. Balski. *High Perform Polym* 2000, 12, 565.
- [158] B.-S. Kim, P. T. Mather. *Macromolecules* 2002, 35, 8378.
- [159] L. Zheng, R. J. Farris, E. B. Couchlin. *Macromolecules* 2001, 34, 8034.
- [160] E. Tegou, V. Bellas, E. Gogolides, P. Agritis. *Microelectron Eng* 2004, 238, 73.
- [161] T.S. Haddad, J.D. Lichtenhan, *Macromolecules* 1996, 29, 7302.
- [162] L. Zheng, R.J. Farris, E.B. Couchlin. *Macromolecules* 2001, 34, 8034.

Chapter 2

Reinforcement of thermoplastic polymer based nanocomposites

2.1 Nanoplatelets-reinforced nanocomposites

Properly dispersed and aligned clay platelets have proven to be very effective for increasing stiffness of the polymer matrix. In particular, a good dispersion of clay generally yields enhanced Young's modulus, storage modulus and tensile strength, but significantly reduced tensile ductility and impact strength compared to neat polymer.

Figure 2.1 shows the typical tensile properties of the PE compatibilized with maleic anhydride (MA-g-PE) filled with oMMT. The tensile strength and modulus tend to increase with increasing clay content. Such an increasing trend is more obvious for the tensile modulus. The increase in the tensile strength is higher at low clay content, indicating that the clay layers are better exfoliated. The reinforcing effect is lower for nanocomposites with higher clay content owing to some clay platelets being partially exfoliated and stacked. From Figure 2.1b, the strain at break decreases with increasing clay content as expected [1]. Osman et al. studied the effect of the degree of exfoliation on tensile properties of the melt compounded PE/oMMT nanocomposites using different organomodifiers [2]. No one lead complete exfoliation in the nanocomposites. Figure 2.2 shows the relative elastic modulus and stress at break of the nanocomposite as a function of the d -spacing of organoclay. Apparently, the modulus steadily increases with increasing d -spacing (increasing of the intercalation degree). The relative yield stress and yield strain versus d -spacing of the PE/oMMT at 2.8 vol% are shown in Figure 2.3. With increasing exfoliation, a monotonous increase in the yield stress and decrease in the yield strain are observed.

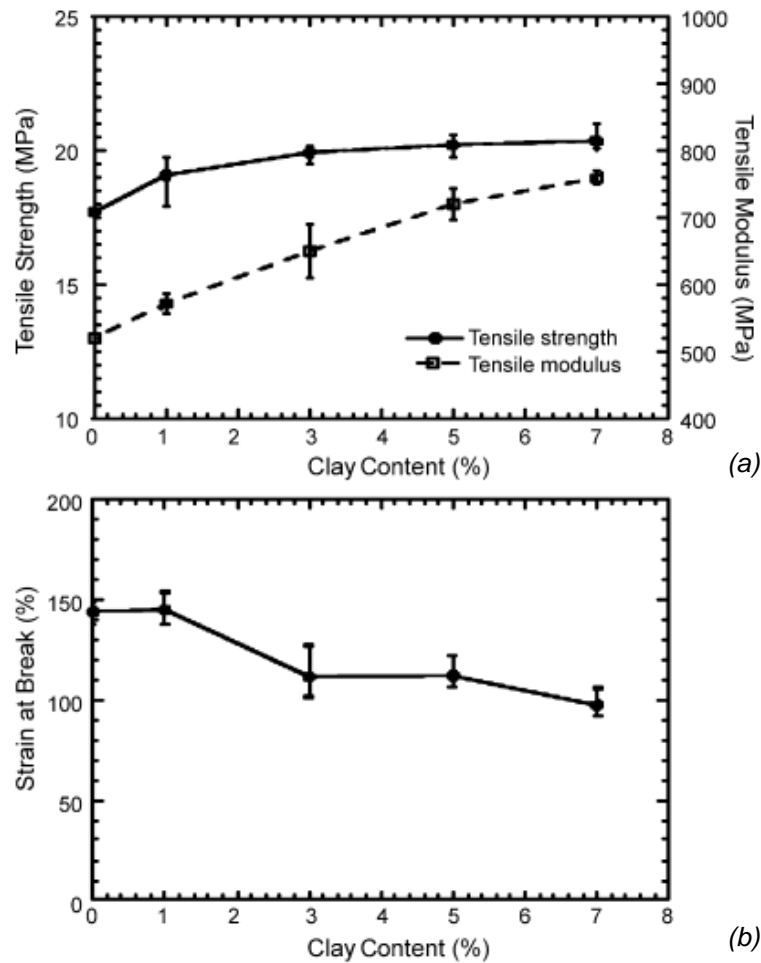


Figure 2.1 Tensile modulus and strength (a) and strain at break (b) vs. clay content for MA-g-PE/oMMT nanocomposites (reprinted from [1]).

Figure 2.4 shows a comparison between the increase in the tensile modulus of a polyamide 6 (PA6) filled with oMMT versus glass fibers [3]. In this example, increasing the modulus by a factor of two relative to that of neat PA6 requires approximately three times more mass of glass fibers than that of oMMT platelets. Thus, the nanocomposite has a weight advantage over the conventional glass fiber composite. Furthermore, if the platelets are aligned in the plane of the sample, the same reinforcement should be seen in all directions within the plane, whereas fibers reinforce only along a single axis in the direction of their alignment [4].

Figure 2.5 shows an analogous comparison of nanocomposites based on thermoplastic polyolefin (TPO) matrix with conventional talc filled TPO [5]. In this case, doubling the modulus of the TPO requires more than four times more talc than oMMT. The PA6 based nanocomposites in Figure 2.4 are very highly exfoliated, whereas the exfoliation of the clay in

the TPO of Figure 2.5 is only partially exfoliated [5]. However, it should be recognized that the talc particles do not have as high aspect ratio as the glass fibers used in these comparisons. Another factor at play here is the lower modulus of TPO than PA6. The lower the matrix modulus, the greater is the relative increase in reinforcement caused by adding a filler [6].

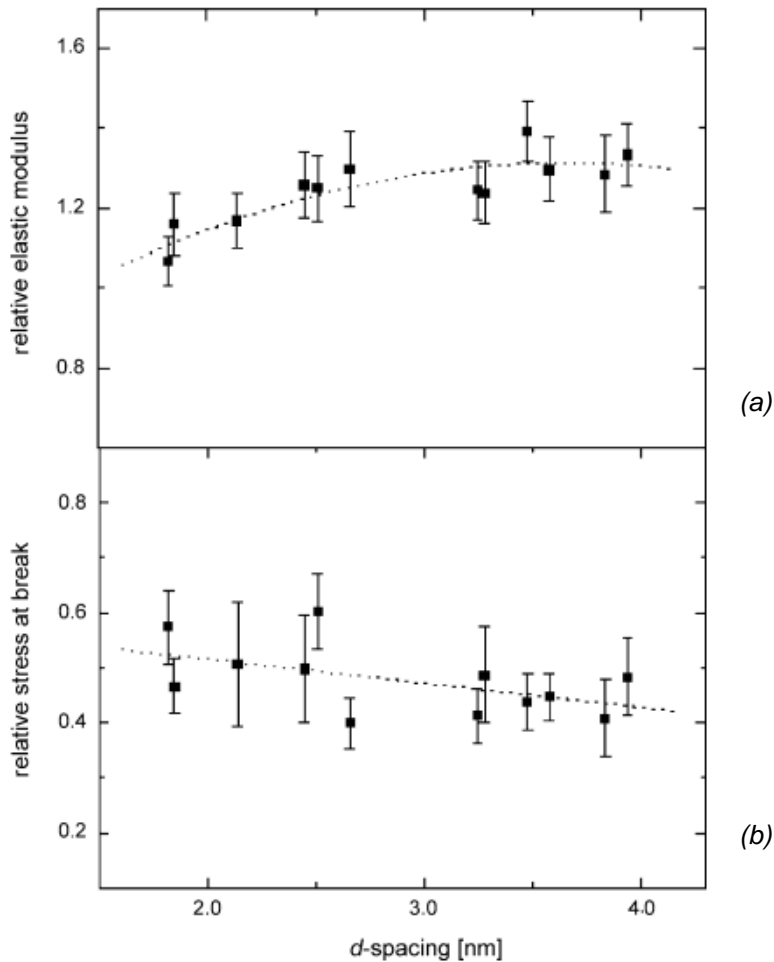


Figure 2.2 The relative elastic modulus (a) and stress at break (b) of PE/oMMT nanocomposites (2.8 vol% of filler) plotted as a function of their d-spacings (reprinted from [2]).

Paul and Robeson [7] attributed the large increase in modulus caused by clay platelets or particles relative to conventional fillers is due to some “nano-effect”. They mean some change in the local properties of the matrix caused by the extremely high surface area filler and the small distances between nanofiller particles even at low mass loadings. Indeed, the polymer/clay nanocomposites exhibit extremely large interface polymers due to the

confinement of polymer chains within the galleries of clay platelets of large surface area per unit volume. It is considered that the confinement of polymer/clay interactions would affect the local chain dynamics to a certain extent. Since several chemical and physical interactions are governed by surfaces, polymer/clay nanocomposites can have substantially different properties from conventional polymer microcomposites. A key issue arises whether the composite mechanics theories of reinforcement can be applied to explain the mechanical properties of polymer/clay nanocomposites.

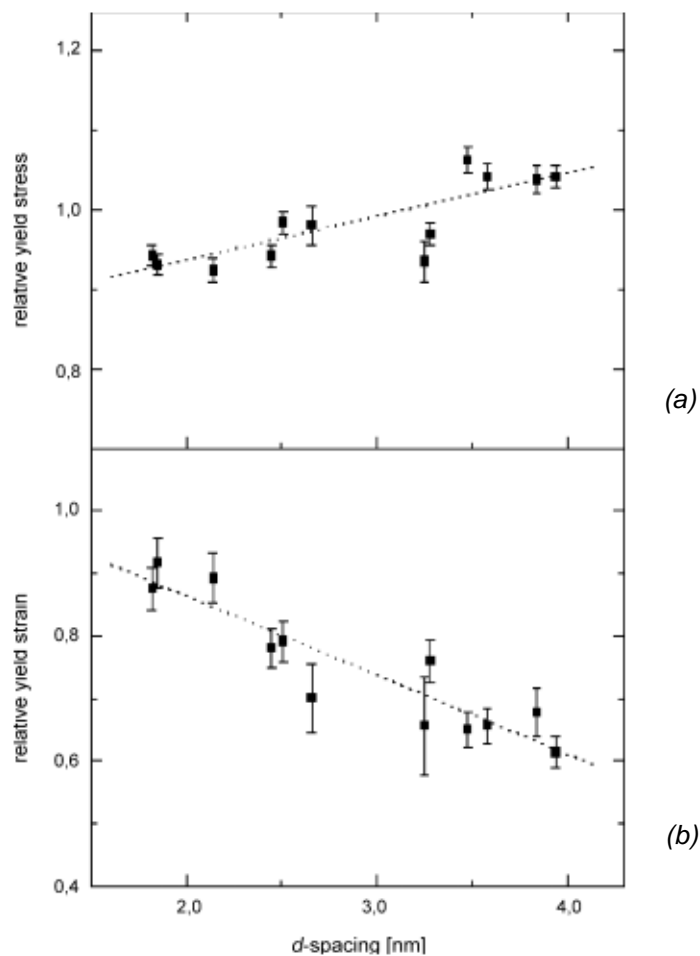


Figure 2.3 The relative yield stress (a) and strain (b) of PE/oMMT nanocomposites (2.8 vol% of filler) plotted as a function of their d-spacings (reprinted from [191]).

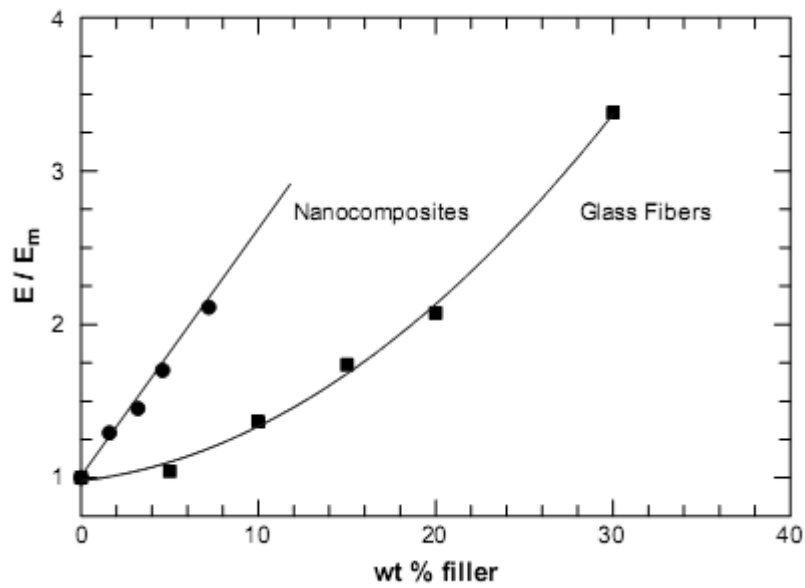


Figure 2.4 Comparison of relative modulus of PA6 based nanocomposites filled with oMMT and glass fiber (aspect ratio ~20) (reprinted from [3]).

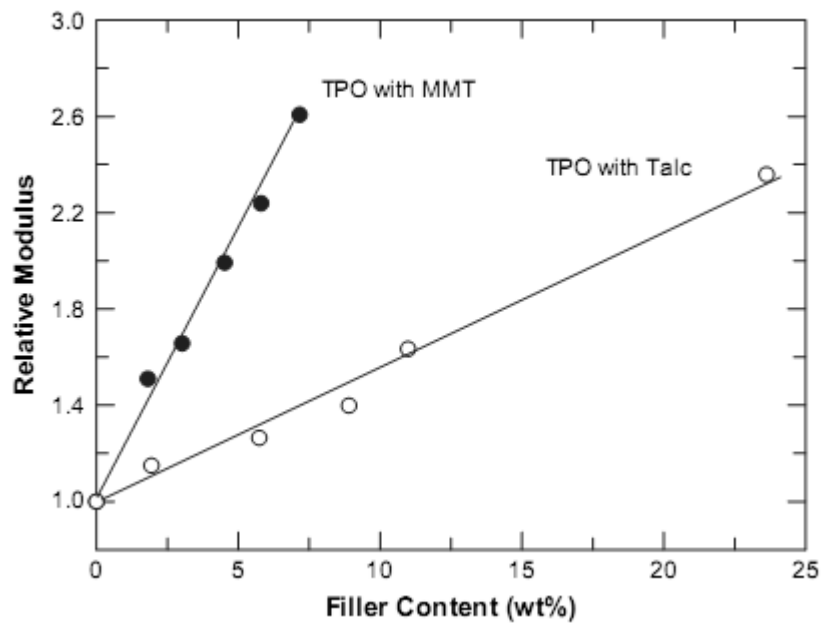


Figure 2.5 Comparison of relative modulus of TPO based nanocomposites filled with oMMT and talc (reprinted from [5]).

Several micromechanical models have been developed to predict the macroscopic behavior of polymer microcomposites. These include Halpin–Tsai, Mori–Tanaka, etc. The models generally include parameters such as the aspect ratio, volume fraction and the orientation of the reinforcement. It appears that the direct use of micromechanical models for polymer/clay nanocomposites is inappropriate without taking into account the intrinsic hierarchical morphology of intercalated nanoclay with large surface area and expanded gallery spacing.

The elastic modulus of the composite material can be predicted from the Halpin–Tsai equation assuming the fibers are discontinuous and aligned uniaxially [8,9]. The longitudinal elastic modulus of composites E_c , is given by

$$\frac{E_c}{E_m} = \frac{1 + \xi\eta\phi}{1 - \eta\phi} \quad (2.1)$$

where E_m is the tensile modulus of the matrix and ϕ is the volume fraction of fiber reinforcement. The constants ξ and η are given by

$$\xi = 2 \left(\frac{l}{d} \right) \quad (2.2)$$

$$\eta = \frac{\frac{E_f}{E_m} - 1}{\frac{E_f}{E_m} + \xi} \quad (2.3)$$

where l/d is the aspect ratio (length/diameter) of the reinforcing fibers.

The Mori–Tanaka mean field theory is used to assess the overall properties such as the effective stiffness tensor C^* of the composites. It is based on Eshelby method for estimating stress state in composite reinforced with misfitting inclusions. The composite is assumed to be composed of a continuous matrix and discrete of inclusions of different stiffness. The effective stiffness tensor C^* is given by the following relation [10,11]:

$$C^* = C_1 + V_2 \{ (C_2 - C_1) A \} \quad (2.4)$$

where C_1 is the matrix phase stiffness tensor, C_2 the inclusion stiffness tensor, V_2 the inclusion volume ratio, and A is the concentration tensor.

For a composite consisting of a single, arbitrarily shaped inclusion perfectly bonded inside the matrix, the dilute strain concentration tensor of the effective particle is given by:

$$A^{(\text{dil})} = [I + SC^{-1}(C_2 - C_1)]^{-1} \quad (2.5)$$

where I is the fourth order unit tensor and S the fourth order Eshelby tensor. As the inclusion volume fraction increases, interaction between the inclusions reduces the accuracy of the dilute approximation. In other words, interactions of the field from other inclusions are expected to influence the evolution of the average fields in the matrix and the reinforcement. The Mori–Tanaka approach includes the effect of particle interaction [12]. In this case, A can be expressed as

$$A = A^{(dil)} [V_1 I + V_2 \{A^{(dil)}\}]^{-1} \quad (2.6)$$

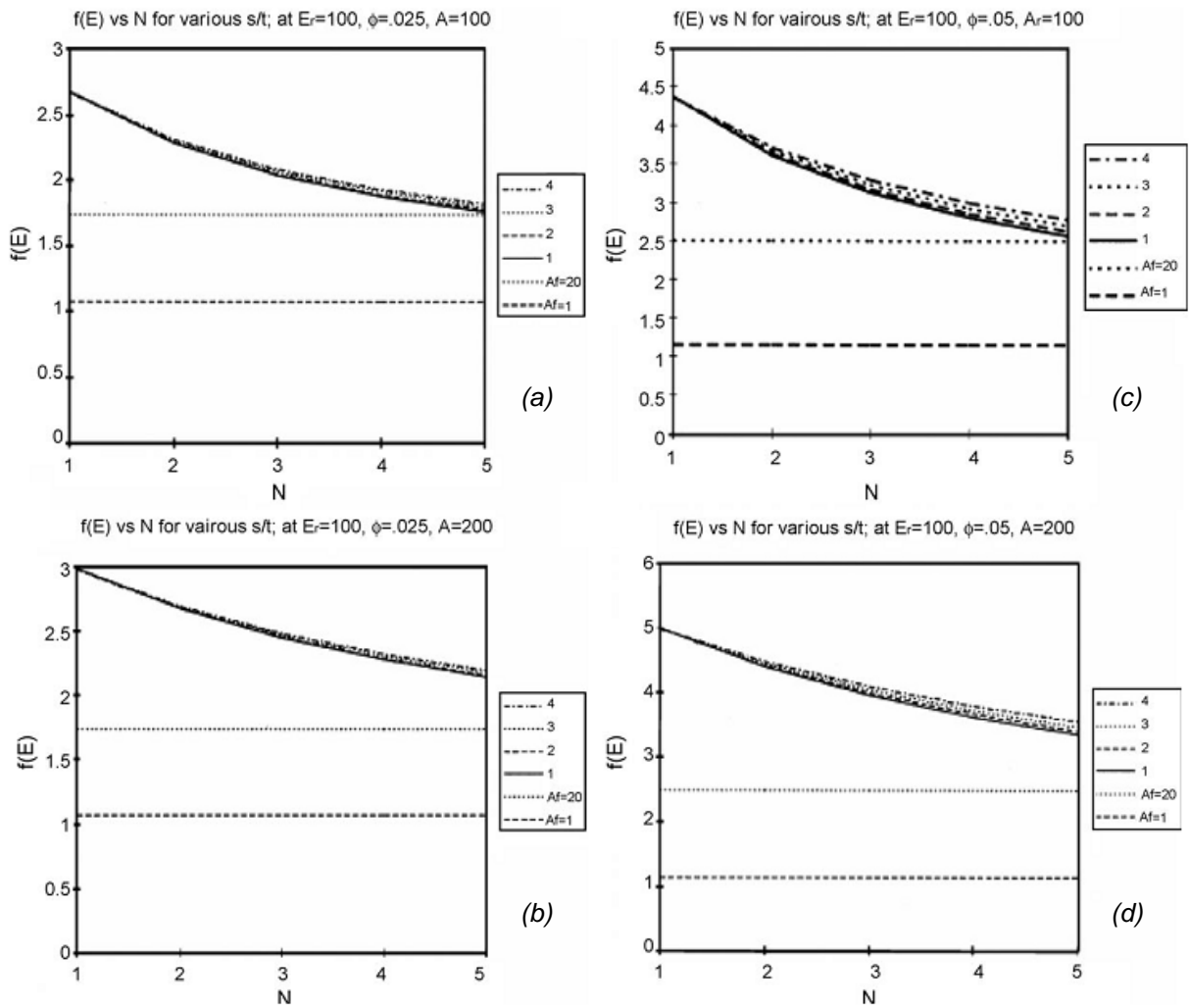


Figure 2.6 Ratio of composite modulus to matrix modulus, $f(E)$, as a function of number N of platelets in a typical stack, for s/t ratios 1, 2, 3 and 4. Dashed horizontal lines corresponding to the $f(E)$ values calculated for platelets of aspect ratio 1 and 20 (as in conventional un-exfoliated fillers) (reprinted from [14]).

where V_1 is the matrix volume ratio. The Mori–Tanaka model has better predictive capability for fillers with relatively high aspect ratios. Tandon and Weng based on the Mori–Tanaka approach and derived the longitudinal modulus (E_{11}) of the composite reinforced with platelets [13]:

$$\frac{E_{11}}{E_m} = \frac{1}{1 + \phi_f [-2v_m A_3 + (1 - v_m) A_4 + (1 + v_m) A_5 A] / 2A} \quad (2.7)$$

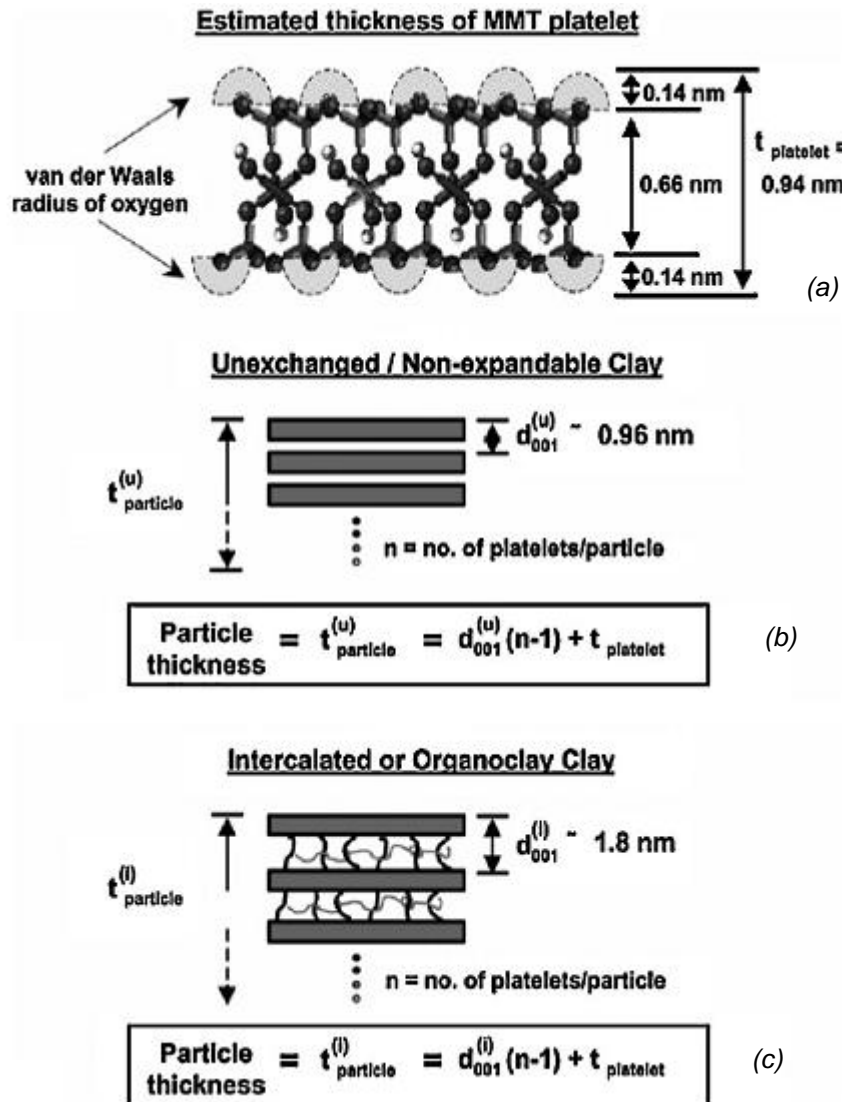


Figure 2.7 Schematic diagrams showing the determination of particle thickness of an individual oMMT platelet (a), an unexchanged or non-expandable clay stack (b), and an organoclay stack intercalated with surfactant and polymer (c) (reprinted from [15]).

where ν_m is the Poisson's ratio of the matrix, and A , A_3 , A_4 and A_5 are calculated from the matrix and filler properties and the components of the Eshelby tensor.

In polymer/clay nanocomposites, parameters associated with hierarchical morphology of the clay such as the silicate interlayer spacing (d_{001}), gallery spacing, platelet thickness, etc. should be incorporated into the micromechanics model. Brune and Bicerano [14] developed a micromechanics model for the prediction of the effects of incomplete exfoliation on the tensile modulus of polymer/clay nanocomposites. They treated the incomplete exfoliate system as composite consisting of a matrix and pseudoparticles which are incompletely exfoliated stacks of individual platelets. They modified the Halpin–Tsai equation for tensile modulus of intercalated (or incompletely exfoliated) nanocomposites as:

$$\frac{E_c}{E_m} = \frac{1 + \xi' \eta' \phi'}{1 - \eta' \phi'} \quad (2.8)$$

$$\eta' = \frac{E_r' - 1}{E_r' + \xi'} \quad (2.9)$$

where E_r' the ratio of the modulus of the platelet stack to that of the matrix, ξ' the aspect ratio of the platelet stack and ϕ' is the volume fraction of platelet stacks in the matrix. In each platelet stack, there are N platelet layers, and the platelets within a stack can be at various distances from each other.

Assuming t is the thickness of the platelet and s the inter-platelet spacing, then

$$\xi' = \frac{\xi}{\hat{N}} \left[\frac{1}{1 + (1 - 1/\hat{N})(s/t)} \right] \quad (2.10)$$

$$\phi' = \phi \left(1 + \left(1 - \frac{1}{\hat{N}} \right) \right) \frac{s}{t} \quad (2.11)$$

$$E_r' = E_r \left[\frac{1}{1 + (1 - 1/\hat{N})(s/t)} \right] + \frac{(1 - 1/\hat{N})(s/t)}{1 + (1 - 1/\hat{N})(s/t)} \quad (2.12)$$

$$\hat{N} = N + (1 - N) \left(\frac{s}{t} \right) \left(\frac{\phi}{1 - \phi} \right) \quad (2.13)$$

where E_r is the ratio of the platelet to the matrix modulus. When $N = 1$, there is only one platelet in a stack. In this case, ξ' , ϕ' and E_r' become ξ , ϕ and E_r , thus reverting back to Halpin–Tsai equation. When $s/t = 0$, there is no interplatelet layer, thus ϕ' and E_r' should be

equal to ϕ and E_r ; ξ' and ξ should be related by a factor equal to the number of layers. Again, the Halpin–Tsai equation is recovered.

Figure 2.6 are the plots showing the ratio of composite modulus to matrix modulus, $f(E)$, as a function of the number N of platelets in a typical stack, for s/t ratios of 1, 2, 3 and 4. The s/t ratio represents the ratio of the distance between the platelets in a stack to the platelet thickness. For well-exfoliated platelets ($N = 1$), $f(E)$ equals the results obtained from the Halpin–Tsai equation. This figure represents combinations of the following parameters: (a) platelet volume fraction (ϕ) values equal to 0.025 and 0.05; (b) platelet aspect ratio (ξ or A/t) values equal to 100 and 200; (c) ratio of platelet to matrix modulus (E_r) equals to 100. Dashed horizontal lines corresponding to the $f(E)$ values calculated for platelets of aspect ratio 1 (cylinders with height = diameter) and 20 (as in conventional un-exfoliated fillers). This figure clearly shows the $f(E)$ values tend to decrease as more platelets are incorporated into a stack. Accordingly, incomplete exfoliation has a very significant detrimental effect on the reinforcement efficiency [14]. It should be noted that no comparison with experimental data was made to verify the validity of their model.

Recently, Fornes and Paul performed simple calculations on the aspect ratio (l/t) of oMMT platelets of the PA6/oMMT nanocomposites [3]. The clay was modified with bis(hydroxyethyl)-(methyl)-rapeseed quaternary ammonium. Rapeseed is natural product composed predominantly unsaturated C22 alkyl chains (45%). They assumed that the composite consists of a matrix and stacks of clay platelet sheets. For the particle thickness (t) determination, they incorporated several parameters such as the silicate interlayer spacing (d_{001}), number of platelets per particle and the thickness of a oMMT platelet (Figure 2.7). From this, the number average particle thickness was determined to be 1.61 nm. On the basis of image analysis from TEM micrographs of nanocomposites, they determined the number average particle length to be 91 nm. This resulted in an aspect ratio of 57. For an exfoliated structure, the platelets were completely delaminated and dispersed independently in the matrix with a thickness of 0.94 nm. Thus an aspect ratio of 97 was determined for an exfoliated structure. They substituted such particle aspect ratio values together with the stiffness of MMT (178 GPa) and PA6 (2.75 GPa) into Halpin–Tsai equation. The theoretical predicted values and experimental results for the stiffness of nanocomposites are shown in Figure 2.8a.

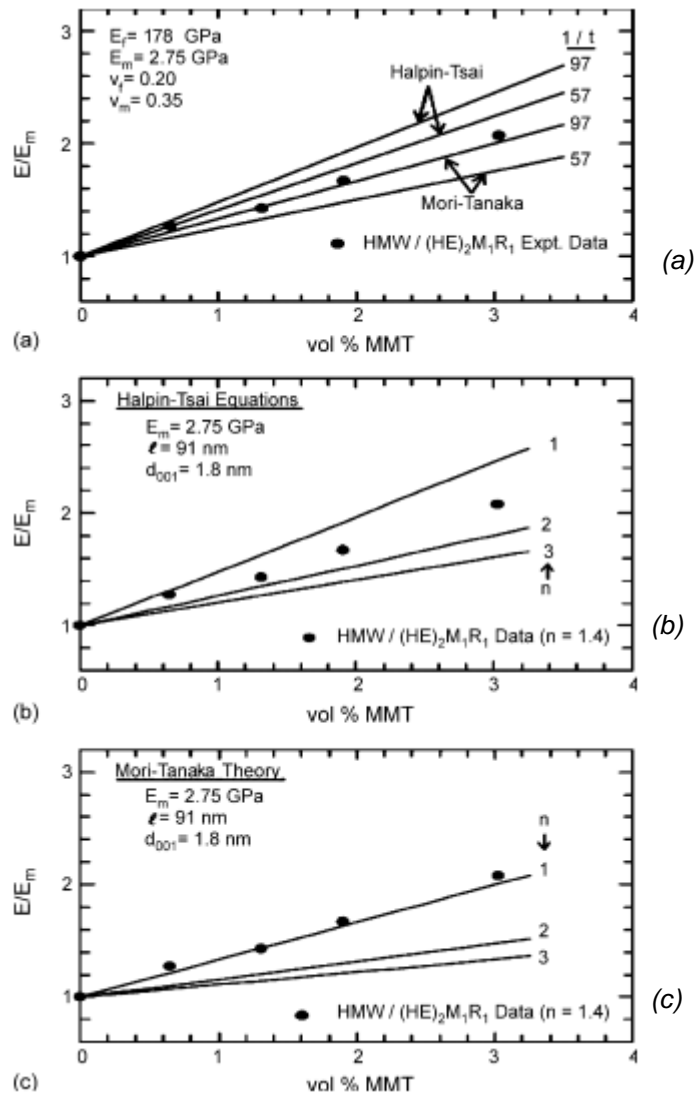


Figure 2.8 Experimental and theoretical stiffness data for PA6 based nanocomposites; model predictions are based on unidirectional reinforcement of pure oMMT ($E_f = 178$ GPa, $l/t = 57$ and 97) corresponding to complete exfoliation (a), and stacks of clay intercalated with polymer having one or more platelets per stack (reprinted from [3]).

Apparently, the experimental results are lower than those of the theoretical prediction, particularly for $l/t = 97$. For the purposes of comparison, elastic modulus prediction from the Mori–Tanaka approach is also shown. The Mori–Tanaka model agrees reasonably with the experimental results at $l/t = 97$ but underpredicts the experimental data at $l/t = 57$. To assess the effect of incompletely exfoliation, the volume fraction ϕ , and stiffness of particle are also modified and evaluated according to geometrical feature and the dispersion of oMMT particles in PA6 as shown in Figure 2.7. Stack properties were based on the experimental

data, i.e. the stacks are 91 nm in length, have a repeat spacing of 1.8 nm, and each individual platelet has a modulus of 178 GPa. They then substituted these values into Halpin–Tsai equation (Figure 2.8b). The experimental data fall between the Halpin–Tsai curves corresponding to 1 and 2 platelets per stack, which is very close to the experimental determined value of 1.4. The experimental data agrees reasonably with Mori–Tanaka model when $n = 1$; this corresponds to a completely exfoliated structure (Figure 2.8c). It is also evident from both theoretical models predicted that increasing the number of platelets per stack results in a decrease of the stiffness of nanocomposite. The composite theories satisfactorily capture the stiffness behavior of the nanocomposites [3].

More recently, Weon and Sue attempted to correlate the experimental stiffness data with those predicted from the Halpin–Tsai and Mori–Tanaka models by incorporating the effective filler structural parameters into the simulations [15]. The thickness of effective filler (Fig. 57) can be expressed as [3]:

$$t_{\text{eff}} = (n - 1)d_{001} + t_p \quad (2.14)$$

The effective filler aspect ratio (α_{eff}), volume fraction (ϕ_{eff}) and modulus (E_f^{eff}) can be written as [16]:

$$\alpha_{\text{eff}} = \frac{l}{t_{\text{eff}}} = \frac{l}{(n - 1)d_{001} + t_p} \quad (2.15)$$

$$\phi_{\text{eff}} = \frac{\psi_{\text{eff}}[(n - 1)d_{001} + t_p] \rho_m}{nt_p \rho_f} \quad (2.16)$$

$$E_f^{\text{eff}} = \frac{nt_p E_f}{[(n - 1)d_{001} + t_p]} \quad (2.17)$$

where ψ_{eff} is effective filler weight fraction, and ρ_f and ρ_m are the densities of the filler and matrix, respectively. From these, the influence of filler aspect ratio on the modulus improvement of the PA6/oMMT nanocomposite is shown in Figure 2.9. Similarly, the Mori–Tanaka model yields better agreement with the experimental data of PA6/oMMT nanocomposite reinforced with the higher aspect ratio fillers.

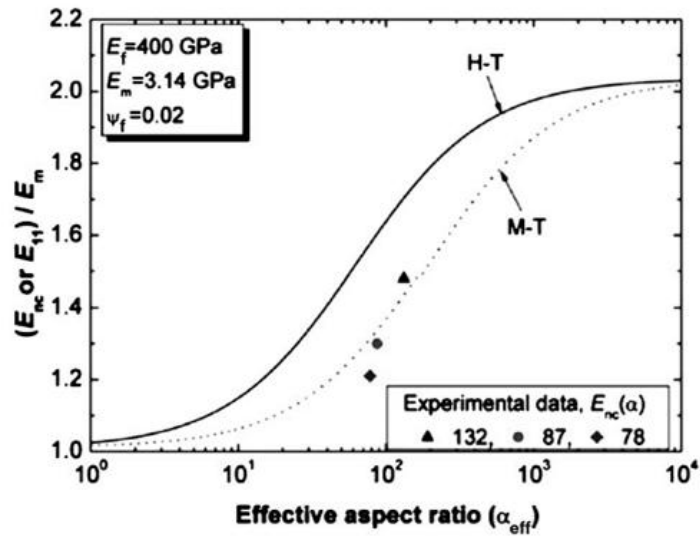


Figure 2.9 Effective filler-based model predictions of the Halpin–Tsai and Mori–Tanaka models for PA6/oMMT nanocomposites (reprinted from [16]).

2.2 Nanoparticles-reinforced nanocomposites

Micron-sized particles of various materials are widely used as mechanical reinforcement of composites, specially to enhance the elastic modulus and the yield strength of the matrix. When the size of the particles are in nanometer scale, it has been observed that the composites achieve novel properties or stronger variations of them. Indeed conventional polymer microcomposites generally require large amounts of fillers (20 vol%) to achieve enhanced stiffness and glass transition temperature [17] but these gains are usually offset by losses in ductility and toughness. Moreover large amount of fillers would also detrimentally affect the processability. Unlike micron-sized fillers, nanoparticles do not lead these effect or in a lesser extent. Singh et al. [18] studied polyester resin/ Al_2O_3 composites with different particles size. Figure 2.10 shows that the initial enhancement in fracture toughness is followed by decreases at higher particle volume fraction. This phenomenon is attributed to the agglomeration of nanoparticles at higher particle volume content. Lopez et al. [19] studied vinyl ester resin/ Al_2O_3 composites with different particles size. They showed an increase of modulus as the filler content increases but a lower strength than the unfilled resin due to non-uniform particle size distribution and particle aggregation. Thompson et al. [20] studied polyimide nanocomposites filled with different metal oxide nanoparticles without to achieve the nanometer scale dispersion. They observed a higher stiffness, comparable or lower strengths

and elongation, and lower dynamic stiffness. Ash et al. [21] studied PMMA/Al₂O₃ composites observing a brittle-to-ductile transition due to the weak interface between matrix and particles. This behavior is attributed to increased polymer chain mobility, due to the presence of smaller particles, and also the capability to relieve tri-axial stress because of poorly bonded larger particles.

In some studies even an improvement of both rigidity and toughness occurred by addition of nanoparticles. Qu et al. [22] prepared PA6/SiO₂ nanocomposites with un-modified and aminobutyric acid-treated silica nanoparticles. Un-modified nanofiller only enhances the tensile stiffness but other mechanical properties remain unchanged or slightly deteriorated (Figure 2.11). The modified one increases the impact strength, tensile ductility and tensile strength (up to 5 wt%, beyond this value the mechanical properties drop). This behavior has been explained in terms of the matrix ligament thickness concept. Mai et al. [23], studying PVC/CaCO₃ nanocomposites, reported that optimal properties such as tensile modulus, tensile yield, tensile strength, elongation at break and impact strength are achieved with 5 wt% of filler content.

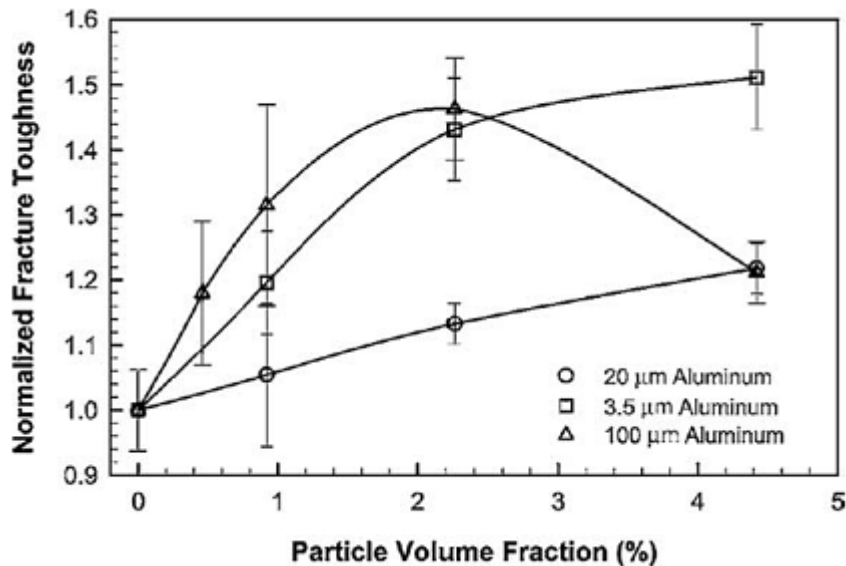


Figure 2.10 Normalized fracture toughness with compared to volume fraction for various sized particles (reprinted from [18]).

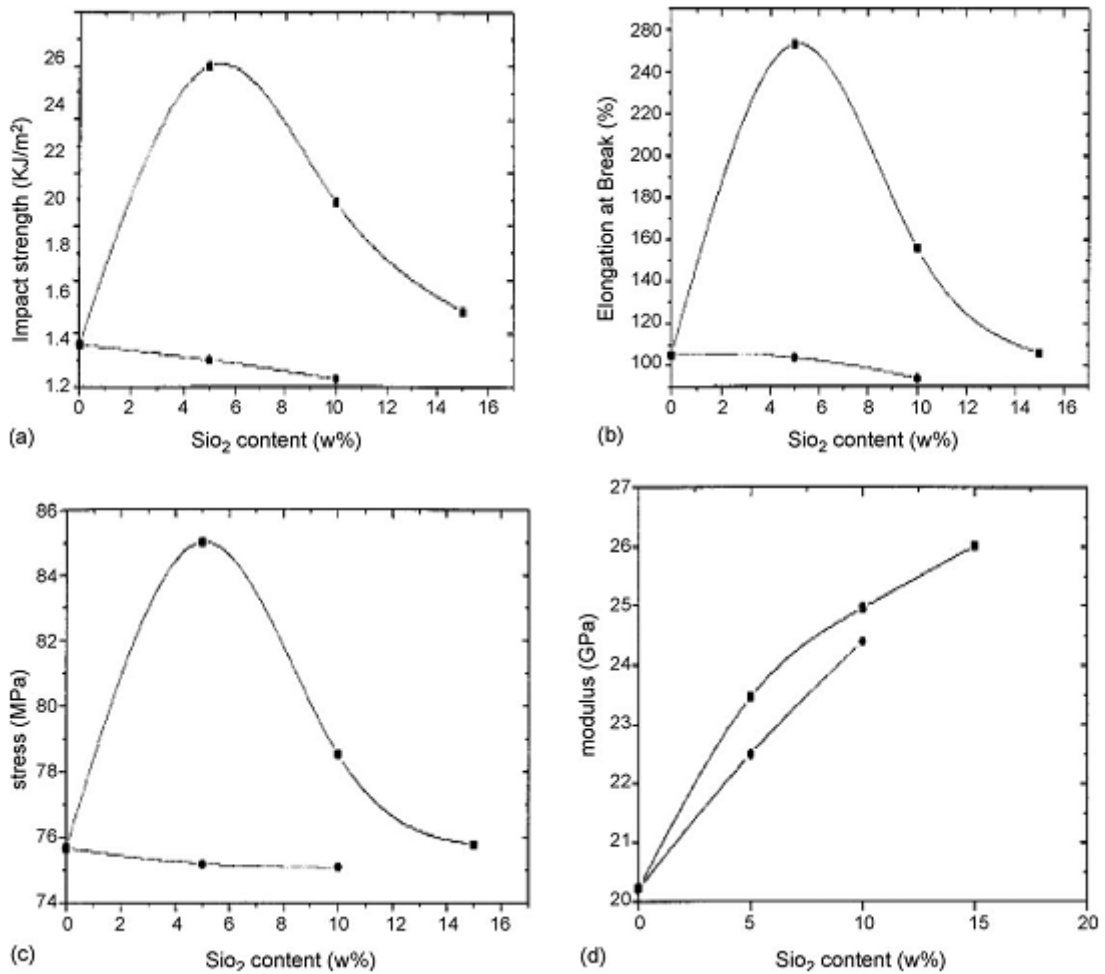


Figure 2.11 Mechanical properties of PA6/SiO₂ nanocomposites as a function of SiO₂ volume content: impact strength (a), elongation at break (b), tensile strength (c) and tensile modulus (d). Modified silica-reinforced composites (■), un-modified silica-reinforced composites (●) (reprinted from [22]).

The presence of inorganic nanoparticles with large surface areas would alter the local stress state of surrounding matrix. Thus, the polymer chain dynamics in the vicinity of particles is substantially different from that observed in the bulk due to specific polymer–nanoparticle interaction. It is well established that the addition of lower modulus elastomer particles to polymer materials leads to enhancement of both ductility and toughness at the expenses of tensile strength and stiffness. It is believed that cavitation of elastomer particles or debonding at the interface between particles and matrix is responsible for such improvement. The cavities relieve the triaxial stress state present in the matrix, inhibiting bulk polymer void formation and subsequent crazing, and promoting shear yielding of the polymer matrix [24–26]. Rigid inorganic nanoparticles are considered to be more effective than elastomers as they

increase both stiffness and toughness of the polymers. It is considered that cavitation of nanoparticles and its successive shear yielding contribute to an improvement in the toughness of nanocomposites.

Gaymans et al. [27] summarized the toughening process of rigid particles into three stages:

- I. Stress concentration. The rigid particles act as stress concentrators owing they have different elastic properties compared to the matrix polymer.
- II. Debonding. Stress concentration gives rise to build up of triaxial stress around the particles, leading to debonding at the particle-polymer interface.
- III. Shear yielding. The voids resulting from debonding alter the stress state in the matrix polymer surrounding the voids. This reduces the sensitivity towards crazing and promotes shear yielding.

The toughening mechanism with rigid particles is shown schematically in Figure 2.12. In order for rigid particles to act as effective toughening agents, they must fulfill certain requirements. These include the particles should be of small size (less than 5 μm), otherwise the voids that are created would act as crack initiation sites; the aspect ratio must be close to unity to avoid high stress concentrations; the particles should be homogeneously distributed in the polymer matrix; the particles must debond prior to the yield strain of the matrix polymer [27].

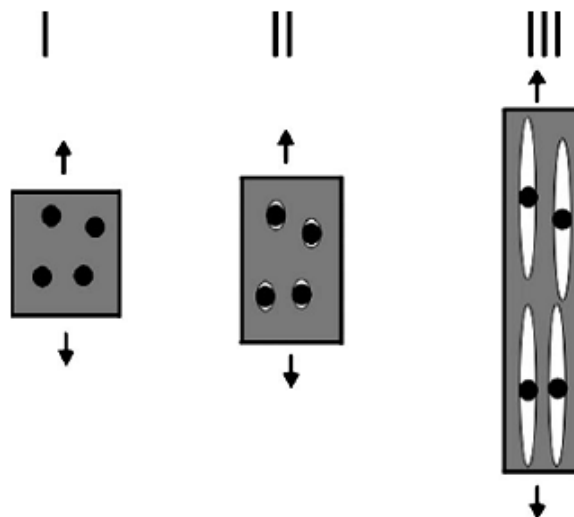


Figure 2.12 Toughening mechanism with rigid particles (reprinted from [27]).

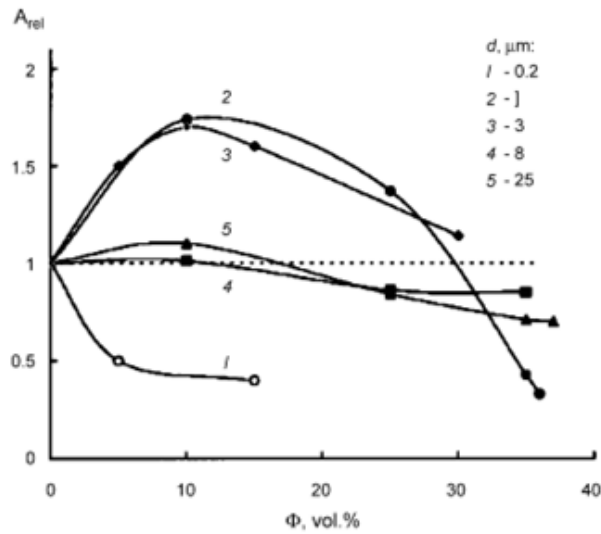


Figure 2.13 Relative notched Izod impact strength of the PP composites vs. content of fillers having different sizes (reprinted from [28]).

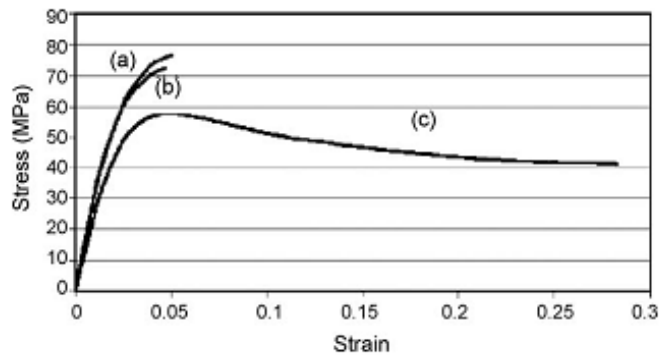


Figure 2.14 Typical stress-strain curves for neat PMMA (a), 2 wt% micrometer-sized Al_2O_3 filled PMMA composite (b), and 2.2 wt% 38 nm alumina filled PMMA nanocomposite (c) (reprinted from [21]).

Dubnikova et al. [28] studied PP based composites filled with $\text{Al}(\text{OH})_3$ and glass particles (1-25 and 0.2 μm respectively). Small $\text{Al}(\text{OH})_3$ particles (1-3 μm) are very effective to toughen PP while glass particles show no toughening effect due to their tendency to agglomeration (Figure 2.13). Schadler et al. [21,29] reported a ductility behavior of $\text{PMMA}/\text{Al}_2\text{O}_3$ nanocomposites and a brittle behavior of $\text{PMMA}/\text{Al}_2\text{O}_3$ microcomposites and neat PMMA (Figure 2.14). The micromechanical deformation mechanism of the nanocomposite involves debonding of particles from the matrix and associated shear yielding of polymer matrix with high-energy absorption.

As hydroxyl group is resided on the surface of silica nanoparticles, homogeneous dispersion of silica in non-polar PP is more difficult to achieve. Bikiaris et al. [30] used MA-g-PP as compatibilizer in PP/SiO₂ nanocomposites since the maleic anhydride can react with the surface hydroxyl group of SiO₂ nanoparticles. The addition of MA-g-PP leads to a significant improvement of tensile modulus and this effect is stronger in the compatibilized nanocomposites (Figure 2.15). In the un-compatibilized nanocomposites the tensile strength at break drops with increasing silica content while slightly decreases in compatibilized ones. The yield stress achieves a maximum at 5 wt% of silica, however it is higher in the compatibilized nanocomposites. The impact strength achieves a maximum at 2.5 wt% of silica and it is generally higher for un-compatibilized nanocomposites.

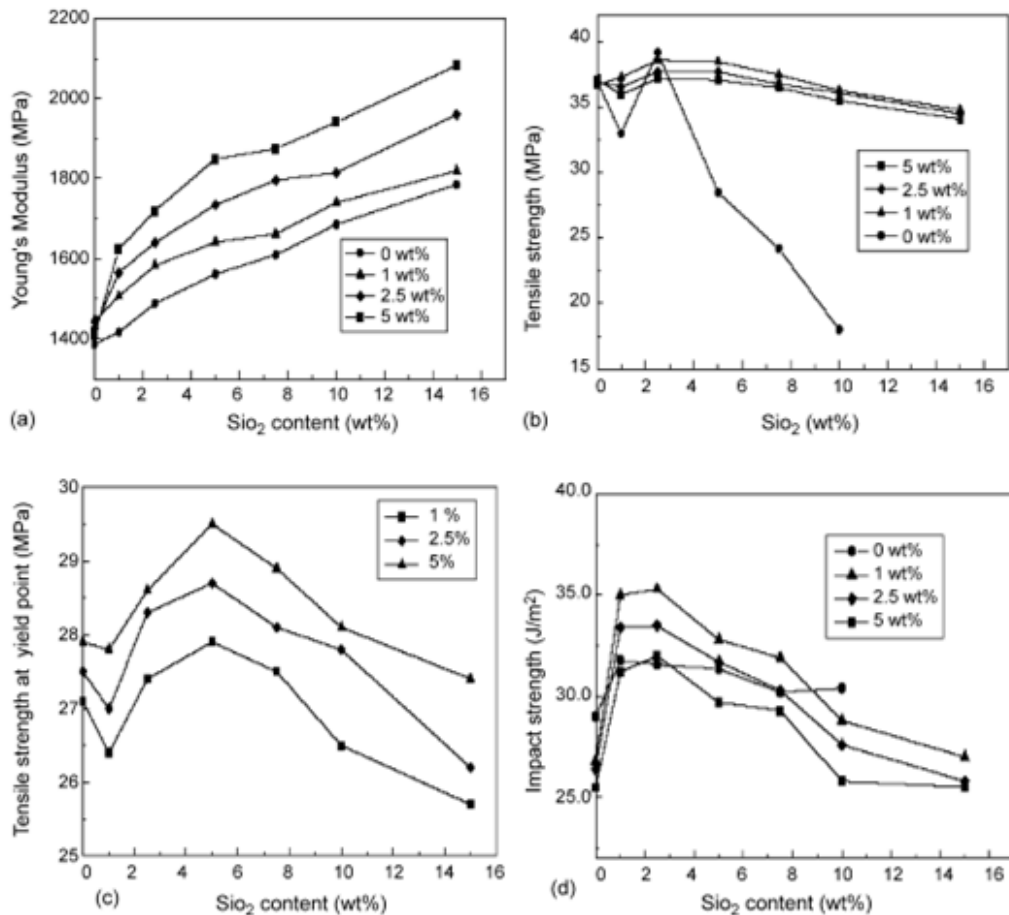


Figure 2.15 Young's modulus (a), tensile strength at break (b), yield stress (c), and impact strength (d) vs. silica content for melt compounded PP/SiO₂ nanocomposites containing different amounts of PP-g-MA as compatibilizer (reprinted from [30]).

References

- [1] J.H. Lee, D. Jung, C.E. Hong, K.Y. Rhee, S.G. Advani, *Compos Sci Technol* 2005, 65, 1996.
- [2] M.A. Osman, J.E.P. Rupp, U.W. Suter, *Polymer* 2005, 46, 1653.
- [3] T.D. Fornes, D.R. Paul. *Polymer* 2003, 44, 4993.
- [4] K.Y. Lee, D.R. Paul. *Polymer* 2005, 46, 9064.
- [5] H.S. Lee, P.D. Fasulo, W.R. Rodgers, D.R. Paul. *Polymer* 2005, 46, 11673.
- [6] T.D. Fornes, D.R. Paul. *Macromolecules* 2004, 37, 7698.
- [7] D.R. Paul, L.M. Robeson. *Polymer* 2008, 49, 31874.
- [8] J.C. Halpin. *J. Compos Mater* 1969, 3, 732.
- [9] J.C. Halpin, J.L. Kardos. *Polym Eng Sci* 1976, 16, 344.
- [10] T. Mori, K. Tanaka. *Acta Metall Mater* 1973, 21, 571.
- [11] Y. Benveniste. *Mech Mater* 1987, 6, 147.
- [12] T. Mura. *Micromechanics of defects in solids*, 2nd Edition, Martinus Nijhoff, Boston, (1987).
- [13] G.P. Tandon, G.J. Weng. *Polym Compos* 1984, 5, 327.
- [14] D.A. Brune, J. Bicerano. *Polymer* 2002, 43, 369.
- [15] J.I. Weon, H.J. Sue. *Polymer* 2005, 46, 6325.
- [16] N. Sheng, M.C. Boyce, D.M. Parks, G.C. Rutledge, J.I. Abes, R.E. Cohen. *Polymer* 2004, 45, 487.
- [17] A. Dasari, R.D.K. Misra. *Acta Mater* 2004, 52, 1683.
- [18] R.P. Singh, M. Zhang, D. Chan. *J Mater Sci* 2002, 37, 781.
- [19] L. Lopez, B.M.K. Song, H.T. Hahn. The effect of particle size in alumina nanocomposites. In *Proceedings of the 14th international conference on composite materials (ICCM-14)*, San Diego (2003) Paper no. 138a.
- [20] C.M. Thompson, H.M. Herring, T.S. Gates, J.W. Connell. *Compos Sci Technol* 2003, 63, 1591.
- [21] B.J. Ash, R.W. Siegel, L.S. Schadler. *Macromolecules* 2004, 37, 1358.
- [22] Y. Qu, F. Yang, Z.Z. Yu, *J. Polym Sci Part B: Polym Phys* 1998, 36, 789.
- [23] X.L. Xie, Q.X. Liu, R.K.Y. Li, X.P. Zhou, Q.X. Zhang, Z.Z. Yu, Y.W. Mai. *Polymer* 2004, 45, 6665.
- [24] A. Lazzeri, C.B. Bucknall. *J Mater Sci* 1993, 28, 6799.

- [25] G.M. Kim, G.H. Michler. *Polymer* 1998, 39, 5689.
- [26] G.M. Kim, G.H. Michler. *Polymer* 1998, 39, 5698.
- [27] W.C.J. Zuiderduin, C. Westzaan, J. Huetink, R.J. Gaymans. *Polymer* 2003, 44, 261.
- [28] I.L. Dubnikova, S.M. Berezina, A.V. Antonov. *J Appl Polym Sci* 2004, 94, 1917.
- [29] B.J. Ash, D.F. Rogers, C.J. Wiegand, L.S. Schadler, R.W. Siegel, B.C. Benicewicz, T. Apple. *Polym Compos* 2002, 23, 1014.
- [30] D.N. Bikirias, A. Vassilou, E. Pavlidou, G.P. Karayannidis. *Eur Polym J* 2005, 41, 1965.

Chapter 3

PET, PMMA, PC based nanocomposites

3.1 PET based nanocomposites

3.1.1 *PET/layered silicates nanocomposites*

Poly(ethylene terephthalate) (PET) is an high performance thermoplastic polymer that combines low cost, good chemical resistance, good spinnability [1] and finds use in a wide variety of applications [2–4]. However, the disadvantages such as low rate of crystallization and low thermal distortion temperature and low modulus have limited its application as an engineering plastic [5]. PET is used in textiles (clothes, curtains, and furniture up-holstery), electrical, automotive, construction, electronic applications, food and beverage packaging (water, soft drink and isotonic beverage bottles, sauce and jam jars, etc.) [6]. The interest of incorporating nanoclay to PET is driven by the possibility of obtaining a lower permeability (food and beverage applications) and improved mechanical properties (textile applications and molded parts) [7–9]. The clay added in PET is expected to act as a heterogeneous nucleating agent, speeding up the crystallization rate and increasing the crystalline fraction [10–12]. The distribution of intercalated aggregates and exfoliated clay platelets also plays an important role in the crystallization of PET. At high filler content the crystallization of the PET was hindered. The decrease in the crystallization is attributed to the increased interactions with the large number of clay platelets present [13].

The degree of property improvement is dependent on the morphology of the PET/clay nanocomposite with a greater degree of exfoliation of clay platelets usually resulting in optimal property improvement. Many studies on PET/clay nanocomposites showed a wide range of partially intercalated or exfoliated morphologies [1,14–20].

PET/organoclay nanocomposites have been prepared by three different methods: in situ polymerization [8,15,16, 21–22], melt blending [23–28] and solution intercalation [14,29,30]. In the in situ method of creating nanocomposites, monomer and nanofiller are dispersed and polymerization is carried out. The chain growth in or around the particles promotes nanocomposite formation having intercalated or exfoliated morphologies. Examples of intercalated, exfoliated and agglomerated (tactoid) morphologies were seen depending on the amount of organically modified clay added to the initial reaction mixture. The dispersion of the clay platelets was also observed to be controlled by surface modification and the polymerization procedures [21]. Solution and in situ polymerization routes are commonly used in research to make nanocomposites, but they are expensive processes. Melt blending is an economically favorable process and a few of experiments have demonstrated some success of this process [18,27,28].

Many researchers have attempted to facilitate better dispersion of nanofillers in PET nanocomposites by utilizing novel compatibilizers [7,31,32]. Intercalated and/or exfoliated nanocomposites were also successfully prepared using polymers containing polar functional groups as compatibilizers [33–35]. Imai et al. [36] used 10-[3,5-bis(methoxycarbonyl)phenoxy] decyltriphenylphosphonium bromide (IP10TP) as compatibilizer in PET/mica nanocomposite prepared via a two-step polymerization. Sanchez-Solis et al. [37]. used pentaerythrytol and maleic anhydride as compatibilizers in PET/oMMT prepared by extrusion. These systems exhibited an intercalation morphology. Zhang et al. used hydroxyethyl isonicotinamide (HENA) [38] and hydroxypentyltrimethylammonium iodide (HPTA) [39] to achieve a homogeneous dispersion of clay in PET. It has been observed that both improve the dispersion and HPTA was more interesting because the higher improvement of the tensile properties and the lower coloration effect in the nanocomposites. Polyester ionomers act as compatibilizer between PET and clay. The use of a PET ionomer with a montmorillonite clay to prepare PET/clay nanocomposites has been previously reported [40–44]. These works involved the use of solid ionomer by melt blending [40, 41] or in situ polymerization [42], and water dispersable ionomer [43,44]. The latter seems to give the best improvement of dispersion; in the aqueous solution, the negatively charged sulfonate groups on the ionomer interact with the positive charges on the clay edges. These ionic interactions ensure that the platelets are kept far enough apart after the removal of the water to result in an exfoliated structure in the PET matrix.

One weakness point of PET is that the melt processing, as well as the in situ polymerization, require high temperatures to be carried out (about 270-280°C). It is well above the thermal decomposition temperature of the conventional ammonium surfactants used to modify the layered silicate. To prepare PET/clay nanocomposites avoiding this phenomena, it can be involved either the solution blending approach [14] or the use of thermally stable surfactants (i.e. alkyl chain imidazolium and phosphonium halides) in both melt processing and in situ polymerization [7,27,36,45–47].

3.1.2 PET/particles nanocomposites

Spherical particles were not widely studied in combination with PET. Their low aspect ratio doesn't make them very effective to reduce the gas permeability in a nanocomposite as nanolplatelets do. The dispersion degree is often very high but, it has to be taken into account that most of nanocomposites are prepared by in situ polymerization process that is lesser favorable from an industrially point of view. Moreover the focus of many previous studies on PET/nanoparticles system are the thermal, rheological and crystallization properties rather than the mechanical and barrier ones.

Liu et al. [48] prepared PET/SiO₂ nanocomposites by in situ polymerization. They observed that SiO₂ increases the crystallizing and melting temperature and does not affect the process of synthesizing pure PET. Di Lorenzo et al. [49] added un-modified and stearic acid modified CaCO₃ in PET during the in situ polymerization. The conclusion was that stearic acid improves the adhesion between filler and matrix as expected. The modified particles increases the glass transition and slightly the thermal stability, acts as nucleating agents, speed up the solidification, conversely, CaCO₃ retards it. A similar work has been carried out by Ge et al. [50] on PET filled with un-modified and sodium stearate modified BaSO₄ particles. They act as nucleating agents and improve the crystallization, especially sodium stearate-BaSO₄. The enhanced interfacial interaction reduces the crystallization free energy barrier for nucleus formation. The modulus increases with both particles, the tensile strength slightly increases (it drops at 5 wt%) and the elongation at break is maintained only adding BaSO₄ particles.

3.1.2 PET/POSS nanocomposites

Similarly to spherical nanoparticles, also PET/POSS nanocomposites have not been widely studied since they usually have poor barrier properties. Zeng et al. [53] studied poly(ethylene terephthalate) (PET) composite fibers made with three types of POSS additives. Significant increases in tensile moduli and strengths were achieved with non-reactive POSS. The high temperature moduli of PET/POSS nanocomposite fibers were found to be rather variable, likely because of the modest compatibility between filler and polymers, which can lead to structural anisotropy within the composite. Ciolacu et al. [54] added trisilanol phenyl POSS in PET to prevent discoloration and to achieve molecular level stabilization during melt processing. It has been verified that POSS stabilizer improves the stability and processability of PET at significantly lower level due to reactive Functionalization. The strong interaction of PET and POSS results in better thermal and color stability of the material. Yoon et al. [55] reported that the tensile strength and modulus of the PET nanocomposites containing epoxy-functionalized POSS showed slightly higher values than PET despite the relatively small amounts (1 wt%) of POSS used. Kim et al. [56] studied the rheological behavior of PET/disilanol isobutyl and trisilanol isobutyl POSS nanocomposites prepared by the in situ polymerization. They reported that the observation of a plateau region of nanocomposites containing 1 wt% of POSS in the plot of G' versus $\log G''$ indicates strong interfacial interactions between PET and POSS. The thermal properties of the composites are similar to the ones of PET, only at 5 wt% there is a relevant increases of degradation temperature. 1 wt % of both POSS leads fine dispersion, while at higher concentrations aggregates were observed. 1 wt % of both POSS strongly increases the tensile strength and modulus. Lim et al. [57] showed a match between the thermal and mechanical properties of PET filled with methyl, isobutyl and phenyl POSS and the corresponding solubility parameters of fillers. A maximum of tensile strength and elongation at break has been achieved at only 0.5 wt% of POSS.

3.2 PMMA based nanocomposites

3.2.1 PMMA/layered silicates nanocomposites

Poly(methyl methacrylate) (PMMA) is an important member in the family of poly(acrylic ester)s. It has some desirable properties, including exceptional optical clarity, high strength, excellent dimensional stability, scratch resistance, low water absorption, high weatherability, and light resistance [58]. PMMA nanocomposites offer the potential for reduced gas permeability and improved thermal and mechanical properties without any loss of optical clarity. Moreover, since the poor heat resistance of PMMA, the clay nanocomposites offer the potential for excellent thermal properties.

Early reports [59–63] on PMMA/oMMT nanocomposites focused on the study of the different preparation methods rather than the structure and properties of the final hybrid. Okamoto et al. [59] and Huang and Brittain [60] studied the effects of different organoclays on the structure of PMMA/oMMT nanocomposites. Tabtiang et al. [61] compared in situ intercalative polymerization with melt intercalation. Okamoto et al. [62,63] studied the dispersed structure change of PMMA/oMMT nanocomposites by copolymerization with three kinds of polar comonomers. The thermal and thermo-mechanical properties of exfoliated PMMA/oMMT nanocomposites have been studied [64–67] and the glass transition temperature (T_g), thermal stability, and flame retardancy have been increased.

Most of the reports on PMMA/clay nanocomposites have been based on in situ polymerization routes for their preparation [59,60,68–75], mainly emulsion polymerization and solution polymerization methods. The first account of the synthesis of PMMA/clay nanocomposites was given by Blumstein [68], where natural sodium montmorillonite was used along with methyl methacrylate (MMA) via free-radical polymerization in the presence of the clay. Biasci et al. [69] obtained intercalated PMMA/clay nanocomposites by two methods: the polymerization of MMA with montmorillonite modified by 2-(N-methyl-N,N-diethylammonium iodide) ethyl acrylate and the direct intercalation of MMA polymers with a oMMT. Lee and Jang [70] prepared PMMA/clay hybrids by emulsion polymerization techniques, and they got intercalated structures. Both the thermal stability and tensile properties have been substantially enhanced. Huang and Brittain [60] prepared PMMA/clay hybrids by the suspension polymerization technique, and they got partially exfoliated

structures. The observed feature common to all these studies was the increase in the T_g of the PMMA/clay hybrids on the formation of the nanocomposites relative to the T_g of PMMA itself. Exfoliated PMMA nanocomposites with various organoclays through emulsion polymerization technique [73] give improvement in thermal degradability. A comparative study of structure, thermal, and mechanical properties of PMMA nanocomposites prepared using suspension, bulk, solution, and emulsion polymerization techniques by Wang et al. [74] has shown that either intercalated or exfoliated nanocomposites are formed depending on chemical nature of organic modifiers. For example, clay modified with fully aliphatic organic modifier results in intercalated nanocomposites, whereas the one containing double bond and allyl group can give either intercalated or exfoliated nanocomposites [74]. The tensile modulus is found to be higher for exfoliated nanocomposites as compared to intercalated ones [74,75], whereas % elongation is known to be lower for nanocomposites in comparison with PMMA. Su and Wilkie [75] have shown that exfoliated PMMA nanocomposites can be formed at lower clay loadings (≤ 0.5 wt %), whereas intercalated nanocomposites formed at higher clay loading (≥ 3 wt %) from bulk polymerization of methyl methacrylate with N-methyl-N,N di(vinyl-benzyl) octadecylammonium modified montmorillonite. Mechanical properties (Young's modulus and tensile strength) and onset of degradation are seen to be higher for nanocomposites as compared to PMMA.

In most of works on PMMA/clay nanocomposites prepared by melt intercalation the main focus is the effect of organic modifier on the final properties [76–83]. Rajkiran et al. [76] found a intercalated and partially exfoliated morphology resulted in a improvement in overall thermal stability. Tensile modulus for the nanocomposite is found to increase linearly with clay loading, while the break strain is found to decrease. These improvement are higher for the clay containing aliphatic quaternary ammonium organic modifier with relatively lower hydrophobicity. Ratinac et al. [77] produced several nanocomposites with different clays by extrusion and bulk polymerization. They found that extrusion produces better structures (higher exfoliation degree and particle density but lower interplaning distance). Liaw et al. [78] produced PMMA/clay nanocomposites at different temperature of processing. They observed a general increase of thermal stability and stiffness, while the tensile strength and the impact strength decrease. Moreover organoclay containing modifiers with single alkyl tails rather than twin alkyl tails have been shown more effective. A similar result has been found by Kumar et al [79].

3.2.2 PMMA/particles nanocomposites

There are several works in literature on polyacrylates /metal oxide particles nanocomposites. They are generally focused on the thermal stability improvement due to the presence of fillers such as SiO₂ [84–88], TiO₂ [89–91], ZnO [92] and ZrO₂ [86], or focused on the modification of optical properties by using fillers such as Bi₄Ti₃O₁₂ [93,94], SiO₂ [95], TiO₂ [96,97], Nb₂O₅ [98], Ta₂O₅/SiO₂ [99,100], ZnO [101].

Concerning the mechanical properties of PMMA/particles nanocomposites only a few of studies have been carried out. Most of them involve the use of surface modifier to increase the affinity between PMMA and fillers. Moreover the main route to prepare these nanocomposites is the free radical polymerization of MMA, while the melt blending is a quite rare used approach. Ash et al. [102] studied the mechanical properties of several PMMA/Al₂O₃ nanocomposites prepared by in situ polymerization, with different particle size and interfacial character. In some material they added methacrylic acid (MAA) to aid the dispersion and 3-glycidoxypropyltrimethoxysilane (GPS) as coupling agent. The particles decrease the stiffness of PMMA resulting in a lower tensile strength and modulus and higher strain to failure. MMA enhances this effect while GPS reduces it giving to the materials similar properties to the neat PMMA. The authors explained that when a weak interface exists between nanoparticle and polymer the room temperature mode of yielding was changed from normal (cavitation) to shear, which led to a brittle-to-ductile transition. This phenomenon was shown to require both the enhanced polymer chain mobility attributed to smaller particles and the ability to relieve the stress triaxality by poorly bonded larger particles. In another study Ash et al. [103] added by polymerization in situ, un-modified and (3-acryloxypropyl) dimethylmethoxysilane modified particles of Al₂O₃. They explained their mechanical behavior assuming that when there is affinity between polymer chains and particle surface, the mobility of the chains is very restricted close to the surface of the particle. Due to the far field effect of interface on the polymer volume, the mobility doesn't achieve the unfilled bulk polymer conditions, therefore, the T_g of nanocomposites increases. At the contrary, if the polymer is not coupled to the nanoparticle filler surface the mobility at the surface is very large, but will drop off as the distance from the particle increases. If the distance between filler nanoparticles is sufficiently small that bulk conditions are never reached, the nanocomposite exhibits a depression in T_g . Hong et al. [104] modified the surface of SiO₂

particles with γ -methacryloxypropyl trimethoxy silane by solution polymerization. They successfully improved the impact strength and the tensile and flexural properties of PMMA.

3.2.3 PMMA/POSS nanocomposites

In recent years, some researchers are shifting their interests toward the synthesis of PMMA/POSS nanocomposites. A variety of PMMA/POSS nanocomposites have been prepared through the physical blending [105–108], copolymerization [109–114] and atom transfer radical polymerization (ATRP) technique [115–118]. In light of the recent work on PMMA/POSS nanocomposites, the thermal properties of composites are strongly influenced by the type of POSS and the preparation methods of composites. Kopesky et al. [105] investigated the miscibility and viscoelastic properties of PMMA/methacryloxypropyl POSS nanocomposites and found that POSS species can lead to lower the T_g . Similar results were also obtained by them in another work using cyclohexyl POSS, methacryl POSS, and trisilanol phenyl POSS [106]. Weickmann et al. [107] reported novel PMMA/POSS composites prepared by self-assembly methodology. Though the toughness was enhanced, the POSS species failed to improve thermal properties. In contrast to nanocomposites prepared by physical blending, copolymers containing tethered POSS often exhibit enhanced thermal properties [109,113,114,119,120]. Toepfer et al. [109] used methacryloxypropyl POSS to prepare crosslinked PMMA nanocomposites resulting in a improvement of thermal degradation temperatures and T_g . Similar results were obtained by using vinyl POSS [113,114]. The increase of T_g results from dual contributions of the motion hindrance of PMMA chain imposed by the nanometer POSS cores and the dipole–dipole interaction between PMMA chains and POSS cores. The thermal stability enhancement is mainly attributed to incorporation of nanoscale inorganic POSS uniformly dispersed at molecular level.

3.3 PC based nanocomposites

3.3.1 PC/layered silicates nanocomposites

Polycarbonate (PC) is an amorphous engineering thermoplastic which combines good thermal stability, transparency, impact resistance. It is used in a wide variety of applications such as medical, optics, automotive [121]. PC/clay nanocomposites have been developed in order to improve the morphological [122,123], thermal [124–127], mechanical [123,124,126,127], tribological [128], fire resistance [129,130], rheological [124,131], properties of the neat polymer.

Huang et al. [122] have reported the synthesis of PC/oMMT using carbonate cyclic oligomers. WAXD patterns indicate that exfoliation of this organoclay occurs after mixing with the cyclic oligomers during the processing. Subsequent ring opening polymerization of the cyclic oligomers converts the matrix into the linear polymer without the disruption of the nanocomposite structure. TEM micrograph revealed a stacked and intercalated structure, despite WAXD patterns indicated an exfoliated morphology. Yoon et al. [123] investigated the effect of matrix molecular weight and organoclay structure on the morphology and mechanical properties of PC based nanocomposite. They observed that a higher molecular weight lead higher shear stress, thus a better dispersion of clay. Moreover, the surfactant having polyoxyethylene and octadecyl alkyl tails shows the most significant improvement in modulus and leads to partially exfoliated platelets. In another work [124] they studied the effect of two different extruders and different clay and surfactants on the mechanical properties, thermal degradation and color formation of PC based nanocomposites. It was found that the extruder with the longer residence time and broader residence time distribution was more effective for dispersing the clay but gave more color. Double bonds, tertiary amines, rather than quaternary ones, and montmorillonite, rather than Laponite, give darker color to nanocomposites. Severe et al. [125] studied the thermal stability of PC/oMMT nanocomposites formed in a twin screw extruder using phosphonium exchanged montmorillonite and synthetic clays. They found that the phosphonium exchanged montmorillonite provided better thermal stability than synthetic clays. Yoo et al. [126] have developed PC/clay nanocomposites using microwave-aided solid state polymerization, Gonzalez et al. [127] blended PC with a miscible polymer which contains the dispersed nanoclay. Carrion et al. studied the tribological properties of PC based nanocomposites filled

with ZnO [132], imidazolium modified particles [133] and oMMT [128]. By adding 3 wt% of oMMT by melt blending they obtained an intercalated morphology resulting in an increase of thermal stability, a decrease of T_g and a strong wear improvement. Lee and Han [131] investigated the properties of PC filled with natural (MMT) and organomodified (oMMT) clay with the expectation that, the carbonyl group in PC would form hydrogen bonds, during melt blending, with the hydroxyl group present on the surface of oMMT. PC/oMMT and PC/MMT nanocomposites exhibited exfoliated and intercalated structure resulting in better mechanical properties of the first due to the more favorable interactions. Rheological measurements showed an increase of dynamic moduli (G' and G'' , at low ω), complex viscosity ($|\eta^*|$, at low ω), steady-state shear viscosity (η , at low $\dot{\gamma}$), with increasing of filler content. They attributed this to the presence of hydrogen bonds, supported by FTIR spectroscopy as well.

3.3.2 PC/particles nanocomposites

Several studies have been carried out on PC filled with different modified or un-modified oxide particles [134–140] and most of them involve more complex synthesis than the simpler melt blending through extrusion. Chandra et al. [134] studied the optical properties of thin PC films filled with 96 nm Al_2O_3 particles coated with poly(styrene-maleic anhydride) (SMA) copolymer. In order to obtain highly transparent nanocomposites Imai et al. [135] prepared sulfonic acid-modified PC filled with TiO_2 and ZrO_2 particles superficially modified with phosphoric acid 2-ethylhexyl ester. They verify the effectiveness of the modifier to improve the dispersion of particles resulting in a better optical quality. The disadvantage of TiO_2 particles is the yellowish of its nanocomposites interaction between phenolic end groups of the polymer chain and Ti. Wang et al. [136] prepared PC/ CaCO_3 nanocomposites with 1 wt% of filler content, by melt blending in order to enhance the processability of PC. They found a decrease of apparent viscosity and T_g , as expected, and an increase of stiffness comparing with the neat PC. They explained the results by assuming that the increased resin–filler interface created extra free volume and, therefore, assisted the large-scale segmental mobility of the polymer-chain segments.

3.3.3 PC/POSS nanocomposites

Due to the presence of phenyl rings in PC, a lot of phenyl-functionalized POSS have been incorporated in PC in order to obtain reinforced transparent PC/POSS nanocomposites [141–144], while Song et al. [145] added trisilanol phenyl POSS in PC to investigate the thermal degradation and the combustion behavior. Schiraldi et al. [141] studied the thermal and mechanical properties of PC based nanocomposites filled with phenyl, trisilanol phenyl, trisilanol isooctyl, Al-phenyl and Al-isobutyl POSS. They found that (i) silanol groups in the POSS cage increase the compatibility with PC, (ii) the aluminum atom in one corner of the cage promotes degradation of the POSS, (iii) isooctyl groups, rather than phenyl ones, have a plasticizer effect. PC/trisilanol phenyl nanocomposites possess the best overall performance among the POSS materials tested, resulting in transparent materials up to 5 wt% and in a slightly enhanced stiffness. Hao et al. [142] found that the phenethyl POSS is miscible in PC on a molecular level up to about 7 wt%, whereas phase separation occurred at higher POSS content, and up to 40 wt% in polystyrene (PS). It was attributed to a preferential interaction, π - π stacking, between the phenyl rings of both systems. In another work, Schiraldi et al. [143] studied melt-mixed PC/phenethyl POSS nanocomposites up to 15 wt% of filler content. Due to immiscibility polymer phase separation occurred even at low concentrations of nanofiller (2.5 wt%) resulting in the formation of dispersed ellipsoidal-shaped particles with dimensions ranging from 200–500 nm. The size of the POSS clusters increases as the POSS content increases. DSC and DMA showed a decrease of T_g as a result of the plasticizing activity of POSS. The PC/POSS hybrid composites displayed a slight increase in the storage modulus. Also, the tensile break stresses were found to increase at the intermediate concentration levels. Both effects were attributed to the presence of POSS microcrystals that caused a restriction to chain mobility overpassing the plasticizing contribution. On the other hand, the formation of macroaggregates is responsible for the progressive brittle behavior detected on the highly-filled composites. Generally, POSS doesn't affect the thermal behavior or the thermal stability of PC. Mulliken et al. [144] investigated the rate-dependent mechanical properties of PC/trisilanol phenyl POSS nanocomposites, in particular the effect of POSS on the α and β molecular mobility mechanisms of PC. The POSS was found to enhance the mobility of secondary (β) molecular motions, unlike the primary one (α). It is such a brittle-to-ductile transition that occurs only in some conditions (low temperatures and high-strain rates).

References

- [1] J.H. Chang, S.J. Kim, Y.L. Joo, S. Im. *Polymer* 2004, 45, 919.
- [2] S.H. Hwang, S.W. Paeng, J.Y. Kim, W. Huh. *Polym Bull* 2003, 49, 329.
- [3] D. Wang, J. Zhu, Q. Yao, C.A. Wilkie. *Chem Mater* 2002, 14, 3837.
- [4] P.C. Lebaron, Z. Wang, T. Pinnavaia. *J Appl Clay Sci* 1999, 12, 11.
- [5] J. Scheirs, T. Long editors. *Modern polyesters*. Chichester: Wiley; 2003
- [6] J. Margolis In *Engineering Thermoplastics. Properties and Applications*, Margolis J (ed.). Marcel Dekker: New York, 1985; 1–19.
- [7] Y. Imai, S. Nishimura, E. Abe, H. Tateyama, A. Abiko, T. Aoyama, H. Taguchi. *Chem Mater* 2002, 14, 477.
- [8] Z. Ke, B. Yongping. *Mater Lett* 2005, 59, 3348.
- [9] G. Zhang, T. Shichi, K. Takagi. *Mater Lett* 2003, 57, 1858.
- [10] T. Wang, L. Chen, Y.C. Chua, X. Lu. *J Appl Polym Sci* 2004, 94, 1381.
- [11] P. Phang, H. Liu. *Polym Int* 2004, 53, 1282.
- [12] Y. Wang, C. Shen, H. Li, Q. Li, J. Chen. *J Appl Polym Sci* 2004, 91, 308 .
- [13] Y. Ke, C. Long, Z. Qi. *J Appl Polym Sci* 1999, 71, 1139.
- [14] C.F. Ou, M.T. Ho, J.R. Lin. *J Appl Polym Sci* 2004, 91, 140.
- [15] T.Y. Tsai, C.H. Li, C.H. Chang, W.H. Cheng, C.L. Hwang, R.J. Wu. *Adv Mater* 2005, 17, 1769.
- [16] S.S. Lee, Y.T Ma, H.W. Rhee, J. Kim. *Polymer* 2005, 46, 2201.
- [17] S.S. Lee, J. Kim. *Polym Sci Eng* 2003, 89, 370.
- [18] A. Pegoretti, J. Kolarik, C. Peroni, C. Migliaresi. *Polymer* 2004, 45, 2751.
- [19] W. Liu, X. Tian, P. Cui, Y. Li, K. Zheng, Y. Yeng. *J Appl Polym Sci* 2004, 91, 1229.
- [20] M.L. Di Lorenzo, M.E. Errico, M. Avella. *J Mater Sci* 2002, 37, 2351.
- [21] Y.C. Ke, Z.B. Yang, C.F. Zhu. *J Appl Polym Sci* 2002, 85, 2677.
- [22] S. H. Kim and S. C. Kim, *J Appl Polym Sci* 2007, 103, 1262.
- [23] Y. Li, J. Ma, Y. Wang, and B. Liang, *J Appl Polym Sci* 2005, 98, 1150.
- [24] Y. Wang, J. Gao, Y. Ma, and U. S. Agarwal, *Compos B Eng* 2006, 37, 399.
- [25] U. Gurmendi, J. I. Eguiazabal, and J. Nazabal, *Macromol Mater Eng* 2007, 292, 169.
- [26] M.C. Lai, K.C. Chang, W. C. Huang, S. C. Hsu, and J. M. Yeh, *J Phys Chem Solids* 2008, 69, 1371.

- [27] C.H. Davis, L.J. Mathias, J.W. Gilman, D.A. Schiraldi, J.R. Shields, P. Trulove, T.E. Sutto, H.C. Delong. *J Polym Sci* 2002, 40, 2661.
- [28] R.A. Kalgaonkar, J.P. Jog. *J Polym Sci* 2003, 41, 3102.
- [29] G. D. Barber and R. B. Moore, *ACS PMSE Proceed* 2000, 82, 241.
- [30] C. F. Ou, M. T. Ho, and J. R. Lin, *J Polym Res* 2003, 10, 127.
- [31] C. Saujanya, Y. Imai, H. Tateyama. *Polym Bull* 2002, 49, 69.
- [32] C. Saujanya, Y. Imai, H. Tateyama. *Polym Bull* 2003, 51, 85.
- [33] N.N. Bhiwankar, R.A. Weiss. *Polymer* 2006, 47, 6684.
- [34] L. Cui, D.R. Paul. *Polymer* 2007, 48, 1632.
- [35] A.C. Chinellato, S.E. Vidotti, G.H. Hu, L.A. Pessan. *Compos Sci Technol* 2010, 70, 458.
- [36] Y. Imai, Y. Inukai, H. Tateyama. *Polym J* 2003, 35, 230.
- [37] A. Sanchez-Solis, A. Garcia-Rejon, O. Manero. *Macromol Symp* 2003, 192, 281.
- [38] G.Z. Zhang, T. Shichi, Z.W. Tong, K. Takagi, *Chem. Lett.* 2002, 3, 410.
- [39] G.Z. Zhang, T. Shichi, Z.W. Tong, K. Takagi, *Mat. Lett.* 2003, 57, 1858.
- [40] G.D. Barber, B.H. Calhoun, R.B. Moore. *Polymer* 2005, 4, 66706.
- [41] S.E. Vidotti, A.C. Chinellato, G.H. HU, L.A. Pessan. *J Polym Sci* 2007, 45, 3084.
- [42] Y. Li, J. Ma, Y. Wang, B. Liang. *J Appl Polym Sci* 2005, 98, 1150.
- [43] J.W. Trexler, R.L. Piner, S.R. Turner, R.B. Barbee. *WO Patent 99/03914*, January 1999.
- [44] A. Ammala, C. Bell, K. Dean. *Compos Sci Techn* 2008, 68, 1328–1337.
- [45] D. Wu, F. Chen, R. Li. *Macromol* 1997, 30, 6737.
- [46] J. Zhu, F.M. Uhl, A.B. Morgan, C.A. Wilkie. *Chem Mater* 2001, 13, 4649.
- [47] J. Zhu, A.B. Morgan, F.J. Lamelas, C.A. Wilkie. *Chem Mater* 2001, 13, 3774.
- [50] W. Liu, X. Tian, P. Cui, Y. Li, K. Zheng, Y. Yang. *J Appl Polym Sci*, 2004, 91, 1229–32.
- [51] M. L. Di Lorenzo, M.E. Errico, M. Avella. *J of Mater Sci* 2002, 37, 2351–8.
- [52] C. Ge, P. Ding, L. Shi, J. Fu. *J Polym Sci* 2009, 47, 655–68.
- [53] J. Zeng, S. Kumar, S. Iyer, D.A. Schiraldi, R.I. Gonzalez. *High Perform Polym* 2005, 17, 403.
- [54] F.C.L. Ciolacu, N.R. Choudhury, N.Dutta, E. Kosior. *Macromol* 2007, 40, 265.
- [55] K.H. Yoon, M.B. Polk, J.H. Park, By.G. Min, D.A. Schiraldi. *Polym Int* 2005, 54, 47.
- [56] J.K. Kim, K.H. Yoon, D.S. Bang, Y.B. Park, H.U. Kim, Y.H. Bang. *J Appl Polym Sci* 2008, 107, 272.

- [57] S.K. Lim, E.P. Hong, Y.H. Song, H.J. Choi, I.J. Chin. *J Mater Sci* 2010, 45, 5984.
- [58] J. Brandrup, E.H. Immergut. *Polymer Handbook*, 3rd ed.; Wiley Interscience: New York, 1989. 6. Y. Li, B. Zhao, S. Xie, S. Zhang. *Polym Int* 2003, 52, 892.
- [59] M. Okamoto, S. Morita, H. Taguchi, Y.H. Kim, T. Kataka, H. Tateyama. *Polymer* 2000, 41, 3887.
- [60] X. Huang, W.J. Brittain. *Macromol* 2001, 34, 3255.
- [61] A. Tabtiang, S. Lumlong, R.A. Venables. *Eur Polym J* 2000, 36, 2559.
- [62] M. Okamoto, S. Morita, Y.H. Kim, T. Kotaka, H. Tateyama. *Polymer* 2001, 42, 1201.
- [63] M. Okamoto, S. Morita, T. Kotaka. *Polymer* 2001, 42, 2685.
- [64] J.M. Hwu, G.J. Jiang, Z.M. Gao, W. Xie, W.P. Pan. *J Appl Polym Sci* 2002, 83, 1702.
- [65] S. Bandyopadhyay, E.P. Giannelis, *Proc Am Chem Soc Div Polym Mater Sci Eng* 2000, 82, 208.
- [66] J. Zhu, P. Start, K. Mauritz, A. Kenneth, C.A. Wilkie. *Polym Degrad Stab* 2002, 77, 253.
- [67] J. Du, J. Zhu, C.A. Wilkie, J. Wang. *Polym Degrad Stab* 2002, 77, 377.
- [68] A. Blumstein. *J Polym Sci Part A: Gen Pap* 1965, 3, 2653.
- [69] L. Biasci, M. Aglietto, G. Ruggeri, F. Ciardelli. *Polymer* 1994, 35, 3296.
- [70] D.C. Lee, L.W. Jang. *J Appl Polym Sci* 1996, 61, 1117.
- [71] G. Chen, X. Chen, Z. Lin, W. Ye. *J Mater Sci Lett* 1999, 18, 1761.
- [72] T. Hirara, T. Kashiwagi, J.E. Brown. *Macromol* 1995, 18, 1410.
- [73] J.P. Zheng, J.X. Wang, S. Gao, K.D. Yao. *J Mater Sci* 2005, 40, 4687.
- [74] D. Wang, J. Zhu, Q. Yao, C.A. Wilkie. *Chem Mater* 2002, 14, 3837.
- [75] S. Su, C.A. Wilkie. *J Polym Sci Part A: Polym Chem* 2003, 41, 1124.
- [76] R.R. Tiwari, U. Natarajan. *J Appl Polym Sci* 2007, 105, 2433.
- [77] K.R. Ratinac, R.G. Gilbert, L. Ye, A.S. Jones, S.P. Ringer. *Polymer* 2006, 47, 6337.
- [78] J.H. Liaw, T.Y. Hsueh, T.S. Tan, Y. Wang, S.M. Chiao. *Polym Int* 2007, 56, 1045.
- [79] S. Kumar, J.P. Jog, U. Natarajan. *J Appl Polym Sci* 2003, 89, 1186.
- [80] Z. Shen, G.P. Simon, Y.B. Cheng. *J Appl Polym Sci* 2004, 92, 2101.
- [81] A. Tabtiang, S. Lumlong, R.A. Venables. *Eur Polym J* 2000, 36, 2559.
- [82] X. Zheng, D.D. Jiang, C.A. Wilkie. *Thermochim Acta* 2005, 435, 202.
- [83] J.H. Park, S.C. Jana. *Polymer* 2003, 44, 2091.
- [84] T.C. Chang, Y.T. Wang, Y.S. Hong, Y.S. Chiu. *J Polym Sci Part B: Polym Chem* 2000, 38, 1972.

- [85] Z.H. Huang, K.Y. Qiu. *Polymer* 1997, 38, 521.
- [86] H. Wang, P. Xu, W. Zhong, L. Shen, Q. Du. *Polym Degrad Stab* 2005, 87, 319.
- [87] T. Kashiwagi, A.B. Morgan, J.M. Antonucci, M.R. Van Landingham, R.H. Harris, W.H. Awad, J.R. Shields. *J Appl Polym Sci* 2003, 89, 2072.
- [88] Y.T. Wang, T.C. Chang, Y.S. Hong, H.B. Chen. *Thermochim Acta* 2003, 397, 219.
- [89] W.C. Chen, S.J. Lee, L.H. Lee, J.L. Lin. *J Mater Chem* 1999, 9, 2999.
- [90] L.H. Lee, W.C. Chen. *Chem Mater* 2001, 13, 1137.
- [91] E. Dzunuzovic, K. Jeremic, J.M. Nedeljkovic. *Eur Polym J* 2007, 43, 3719.
- [92] R.Y. Hong, J.Z. Qian, J.X. Cao. *Powder Technology* 2006, 163, 160.
- [93] R. Palkovits, H. Althues, A. Ruplecker, B. Tesche, A. Dreier, U. Holle, G. Fink, C.H. Cheng, D.F. Shantz, S. Kaskel. *Langmuir* 2005, 21, 6048.
- [94] H.L. Yang, R. Quan, G.H. Zhang, Y.T. Chow, H.P. Chan, P.L. Chu. *Opt. Laser Technol* 2005, 37, 259.
- [95] C.K. Chan, S.L. Peng, I.M. Chu, S.C. Ni. *Polymer* 2001, 42, 4189.
- [96] A.H. Yuwono, J.M. Xue, J. Wang, H.I. Elim, W. Ji, Y. Li, T.J. White. *J Mater Chem* 2003, 13, 1475.
- [97] L.H. Lee, W.C. Chen. *Chem Mater* 2001, 13, 1137.
- [98] H. Matakai, S. Yamaki, T. Fukui. *Jpn J Appl Phys* 2004, 43, 5819.
- [99] H. Schulz, L. Madler, S.E. Pratsinis, P. Burtscher, N. Moszner. *Ad Funct Mater* 2005, 15, 830.
- [100] V. Khrenov, M. Klapper, M. Koch, K.Mullen. *Macromol Chem Phys.* 2005, 206, 95.
- [101] M.M. Demir, K. Koynov, U. Akbey, C. Bubeck, I. Park, I. Lieberwirth, G. Wegner. *Macromol* 2007, 40, 1089.
- [102] B.J. Ash, R.W. Siegel, L.S. Schadler. *Macromol* 2004, 37, 1358.
- [103] B.J. Ash, D.F. Rogers, C.J. Wiegand, L.S. Schadler, R.W. Siegel, B.C. Benicewicz, T. Apple. *Polym Comp* 2002, 23, 1014.
- [104] R.Y. Hong, H.P. Fu, Y.J. Zhang, L. Liu, J. Wang, H.Z. Li, Y. Zheng. *J Appl Polym Sci* 2007, 105, 2176.
- [105] E.T. Kopesky, T.S. Haddad, G.H. McKinley, R.E. Cohena. *Polymer* 2005, 46 4743.
- [106] E.T. Kopesky, G.H. McKinley, R.E. Cohen. *Polymer* 2006, 47, 299.
- [107] H. Weickmann, R. Delto, R. Thomann, R. Brenn, W. Döll, R. Mülhaupt. *J Mater Sci* 2007, 42, 87.

- [108] E.T. Kopesky, T.S. Haddad, E.C. Robert, H.M. Gareth. *Macromol* 2004, 37, 8992.
- [109] O. Toepfer, D. Neumann, N.R. Choudhury, A. Whittaker, J. Matisons. *Chem Mater* 2005, 17, 1027.
- [110] Q. Zou, S. Zhang, Q. Tang, S. Wang, L. Wu. *J Chromat* 2006, A 1110, 140.
- [111] Q. Zou, S. Zhang, S. Wang, L. Wu. *J Chromat* 2006, A 1129, 255.
- [112] N. Amir, A. Levina, M.S. Silverstein. *J Polym Sci Part A: Polym Chem* 2007, 45, 4264.
- [113] H. Xu, B. Yang, J. Wang, S. Guang, C. Li. *J Polym Sci Part A: Polym Chem* 2007, 45, 5308.
- [114] C. Zhao, X. Yang, X. Wu, X. Liu, X. Wang, L. Lu. *Polym Bull* 2008, 60, 495.
- [115] W. Zhang, B.X. Fu, Y. Seo, E. Schrag, B. Hsiao, P.T. Mather, N.L. Yang, D. Xu, H. Ade, M. Rafailovich, J. Sokolov. *Macromol* 2002, 35, 8029.
- [116] K. Koh, S. Sugiyama, T. Morinaga, K. Ohno, Y. Tsujii, T. Fukuda, M. Yamahiro, T. Iijima, H. Oikawa, K. Watanabe, T. Miyashita. *Macromol* 2005, 38, 1264.
- [117] R.R. Costa, W.L. Vasconcelos, R. Tamaki, R.M. Laine. *Macromol* 2001, 34, 5398.
- [118] K. Ohno, S. Sugiyam, K. Koh, Y. Tsujii, T. Fukuda, M. Yamahiro, H. Oikawa, Y. Yamamoto, N. Ootake, K. Watanabe. *Macromol* 2004, 37, 8517.
- [119] A. Romo-Uribe, P.T. Mather, T.S. Haddad, J.D. Lichtenhan. *J Polym Sci Part B: Polym Phys* 1998, 36, 1857.
- [120] H. Xu, B. Yang, J. Wang, S. Guang, C. Li. *Macromol* 2005, 38, 10455.
- [121] J.L. De Rudder. Commercial applications of polycarbonates. In *Handbook of polycarbonate science and technology*. D.G. LeGrand, J.T. Bendler editors, Marcel Dekker, New York (2000).
- [122] X. Huang, S. Lewis, W.J. Brittain, R.A. Vaia. *Macromolecules* 2000, 33, 2000.
- [123] P.J. Yoon, D.L. Hunter, D.R. Paul. *Polymer* 2003, 44, 5323.
- [124] P.J. Yoon, D.L. Hunter, D.R. Paul. *Polymer* 2003, 44, 5341.
- [125] G. Severe, A.J. Hsieh, B.E. Koene. *ANTEC* 2000, 2, 1523.
- [126] Y. Yoo, K.Y. Choi, J.H. Lee. *Macromol Chem Phys* 2004, 205, 1863.
- [127] I. Gonzalez, J.I. Eguiazabal, J. Nazabal. *Polym Eng Sci* 2006, 46, 864.
- [128] F. J. Carrion, A. Arribas, M.D. Bermudez, A. Guillamon. *Eur Polym J* 2008, 44, 968.
- [129] Q.X. Dong, Q.J. Chen, W. Yang, Y.L. Zheng, X. Liu, M.B. Yang. *J Appl Polym Sci* 2008, 109, 659.
- [130] F. Yang, I. Bogdanova, G.L. Nelson. *Polym Adv Technol* 2008, 19, 602.

- [131] K.M. Lee, C.D. Han. *Polymer* 2003, 44, 4573.
- [132] F.J. Carrion, J. Sanes, M.D. Bermudez. *Wear* 2007, 262, 1504.
- [133] F.J. Carrion, J. Sanes, M.D. Bermudez. *Mater Lett* 2007, 61, 4531.
- [134] A. Chandra, L.S. Turng, P. Gopalan, R.M. Rowell. *Compos Sci Technol* 2008, 68, 768.
- [135] Y. Imai, A. Terahara, Y. Hakuta, K. Matsui, H. Hayashi, N. Ueno. *Eur Polym J* 2009, 45, 630.
- [136] Z. Wang, G. Xie, X. Wang, G. Li, Z. Zhang. *Mater Lett* 2006, 60, 1035.
- [137] H.H. Kausch, G.H. Michler. *J Appl Polym Sci* 2007, 105, 2577.
- [138] C.V. Avadhani, Y. Chujo. *Polym Prepr Jpn* 1998, 47, 1010.
- [139] M. Arakawa, K. Sukata, M. Shimada, Y. Agari. *J Appl Polym Sci* 2006, 100, 4273.
- [140] M. Böhning, H. Goering, N. Hao, R. Mach, A. Schönhals. *Polym Adv Technol* 2005, 16, 262.
- [141] Y. Zhao, D.A. Schiraldi. *Polymer* 2005, 46, 11640.
- [142] N. Hao, M. Böhning, H. Goering, A. Schönhals. *Macromolecules* 2007, 40, 2955.
- [143] M. Sánchez-Soto, D.A. Schiraldi, S. Illescas. *Eur Polym J* 2009, 45, 341.
- [144] A. D. Mulliken, M.C. Boyce. *J Eng Mater Tech* 2006, 128, 543.
- [145] L. Song, Q. He, Y. Hu, H. Chen, L. Liu. *Polym Degrad Stab* 2008, 93, 627.

Chapter 4

Processing and characterization of polymers

4.1 Processing of polymers

4.1.1 Melt blending: extruder

Plastic pellets or beads (also referred to as resin) are fed from the hopper along a feed screw through a barrel chamber. As the resin travels along the barrel, it is subject to friction, compression, and heated zones. The result is that the resin melts and further travel at the exit end of the screw serves to mix the melt homogeneously. The melt enters a chamber designed to ensure an evenly distributed flow to the die. In many machines, a melt pump is used to prevent any pressure surges. Also, breaker plates serve to prevent any solid particles or foreign objects from passing through the die.

The die is a precisely machined part with a patterned opening such that the extruded plastic takes that die pattern for its cross sectional area. With products such as extruded sheet, there are adjustments to the die to allow for a variety of sheet thicknesses with one die. Shapes are varied, and typically are holes for filament, annular rings for pipe and tube, or geometric patterned shapes for items such as vinyl siding and window frame stock. All die surfaces must be free from defects otherwise unwanted patterns will appear on the extruded product. Product from the die solidifies quickly. Depending on the end product, this may be achieved by immersion in cooling water, air cooling, or contact with chill rolls. As mentioned above, overheating the melt is to be avoided at all costs, or the product will not form properly on solidification. Once solid, the product material can be wound, spun, or cut in defined lengths depending upon its intended end-use.

The feedscrew, barrel, and temperature controller form a section of the extruder called the plastification unit. Plastification is defined as the conversion of a thermoplastic to a melt and is critical to successful extrusion processes.

The most important component of any extruder is the screw. It is often impossible to extruder satisfactorily one material by using a screw designed for another material. Therefore screw designs vary with each material. The screw consists of a steel cylinder with a helical channel cut into it (Figure 4.1). The helical ridge formed by the machining of the channel is called the flight, and the distance between the flights is called the lead. The lead is usually constant for the length of the screw in single-screw machines. The helix angle is called pitch. Helix angles of the screw are usually chosen to optimize the feeding characteristics. The screw outside diameter is generally just a few thousandths of an inch less than the inner diameter of the barrel. The minimal clearance between screw and the inner diameter prevents excessive buildup of resin on the inside barrel wall and thus maximizes heat transfer.

Screws are characterized by their length-diameter ratio (commonly written as L/D ratios). L/D ratios most commonly used for single-screw extruders range from 15:1 to 30:1. Ratios of 20:1 and 24:1 are common for thermoplastics, whereas lower values are used for rubbers. A long barrel gives a more homogeneous extrudate, which is particularly desirable when pigmented materials are handled.

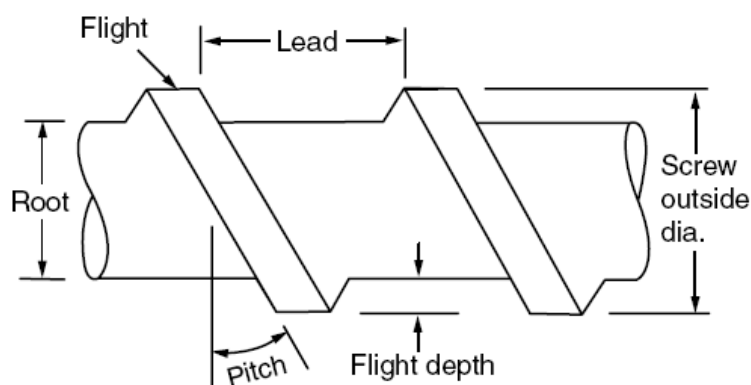


Figure 4.1 Detail of screw.

The screw is usually divided into three sections, namely, feed, compression, and metering (Figure 4.2). One of the basic parameters in screw design involves the ratio of lengths between the feed, compression (or transition), and metering sections of the screw. Each

section has its own special rate. The feed section picks up the powder, pellets, or beads from under the hopper mouth and conveys them forward in the solid state to the compression section. The feed section is deep flighted so that it functions in supplying enough material to prevent starving the forward sections.

Multiple-screw extruders (that is, extruders with more than a single screw) were developed largely as a compounding device for uniformly blending plasticizers, fillers, pigments, stabilizers, etc., into the polymer. Subsequently, the multiple-screw extruders also found use in the processing of plastics.

Multiple-screw extruders differ significantly from single-screw extruders in mode of operation. In a single-screw machine, friction between the resin and the rotating screw, makes the resin rotate with the screw, and the friction between the rotating resin and the barrel pushes the material forward, and this also generates heat. Increasing the screw speed and/or screw diameter to achieve a higher output rate in a single-screw extruder will therefore result in a higher buildup of frictional heat and higher temperatures. In contrast, in twin-screw extruders with intermeshing screws the relative motion of the flight of one screw inside the channel of the other pushes the material forward almost as if the machine were a positive-displacement gear pump which conveys the material with very low friction.

In two-screw extruders, heat is therefore controlled independently from an outside source and is not influenced by screw speed. This fact becomes especially important when processing a heat-sensitive plastic like poly(vinyl chloride) (PVC). Multiple-screw extruders are therefore gaining wide acceptance for processing vinyls, although they are more expensive than single-screw machines. For the same reason, multiple-screw extruders have found a major use in the production of high-quality rigid PVC pipe of large diameter.

Several types of multiple-screw machines are available, including intermeshing co-rotating screws (in which the screws rotate in the same direction, and the flight of one screw moves inside the channel of the other), intermeshing counter-rotating screws (in which the screws rotate in opposite directions), and non-intermeshing counter-rotating screws.

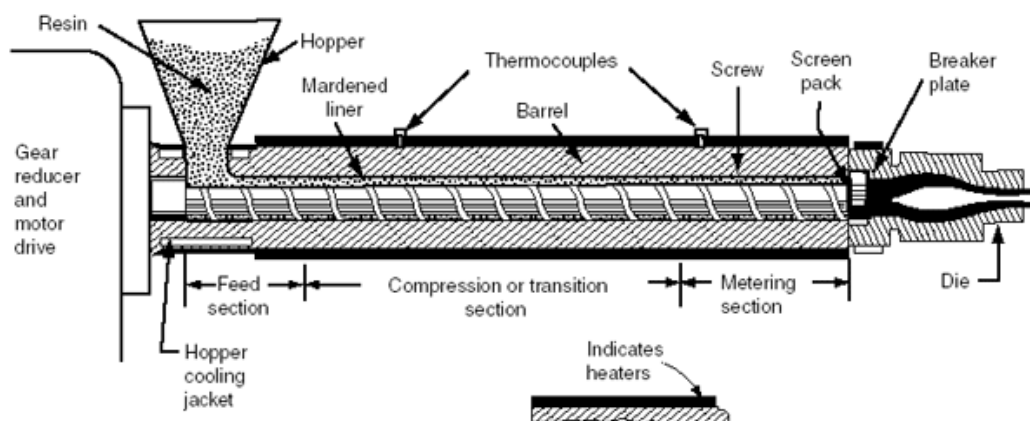


Figure 4.2 Scheme for a typical single-screw extruder showing extruding pipe.

4.1.2 Melt blending: Brabender[®] plastograph

The Brabender[®] plastograph (Figure 4.3) is a torque rheometer for applicational investigations or processing tasks in laboratories and simulation. It allow to energetically mix small amounts (50 g) of material. It is a suitable device for rheological measurements and preliminary test of screening.

It has a digital 3-kW motor, a torque measuring range of 150 Nm and speed range from 1 to 150 rpm. The melt temperature is controllable and monitored by four thermocouples placed inside the mixing chamber. The starting materials are charged through the hopper into the chamber, where they are heated and are subjected to shear stress by two screws that rotate at different speed.

The measuring principle is based on making visible the resistance the sample material opposes to the rotating screws. The corresponding torque moves a dynamometer out of its zero position. In compliance with the existing standards and test specifications, a typical plastogram (torque and stock temperature vs. time) is recorded for each sample material. This diagram shows the relationship between torque (viscosity) and temperature/time in consideration of structural changes of the material. The measured data are displayed numerically as a table and/or graphically as a diagram during the measurement on the monitor and can be printed and stored.

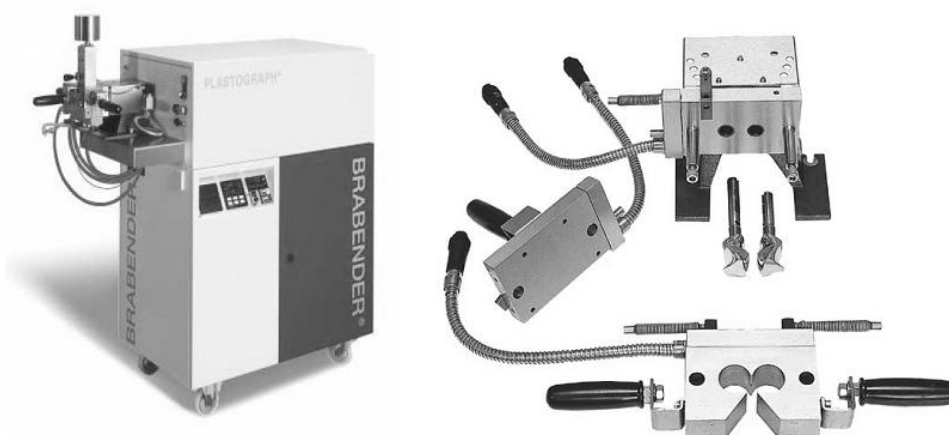


Figure 4.3 Brabender® plastograph and the mixing chamber in details.

4.1.3 Compression molding

The compression molding press is constituted by two heating plates, one is fixed and one is mobile, controlled by a pneumatic system. Normally the plates can be cooled by a water and/or air cooling system. The temperature and the pressure (eventually the cooling as well) are controllable through a control panel. The most recent device are equipped with a electronic panel that allows to program the press setting temperature and pressure of a multiple-phase program. In order to obtain specimens with a fixed shape, a metal sheet (mold) filled with polymer pellets is placed between the plates. Normally two Teflon sheets are used between the polymer and the plates to avoid the sticking.

4.1.4 Injection molding

The equipment necessary for the injection molding consists of two main elements. The injection unit, similar to an extruder, and the clamping unit (Figure 4.4). The central element of this technique is the mold, that contains a cavity, into which the plastic material is injected and which forms the final part geometry. The complete injection molding cycle takes place in several steps:

1. Start of plastification: the screw rotates and transports melt to the screw chamber in front of the screw tip. The screw returns, sliding axially.

2. End of plastification: screw rotation is switched off. In the screw chamber there is now just enough material to make the molding.
3. Closing the mold: the clamping unit moves forward until the mold halves are in close contact.
4. Start of injection: the screw moves forward axially without rotation and transports the melt into the cavity.
5. End of injection and cooling of the molding: the mold is volumetrically filled with hot melt. As the molded part in the mold cools down from melt temperature, further melt is conveyed into the cavity to compensate for volume contraction. Subsequently, the injection unit starts plasticating and preparing material for the next shot (repeat of step 1).
6. Ejection of the molding: after the molded part has cooled sufficiently, the mold opens and the finished molded part is ejected. The plasticating procedure is finished (repeat of step 2) and the production of the next molding can start (step 3).

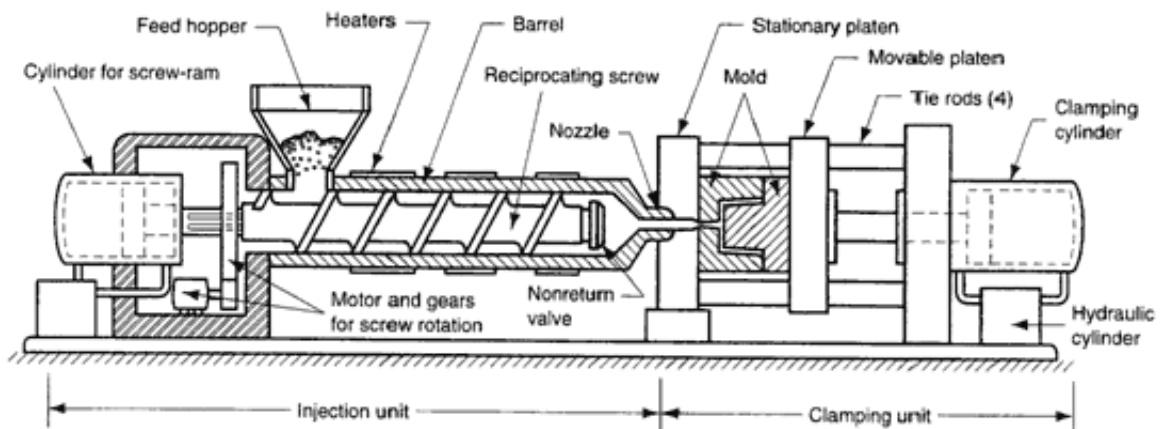


Figure 4.4 Scheme of the injection molding equipment.

4.1.5 Blow molding

PET Blow Molding is a highly developed molding technology. It is best suited for basically hollow parts such as plastic bottles with uniform wall thicknesses, where the outside shape is a major consideration. Blow molding also consumes about ten percent of all plastic worldwide. The types of PET blow molding process are described subsequently.

- *Extrusion blow molding* is the simplest type of blow molding. A hot tube of plastic material is dropped from an extruder and captured in a water cooled mold. Once the molds

are closed, air is injected through the top or the neck of the container; just as if one were blowing up a balloon. When the hot plastic material is blown up and touches the walls of the mold the material "freezes" and the container now maintains its rigid shape.

- *Injection blow molding* is part injection molding and part blow molding and can be broken down into three stages. The first stage is where the melted plastic is injected into a split steel mold cavity from the screw extruder. The mold produces a preform preform which resembles a test tube with a screw finish on the top. The preform is then transferred on a core rod to the second part of the injection blow molding stage. The preform is then placed inside another cold and usually aluminum blow mold cavity. Air is then injected through the core rod till the preform takes the shape of the cavity. While still on the core rod, the container is then transferred to a desired location for the third stage, where it is ejected from the machine.
- *Stretch blow molding* is best known for producing PET bottles commonly used for water, juice and a variety of other products. One of the major advantages of stretch blow molding is the ability to stretch the preform in both the hoop direction and the axial direction. This biaxial stretching of material increases the tensile strength, barrier properties, drop impact, clarity, and top load in the container. Stretch blow molding is divided into two different categories single-stage and two-stage. Single-stage uses the extruder to inject preform into a preform mold where the plastic is rapidly cooled to form the preform. The preform is then reheated and placed in the bottle mold. Then softened preform stretches to about twice its original length. Compressed air is then blown into the stretched preform to expand to the bottles mold. Once the bottle is cooled the mold is opened and the finished bottle is emptied from the mold cavity. Two-stage stretch blow molding is the same as single-stage, except the preforms are already made.

4.2 Characterization of polymers

4.2.1 Tensile test

The tensile test is performed following the procedure described in UNI ISO EN 527 Standard.

The instrument is a tensile test device in which the specimen held vertically at the two extremity by two grips. The bottom grip is fixed while the top one moves vertically stretching the specimen at constant rate. The instrument records the shift of the top grip and the force applied to the material, as function of the time. These data are elaborated to obtain the stress-strain curve. These are obtained by:

$$\sigma = \frac{F}{A} \qquad \varepsilon = \frac{\Delta L}{L_0} \qquad (4.1, 4.2)$$

where σ is the normal stress on a plane perpendicular to the longitudinal axis of the specimen, F is the applied load, A is the original cross sectional area, ε is the normal strain in the longitudinal direction, ΔL is the change in the specimen's gage length and L is the original gage length. An example of the stress-strain curve is shown in Figure 4.5.

The initial portion of the stress-strain diagram for most materials used in engineering structures is a straight line. For the initial portion of the diagram, the stress σ is directly proportional to the strain ε . Therefore, for a specimen subjected to a uniaxial load, we can write (Hooke's law):

$$\sigma = E\varepsilon \qquad (4.3)$$

where E is the Young modulus or modulus of elasticity.

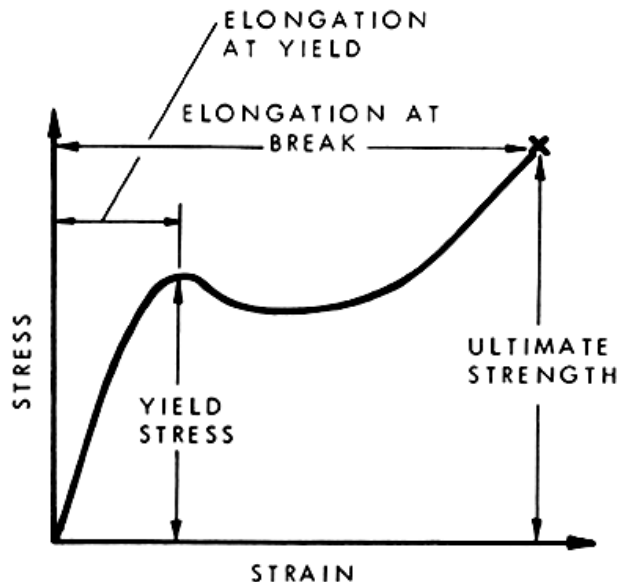


Figure 4.5 Stress-strain curve.

4.2.2 Flexural test

The flexure test is performed following the procedure described in UNI ISO EN 128 Standard. The instrument is the same of the tensile test, the apparatus that hold the specimen, the specimen are different. The specimen is supported at the two ends and a force is applied downward in its middle. The flexural elastic modulus E_f is calculated from:

$$E_f = \frac{L^3 F}{4bd^3 \delta} \quad (4.4)$$

where L is the length of the support span, b is the specimen length, d is the specimen thickness, F is the force applied to the specimen, δ is the midpoint deflection.

4.2.3 Thermogravimetric analysis (TGA)

Through the thermogravimetric analysis it is possible to measure the mass variation of a sample subjected to heating in inert or oxidant atmosphere, by varying the temperature. The data are recorded in a thermogram, that shows the thermal decomposition curve. The commonest procedure is the heating of the sample at constant heating rate, that results in a curve that show the decrease of the mass as the temperature increases. This technique is useful to evaluate the presence of an eventual inorganic residue in polymer materials (additives), to investigate thermal or thermal-oxidative decomposition phenomena (depending upon the presence of oxygen) and to verify the thermal stability of the material. The instrument is constituted by a furnace, in which is possible to control the atmosphere, a scale pan, a dispositive to check and tune the temperature (Figure 4.6).

The micro-balance plays a significant role, during measurement the change in sample mass affects the equilibrium of the balance. This imbalance is fed back to a force coil, which generates additional electromagnetic force to recover equilibrium. The amount of additional electromagnetic force is proportional to the mass change. During the heating process the temperature may go as high as 1500°C inside the furnace.

Typically, in this work, to evaluate the thermal stability of a material, some parameters will be measured (Figure 4.7):

- T_{onset1} = first offset temperature, as the starting degradation temperature.
- T_{onset2} = second offset temperature, as the ending degradation temperature.

- T_{maxMLR} = temperature at maximum mass loss rate, that graphically correspond to the position of peak of the derivative curve in the thermogram.
- $T_{0.05}$ = temperature at 5% loss weight. In many studies the temperature value related to a fixed loss weight is taken as thermal stability index.

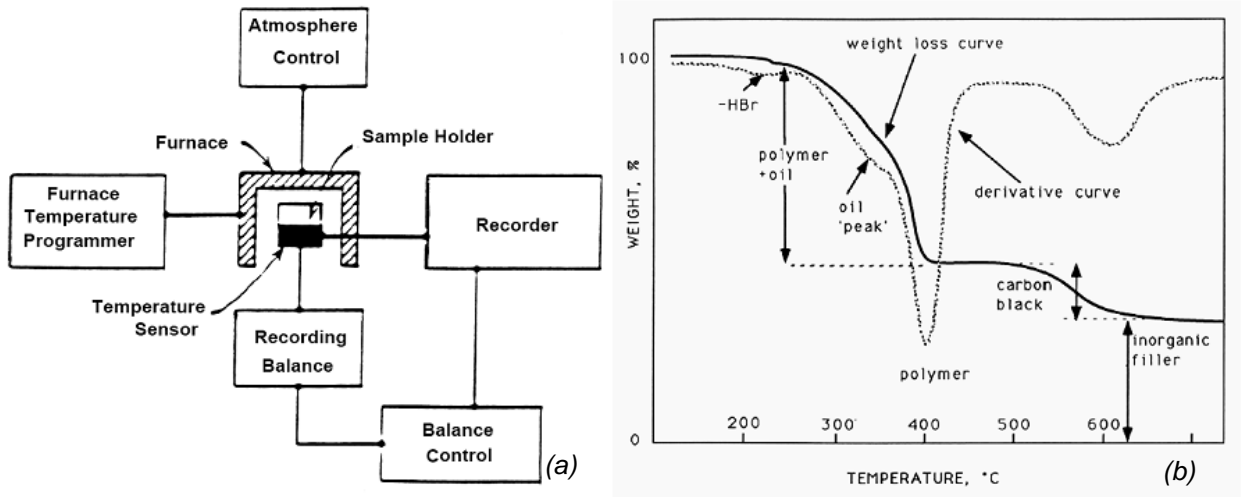


Figure 4.6 TGA: apparatus (a), example of thermogram (b).

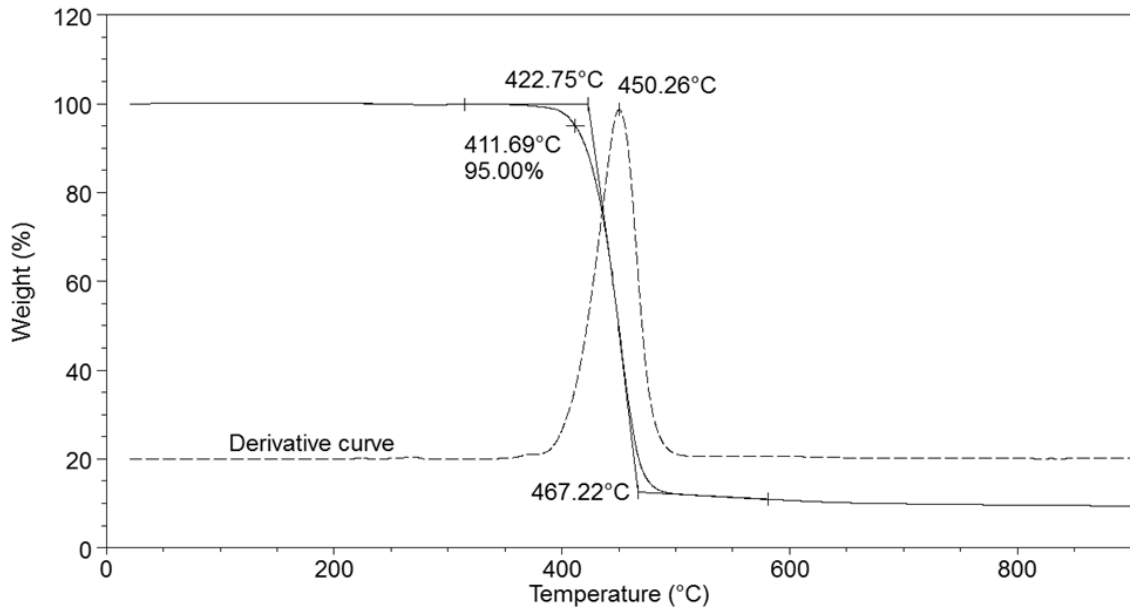


Figure 4.7 Example of TGA parameters (PET in inert atmosphere at 20°C/min): in the graph T_{onset1} (422.75°C), T_{onset2} (467.22°C), T_{maxMRL} (450.26°C), $T_{0.05}$ (411.69°C) are shown.

4.2.4 Differential scanning calorimetry (DSC)

Differential scanning calorimetry (DSC) is a technique measures the amount of heat absorbed or released by a sample as it is heated or cooled or kept at constant temperature (isothermal). The sample and reference material are simultaneously heated or cooled at a constant rate. This technique is applied to most of the polymers in evaluating the curing process of the thermoset materials as well as in determining the heat of melting and melting point of thermoplastic polymers, glass transition temperature (T_g), endothermic and exothermic behavior. Through the adjunct process of isothermal crystallization it provides information regarding the molecular weight and structural differences between very similar materials.

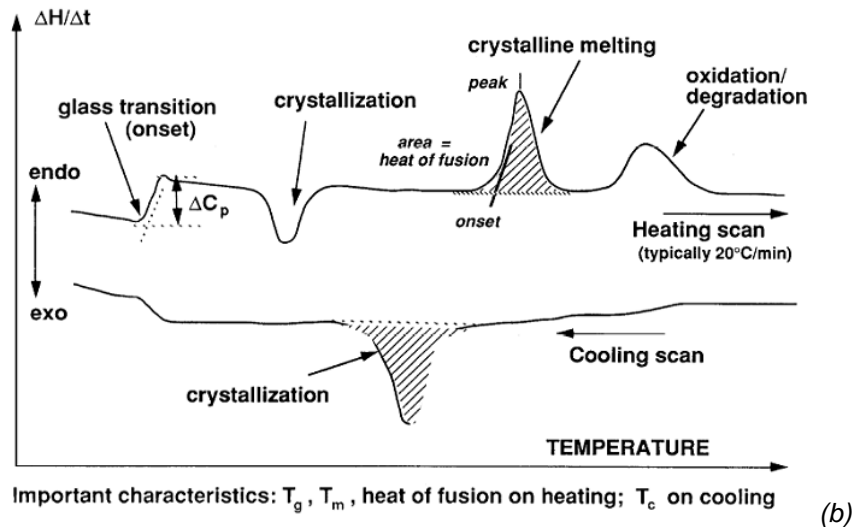
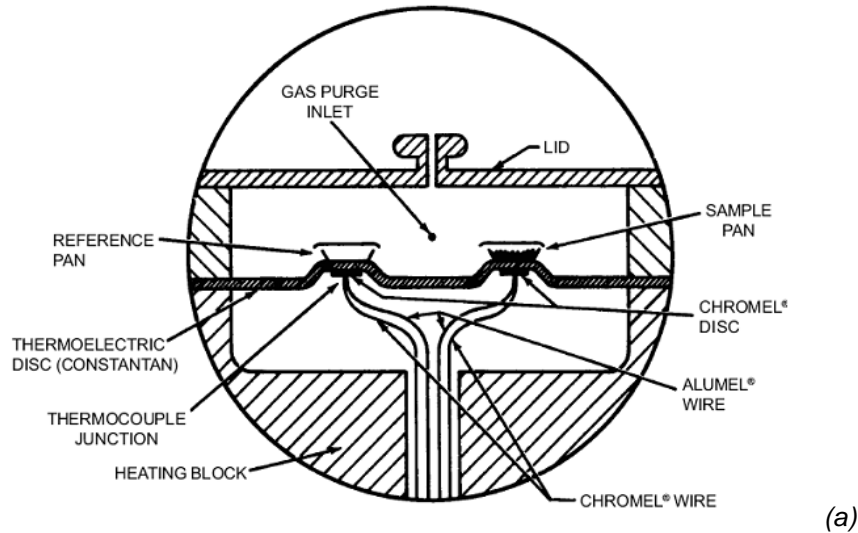


Figure 4.8 Scheme of the DSC cell (a), example of thermogram (b).

As shown in Figure 4.8, a hermetically sealed aluminum pan, containing the sample, and an empty reference are placed in a cell. The sample and reference are simultaneously heated or cooled at a constant rate under inert atmosphere. The difference in temperature between them is measured by thermocouples and it is proportional to the difference in heat flow (from the heating source i.e. furnace), between the two materials. During the analysis, every time a material transition occurs, an amount of energy is given to the sample in order to keep it at the same temperature of the reference.

Normally, the parameters determined by DSC are the transition temperatures (glass transition T_g , melting T_m , crystallization T_c) and the associated enthalpies (melting ΔH_m , crystallization ΔH_c). In a semicrystalline polymer, the crystalline content is calculated from [1]:

$$X_c = \frac{\Delta H_m}{\Delta H_m^0} 100 \quad (4.5)$$

where ΔH_m^0 is the heat of melting of the 100% crystalline polymer.

4.2.5 Dynamic mechanical analysis (DMA)

During the dynamic mechanical analysis a sinusoidal strain is applied to the sample. The mechanical response is measured as function of the temperature, that typically varies linearly in the time. This technique allows to investigate particular motions of polymeric chains and thus to obtain important information. The sample is subjected to tensile, flexure, torque or compression sinusoidal stress that lead a sinusoidal strain:

$$\varepsilon = \varepsilon_0 \sin \omega t \quad (4.6)$$

and the associated stress is shifted of an angle δ :

$$\sigma = \sigma_0 \sin(\omega t + \delta) \quad (4.7)$$

Depending on the response of the sample, the angle δ can exhibit different values:

- $\delta = 0^\circ$, perfectly elastic solid
- $\delta = 90^\circ$, perfectly viscous fluid
- $0 < \delta < 90^\circ$, viscoelastic systems (like generally polymers are).

The delay between strain and stress is a result of the time necessary for molecular rearrangements.

After trigonometric consideration the previous relation can be expressed as:

$$\sigma = \sigma_0 \sin(\omega t) \cos \delta + \sigma_0 \cos(\omega t) \sin \delta \quad (4.8)$$

Thus the stress applied to the sample is sum of two contributes, the which one of the elastic solid and the which one of the viscous fluid. As the stress, the elastic modulus is sum of those two contributes as well, the storage modulus and the loss modulus (E' and E'' respectively) [2]:

$$E' = \frac{\sigma_0}{\varepsilon_0} \cos \delta \quad E'' = \frac{\sigma_0}{\varepsilon_0} \sin \delta \quad (4.9, 4.10)$$

Their ratio is defined as:

$$\tan \delta = \frac{E''}{E'} \quad (4.11)$$

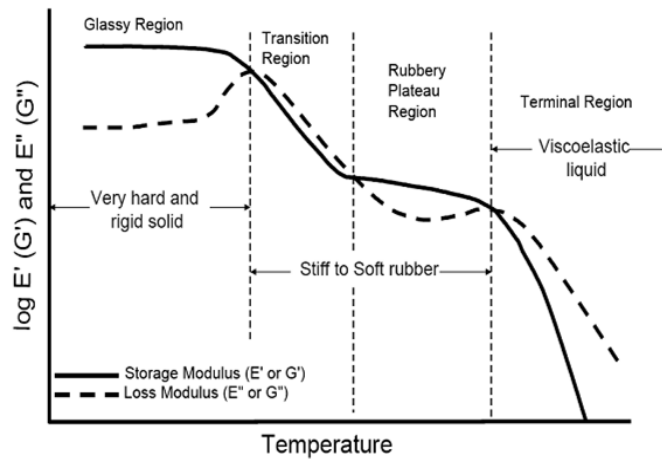


Figure 4.9 DMA: example of storage and loss modulus trends as function of temperature (3 points bending mode).

DMA allows to determine the storage modulus, loss modulus and $\tan \delta$ as function of the temperature, as shown in Figure 4.9. Their trends are closely related to the phase and structure variations of the polymers. Indeed the trends are associated to resonance effects between the frequency of the applied stress and definite molecular motions that are spontaneously active at specific temperatures. From a structural point of view, during the heating, the polymer chain is subjected to some movements, called thermal transitions. Normally, DMA is a useful technique to obtain the glass transition temperature T_g , that is the minimum temperature at which are possible coordinate movements of chain ends. Macroscopically, is the temperature

at which an amorphous material transitions, from a *rigid, glassy* state to *soft, rubbery* state. The commonest way to obtain the T_g from DMA is to assume it as the temperature of the peak of $\tan \delta$.

4.2.6 X ray diffraction (XRD)

The diffraction of X rays is a good tool to study the nature of the crystalline substances. In crystals the ions or molecules are arranged in well-defined positions in planes in three dimensions. The impinging X rays are reflected by each crystal plane. Since the spacing between the atoms and hence the planes can't be same or identical for any two chemical substances, this technique provides vital information regarding the arrangement of atoms and the spacing in between them and also to find out the chemical compositions of crystalline substances. The sample under study can be of either a thin layer of crystal or in a powder form. Since, the power of a diffracted beam is dependent on the quantity of the corresponding crystalline substance, it is also possible to carry out quantitative determinations.

The X rays are produced when a electrically charged particle with a sufficient kinetic energy is quickly decelerated. The X radiation is generated by a X ray tube containing a electrons source and two metal electrodes at high potential difference. The electrons hit the anode with high energy and, during the collision, they produce X rays that are emitted in all the directions. Some electron loss their energy during the collision producing X ray with a minimum wavelength λ . The relation between λ and the applied potential difference is:

$$\lambda_{min} = \frac{hc}{eV} \quad (4.12)$$

where c is the speed of light, V is the potential difference, h is the Plank constant and e is the electron charge.

The X rays can interact with ordered structures through reflection and scattering phenomena by the crystalline planes. An X ray which reflects from the surface of a substance has travelled less distance than an X ray which reflects from a plane of atoms inside the crystal. The penetrating X ray travels down to the internal layer, reflects, and travels back over the same distance before being back at the surface. The distance travelled depends on the separation of the layers and the angle at which the X ray entered the material. For this wave to be in phase with the wave which reflected from the surface it needs to have travelled a whole

number of wavelengths while inside the material. Bragg expressed this in an equation now known as Bragg's Law [3]:

$$n\lambda = 2d \sin \theta \quad (4.13)$$

where n is the reflection order, θ is the Bragg angle, d is the interplane distance. When n is an integer (1, 2, 3 etc.) the reflected waves from different layers are perfectly in phase with each other and the overall radiation with θ angle is intensified (Figure 4.10).

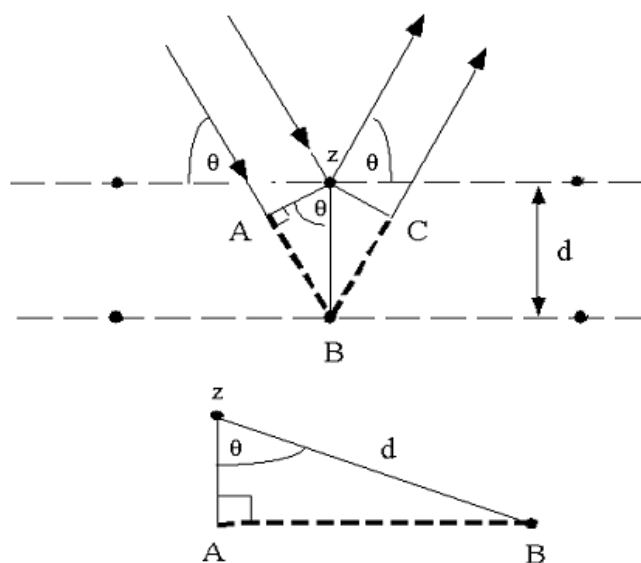


Figure 4.10 Diffraction of X rays by crystalline planes.

Concerning semicrystalline polymers, it is possible to determine the average size of crystallites by using the Scherrer equation [4]:

$$D = \frac{K\lambda}{\beta \cos \theta} \quad (4.14)$$

where D is the average size of the crystalline domains, K is the shape factor, β is the full width at half maximum of the peaks of the XRD spectrum (FWHM).

4.2.7 Transmission electron microscopy (TEM)

Transmission electron microscopy is used to study the local structures, morphology, and dispersion of multi-component polymers, cross sections and crystallization of metallic alloys and semiconductors, microstructure of composite materials, etc.

In this technique, a beam of high-energy electrons (typically 100-400 keV) is collimated by magnetic lenses and allowed to pass through a specimen under high vacuum. The thickness of the sample must be enough thin to allow the transmission of some incident electrons: when they pass through the material, some of them are absorbed and some are irregularly scattered when they find discontinuity of uniform atomic arrangements. The transmitted beam and a number of diffracted beams can form a resultant diffraction pattern, which is imaged on a fluorescent screen kept below the specimen. The diffraction pattern gives the information regarding lattice spacing and symmetry of the structure under consideration. Alternatively, either the transmitted beam or one of the diffracted beams can be made to form a magnified image of the sample on the viewing screen as bright-and darkfield imaging modes respectively, which give information about the size and shape of the micro-structural constituents of the material. High-resolution image, that contains information about the atomic structure of the material, can be obtained by recombining the transmitted beam and diffracted beams together.

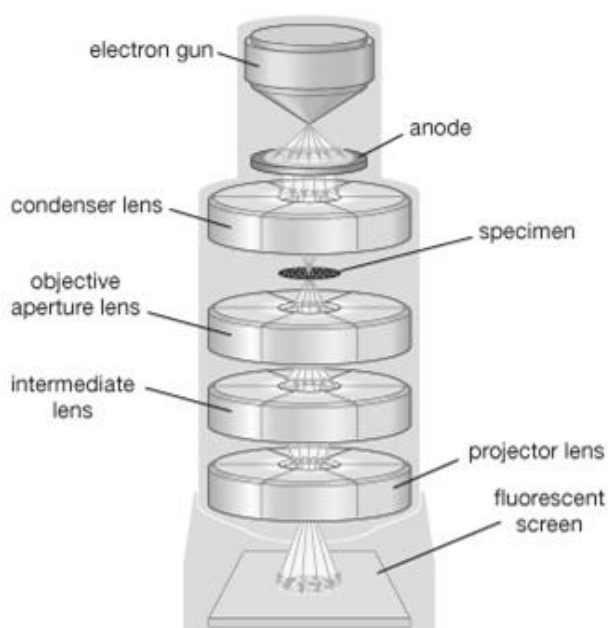


Figure 4.11 Scheme of the TEM apparatus.

The instrumentation comprises of a tungsten filament or LaB₆ or a field emission gun as source of electron beam, objective lens, imaging lens, CCD camera, monitor, etc. A simple scheme is shown in Figure 4.11.

4.2.8 Melt flow index (MFI)

Melt flow index is measured using the melt indexer, shown in Figure 4.12, according to the Standard method ASTM D-1238-70. The apparatus is a constant shear stress type capillary rheometer. A polymer sample is charged into the barrel of the melt indexer and compressed to eliminate air entrapment. After at least five minutes of heating time, a desired weight is placed on the plunger, extruding the melt. Because polymer melts are viscoelastic and take some time to reach the steady-state flow, the melt is extruded without taking measurement during the transition period suggested in the ASTM method. Then, the extrudate is cut, and the subsequent extrudate is collected for a sufficient length of time until a reasonable amount of the extrudate is accumulated. The collected extrudate is weighed to calculate the melt flow index. The extrudate diameter is measured to calculate the extrudate swell ratio [5]:

$$SR = \left(\frac{D_e}{D_c}\right)^2 \quad (4.15)$$

where D_c and D_e are the capillary and extrudate diameter respectively.

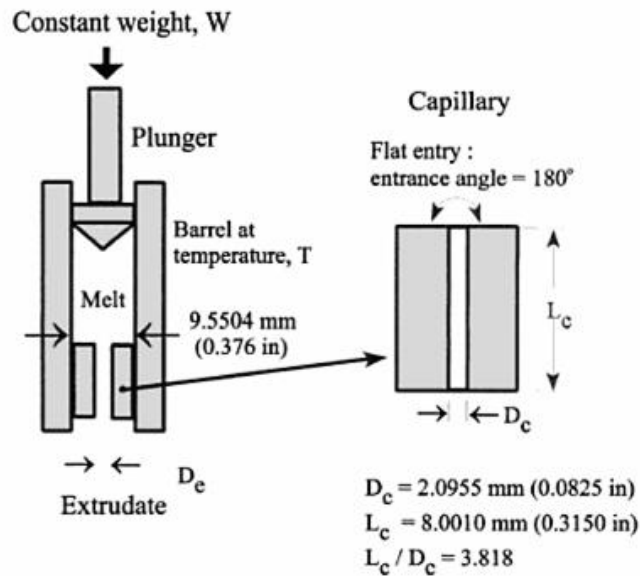


Figure 4.12 Melt flow indexer (ASTM D-1238-70)

Melt flow index is given by the weight of the extrudate in grams per 10 min. It is inversely proportional to the viscosity of the polymer at the particular temperature and shear stress of measurement. It does not give any information on the shear and the temperature sensitivities of the viscosity.

4.2.9 Intrinsic viscosity

The ratio of a solution's specific viscosity to the concentration of the solute, extrapolated to zero concentration. Intrinsic viscosity reflects the capability of a polymer in solution to enhance the viscosity of the solution. The viscosity behavior of macromolecular substances in solution is one of the most frequently used approaches for characterization. The intrinsic viscosity number is defined as the limiting value of the specific viscosity/concentration ratio at zero concentration. Intrinsic viscosity is determined by measuring the relative viscosity at several different concentrations and then extrapolating the specific viscosity to zero concentration. The variation of the viscosity number with concentration depends on the type of molecule as well as the solvent. In general, the intrinsic viscosity of linear macromolecular substances is related to the molecular weight or degree of polymerization. With linear macromolecules, viscosity number measurements can provide a method for the rapid determination of molecular weight when the relationship between viscosity and molecular weight has been established. Intrinsic viscosity is calculated by determining the reduced viscosity η_{sp}/c and extrapolating to infinite dilution [6]:

$$[\eta] = \left(\frac{\eta_{sp}}{c} \right)_{c \rightarrow 0} = \left(\frac{\eta_r - 1}{c} \right)_{c \rightarrow 0} \quad (4.16)$$

where c is the concentration of polymer in grams per 100 mL of solution, $\eta_r = t/t_0$ is the relative viscosity, η_{sp} is the specific viscosity.

The molecular weight M_n can be calculated from the Mark-Houwink equation [7]:

$$[\eta] = KM_n^a \quad (4.17)$$

where K and a are constants the values of which depend on the nature of the polymer and solvent as well as on temperature.

4.2.10 Oxygen permeability

The oxygen permeability test is performed through a permeabilimeter on a thin film. It takes place between two cells. During the first phase of the test, the conditioning, a nitrogen flow pass through both the cells in order to remove the residue oxygen and then to keep its content to a very low fixed value, that is assumed to be the reference level. When the steady-state has been achieved, oxygen begins to flow in the top cell and nitrogen still flows in the bottom cell. The sensor measure the oxygen that permeates through the film and is carried out by the nitrogen in the bottom cell. When this gas transmission rate (*GTR*) achieves the steady-state the instrument records the value. Every test is performed at constant temperature and relative humidity.

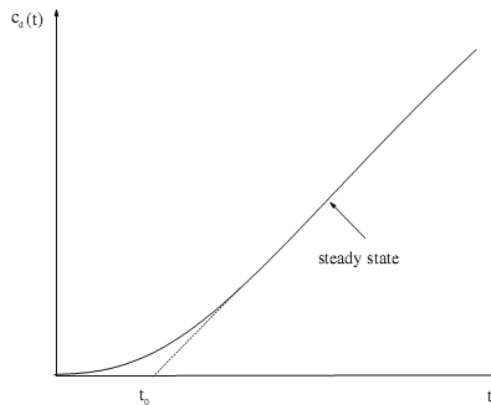


Figure 4.13 Typical diagram of experimental measurements. The time lag is estimated from extrapolation of the steady state line.

In this paragraph, a brief description of the experimental determination of the permeability constant is reported. In Chapter 14 the transport properties of polymers will be discussed more in detail. The constant permeability K is calculated from:

$$K = GTR \frac{P}{l} \quad (4.18)$$

where P is the pressure, l is the film thickness. The extrapolation of the time lag t_0 (Figure 4.13) from the concentration (c_d) versus time (t) plot allows to calculate the diffusion coefficient D from [8]:

$$t_0 = \frac{l^2}{6D} \quad (4.19)$$

If one assumes the diffusion coefficient to be constant the solubility coefficient S can be calculated from [8]:

$$K = DS \quad (4.20)$$

4.2.11 Fourier transform infrared spectroscopy (FTIR)

It involves the absorption of electromagnetic radiation in the infrared region of the spectrum which results in changes in the vibrational energy of molecule. Since, usually all molecules will be having vibrations in the form of stretching, bending, etc., the absorbed energy will be utilized in changing the energy levels associated with them. It is a valuable and formidable tool in identifying organic compounds which have polar chemical bonds (such as OH, NH, CH, etc.) with good charge separation (strong dipoles).

The instrument utilizes a single beam of un-dispersed light. It is passed through the sample and the absorbances at all wavelengths are received at the detector simultaneously. A computerized mathematical manipulation (known as Fourier Transform) is performed on this data, to obtain absorption data for each and every wavelength. To perform this type of calculations interference of light pattern is required for which the FTIR instrumentation contains two mirrors, one fixed and one moveable with a beam splitter in between them. Before scanning the sample a reference or a blank scanning is required.

4.2.12 Prediction of partial solubility parameters

The closer the solubility factors of one substance to those of another, the higher the solubility. The Flory-Huggins theory correlates the Hildebrand solubility parameters δ_A and δ_B to the interaction parameter χ_{AB} that is widely used to characterize a variety of polymer/solvent, polymer/polymer, and polymer/nanoparticle interactions:

$$\chi_{AB} = \frac{V_r}{RT} (\delta_A - \delta_B)^2 \quad (4.21)$$

where R is the gas constant, T is the temperature, V_r is the molar volume of the smallest repeat unit.

Hildebrand proposed that the solubility parameter δ follows the equation (at 298 K):

$$\delta = \left(\frac{E_{\text{coh}}}{V} \right)^{\frac{1}{2}} \quad (4.22)$$

where E_{coh} is the cohesive energy and V is the molar volume. He tried to correlate solubility with the cohesive properties of the solvents. According to him, the enthalpy of mixing between two components can be calculated by

$$\Delta h_{\text{M}} = \phi_1 \phi_2 (\delta_1 - \delta_2)^2 \quad (4.23)$$

where Δh_{M} is the enthalpy of mixing per unit volume, ϕ_1 and ϕ_2 are the volume fractions of components 1 and 2, δ_1 and δ_2 are the solubility parameters of components 1 and 2.

To derive this equation it was assumed that no specific forces are active between the structural units of the substances involved. Therefore it does not hold for crystalline polymers. Moreover it doesn't take into account polar groups or hydrogen bonds. A first requirement of mutual solubility is that δ of the components do not differ too much. Moreover, for some couples of components it is needed that the degree of hydrogen bonding is about equal.

Hildebrand considered only dispersion forces between structural units. Hansen et al. [9] proposed a practical extension of the Hildebrand parameter method to polar and hydrogen-bonding systems, primarily for use in polymer-liquid interactions. The solubility parameter is constituted by three components:

$$\delta^2 = \delta_{\text{d}}^2 + \delta_{\text{p}}^2 + \delta_{\text{h}}^2 \quad (4.24)$$

where δ_{d} is the dispersion component, δ_{p} is the polar component, δ_{h} is the hydrogen bonding component. The equivalent of Equation 4.23 is:

$$\Delta h_{\text{M}} = \phi_1 \phi_2 [(\delta_{\text{d}1} - \delta_{\text{d}2})^2 + (\delta_{\text{p}1} - \delta_{\text{p}2})^2 + (\delta_{\text{h}1} - \delta_{\text{h}2})^2] \quad (4.25)$$

Hansen developed a method to determine the partial solubility parameters of many solvents presumed the applicability of Equations 4.24 and 4.25. Unlike the solvents, for polymers, solubility parameters cannot be calculated from heat of vaporization data because of their non-volatility.

Hoftyzer and Van Krevelen, did the same assumptions of Hansen, developed a method to predict the partial solubility parameters by adding the group contributions, using the following equations:

$$\delta_d = \frac{\sum F_{di}}{V} \quad (4.26)$$

$$\delta_p = \frac{\sqrt{\sum F_{pi}}}{V} \quad (4.27)$$

$$\delta_h = \sqrt{\frac{\sum E_{hi}}{V}} \quad (4.28)$$

where i is the structural group within the molecule, F_{di} is the group contribution to dispersion forces, F_{pi} is the group contribution to polar forces, E_{hi} is the group contribution to hydrogen bond energy, V is the group contribution to the molar volume.

Hoy's system involves additive four molar function, two auxiliary equations and different expressions to calculate the solubility parameters. For amorphous polymers the following equations are valid:

$$F_t = \sum N_i F_{ti} \quad (4.29)$$

$$F_p = \sum N_i F_{pi} \quad (4.30)$$

$$V = \sum N_i V_i \quad (4.31)$$

$$\Delta_T = \sum N_i \Delta_{Ti} \quad (4.32)$$

$$\alpha = \frac{777\Delta_T}{V} \quad (4.33)$$

$$\bar{n} = \frac{0.5}{\Delta_T} \quad (4.34)$$

$$\delta = \frac{F_t + B/\bar{n}}{V} \quad (4.35)$$

$$\delta_p = \delta \left(\frac{1}{\alpha} \frac{F_p}{F_t + B/\bar{n}} \right)^{1/2} \quad (4.36)$$

$$\delta_h = \delta \left(\frac{\alpha - 1}{\alpha} \right)^{1/2} \quad (4.37)$$

$$\delta_d = (\delta^2 - \delta_p^2 - \delta_h^2)^{1/2} \quad (4.38)$$

where F_t is the molar attraction function, F_p is the polar component of F_t , Δ_T is the Lynderson correction for non-ideality, α is the molecular aggregation number, \bar{n} is the number of repeating units per effective chain segment of the polymer.

The distance between solubility parameters can be measured using a Euclidean distance [10]:

$$R_{12} = \sqrt{4(\delta_{d1} - \delta_{d2})^2 - (\delta_{p1} - \delta_{p2})^2 - (\delta_{h1} - \delta_{h2})^2} \quad (4.39)$$

References

- [1] G.M. Swallowe, J.O. Fernandez, S. Hamdan. J Phys IV 1997, 7, 453.
- [2] K.P. Menard. Dynamic mechanical analysis: a practical introduction, 2nd Edition. CRC Press, USA (2008).
- [3] C. Hammond. The basic of crystallography and diffraction, 3rd Edition. Oxford University Press, USA (2009).
- [4] U. Holzwarth, N. Gibson. Nature Nanotech 2011, 6, 534.
- [5] C.I. Chung. Extrusion of polymers: theory and practice. Carl Hanser Verlag, Munich, (2000).
- [6] J.M. Dealy, R.G. Larson. Structure and rheology of molten polymers: from structure to flow behavior and back again. Carl Hanser Verlag, Munich (2006).
- [7] G. Guerra, Europena Polymer Federation. Polymer-solvent complexes and intercalates II. Wiley-VCH (1999).
- [8] J. Crank. Methods of measurement. In Diffusion in Polymers. J. Crank, G.S. Park editors, Academic Press, London and New York (1968) pp 1-39.
- [9] C.M. Hansen. In Solvent Theory and Practice, Advances in Chemistry Series No. 124, edited by R.W. Tess, American Chemical Society, Washington D.C., Chapter 4 (1973).
- [10] U. Krewer, M.A. Liauw, L. Technische, M. Ramakrishna, M. Hari Babu, K.V. Ind Eng Chem Res 2002, 41, 4534.

Chapter 5

PET/MXD6/oMMT nanocomposites for packaging application

5.1 Introduction

In this activity poly(ethylene terephthalate) (PET) and poly(*m*-xylylene adipamide) (MXD6) nanocomposites filled with organomodified montmorillonite (oMMT) have been studied. In particular, the effects on the thermo-mechanical, morphological and barrier properties achieved by using different mixing sequences have been compared. PET has been blended with MXD6 to reduce the oxygen permeability, since it is an aromatic polyamide with good gas barrier properties, and oMMT has been added to enhance both mechanical and barrier properties because its capability to increase the tortuosity of the oxygen path. A subsequent step involved the development of nanocomposites bottles by blow molding, in order to verify the industrial feasibility.

5.2 Raw materials

Matrix polymer is constituted by a continuous phase of poly(ethylene terephthalate) (PET 9921, i.e., PET copolymer with intrinsic viscosity of 0.80 dL/g, Eastman Chemical Co.) and by a dispersed phase of poly(*m*-xylylene adipamide) (Nylon MXD6, Mitsubishi Gas Chemical Co.) (Figure 5.1a). As fillers, Dellite 72T (D72T) provided by Laviosa Chimica Mineraria S.p.A. has been used. It is a montmorillonite modified with dimethyl dihydrogenated tallow ammonium (Figure 5.1b).

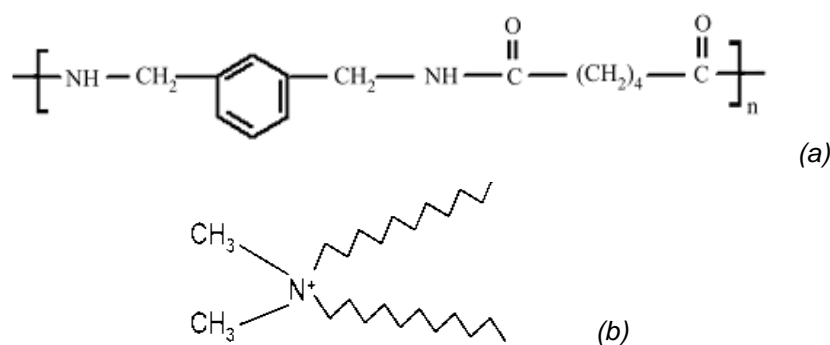


Figure 5.1 Repeating unit of MXD6 (a), dimethyl dihydrogenated tallow ammonium salt used as organomodifier of D72T (b).

5.3 Preparation of samples

The polymeric matrix used in this study is a PET/MXD6 blend (9/1 w/w) and the D72T content was fixed at 3.5 wt % (about 3 wt% amount of inorganic). The nanocomposites were prepared by melt compounding using a co-rotating, intermeshing twin screw extruder. Before processing, to avoid polymer hydrolysis, PET, MXD6 and D72T were dried at 80°C for 48 h under vacuum. In the first step a PET/D72T nanocomposite has been extruded and then MXD6 has been added in a second step. In a previous activity it has been verified that is the mixing sequence that gives the best properties to the nanocomposite [1]. During the first extrusion step the temperature profile of the extruder chamber, from hopper to die, was 210-250-250-250-245°C and a screw speed of 35 rpm was used. During the second extrusion steps a profile of 210-260-260-260-255°C and screw speed of 100 rpm was imposed. After every extrusion, all materials were dried at 160°C for 4 h under 4 kg/h air flow before further processing or characterization.

5.4 Main results

The characterization on molded specimens and films showed the capability of 3.5 wt % of D72T to improve the mechanical and barrier properties of PET/MXD6 blend without to compromise the transparency of a thin film [1]. Moreover a preferential localization of the clay inside the MXD6 domains has been observed.



Figure 5.2 From left to right: PET, PET/MXD6, PET/MXD6/D72T bottles.

In Figure 5.2 the PET, PET/MXD6, PET/MXD6/D72T bottles are shown. Despite the bottle neck of the nanocomposite is transparent, the body turns opaque after the blowing step.

Moreover, the addition of clay gives to the bottle a brownish color. This is due to the brown color of D72T (due to metal cations substituted in the MMT lattice) combined with a not perfect dispersion at the nanoscale level. That is often unwanted in the packaging market and the material do not result interesting from a commercial point of view. It is well know that the clay affects the crystallization behavior of the semicrystalline polymers. Commonly it acts as a nucleating agent accelerating the crystallization, increasing the crystallization temperature and the crystallinity content. Normally, during the drawing of the sidewall of the bottles, the crystallization of PET occurs, resulting in formation of crystallites having size enough small to avoid the transmission of the visible light. The addition of fillers could increase the crystallite size during the drawing, prejudicing the optical clarity of the bottle.

XRD analysis of D72T, PET/MXD6 bottle, PET/MXD6/D72T bottle and preform are shown in Figure 5.3. Comparing the D72T spectrum with the nanocomposites ones, a left shift of the diffraction peaks of D72T is observed. It means that the d -spacing between the layers of

D72T has been increased after the incorporation of clay in the polymer blend, reaching a good intercalation level between filler and matrix.

The difference between the nanocomposite bottle and the preform is the presence of the crystalline PET peak at high 2θ . The PET peaks of the filled and unfilled bottle have the same shape, meaning the same shape and size of crystallites.

TEM micrographs of the perpendicular section of the sidewall surface of the PET/MXD6/D72T bottle are shown in Figure 5.4. In Figure 5.4a the delamination of the nanocomposite, parallel to the surface, can be observed. The width of the gaps is about 1–3 μm . Higher magnification shows the highly oriented dispersion of clay (Figure 5.4b). The MXD6 phase is homogeneously dispersed and it is present in the form of elongated domains, in which the D72T is preferentially localized, rather than in the PET matrix (Figure 5.4c). Figure 5.4d shows the unoriented morphology of the injection molded specimen.

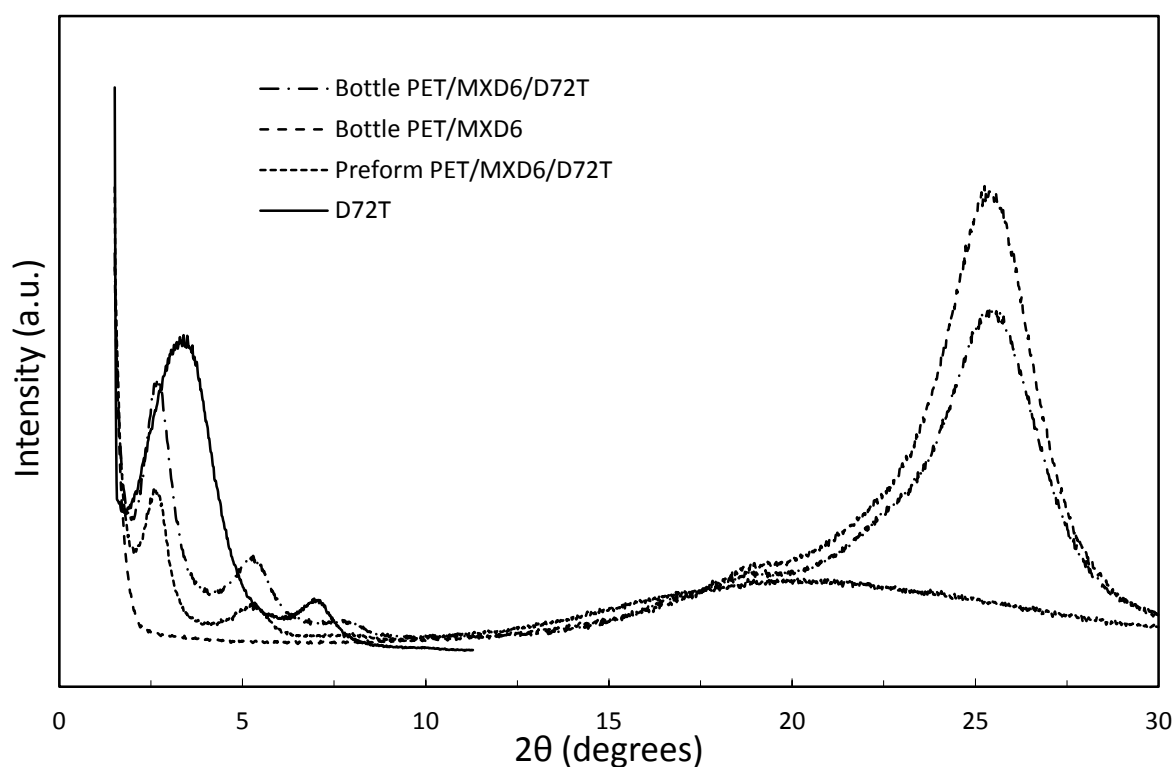


Figure 5.3 XRD spectra of as-received D72T, PET/MXD6 bottle, PET/MXD6/D72T bottle and preform.

The morphology of these ternary nanocomposites can be assumed as a binary system in which rigid domains (MXD6/D72T) are dispersed in a lesser rigid PET matrix. It is reasonable to think that, during the drawing of the material, this morphology leads stress concentration in the PET phase that results in formation of slits. The delamination occurs along some preferential planes parallelly to the surface. Another aspect associated to the delamination is the poor adhesion between clay and polymer and between PET and MXD6. The oriented structure provides many weak planes in which the slits can propagate.

The loss of transparency observed in the nanocomposite bottles is attributed to the size of slits, since they are comparable with the wavelength of the visible light. It can be diffracted by the multiple surface in the materials preventing the transmission through the material.

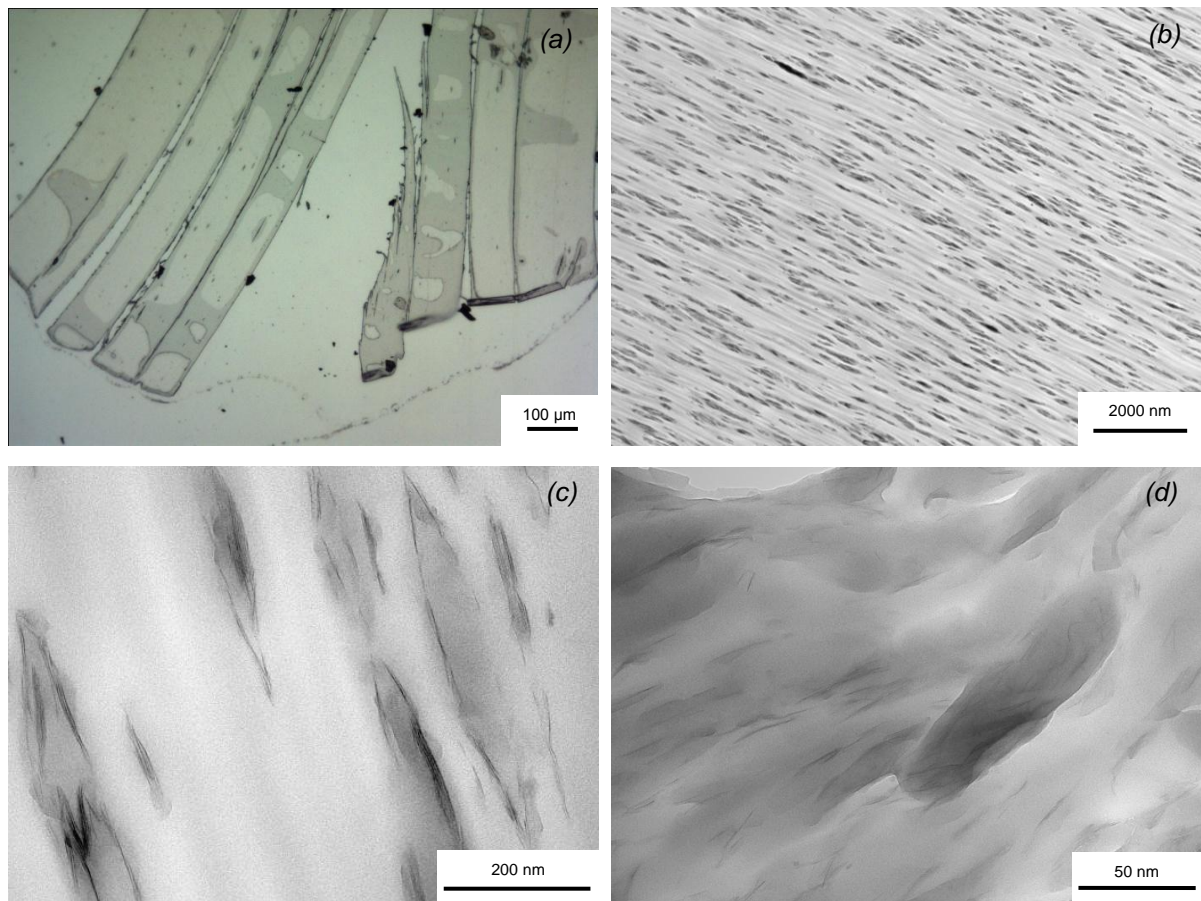


Figure 5.4 TEM micrographs of PET/MXD6/D72T nanocomposite: stretched bottle sidewall at different magnifications (a,b,c) and molded specimen (d).

5.5 Conclusion

PET/MXD6/oMMT nanocomposites have been produced by melt blending. Mechanical and oxygen permeability tests showed an improvement of the tensile and barrier properties by adding the clay.

The sidewall of the nanocomposite bottles loses the transparency after the blow molding, turning in a opaque appearance. It has been demonstrated by XRD analysis that the oMMT doesn't affect the crystallites size of PET. By TEM micrographs the delamination of material has been observed, resulting in slits parallel to the sidewall of the bottles. The slits have a width such that the transmitted light can be diffracted. The origin of the delamination has been attributed to the morphology. Stress concentration due to rigid domains and weak interfaces between the structural components result in the their detachment.

References

- [1] S. Donadi, M. Modesti, A. Lorenzetti, S. Besco. *J of Appl Polym Sci* 2011, 122 , 3290.

Chapter 6

The effect of processing on PET properties

6.1 Introduction

The PET is a very processing sensitive polymer since it absorbs easily the environmental moisture and it requires high temperatures to be melted (about 270°C). It undergoes to several types of degradation under different conditions [1]: thermal, thermal-oxidative and hydrolytic. Heat, oxygen and water are the main responsible of the decrease of the molecular weight. The most widely accepted mechanism of thermal and thermal-oxidative degradation is the random chain-scission that leads the formation of carboxyl end-groups. The hydrolysis is a random chain-scission reaction under solid-state conditions [2] that leads carboxyl and hydroxyl end-groups. When PET degrades, not only a reduction of the molecular weight occurs, the formation of chromophoric systems, acetaldehyde and crosslinks may occur as well. In packaging applications the release of acetaldehyde in the product stored inside changes its organoleptic properties.

Since the nanocomposites production involves at least one processing step, it is probable that the final properties are affected by the degradation phenomena. For this reason the nanocomposite properties analyzed in this activity have been compared with the which ones of the extruded PET, rather than the neat PET. In particular mechanical and rheological properties, and transition temperatures could be affected by the processing. These aspects have been investigate by mechanical test, DSC and intrinsic viscosity measurement.

6.2 Raw materials

The poly(ethylene terephthalate) (PET) provided by Gatronova Industries was the A80 grade (0.80 dL/g intrinsic viscosity).

6.3 Preparation of samples

PET was previously dried at 160°C for 2 hours. PET was extruded using a co-rotating, intermeshing twin screw extruder (Collin Teach-line zk25t) with a the temperature profile, from hopper to die, of 210-250-260-260-255°C and a screw rate of 100 rpm. The extruded materials were dried at 160°C for 2 hours. The specimens for the mechanical tests were produced by injection molding.

6.4 Characterization

Mechanical properties

The mechanical properties of all materials were measured by Galdabini (mod. Sun 2500) dynamometer. Dog-bone shaped specimens produced by injection molding have been subjected to the tensile test (ASTM D638) in order to measure the tensile modulus, with the aid of an extensimeter (1 mm/min tensile rate), and the yield stress and elongation at break (50 mm/min tensile rate).

Rectangular bars (126x12.6x3.2 mm) produced by injection molding have been subjected to the flexural test in order to measure the tensile modulus (1.3 mm/min test rate, 50 mm support span, according to ASTM D790).

DSC

The thermal transitions and the crystallization behavior were examined using a TA Instruments Q200 DSC differential scanning calorimeter working in heat-cool-heat mode, at heating and cooling rate of 10°C/min from 40 to 280°C.

Intrinsic viscosity

Measurement of intrinsic viscosity have been performed by a Cannon Ubbelohde Type 1B viscosimeter described in ASTM D 446. The solvent is a 60/40 w/w phenol/1,1,2,2-tetrachloroethane solution [3].

The intrinsic viscosity $[\eta]$ of PET at 30°C can be calculated using the Billmeyer's equation from ASTM D 4603 [4]:

$$[\eta] = 0.25 \frac{(\eta_r - 1 + 3 \ln \eta_r)}{C} \quad (6.1)$$

where C is the polymer solution concentration, $\eta_r = t/t_0$ is the relative viscosity, t is the average solution flow time, t_0 is the average solvent flow time.

The molecular weight M_n can be calculated from the Mark-Houwink's equation (Equation 4.17). For PET solubilized in a phenol/TCE solution (60/40 w/w) at 30°C, $K = 3.72E-04$ dL/g and $a = 0.73$ [5].

6.5 Results and discussion

6.5.1 Mechanical properties

For a generic property $S = f(M_n)$:

$$S = S_\infty - \frac{A}{M_n} \quad (6.2)$$

where S_∞ is the maximum value of the property associated to a infinite molecular weight, A is a constant. For example, consider the property of tensile strength: at low molecular weight it is very low but rapidly increases when the molecular weight increase. When M_n is high the strength increases slowly eventually achieving a maximum value S_∞ , associated to a theoretical infinite molecular weight.

In Figure 6.1 the mechanical properties of the neat and the extruded PET are shown. Only the elongation at break is different between the two samples (Figure 6.1b). It is not attributed to a decrease of molecular weight because the other properties don't get worse by effect of the processing. The low elongation at break of the extruded PET could be associated to a higher sensitivity of the propagating neck during the cold drawing. Almost all specimens do not achieve the complete drawing along the gauge length, thus the elongation at break of the

material should be higher than the experimental values. A long error bar means a wide variability of the property and it is usually due to a more inhomogeneous structure that leads the premature break of the specimen.

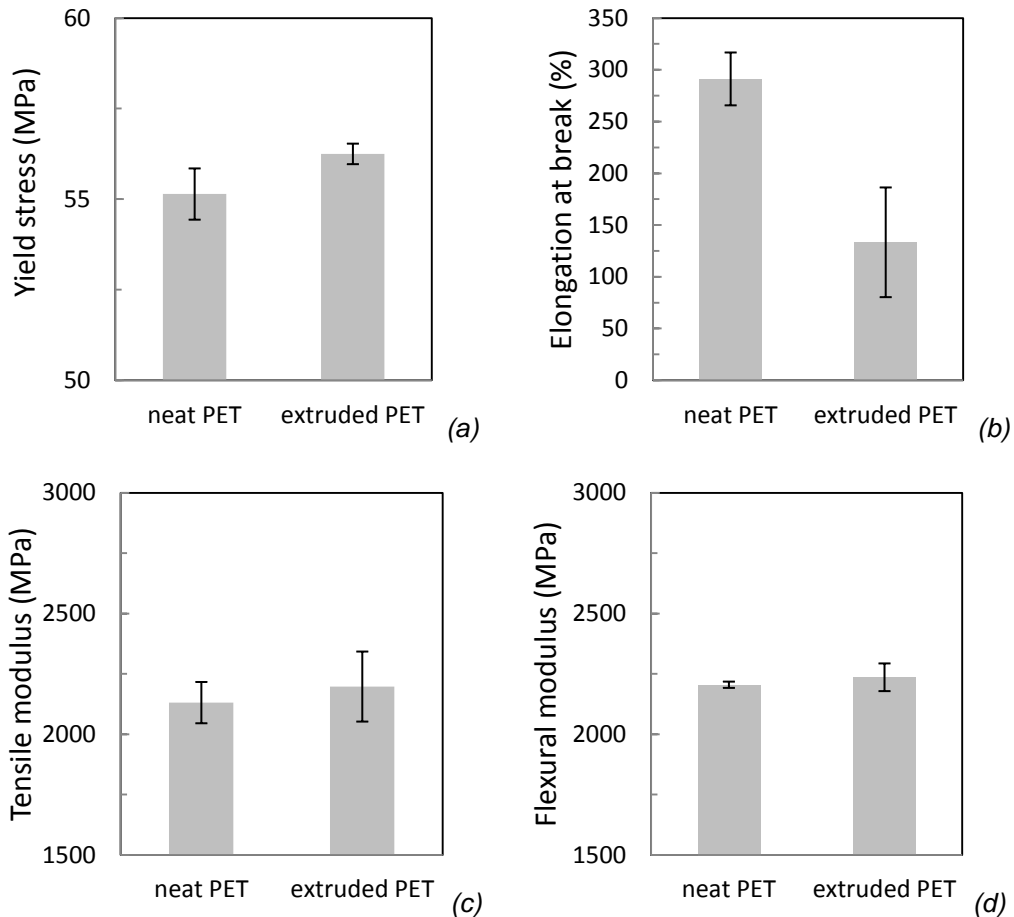


Figure 6.1 Mechanical properties of neat and extruded PET: yield stress (a), elongation at break (b), tensile modulus (c), flexural modulus (d).

6.5.2 DSC

The glass transition temperature strongly depends by the free volume of a polymer, mostly associated to the amount of chain ends. As the molecular weight decreases, the concentration of chain ends increases and the mobility averaged over all repeat units is enhanced, resulting in a decrease of the glass transition temperature (T_g). The most used relation between molecular weight M_n and glass transition temperature is given by Flory-Fox equation [6]:

$$T_g = T_{g,\infty} - \frac{K}{M_n} \quad (6.3)$$

where $T_{g,\infty}$ is the maximum glass transition temperature that can be achieved at a theoretical infinite molecular weight, K is the parameter related to the free volume.

The T_g of neat and extruded PET have been measured by DSC. They don't exhibit any relevant difference (about 76°C) (Figure 6.2).

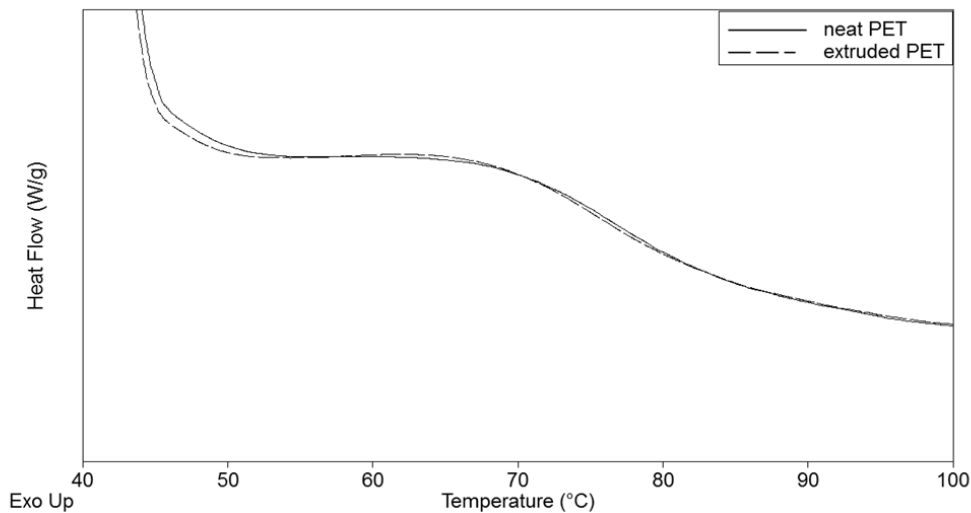


Figure 6.2 T_g signal by DSC analysis of neat and extruded PET.

6.5.3 Intrinsic viscosity

The parameters used to calculate M_n of the neat and extruded PET are reported in Table 6.1. The latter exhibits a decrease of the molecular weight due to the processing. In Figure 6.3 the Mark-Houwink relationship of the studied system is shown. Despite the molecular weight is reduced by about 5%, the influence on mechanical properties is not relevant because of the existing of the inverse correlation between the two properties: when the molecular weight is higher than the critical value required to create entanglement its influence is low. Indeed, using the Equation 6.4 to calculate the T_g , 79.03 and 78.96°C, for neat PET and extruded PET respectively, are obtained (for PET $T_{g,\infty} = 80.36$ °C and $K = 47784$ Kg/mol [7]). Figure 6.4 shows that the values of molecular weight of samples correspond to a similar value in T_g .

	m (g)	C (g/dL)	t_0 (s)	t (s)	η_r	$[\eta]$ (dL/g)	M_n (g/mol)
Neat PET	0.1245	0.4980	61.4	89.1	1.451	0.787	35939
Extruded PET	0.1241	0.4964	61.4	87.8	1.430	0.757	34056

Table 6.1 Parameters from intrinsic viscosity measurement of neat and extruded PET.

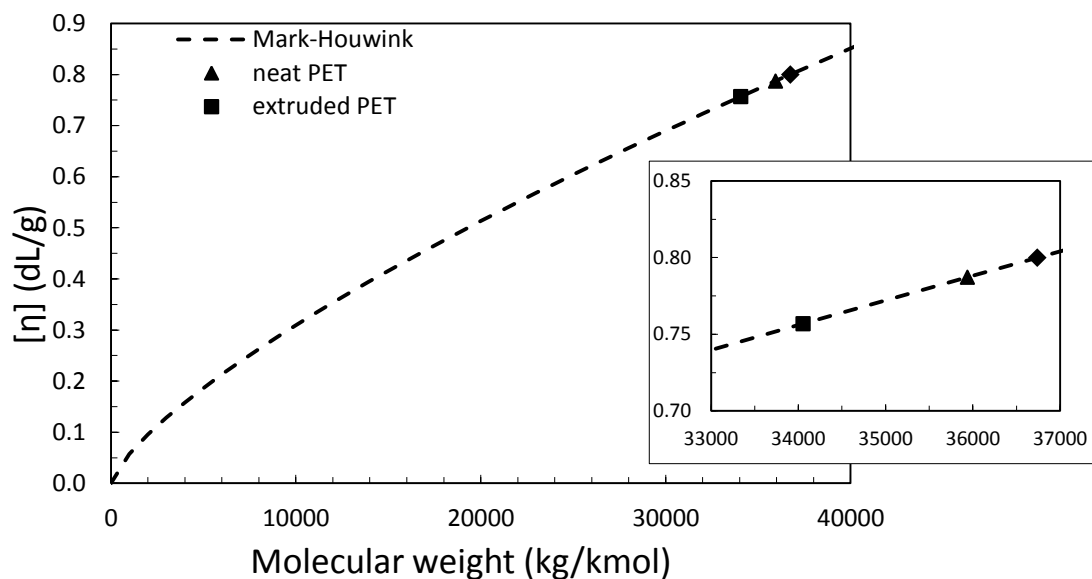


Figure 6.3 Mark-Houwink relationship of PET in a phenol/TCE solution (60/40 w/w) at 30°C.

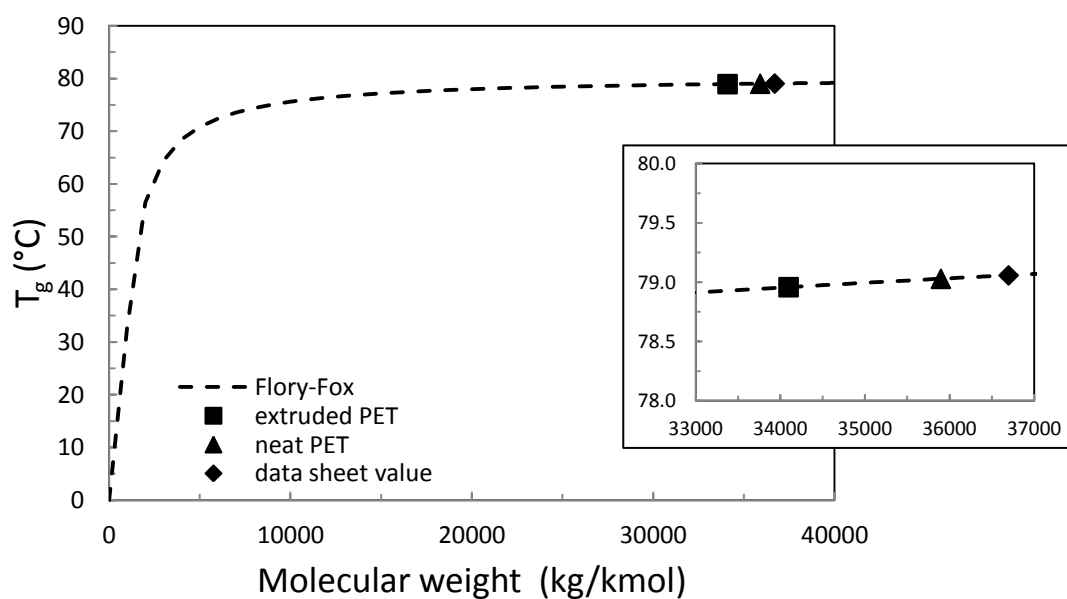


Figure 6.4 Fox-Flory relation of PET.

6.6 Conclusion

Mechanical properties, glass transition temperature and intrinsic viscosity of neat and extruded PET have been measured in order to verify the effect of processing.

The intrinsic viscosity after the extrusion of the PET slightly decreases, meaning a reduction of the molecular weight due to some degradation phenomena. This variation is rather irrelevant, since the DSC curves show the same glass transition temperature and the mechanical properties don't vary significantly, except the tensile elongation at break. The specimens of extruded PET do not exhibit differences in the deformation properties, just the failure occurs before the complete elongation.

In the following chapters the extruded PET will be assumed as reference material to compare the properties of PET based nanocomposites.

References

- [1] S.A. Jabarin. Poly(ethylene terephthalate) (chemistry and preparation). In Polymeric materials encyclopedia. J.C. Salamone, CRC Press, Boca Raton (1996).
- [2] A. Launay, F. ThomINETTE, J. Verdu. Polym Degrad Stab 1999, 63, 385.
- [3] Technical Bulletin: Inherent viscosity of poly (ethylene terephthalate). SPI - The Plastic Bottle Institute, PBI 23-1986.
- [4] F.W. Billmeyer Jr. J Polym Sci 1949, 4, 83.
- [5] H.F. Mark, C.G. Overberger, N.M. Bikales, G. Menges. Encyclopedia of polymer science and engineering. John Wiley and Sons, New York (1985).
- [6] T.G. Fox, P.J. Flory. J Appl Phys 1950, 21, 581.
- [7] S.D. Kim, S. Chakravarti, J. Tian, P. Bell. Polymer 2010, 51, 2199.

Chapter 7

PET/POSS nanocomposites: effect of POSS functionalization

7.1 Introduction

As described in Chapter 5, concerning a previous activity on PET/MXD6/oMMT nanocomposites, the oMMT dispersed in the polymer improves both mechanical and gas barrier properties [1]. Moreover the blow molding on nanocomposite bottles has been carried out without drawbacks. Despite that, the bottles lose their transparency after drawing and results in a brownish color. This is an aspect that has to be evaluated to make them commercially interesting. The reason of the transparency loss has been attributed to the delamination due to the presence of isolated rigid domains, that act as stress concentrators, and to the weak interface between the components.

The polyhedral oligomeric silsesquioxane (POSS) represents a new class of organic-inorganic hybrid nanosized filler. Due to the molecular size, colorless appearance, isometric shape, and wide range of commercially available compatibilizations, the POSS could reduce the troubles described in Chapter 5. Despite better mechanical properties are normally achieved when then interaction between matrix and fillers are strong, significant increases in tensile moduli and strenghts were achieved adding non-reactive POSS in PET fibers [2]. Other studies were carried out on PET filled with reactive POSS [3–6]. An improvement of mechanical properties was obtained adding silanol- and amine-functionalized POSS due to the strong interaction matrix-fillers [4,5].

In this activity two different kind of POSS have been added to PET to improve the mechanical porperties. The low aspect ratio of the filler doesn't allow a strong enhancement of the barrier properties, but however there should be an increase of the gas pathway to cross through the material. For this reason, a small amount of oMMT has been added

simultaneously with POSS. Moreover, it was interesting to compare the dispersion of clay in the two different PET/POSS nanocomposites.

7.2 Raw materials

The poly(ethylene terephthalate) (PET) provided by Gatronova Industries was the A80 grade (0.80 dL/g intrinsic viscosity). Polyhedral oligomeric silsesquioxanes (POSS) provided by Hybrid Plastics were the octaisobutyl POSS (POSSo), 1,2-propanediol isobutyl POSS (POSSp) (Figure 7.1). The organic modified montmorillonite provided by Laviosa Chimica Mineraria S.p.A. was Dellite 72T (D72T) which is a montmorillonite modified with dimethyl dihydrogenated tallow ammonium (Figure 5.1b).

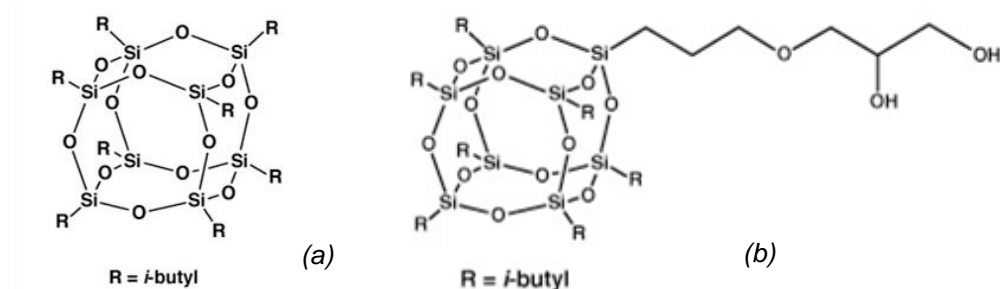


Figure 7.1 Structures of POSSo (a), POSSp (b).

7.3 Preparation of samples

PET and D72T were previously dried at 160°C for 2 hours and 80°C overnight respectively. PET/POSS and PET/POSS/D72T nanocomposites filled at 2 wt % and 2/1 wt% respectively were prepared mixing by melt compounding using a co-rotating, intermeshing twin screw extruder (Collin Teach-line zk25t) with a the temperature profile, from hopper to die, of 210-250-260-260-255°C and a screw rate of 100 rpm. The extruded materials were dried at 160°C for 2 hours. The specimens for the mechanical tests were produced by injection molding. The films for the oxygen permeability test were produced by compression molding quenching from 210°C to avoid the crystallization of the structure.

7.4 Characterization

Mechanical properties

The mechanical properties of all materials were measured by Galdabini (mod. Sun 2500) dynamometer. Dog-bone shaped specimens produced by injection molding have been subjected to the tensile test (ASTM D638) in order to measure the tensile modulus, with the aid of an extensimeter (1 mm/min tensile rate), and the yield stress and elongation at break (50 mm/min tensile rate).

Rectangular bars (126x12.6x3.2 mm) produced by injection molding have been subjected to the flexural test in order to measure the flexural modulus (1.3 mm/min test rate, 50 mm support span, according to ASTM D790).

DSC

The thermal transitions and the crystallization behavior were examined using a TA Instruments Q200 DSC differential scanning calorimeter working in heat-cool-heat mode, at heating and cooling rate of 10°C/min from 40 to 280°C.

TGA

The thermal behavior was measured by thermogravimetric analysis (TGA) on a TA instruments SDT Q600. Every run was carried out under a 100 mL/min air flow from room temperature to 800°C heating at 20°C/min. In order to verify the thermal stability during the processing isothermal runs at 275°C for 5 minutes have been performed on POSS.

MFI

The melt flow index of the materials has been measured according to the ASTM D1238 (265°C, 2160 g).

XRD

The degree of intercalation and exfoliation of the clay was monitored by X ray diffraction (Philips model X'PERT PRO). The XRD analyses were carried out in reflectance mode with Cu anode material ($K_{\alpha 1} = 1.54056$ nm, $K_{\alpha 2} = 1.54439$ nm). The diffractograms were scanned in a 2θ range from 1.50 to 30.00° at scan rate of 0.02°/s. The d -spacings have been calculate by using Equation 4.13.

Oxygen permeability

The barrier properties were investigated by a permeability tester (Extrasolution, MultiPerm), testing 50 cm² quenched thin films under 11.2 mL/min oxygen gas flow, at 23°C and 50% relative humidity. The constant permeability K is calculated by using Equation 4.18.

TEM

The morphology was investigated also by high magnification transmission electron microscopy (TEM, Philips EM 208). Samples for TEM analyses were cut from ultra-thin specimens using a Leica Ultracut UCT ultramicrotome.

7.5 Results and discussion

7.5.1 Mechanical properties

In Figure 7.2 the mechanical properties of the nanocomposites and the unfilled PET are shown. The yield stress (Figure 7.2a) of all materials doesn't exhibit any relevant difference since the error bars are of the same order of magnitude than the deviation of the average values.

Both PET/POSS_o and PET/POSS_p nanocomposites exhibit a higher elongation at break than the unfilled PET (Figure 7.2b). In both cases D72T reduces the elongation at break but the behavior of materials is still ductile. The embrittlement, that often occurs after the addition of clay, is not observed because the low content of D72T (1 wt%) is probably much lower than the percolation threshold. The higher elongation at break by the addition of POSS_p rather than POSS_o could be explained by assuming a more finely dispersion of the clusters size. Another possible explanation is that the interface between POSS_p and PET is stronger due to the higher polarity and to the capability to form hydrogen bonds between the hydroxyl groups of the fillers and the oxygen of the ester groups of the matrix. Anyway both POSS seems to have a toughening effect as explained in Chapter 2. The POSS clusters act as nanoparticles resulting in a cavitation mechanism that improve the toughness of the polymer [7]. The tensile modulus of the POSS filled materials is close to the one of the PET (Figure 7.2c). The addition of POSS doesn't lead any improvement. The two possible reasons are the coarse size of the clusters and a poor adhesion of the interface between them and the matrix. The addition

of D72T increases only slightly the modulus probably because the low content, as previously mentioned, and the dispersed clay is not enough to form a network. Moreover, D72T could be poorly dispersed in the PET in the form of stacks or partially intercalated structures, rather than exfoliated platelets. It has to be taken into account that the variation of modulus are close to the order of magnitude of the standard deviations, in particular for PET/Pp/D. The flexural modulus exhibits a similar trend (Figure 7.2d). A little stronger effect seems to have the D72T in the PET/Po/D nanocomposite than in the PET/Pp/D one.

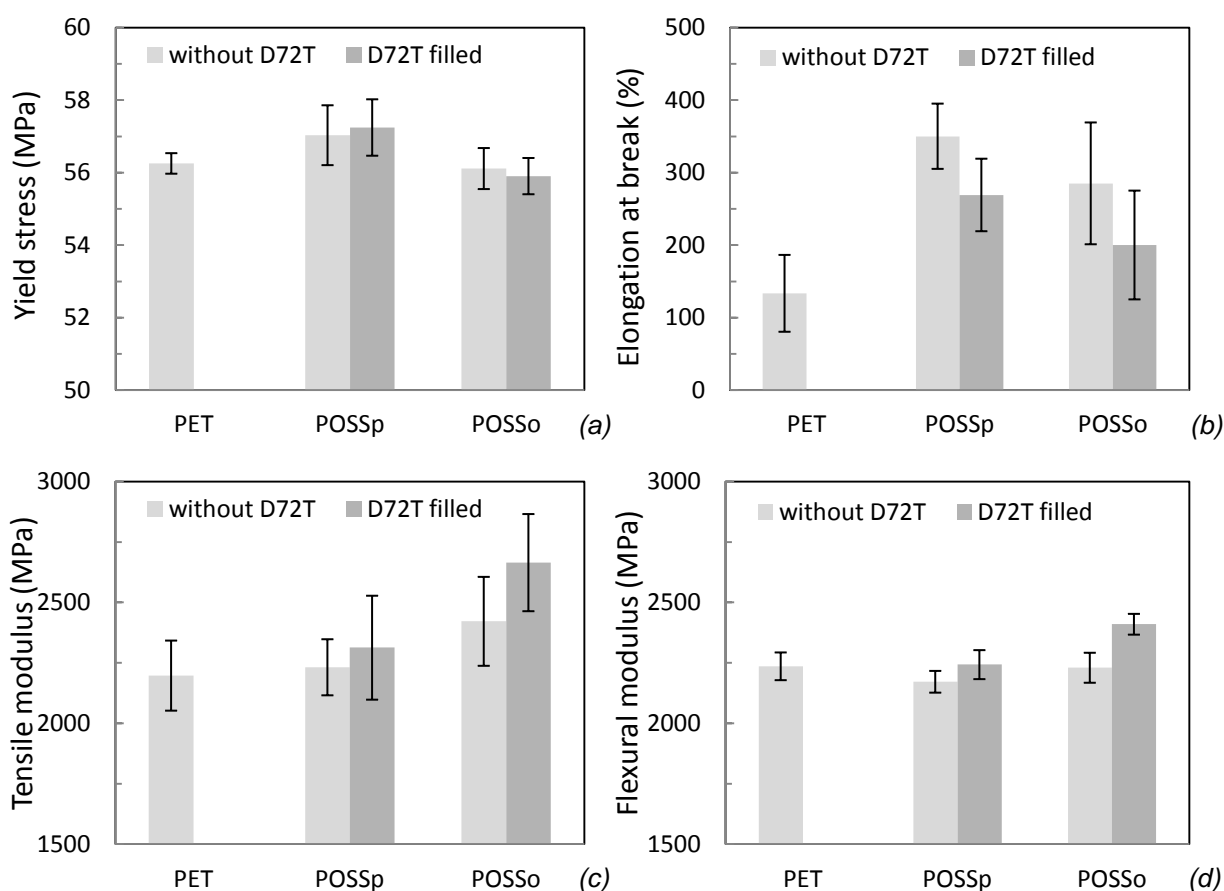


Figure 7.2 Mechanical properties of PET and its nanocomposites: yield stress (a), elongation at break (b), tensile modulus (c), flexural modulus (d).

7.5.2 DSC

Figure 7.3 and 7.4 show the crystallization and melting peaks, respectively, of the nanocomposites and the unfilled PET, by DSC analysis. The crystallization peaks of nanocomposites are sharper than PET, meaning a strong increase of the crystallization rate,

while the melting peaks don't exhibit any relevant difference in shape. The crystallization/melting temperatures (T_c and T_m) and enthalpies (ΔH_c and ΔH_m) are reported in Table 7.1. T_c of PET is relative to the sharper peak at higher temperature but its crystallization occurs during a wide temperature range. Taking into account this, it is clear the nucleating effect of the filler since the peaks of nanocomposites take place at higher temperature, in particular for D72T filled nanocomposites. ΔH_c of the PET/POSS nanocomposites don't exhibit any variation compared with the PET, while PET/POSS/D72T nanocomposites exhibit a higher value, meaning a higher crystallinity content. Melting peaks exhibit no relevant differences. Both the two classes of fillers act as heterogeneous nucleating agent. The nucleating activity of the oMMT on PET matrix is well known and has been subjected to many studies [8]. The nucleating activity of the POSS has been seen on PP matrix, leading a lower degree of supercooling required for crystallization [9].

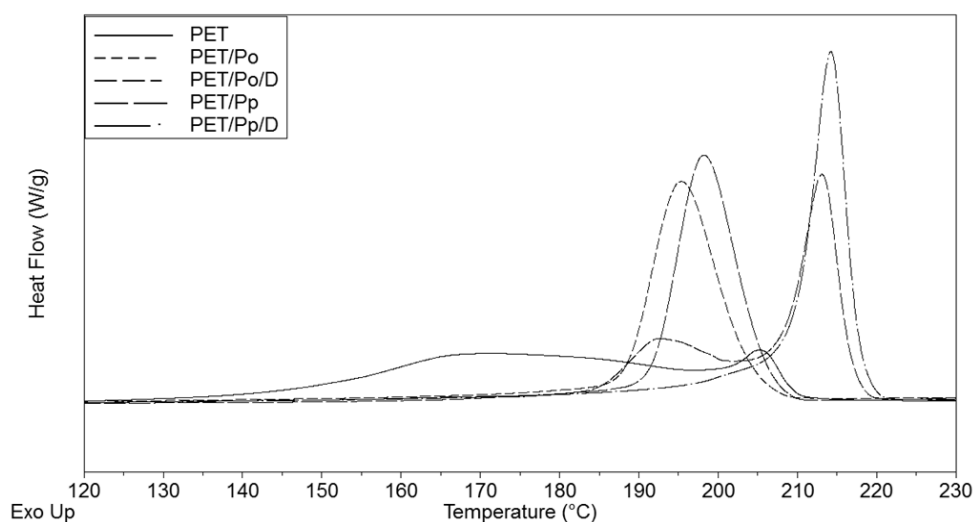


Figure 7.3 Crystallization peaks of PET and its nanocomposites.

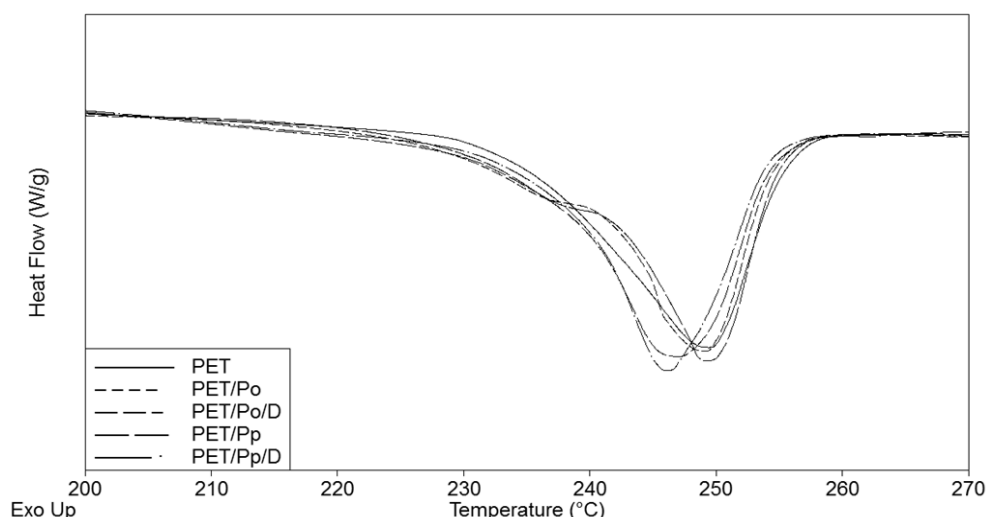


Figure 7.4 Melting peaks of PET and its nanocomposites.

Sample	T_c (°C)	ΔH_c (J/g)	T_m (°C)	ΔH_m (J/g)
PET	205.2	44.5	249.4	37.5
PET/Po	195.3	43.7	249.0	38.1
PET/Po/D	213.1	46.9	246.9	39.8
PET/Pp	199.0	44.7	249.3	38.9
PET/Pp/D	214.2	47.9	246.1	38.3

Table 7.1 DSC parameters of PET and its nanocomposites: crystallization/melting temperatures (T_c and T_m) and enthalpies (ΔH_c and ΔH_m).

7.5.3 TGA

The thermo-oxidative degradation of both POSS occurs in two step (Figure 7.5). The first in the range of 200–300°C/min is due to the degradation of the organic part, the second, in the range of 300–500 °C/min, is related to the sublimation of the silicon-oxygen cubic cage. As seen in a study on POSS thermal degradation, the oxygen plays an active role in the degradation process [10]. The authors proposed two competitive mechanisms are involved: the evaporation process, influenced by length of the alkyl chains, and the oxidation, that involves their degradation by radical process. The thermally stable residue has seen to have a Si–O–Si network structure, similarly to the amorphous silica. Despite the inorganic weight fraction of POSSo is slightly higher than that of POSSp, the latter exhibits a higher residue (R_{800} in Table 7.2). Moreover, it is more thermally stable above 300°C. In the temperature

range of processing (260-275°C) the thermal stability of the two POSS are similar, even the POSSo seems to be more stable than the POSSp. To reproduce a similar degradation as during the processing isothermal TGA at 275°C for 5 min have been performed. It has been observed a different residues of two POSS (R_{275} in Table 7.2), in particular a higher thermal stability of POSSp than POSSo.

The TGA analysis on nanocomposites show a worsening of the thermal stability, in particular if D72T is added (Figure 7.6). Referring at the main degradation of PET, the temperature of the maximum of mass loss rate (T_{maxMLR}) and the temperature at 5% weight loss ($T_{0.05}$) are reported in Table 7.2.

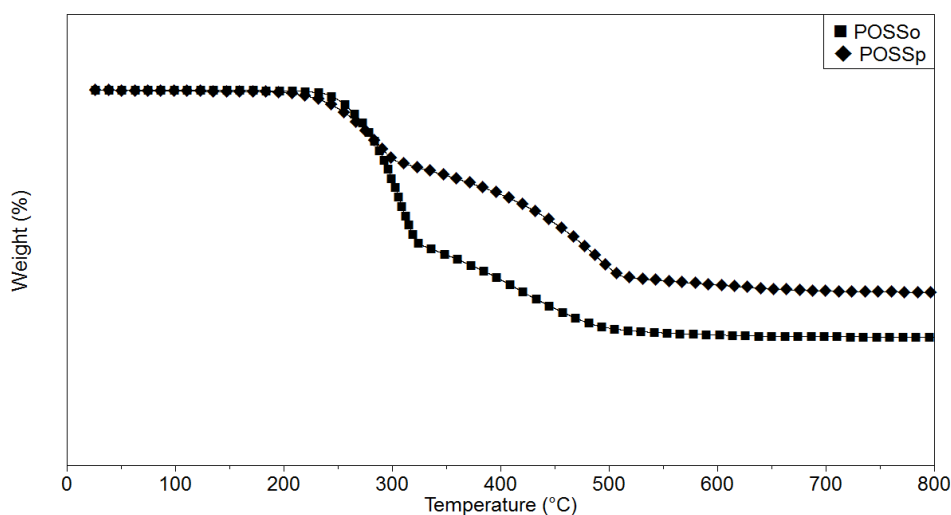


Figure 7.5 TGA under air flow of POSS.

Sample	wt_{inor} (%)	R_{800} (%)	R_{275} (%)
POSSp	44	45.9	78.3
POSSo	48	34.2	57.7

Table 7.2 TGA parameters of POSS: inorganic weight fraction (wt_{inor}), residue after thermo-oxidation at 800°C (R_{800}), residue after 5 min isotherm at 275°C (R_{275}).

The inorganic content is too low to form a effective insulating layer and the low aspect-ratio structure of POSS is not able to slow down the gas diffusion. Moreover, the alkyl-ammonium modified MMT promotes the PET degradation thorough the Hoffman elimination reaction. It forms some products (ammine, water and others) [11] and it has been suggested they

accelerate the degradation of matrix in PET/oMMT nanocomposites [12]. For this reason both T_{maxMLR} and $T_{0.05}$ of D72T filled nanocomposites are lower than the ones of the PET.

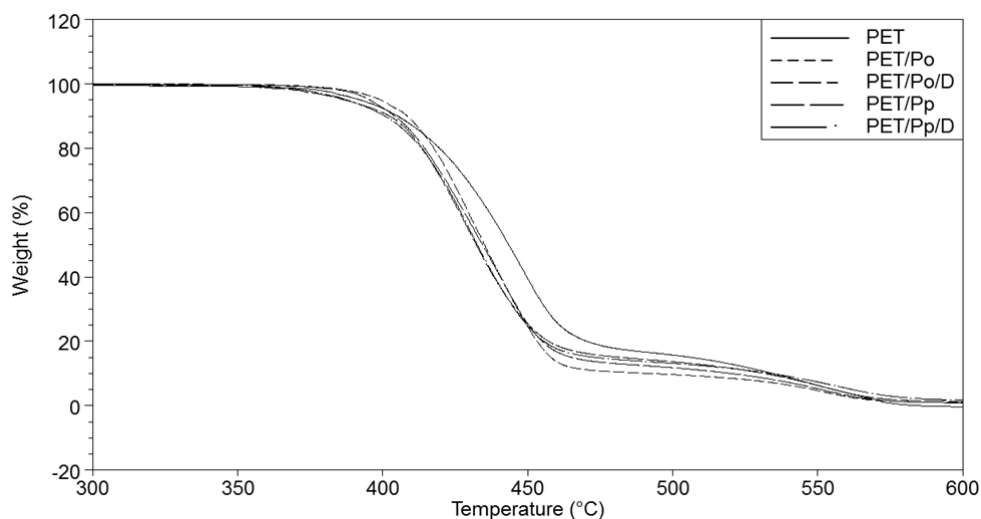


Figure 7.6 TGA of PET and their nanocomposites.

Sample	T_{maxMLR} (°C)	$T_{0.05}$ (°C)
PET	447	392
PET/Pp	433	395
PET/Pp/D	429	388
PET/Po	432	399
PET/Po/D	428	387

Table 7.3 TGA parameters of PET and their nanocomposites: temperature of the maximum of mass loss rate (T_{maxMLR}), temperature at 5% weight loss ($T_{0.05}$).

7.5.4 MFI

Commonly by adding the oMMT the MFI may decrease, meaning a higher viscosity due to the slowing down of the chains motion during the melt flow [13]. If the percolation threshold has not been achieved, even an increase of MFI could result by addition of nanoparticles [14]. This effect is more effective when the platelets are well exfoliated and homogeneously dispersed into the matrix and when the interaction between surfactants and polymer is strong [15]. In our case the addition of D72T doesn't lead any relevant decrease of the MFI probably due to the low inorganic content and to a poor dispersion level (Figure 7.7). The POSSo

slightly increase the MFI, while the POSSp reduces clearly the melt viscosity. It has been observed that the isobutyl groups of POSS act as plasticizer promoting the mutual sliding of polymer chains [16].

The rheological properties of a nanocomposites are affected by the interaction between the filler surface and the matrix and by the aspect ratio of the filler [15]. The POSS molecules, compared with the oMMT platelets, have smaller size, higher specific surface area and lower aspect ratio. Commonly, the POSS are not present in the molecular form but in clusters, so reducing the interactions with the matrix. The POSS clusters, unlike the tactoid structures, don't allow the embedding of the polymeric chains that reduce their mobility. A lubricant activity of the POSS has been observed in PPSU/POSS nanocomposites, due to the friction reduction between the polymeric chains and the inner surface of the extruder [17]. In a study on PMMA/POSS nanocomposites it has been proposed that it is due to an increase of free volume [18].

Moreover, the POSSp, due to its hydroxyl group, may react during processing with carboxyl ends or ester groups of PET, unlike the unreactive POSSo. In the first case POSS terminated chains should be produced with water elimination. It is detrimental because the water promotes the transesterification reaction that reduces the molecular weight and the viscosity as well. In the second case the transesterification reaction occurs directly. In both the cases it could decrease the melt viscosity affecting negatively the mechanical properties. The absence of any improvement in the modulus of PET by addition of POSSp could be attributed to the partial transesterification of the PET chains, that it is in competition with the reinforcement action of the filler.

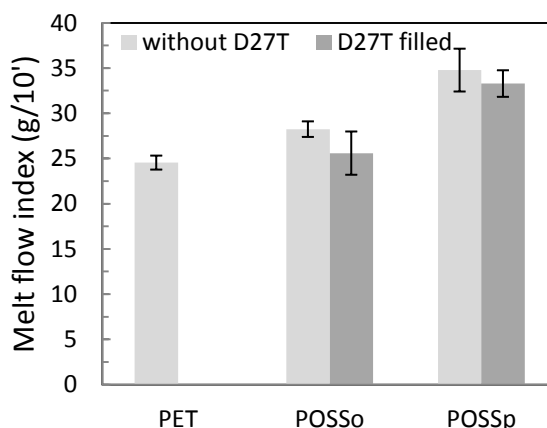


Figure 7.7 MFI of PET and their nanocomposites.

7.5.5 XRD

In Figure 7.8 the XRD spectra of D72T, PET and nanocomposites are shown. The peaks of D72T in the nanocomposites are clearly seen while the peaks of POSS are difficultly distinguishable from the baseline. At higher 2θ there is the crystallinity peak of the polymer. The magnification in the range of 1–10 degrees shows the shift of the first and second order peaks of the D72T at lower 2θ (Figure 7.9), meaning intercalation of the polymer in the clay interlayers. A further magnification in the range of 7–10 nm shows the peaks of crystalline agglomerates of POSS (Figure 7.10). The POSSo filled materials exhibit two peaks, unlike the which ones POSSp-filled, sharper in the PET/Po spectra and broader in the PET/Po/D one. As seen in a study involving POSSo, its XRD spectrum has the two main peaks at 8.0° and 8.8° and many other at higher 2θ [8]. All the peak positions and the related d -spacing are listed in Table 7.4. The decrease of d -spacing of the D72T in the nanocomposite is quite small, meaning a poor intercalation degree. The difference between PET/Pp/D and PET/Po/D is small as well. The first exhibits a slightly higher d -spacing of clay that can be associated to the lower melt viscosity that leads weaker shear stress transfer during the processing. It is an important factor that determines the level of dispersion, another one is the mobility of the polymer chains during the mixing.

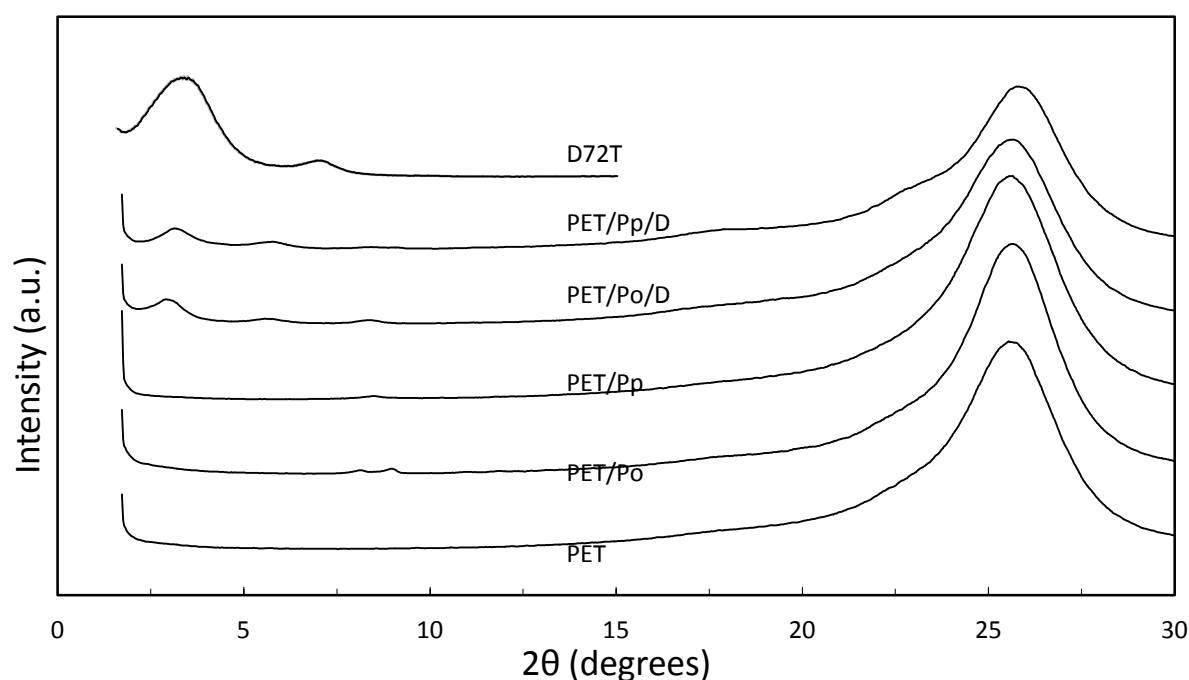


Figure 7.8 XRD spectra of the D72T, PET and their nanocomposites.

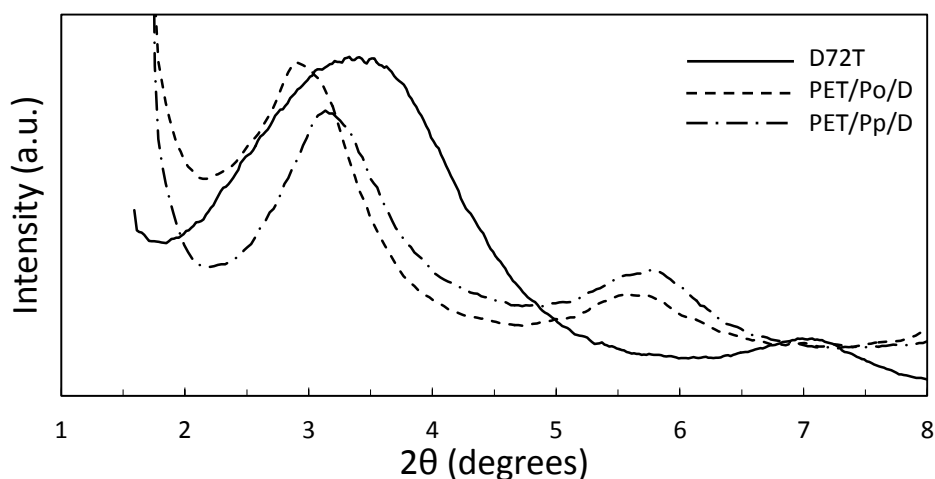


Figure 7.9 Magnification of the XRD spectra to show the shift at lower 2θ of the D72T peaks.

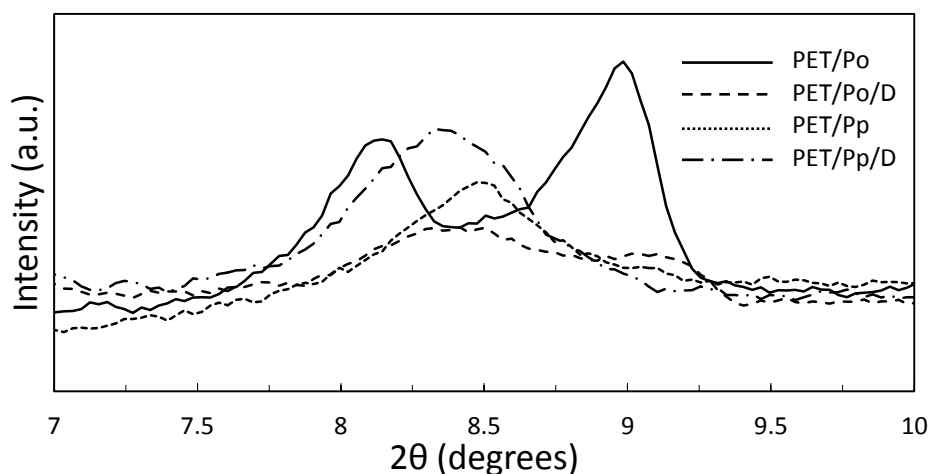


Figure 7.10 Magnification of the XRD spectra to show the peaks of POSS crystalline aggregate.

Sample	2θ (degrees)		d -spacing (\AA)	
	D72T	POSS	D72T	POSS
D72T	3.37	-	26.2	-
PET/Po	-	8.13, 8.98	-	10.9, 9.08
PET/Po/D	2.91	8.42, 9.07	30.1	10.4, 9.07
PET/Pp	-	8.50	-	10.5
PET/Pp/D	3.10	8.36	28.4	10.6

Table 7.4 Values of d -spacing of D72T compared with the nanocomposites.

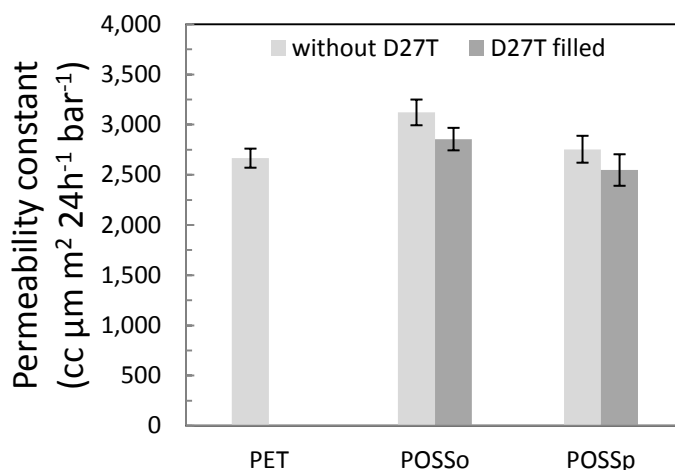


Figure 7.11 Permeability constant of PET and their nanocomposites.

7.5.6 Oxygen permeability

In Figure 7.11 the permeability constant of the nanocomposites compared to the PET is shown. No improvements of the permeability by effect of the fillers are observed. The PET/Po film has the highest permeability that is slightly improved by adding the D72T. The POSSp filled materials don't exhibit any difference compared to the PET.

The mechanism to improve the barrier properties in the nanocomposite materials is the creation of a tortuous path due to the orientation of the platelets. If the orientation is random the diffusivity of the gasses is anyway slowed down but in a lower extent. Concerning isodimensional fillers, like spherical particles and POSS clusters, this mechanism has a lesser influence. Moreover, the films subjected to the permeability tests are amorphous in order to discriminate the barrier effect of the fillers and do not take into account the one of the crystallites. In PS membranes filled with a high POSS content a higher oxygen permeability, compared with the polymer, has been observed, due to the high free volume at the matrix-fillers interface [19]. TEM micrographs showed a very fine and packed dispersion of nanosize cluster of POSS but the effect barrier is not enough to compensate the increase of free volume. The free volume is affected by the interactions between matrix and the clusters surface. In PP nanocomposites it has been observed that the permeability increases when the SiO₂ particles are not compatibilized, due to the formation of voids around the nanoparticles through which gases could freely permeate [20–22].

In our case the lower permeability of the PET/Pp than the PET/Po could be attributed to the more favorable interactions PET-POSSp, resulting in a lower free volume. The clay slightly reduces the permeability as expected. It has to be taken into account that the standard deviation is of the same order of magnitude of the permeability constant variation. The increase of free volume due to the presence of the filler will be discussed more in details in Chapter 14.

7.5.7 TEM

The nanocomposites bottles are developed by stretch blow molding. Compared to the PET (Figure 7.12a) the PET/Pp exhibits a very good transparency of the sidewall, only in the neck is still translucent, due to the higher thickness (Figure 7.12b). By adding the oMMT the transparency decreases and the bottle turns in a light brownish color, as seen in Chapter 5 (Figure 7.12c). Despite the performance of the PET/Po looks like the PET/Pp one, after drawing the bottle is still opaque (Figure 7.12d). Also in this case, the addition of clay leads a brown color to the bottle (Figure 7.12e).

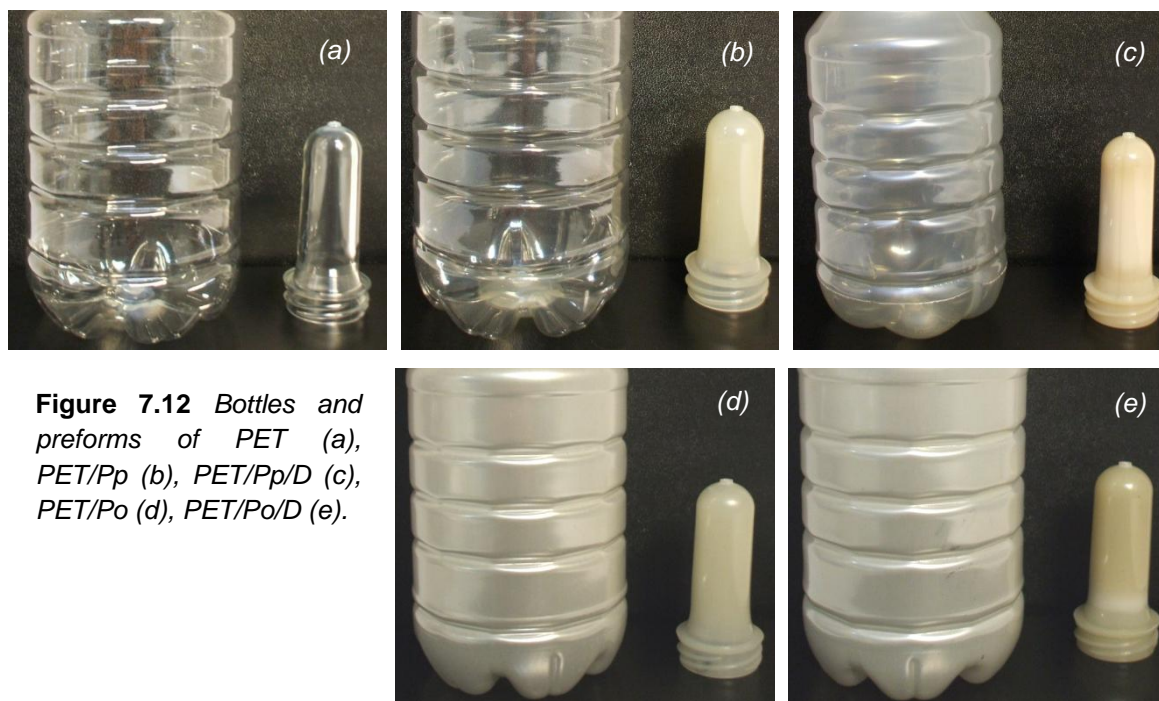


Figure 7.12 Bottles and preforms of PET (a), PET/Pp (b), PET/Pp/D (c), PET/Po (d), PET/Po/D (e).

In order to verify the dispersion of the POSS in the matrix the drawn part of the bottles has been subjected to TEM microscopy. Analyzing the morphology of the materials in a plane

perpendicular to the side wall of the bottle is possible to verify the presence of delamination due to the stress concentration caused by the presence of coarse POSS aggregates.

TEM micrograph of PET/Po bottle shows many microvoids and slits parallel to the bottles wall (Figure 7.13). The slits achieve 100 μm length and 5 μm width. Inside the slits, at their ends or in the middle, are visible some big clusters of POSSo. Higher magnifications show clearly the detrimental role of these inorganic aggregates of about 1.5 μm size (Figure 7.14). They act as starting point for the propagations of slits, subsequent to the cavitation mechanism [7]. The agglomerates of POSSo are very heterogeneous concerning both the size and the shape. The size of isodimensional clusters are quite variable from 100 to 200 nm (Figure 7.15a), while irregular shaped clusters are around 300 nm (Figure 7.15b). Some of them are affected by the draw, exhibiting an elongated shape parallelarly to the draw direction, of 300–500 nm length (Figure 7.15c).

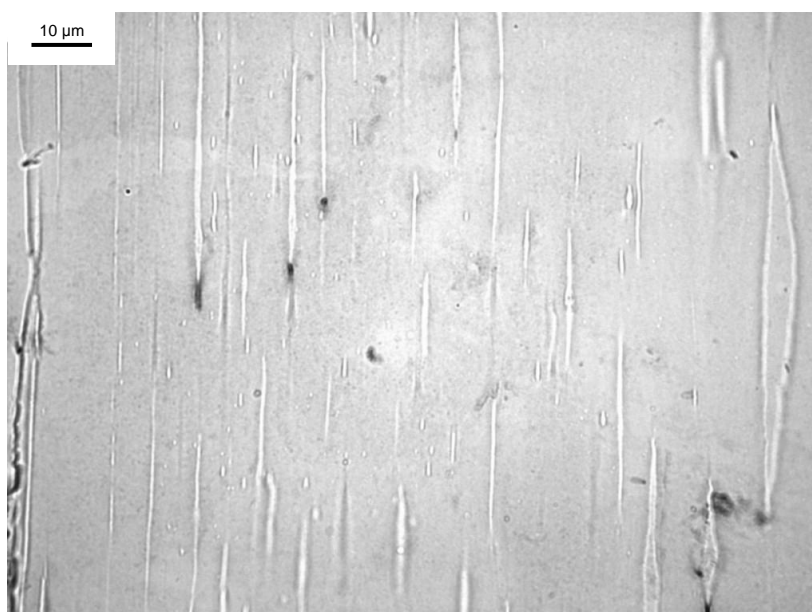


Figure 7.13 TEM micrograph of the PET/Po bottle (surface perpendicular to the drawn part of the side wall). The low magnification shows the slit distribution.

TEM micrograph of PET/Pp bottle shows very narrow slits (Figure 7.16) up to around 50 μm length. Higher magnifications show the presence of agglomerates along slits wide 40–100 nm. When its size are too high the agglomerates take place along a line leading the propagation of a crack. These elongated agglomerates can achieve 1 μm length (Figure 7.17).

The dispersion of the POSSp is more homogeneous and the size of clusters is generally smaller. Some of them achieve size of 100 nm (Figure 7.18a), some are present in particles of diameter 10-20 nm (Figure 7.18b). Similarly to the POSSo, some clusters are stretched along the draw direction, achieving 200–300 nm (Figure 7.18c).

The dispersion degree of POSSp is better than the POSSo since the clusters particles are smaller and have a narrower size distribution. Moreover in the PET/Po bottle there are some big clusters that cause stress concentration and lead very wide cracks. The interface is weak because many clusters are surrounded by voids along the drawn direction, that are the two points where the crack starts to propagate.

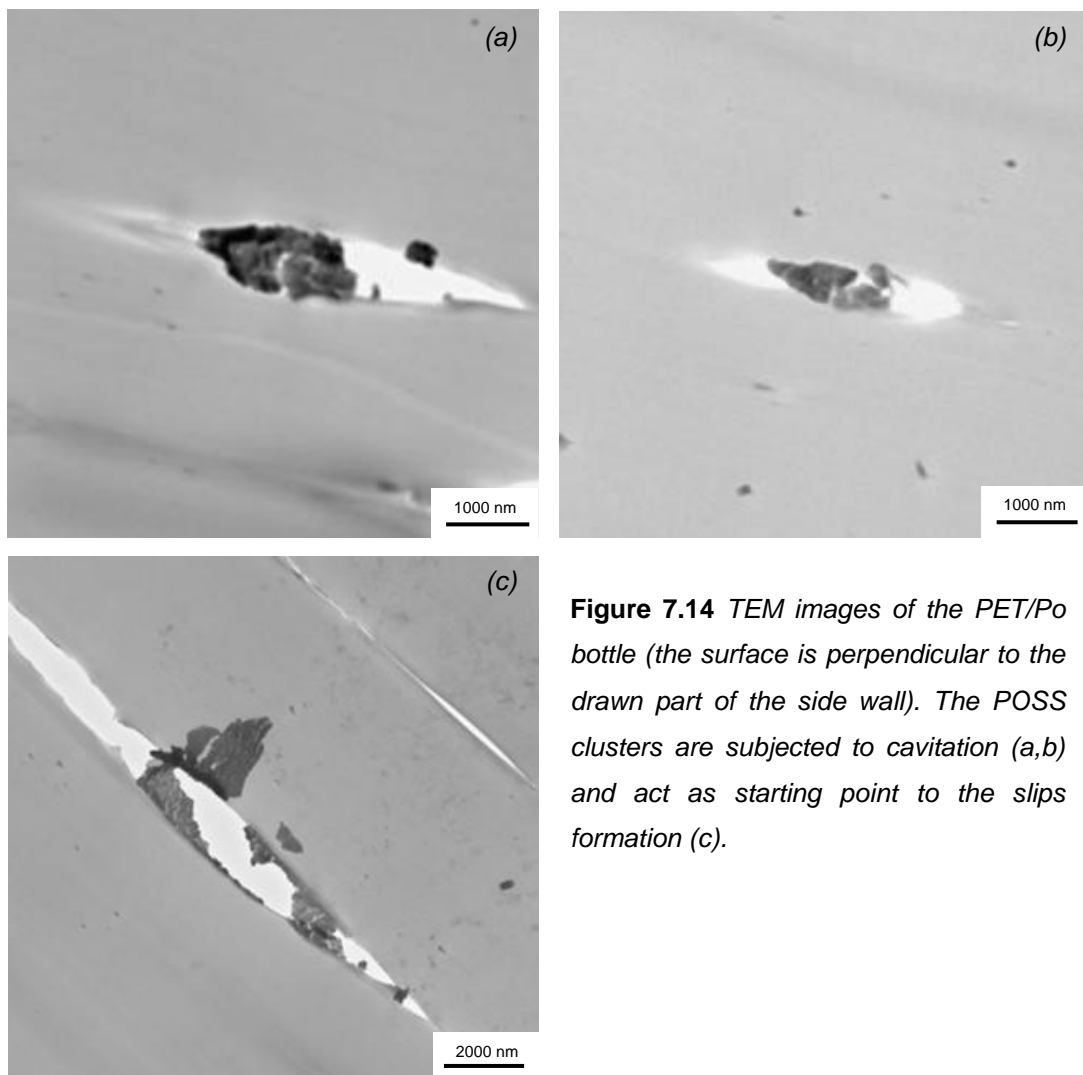


Figure 7.14 TEM images of the PET/Po bottle (the surface is perpendicular to the drawn part of the side wall). The POSS clusters are subjected to cavitation (a,b) and act as starting point to the slips formation (c).

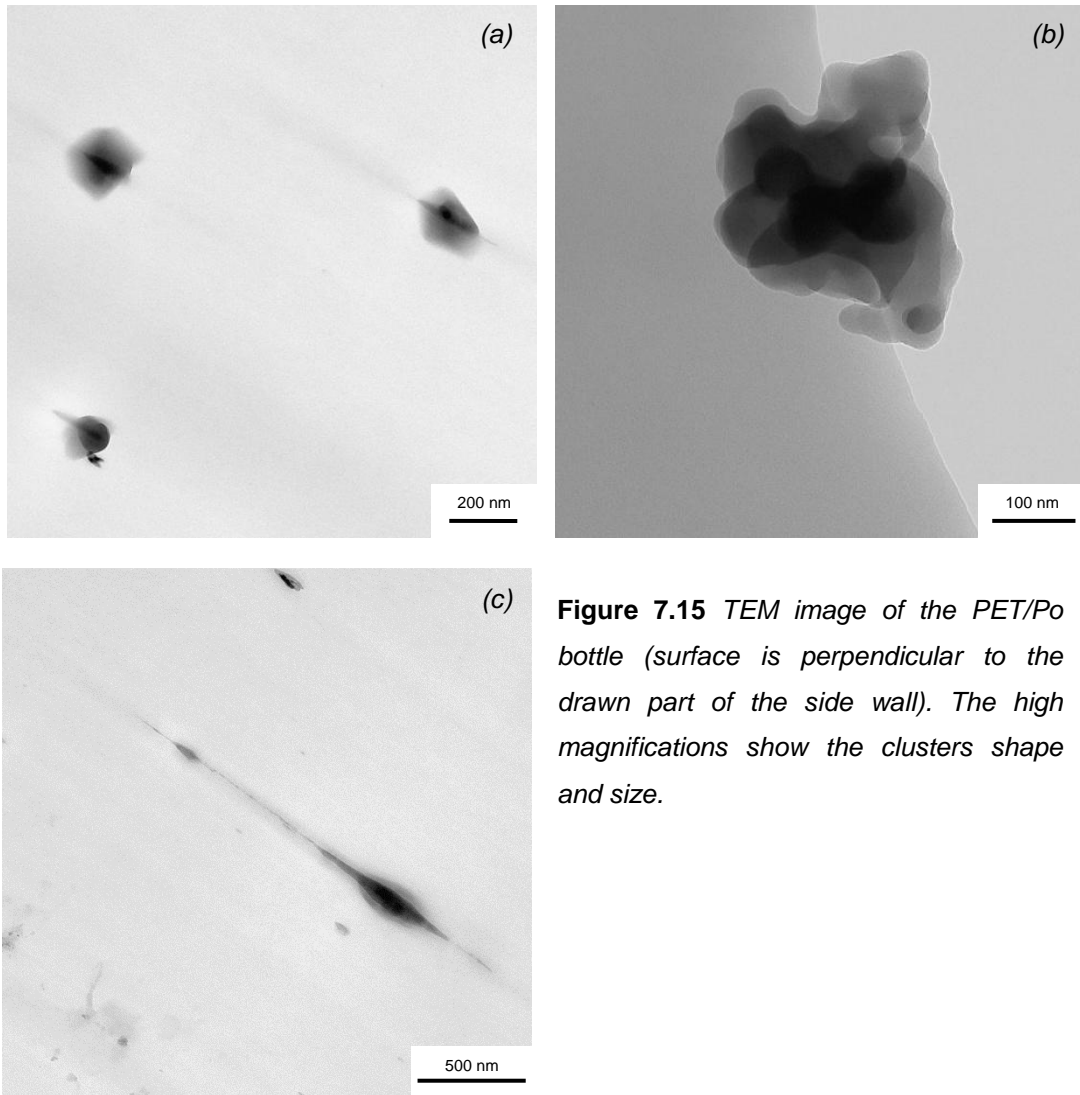


Figure 7.15 TEM image of the PET/Po bottle (surface is perpendicular to the drawn part of the side wall). The high magnifications show the clusters shape and size.

Similarly, the POSSp clusters form cracks when they have big size but they seem to be more flexible and they deformed following the slit edge, unlike the POSSo. For this reason the slits are narrower and longer. There is no evidence of debonding as seen in PET/Po bottles and thus it is supposed the cavitation mechanism does not occur during the stretching of this material.

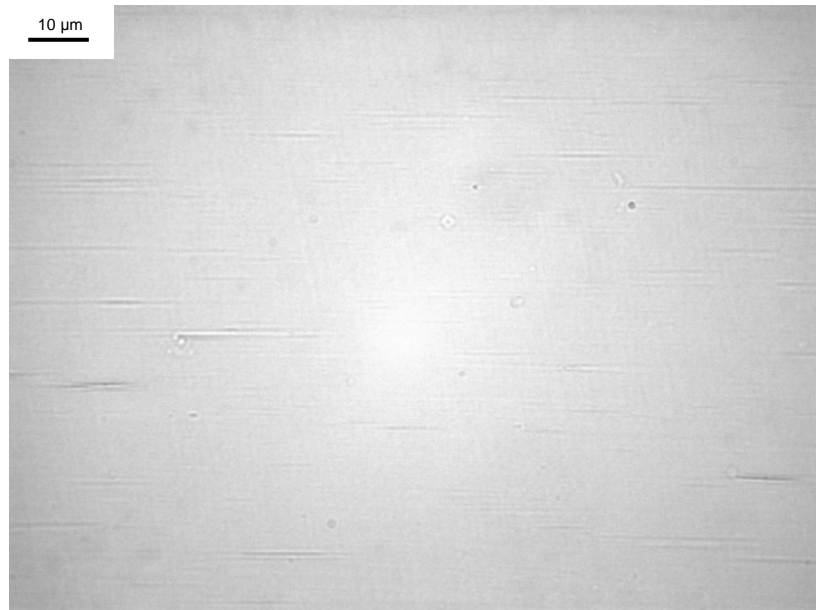


Figure 7.16 TEM micrograph of the PET/Pp bottle (surface perpendicular to the drawn part of the side wall). The low magnification shows the slit distribution.

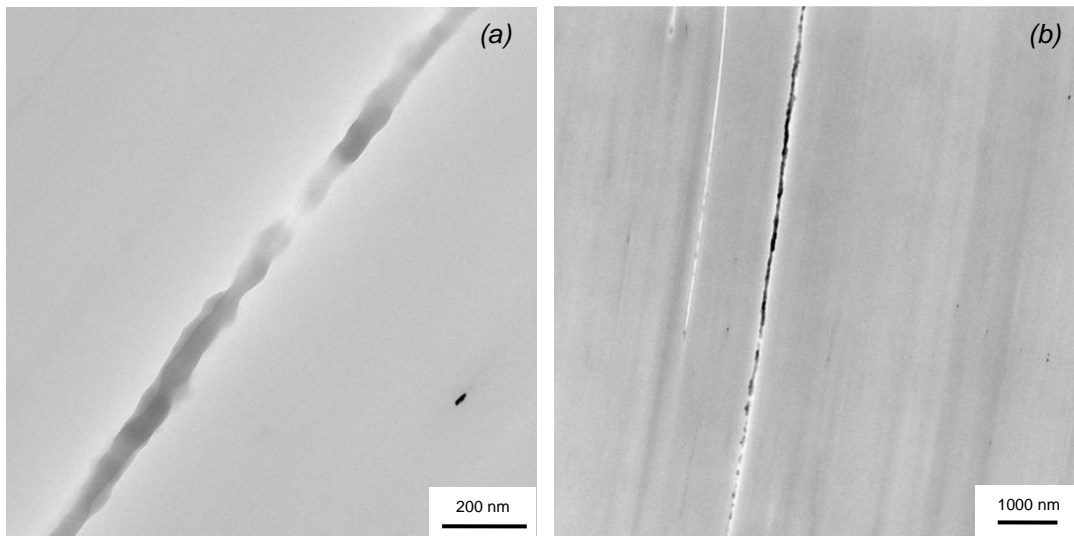


Figure 7.17 TEM micrograph of the PET/Po bottle (surface is perpendicular to the drawn part of the side wall). The medium magnifications show the elongated clusters acting as starting point to the slips formation.

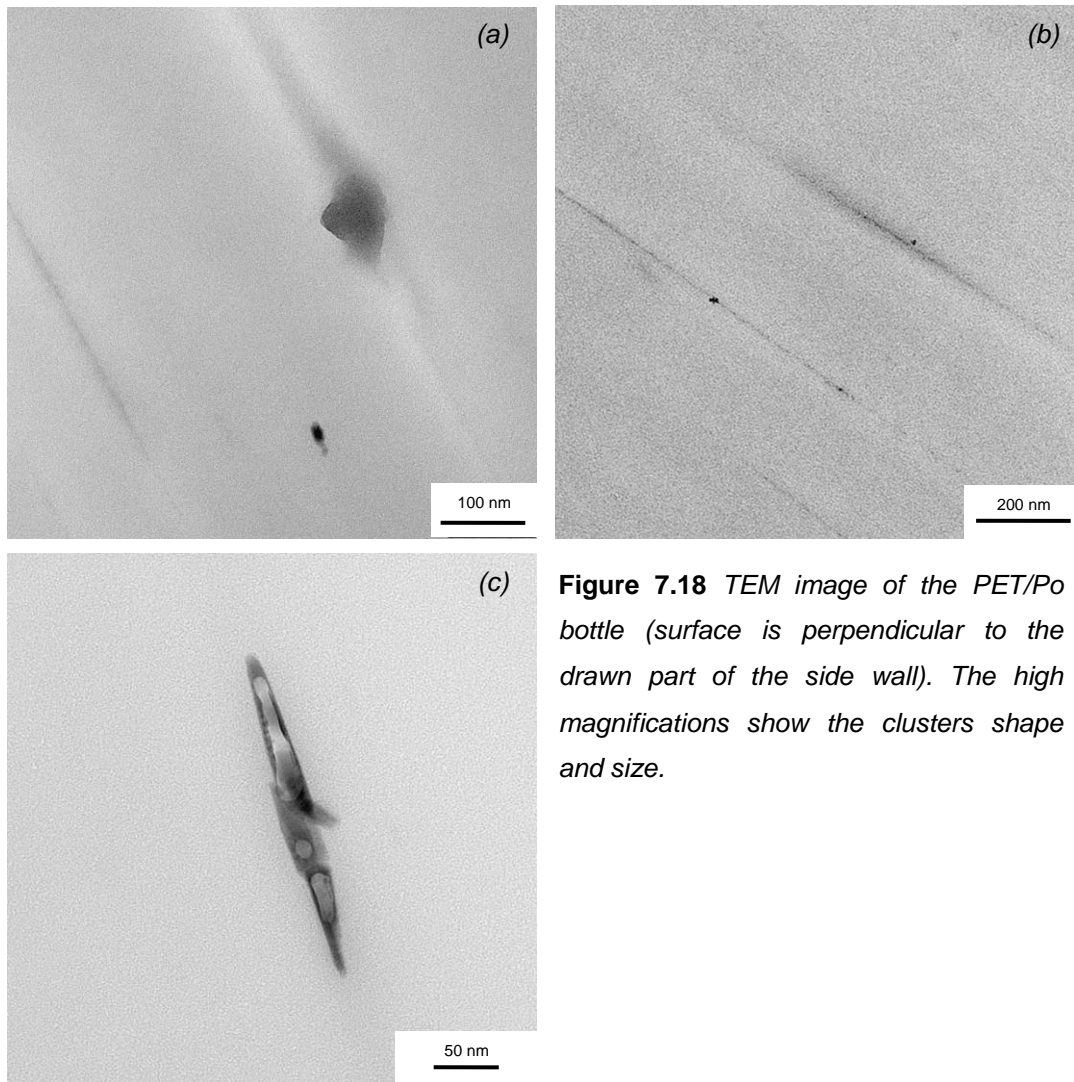


Figure 7.18 TEM image of the PET/Po bottle (surface is perpendicular to the drawn part of the side wall). The high magnifications show the clusters shape and size.

7.6 Conclusion

The characterization on PET based nanocomposites for packaging application has been carried out, in order to compare two different kind of a new class of fillers. 1,2-propanediol isobutyl POSS (POSSp) and octaisobutyl POSS (POSSo) have been added by melt blending in a PET matrix at 2 wt %, preparing PET/Pp and PET/Po nanocomposites. In order to improve the barrier properties of these materials an organomodified montmorillonite (Dellite 72T, D72T) has been added at 1 wt % as well, obtaining PET/Pp/D and PET/Po/D nanocomposites.

The main differences between the POSSp and the POSSo is the possibility, of the first, to react or to form hydrogen bounds with the matrix, while the second is completely non-

reactive and non-polar. Despite the POSSp has a better affinity with the matrix than the POSSo, it doesn't increase the stiffness. A hypothesis is that the reinforcement activity is counteracted by the decrease of the molecular weight due to the transesterification reaction that occurs between the POSSp hydroxyl group and the matrix. Melt flow index measurements show a drop of the viscosity in the PET/Pp nanocomposites to support the occurring of the reaction. The POSSo has a lower affinity with the PET, leading the presence of big size clusters and weak interface. For these reasons the tensile specimens break easily during the cold drawing.

Both POSS don't act as a barrier to the gas diffusion due to low aspect ratio and content. For this reason no improvement of thermal stability and oxygen permeability have been observed. The increase of free volume promotes the gas diffusion, in particular by adding POSSo because its poor interaction with the matrix. Both POSS act as nucleating agent increasing the crystallization temperature and accelerating the thermal transition but they don't increase the crystalline content.

Nanocomposites bottles development has been successfully carried out because thanks to the ability of POSS to don't hinder the processability. The sidewall of the PET/Po bottles is opaque, while the PET/Pp bottles are transparent and rather haze. That is not directly due to a different size of the dispersed clusters but to the thick and amount of slits oriented parallelly to the bottle wall, as it has been revealed by TEM. They are present especially in the PET/Po bottle due to the stress concentration caused by some coarse clusters, that results in a cavitation mechanism. The thick of the slits is bigger than the wavelength of visible light, thus the scattering hinders the light to be transmitted through the bottle sidewalls. Moreover many discontinuity points at the PET-POSSo interface have been observed, due to the poor adhesion. POSSp aggregates are finer and have the feature to deform themselves along the flow line of the bottles.

By adding the D72T a different dispersion has been observed by XRD analysis. D72T is intercalated into the matrix but in the PET/Pp/D it has a slight lower *d*-spacing distance probably due to a lower viscosity during the processing, thus, lower shear stress. The low amount of D72T is not enough to improve the thermal stability, on the other hand the matrix degradation could occur thanks to the Hoffman elimination reaction. As commonly happen in the polymer/oMMT nanocomposites, the oxygen permeability and the modulus are slightly

improved, while the elongation at break decreases. All these deviations in properties, resulting by the addition of D72T, have been observed in a small extent because its low content.

The nucleating activity of the D72T has been seen leading a further increase of the crystallization temperature and a higher crystallinity content, as is commonly verified in PET/oMMT nanocomposites.

References

- [1] S. Donadi, M. Modesti, A. Lorenzetti, S. Besco. *J Appl Polym Sci* 2011, 122, 3290.
- [2] J. Zeng, S. Kumar, S. Iyer, D.A. Schiraldi, R.I. Gonzales. *High Perform Polym* 2005, 17, 403.
- [3] F.C.L. Ciolacu, N.R. Choudhury, N. Dutta, E. Kosior. *Macromolecules* 2007, 40, 265.
- [4] J.K. Kim, K.H. Yoon, D.S. Bang, Y.B. Park, H.U. Kim, Y.H. Bang. *J Appl Polym Science* 2008, 107, 272.
- [5] H.U. Kim, Y.H. Bang, S.M. Choi, K.H. Yoon. *Compos Sci Technol* 2008, 68, 2739.
- [6] K.H. Yoon, M.B Polk, J.H. Park, B.G. Min, D.A. Schiraldi. *Polymer* 2005, 54, 47.
- [7] W.C.J. Zuiderduin, C. Westzaan, J. Huetink, R.J. Gaymans. *Polymer* 2003, 44, 261.
- [8] R. Sharma, H. Joshi, P. Jain. *J Chem Eng Mater Sci* 2011, 2, 39.
- [9] A. Fina, D. Tabuani, A. Frache, G. Camino. *Polymer* 2005, 46, 7855.
- [10] A. Fina, D. Tabuani, F. Carniato, A. Frache, E. Boccaleri, G. Camino. *Thermochimica Acta* 2006, 440, 36.
- [11] W. Xie, Z. Gao, W. Pan, D. Hunter, A. Singh, R. Vaia. *Chem Mater* 2001, 13, 2979.
- [12] K. Stoeffler, P.G. Lafleur, J. Denault. *Polym Degrad Stab* 2008, 93, 1332.
- [13] W.S. Chow, Z.A. Mohdlshak, J. Karger-Kocsis. *Macromol Mater Eng* 2005, 290, 122.
- [14] K. Wang, S. Liang, J. Deng, H. Yang, Q. Zhang, Q. Fu, X. Dong, D. Wang, C.C. Han. *Polymer* 2006, 47, 7131.
- [15] S. Bhattacharya, R.K. Gupta, S. Bhattacharya. The rheology of polymeric nanocomposites. In *Polymer nanocomposites handbook*. R.K. Gupta, E. Kennel, K.J. Kim, CRC Press (2010).
- [16] Y. Zhao, D.A. Schiraldi. *Polymer* 2005, 46, 11640.
- [17] P.J. Jones, R.D. Cook, C.N. McWright, R.J. Nalty, V. Choudhary, S.E. Morgan. *J Appl Polym Sci* 2011, 121, 2945.

- [18] M.E. Romero-Guzmán, A. Romo-Uribe, B.M. Zárate-Hernández, R. Cruz-Silva. *Rheol Acta* 2009, 48, 641.
- [19] H. Rios-Dominguez, F.A. Ruiz-Trevino, R. Contreras-Reyes, A. Gonzalez-Montiel. *J Membr Sci* 2006, 271, 94.
- [20] V.N. Dougnac, R. Alamillo, B.C. Peoples, R. Quijada. *Polymer* 2010, 51, 2918.
- [21] S. Takahashi, D.R. Paul. *Polymer* 2006, 47, 7519.
- [22] S. Takahashi, D.R. Paul. *Polymer* 2006, 47, 7535.

Chapter 8

PET/POSS nanocomposites: a screening of different POSS

8.1 Introduction

In the previous activity, it has been proved that the POSS, unlike the oMMT, has the feature to maintain the transparency of the product even after the blow molding. It depends to the compatibility with the matrix, in particular to the size of clusters and the interface adhesion. Coarse clusters and poor adhesion promote the formation of slits during the drawing. The ideal solution could be a multi-functionalized POSS able to crosslink the PET chains, or a bi-functionalized POSS that acts as a chain extender. A mono-functionalized POSS may react with the chain ends or through grafting along the chains backbone. In both cases the POSS is bounded and it decreases the chains mobility. Other reactions could short the chains, lowering the molecular weight, as seen in the Chapter 7.

Thus the reactivity and solubility of POSS are two important aspects that determine the final morphology and properties of the nanocomposites. In the next activity several kinds of POSS have been added to the PET. They differ to the organic chains bonded at the corners of the silicon-oxygen cage, that are required to compatibilize the molecule. They have been chosen because their high affinity with polyesters or because they are potentially reactive with them. To predict their suitability as reinforcing fillers of PET, TGA analysis have been performed on the different POSS in order to verify their thermal stability, since PET requires high processing temperatures. Also the crystallization properties have been investigate in order to verify if these POSS act as nucleating agents. This is an aspect that has to be evaluated because, in a industrial process, preforms are heated before to be blowed, at temperatures enough low to do not induce crystallization. Finally, the partial solubility parameters of PET and POSS have been calculated to qualitatively predict the level of dispersion into the matrix.

8.2 Raw materials

The poly(ethylene terephthalate) (PET) provided by Gatronova Industries was the A80 grade (0.80 dL/g intrinsic viscosity). Polyhedral oligomeric silsesquioxanes provided by Hybrid Plastics were the glycidyl POSS (gPOSS), trisilanol isobutyl POSS (tsiPOSS), trisilanol phenyl POSS (tspPOSS), polyethylene glycol POSS (pegPOSS), trans-cyclohexanediol isobutyl POSS (tcdiPOSS), amic acid isobutyl POSS (aaiPOSS) (Figure 8.1).

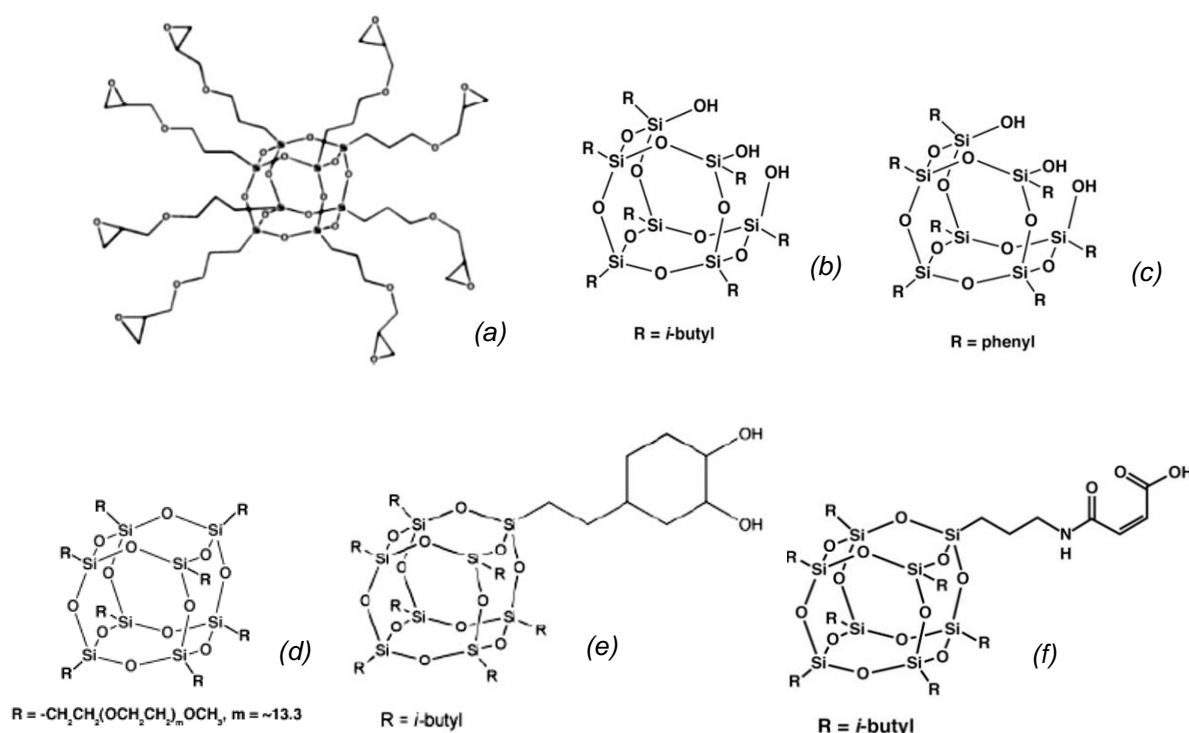


Figure 8.1 Structures of gPOSS (a), tsiPOSS (b), tspPOSS (c), pegPOSS (d), tcdiPOSS (e), aaiPOSS (f).

8.3 Preparation of samples

The PET was previously dried at 160°C for 2 hours. PET/POSS nanocomposites filled at 1 and 3 wt% were prepared mixing by melt compounding using a co-rotating, intermeshing twin screw extruder (Collin Teach-line zk25t) with a the temperature profile, from hopper to die, of 210-250-260-260-255°C and a screw rate of 100 rpm.

8.4 Characterization

DSC

The thermal transitions and the crystallization behavior were examined using a TA Instruments Q200 DSC differential scanning calorimeter working in heat-cool-heat mode, at heating rate of 10°C/min and cooling rate of 5°C/min from 40 to 280°C.

TGA

The thermal behavior was measured by thermogravimetric analysis (TGA) on a TA instruments SDT Q600. Every run was carried out under a 100 mL/min nitrogen and air flow from room temperature to 300°C heating at 5°C/min, to better evaluate the possible degradation during the processing, and from 300 to 800°C at 20°C/min.

Solubility

The solubility parameters have been calculated through the Hoftyzer-van Krevelen and Hoy methods described in Paragraph 4.2.12. They predict the square of the total solubility parameter as sum of the square of the three contributes (dispersive forces, polar forces, hydrogen bonds). Both the methods have a 10% accuracy thus the average value should be a good compromise.

8.5 Results and discussion

8.5.1 DSC

The crystallization and melting peaks of all nanocomposites are showed in Figure 8.2, 8.3 and 8.4, 8.5 respectively. Generally they exhibit an increase of the crystallization temperature (T_c) compared with the neat PET, while the melting temperature (T_m) doesn't undergo to relevant variations. The crystallization and melting enthalpies (ΔH_c and ΔH_m) are rather close to which ones of the neat PET (Table 8.1). For the PET/gPOSS and the PET/tspPOSS nanocomposites seems to be no relation between the T_c and the filler content, while for the others nanocomposites the T_c of the 3 wt % filled ones is similar or slightly higher than the 1 wt % filled ones. This common nucleating activity is more pronounced in PET/pegPOSS

nanocomposites rather than the others. They exhibit the highest ΔH as well, while the tspPOSS gives the lowest value.

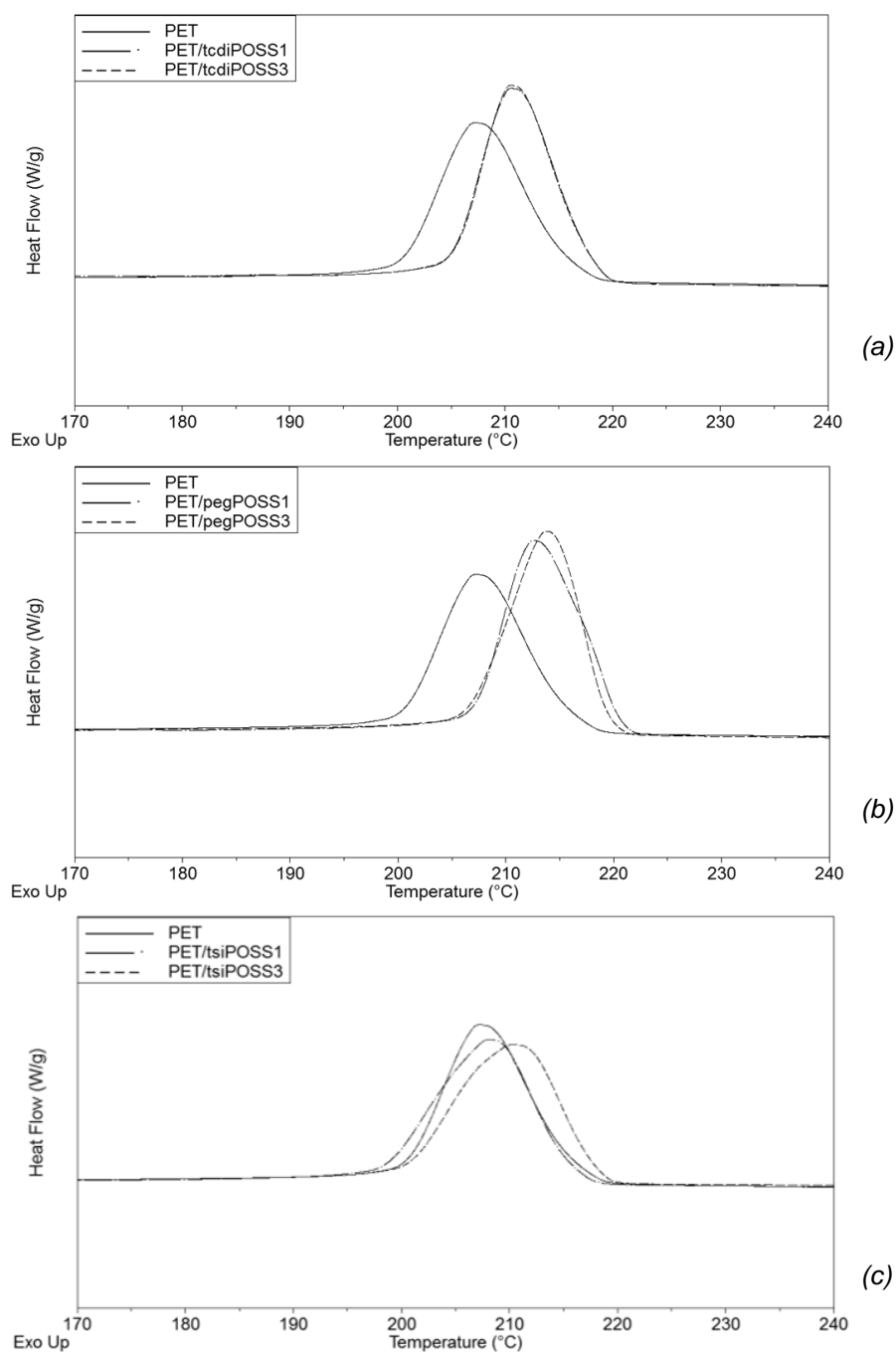


Figure 8.2 Crystallization peaks of PET and its nanocomposites: PET/tcdiPOSS (a), PET/pegPOSS (b), PET/tspiPOSS (c).

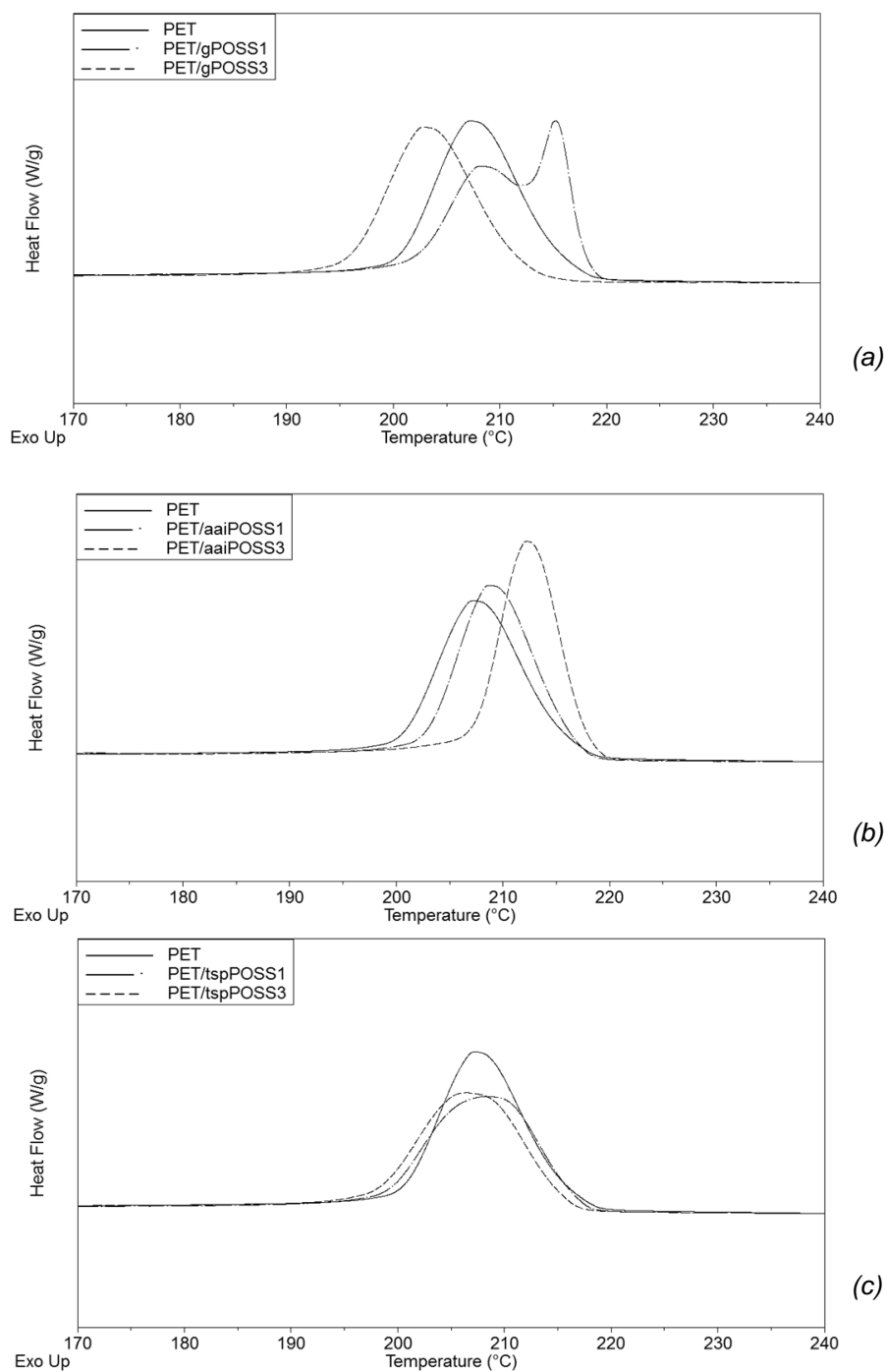


Figure 8.3 Crystallization peaks of PET and its nanocomposites: PET/gPOSS (a), PET/aaiPOSS (b), PET/tspPOSS (c).

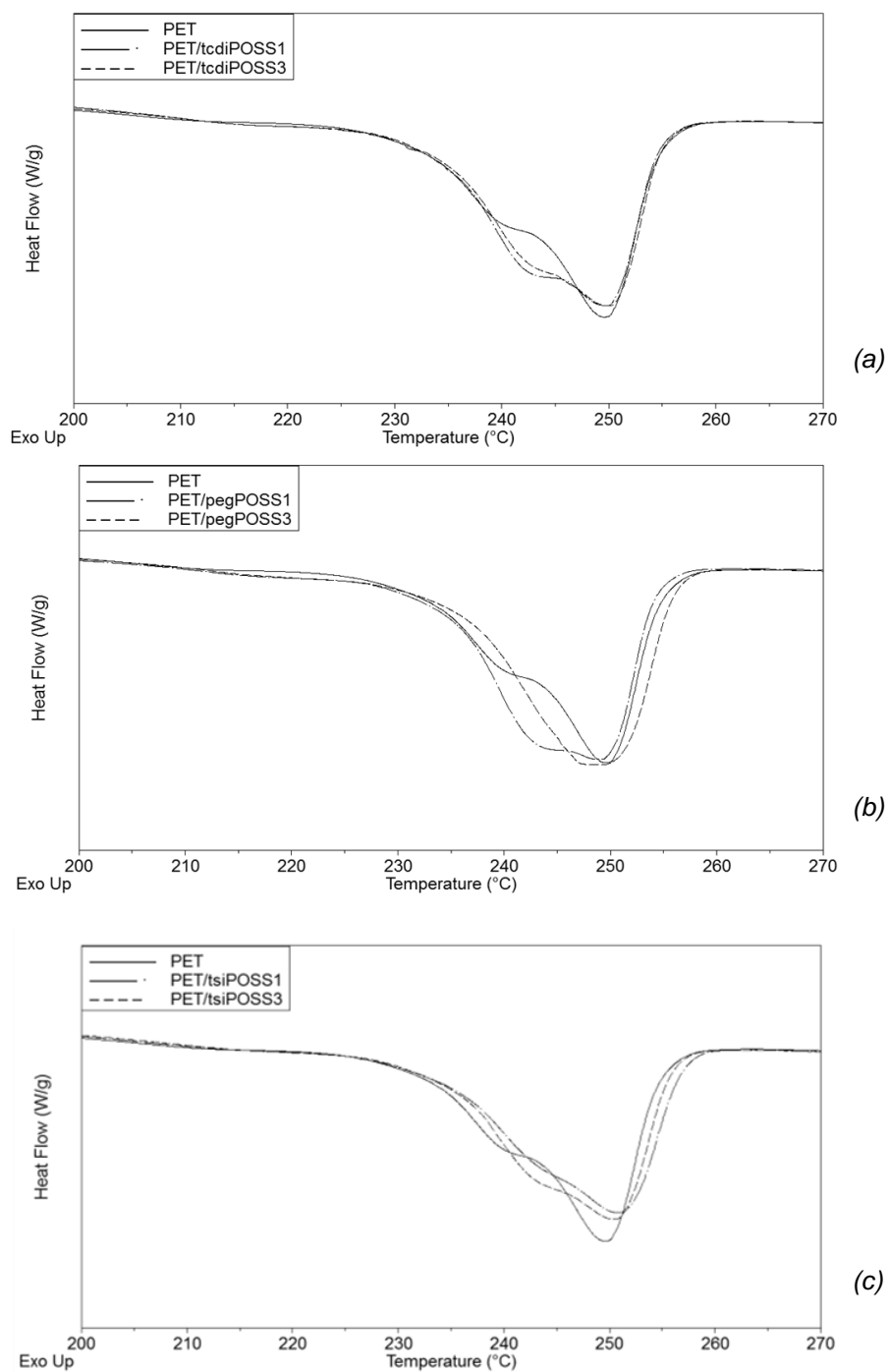


Figure 8.4 Melting peaks of PET and its nanocomposites: PET/tcdiPOSS (a), PET/pegPOSS (b), PET/tsiPOSS (c).

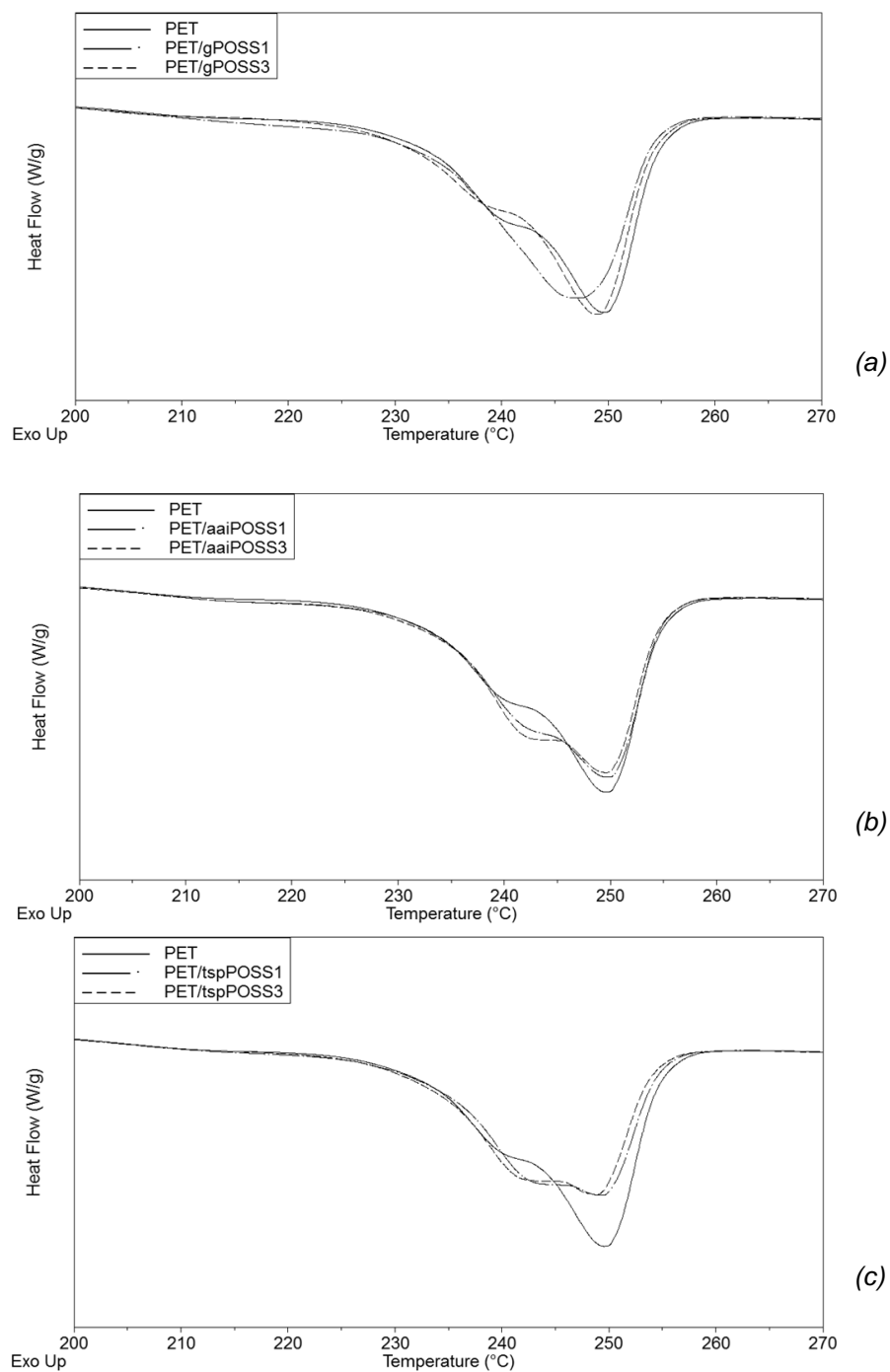


Figure 8.5 Melting peaks of PET and its nanocomposites: PET/gPOSS (a), PET/aaiPOSS (b), PET/tspPOSS (c).

Sample	T_c (°C)	ΔH_c (J/g)	T_m (°C)	ΔH_m (J/g)
PET	207.3	48.1	249.5	47.5
PET/gPOSS1	208.5-215.2	47.7	247.1	50.3
PET/gPOSS3	203.2	47.5	249.0	50.6
PET/tsiPOSS1	208.1	49.4	259.4	49.7
PET/tsiPOSS3	210.3	49.9	250.9	49.8
PET/tspPOSS1	208.5	43.6	249.3	44.8
PET/tspPOSS3	206.5	43.9	248.8	46.1
PET/pegPOSS1	212.6	52.0	249.0	54.2
PET/pegPOSS3	213.8	52.2	248.5	54.7
PET/tcdiPOSS1	210.8	50.1	250.4	49.7
PET/tcdiPOSS3	210.8	50.9	250.0	52.2
PET/aaiPOSS1	208.8	47.4	249.8	50.3
PET/aaiPOSS3	212.2	48.6	249.9	51.4

Table 8.1 DSC parameters of PET and its nanocomposites: crystallization/melting temperatures (T_c and T_m) and enthalpies (ΔH_c and ΔH_m).

All the other nanocomposites have a similar or slight higher ΔH than the neat PET. At the contrary of the mostly oMMT-filled nanocomposites there is not a relevant increase of the crystallization rate since the width of the peaks are similar to the neat PET. The nucleating activity of POSS is not always verified: in PP/octamethyl POSS a strong nucleating activity of the filler has been that lead a significant increase of the crystallization rate [1], other authors observed that the octamethyl POSS acts as a nucleating agent when added in PP, unlike the octaisobutyl POSS [2,3].

8.5.2 TGA

In Figure 8.6 and 8.7 the TGA of each POSS under nitrogen and air flow, respectively, are reported. The residues at 800°C have the same values of the inorganic content (Si-O cage) of each POSS, except some cases (Table 8.2). The aaiPOSS, tcdiPOSS have a similar structure and both exhibit a residue under inert atmosphere much lower than their inorganic content. It has been observed that POSS shows a competition between evaporation/sublimation and decomposition when it is heated in nitrogen [4]. The same is observed for the tsiPOSS. The tspPOSS has a residue higher than its inorganic content, probably because the presence of

thermally stable organic residue derived from the aromatic rings. The pegPOSS, due to its long organic chains, has a very low inorganic content (and a liquid appearance).

In order to compare the thermal stability of each POSS, the temperature at a 5% weight loss ($T_{0.05}$) has been reported in Table 8.3. The tspPOSS is the most stable, thanks to the phenyl groups, followed by the gPOSS, while pegPOSS has the lower stability, despite its long organic chains.

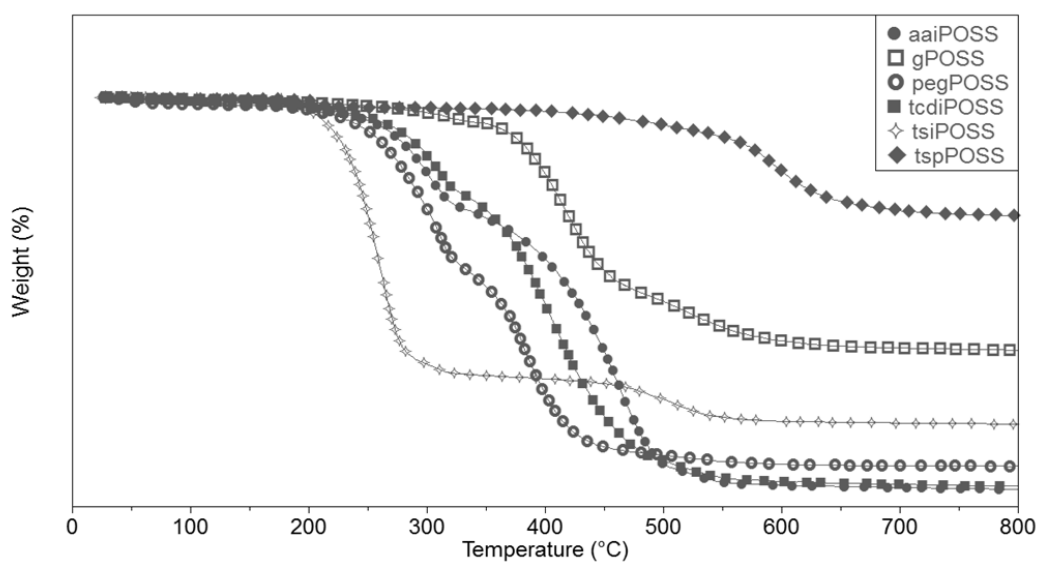


Figure 8.6 TGA under nitrogen flow of POSS.

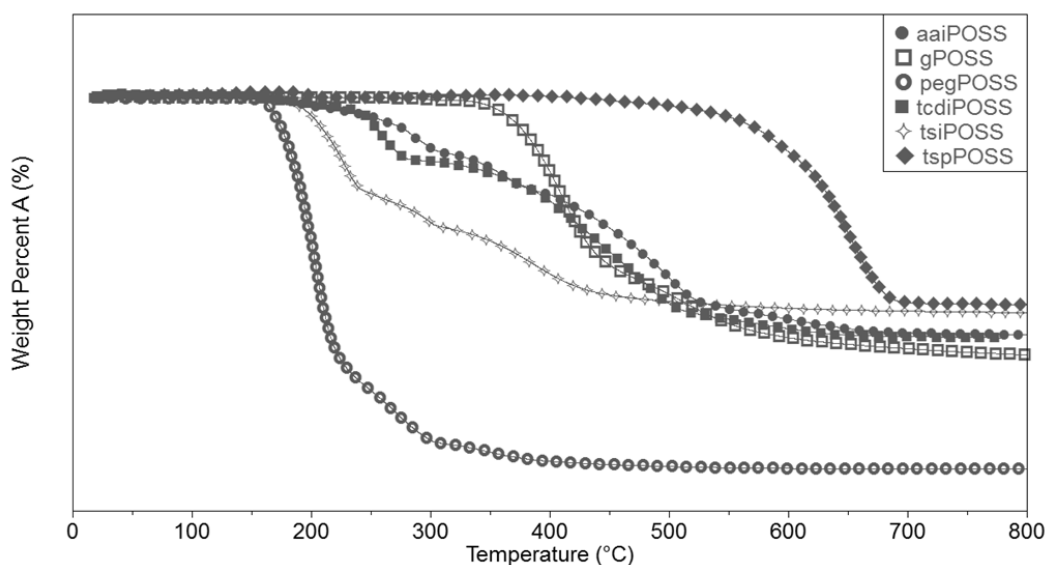


Figure 8.7 TGA under air flow of POSS.

The residue at 275°C (R_{275}) is useful to verify the extent of degradation during the processing. Their values are reported in Table 8.3. As expected, tspPOSS and gPOSS don't exhibit any relevant weight loss, the aaiPOSS and tcdiPOSS lose about 10–15% of weight. The pegPOSS is very sensitive to the oxidant atmosphere since its degradation at the processing temperature is almost complete. On the contrary the tsiPOSS loses more weight under inert atmosphere and has a very low thermal stability at 275°C if compared with the other fillers.

Concerning the tsiPOSS the thermal and thermo-oxidative degradations of isobutyl groups occurs in the range of 175–250°C, thus below the processing temperature. In inert atmosphere the weight loss at 500°C could involve the sublimation of the inorganic cages. It has been observed that POSS shows a competition between evaporation/sublimation and decomposition when heated in nitrogen [4] leading a residue lower than its inorganic content. The degradation in oxidizing atmosphere occurs in two steps (175–240°C and 240–400°C) as previously seen, due to the evaporation and oxidation mechanisms [5]. The condensation of silanol groups is not visible because it occurs in the same range of temperature of the alkyl degradation. Heating tsiPOSS at 280°C under nitrogen results in production of a resinous organosilicate material [6]. The tspPOSS is very thermally stable and doesn't undergo to degradation at the processing temperature thanks to its phenyl groups. The residue at 800°C under nitrogen flow is much higher than the inorganic content because the presence of thermally stable organic residue as well. The mass loss that occurs at 200–210°C in both the atmosphere is attributed to the condensation of Si–OH groups and rearrangement reactions [7]. The aaiPOSS and tcdiPOSS have a similar structure and thermogravimetric curves. In both the atmospheres, the degradation occurs in one step in the range of 200–500°C. The residue at 800°C (R_{800}) under air flow corresponds to the inorganic content (wt_{inor}), while the residue under nitrogen flow is much lower due to the sublimation (Table 8.2). The gPOSS has similar behavior in both the atmospheres (degradation at 300–500°C), while pegPOSS is very sensitive to the thermo-oxidative degradation. Despite its weight loss starts at the same temperature, under air and oxygen flow, in the first case it is almost twice faster. gPOSS and pegPOSS have a residue at 800°C corresponding to the inorganic content in both the atmospheres.

Sample	wt_{inor} (%)	Air flow			Nitrogen flow		
		$T_{0.05}$ (°C)	R_{800} (%)	R_{275} (%)	$T_{0.05}$ (°C)	R_{800} (%)	R_{275} (%)
aaiPOSS	42.8	254	42.7	92.8	243	4.3	90.1
gPOSS	31.1	367	37.8	100.0	317	38.2	97.2
pegPOSS	7.7	171	10.2	22.8	228	9.9	84.6
tcdiPOSS	43.4	248	41.9	86.1	250	5.1	92.1
tsiPOSS	43.0	202	47.8	73.9	209	20.3	41.8
tspPOSS	36.6	553	49.8	100.0	458	71.1	97.4

Table 8.2 TGA parameters of POSS: inorganic weight fraction (wt_{inor}), temperature at 5% loss weight ($T_{0.05}$), residue after thermo-oxidation at 800°C (R_{800}), residue after 5 min isotherm at 275°C (R_{275}).

Sample	Air flow		Nitrogen flow	
	I step (°C)	II step (°C)	I step (°C)	II step (°C)
aaiPOSS	150-400	400-500	200-500	-
gPOSS	350-450	450-600	300-600	-
pegPOSS	160-300	-	200-400	-
tcdiPOSS	150-250	250-500	200-500	-
tsiPOSS	175-240	240-400	200-250	500
tspPOSS	200	400-700	210	400-650

Table 8.3 Temperature ranges of degradation of the different POSS.

8.5.3 Solubility

In a study on PET/POSS nanocomposites the Hoftyzer and van Krevelen methods were used to predict the thermodynamic interaction between the matrix and the fillers [8]. These two methods have been applied to verify the solubility of POSS in the PET matrix.

The partial solubility parameters calculated by Hoftyzer-van Krevelen and Hoy's methods are reported in Table 8.4. The average values between them are shown in Table 8.5. The two methods give different results. The dispersion contributions according to Hoy's method are more or less similar between the different POSS, unlike the Hoftyzer-van Krevelen one. The latter attributes a lower polar contribution to hydroxyl groups of tsiPOSS and tspPOSS than the Hoy's method.

Figure 8.8 shows the bidimensional representation (δ_H - δ_V plot, where $\delta_V = \sqrt{\delta_d + \delta_p}$ [9]) of the partial solubility parameters of PET and POSS, in which the circle (radius of 5 units) is the solubility field of PET. Three different levels of solubility can be assumed for POSS. The most soluble fillers seem to be gPOSS, tspPOSS and pegPOSS, tsiPOSS is placed close to the boundaries of the solubility field, while aaiPOSS, tcdiPOSS are quite far from the circle of Figure 8.8. that is due to the low polar contribute of these two POSS because they have isobutyl groups on seven corners of the cage that reduce the overall polarity of the molecule. The tsiPOSS has isobutyl groups as well, but the three hydroxyl groups provide a good polarity to it.

Samples	δ of Hoftyzer-van Krevelen method ($J^{1/2}cm^{-3/2}$)				δ of Hoy method ($J^{1/2}cm^{-3/2}$)			
	δ_d	δ_p	δ_h	δ	δ_d	δ_p	δ_h	δ
pegPOSS	17.1	10.2	8.7	21.8	16.7	9.9	8.4	21.2
tsiPOSS	14.6	2.4	9.9	17.8	16.4	7.8	3.4	18.5
tspPOSS	19.8	3.1	10.6	22.6	16.0	10.3	7.0	20.3
tcdiPOSS	14.6	1.5	2.7	14.9	16.0	2.8	2.8	16.5
gPOSS	17.1	7.5	7.5	20.1	18.1	8.2	9.4	22.0
aaiPOSS	15.2	1.3	1.9	15.3	16.1	3.0	1.5	16.4
PET	18.1	6.9	9.9	21.7	15.0	13.1	10.5	22.6

Table 8.4 Solubility parameters of PET and POSS: dispersive (δ_d), polar (δ_p), hydrogen bonding (δ_h) components, total (δ).

Samples	Average δ ($J^{1/2}cm^{-3/2}$)				
	δ_d	δ_p	δ_h	δ	δ_v
pegPOSS	16.9	10.1	8.6	21.5	19.7
tsiPOSS	15.5	5.1	6.7	18.1	16.3
tspPOSS	17.9	6.7	8.8	21.4	19.1
tcdiPOSS	15.3	2.2	2.7	15.7	15.5
gPOSS	17.6	7.8	8.5	21.1	19.3
aaiPOSS	15.6	2.2	1.7	15.9	15.8
PET	16.6	10.0	10.2	22.1	19.3

Table 8.5 Average solubility parameters of PET and POSS: dispersive (δ_d), polar (δ_p), hydrogen bonding (δ_h) components, total (δ), dispersive/polar component (δ_v).

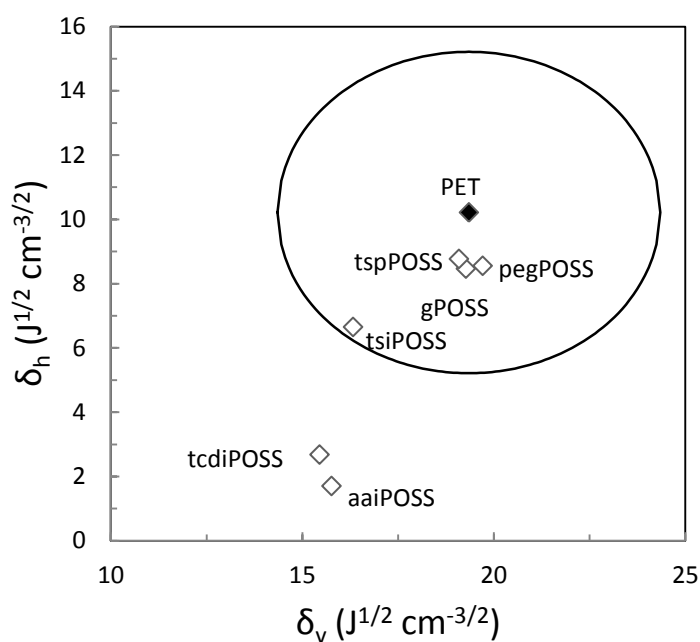


Figure 8.8 δ_h - δ_v plot of PET and POSS.

Sample	R_{PET} ($J^{1/2} cm^{-3/2}$)
pegPOSS	1.8
tsiPOSS	6.4
tspPOSS	4.5
tcdiPOSS	11.2
gPOSS	3.5
aaiPOSS	11.7

Table 8.6 Euclidian distances in solubility between PET and POSS.

The Euclidean distances are reported in Table 8.6. Equation 4.39 takes in consideration that the van der Waals interfacial interaction between POSS and PET depends mostly from the dispersion component δ_d [8]. The values are in good agreement with the relative solubility observed in Figure 8.8. Comparing the R_{PET} values the gPOSS seems to be the most soluble in PET.

8.6 Conclusion

TGA analysis showed a poor thermal stability of tsiPOSS and pegPOSS. It is interesting the opposite thermal behavior they exhibited if subjected to inert or oxidizing atmosphere. The tcdiPOSS and aaiPOSS exhibit a moderate stability and a low sensitivity to the kind of atmosphere. The gPOSS and, in particular, the tspPOSS have the best thermal stability.

By DSC analysis has been observed that all POSS generally exhibit a nucleating activity since they increase the crystallization temperature, except tspPOSS and gPOSS. The pegPOSS leads a higher crystallinity content and the tspPOSS a lower one.

The prediction of the solubility parameters gave similar results by using the Hoftzyer and van Krevelen and Hoy methods. The aaiPOSS and tcdiPOSS exhibit the highest distance in solubility from PET, due to their low polar aspect, while tspPOSS, pegPOSS and, in particular, gPOSS seem to be the most soluble.

References

- [1] B.X. Fu, L. Yang, R.H. Somani, S.X. Zong, B.S. Hsiao, S. Phillips, R. Blanski, P. Ruth. *J Polym Sci* 2001, 39, 2727.
- [2] A. Fina, D. Tabuani, A. Frache, G. Camino. *Polymer* 2005, 46, 7855.
- [3] M. Pracella, D. Chionna, A. Fina, D. Tabuani, A. Frache, G. Camino. *Macromol Symp* 2006, 234, 59.
- [4] A. Fina, H.C.L. Abbenhuis, D. Tabuani, A. Frache, G. Camino. *Polym Degrad Stab* 2006, 91, 1064.
- [5] A. Fina, D. Tabuani, F. Carniato, A. Frache, E. Boccaleri, G. Camino. *Thermoc Acta* 2006, 440, 36.
- [6] J. Zeng, C. Bennett, W.L. Jarrett, S. Iyer, S. Kumar, L.J. Mathias, D.A. Schiraldi. *Compos Interf* 2005, 11, 673.
- [7] P.J. Jones, R.D. Cook, C.N. McWright, R.J. Nalty, V. Choudhary, S.E. Morgan. *J Appl Polym Sci* 2011, 121, 2945.
- [8] S.K. Lim, E.P. Hong, Y.H. Song, H.J. Choi, I.J. Chin. *J Mater Sci* 2010, 45, 5984.
- [9] E.B. Bagley, T.P. Nelson, J.M. Scigliniano. *J Paint Technol* 1971, 43, 35.

Chapter 9

PET/tspPOSS nanocomposites

9.1 Introduction

In a previous activity different kind of POSS with a good propensity to be well dispersed into the PET have been studied. The PET filled with trisilanol phenyl POSS (tspPOSS) exhibited the best transparency (Figure 9.1). The excellent thermal stability and the presence of phenyl groups induced us to consider the tspPOSS a suitable filler to reinforce the PET. In a previous study on PET/POSS nanocomposites produced by polymerization in situ has been hypothesized that chain extensions and branching reactions could occur between the PET and the trisilanol isobutyl POSS (tsiPOSS) [1] as showed in Figure 9.2. By MALDI-MS analysis they observed a decrease of $-COOH$ ends of PET due to the reaction with tsiPOSS. Also in a study on PET/POSS nanocomposites with both disilanol and trisilanol isobutyl POSS produced by compression molding the crosslinking reaction has been hypothesized to occur after light scattering measurements. In particular they showed the increase of radius of gyration and molecular weight of nanocomposites [2]. Rheological analysis on nanocomposites at 1 wt% of POSS suggested a strong interfacial interaction between matrix-filler. Moreover, since the incompletely condensed cage of tspPOSS contains three pendant hydroxyl groups, they have the opportunity to hydrogen-bond with the ester groups on the PET chains [3].

In the following activity PET/tspPOSS nanocomposites with 0.3, 1, 3, 5, 7 wt% have been prepared. In addition to the conventional characterization, nanocomposites bottles have been developed as well, to verify the occurring of delamination as it happened using other kinds of POSS (Chapter 7).

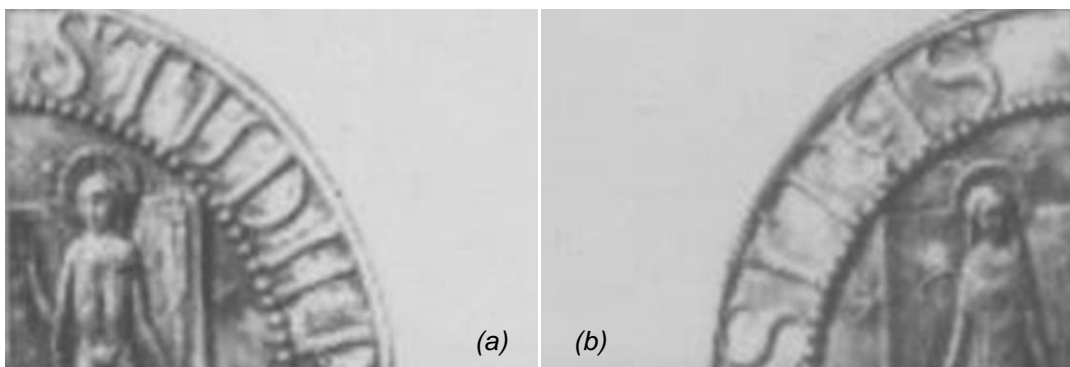


Figure 9.1 Pictures of PET (a) and PET/tspPOSS 3 wt% nanocomposites (b) (plates 2 mm thick).

9.2 Raw materials

The poly(ethylene terephthalate) (PET) provided by Gatronova Industries was the A80 grade (0.80 dL/g intrinsic viscosity). Trisilanol phenyl POSS (tspPOSS) has been provided by Hybrid Plastics (Figure 8.1c).

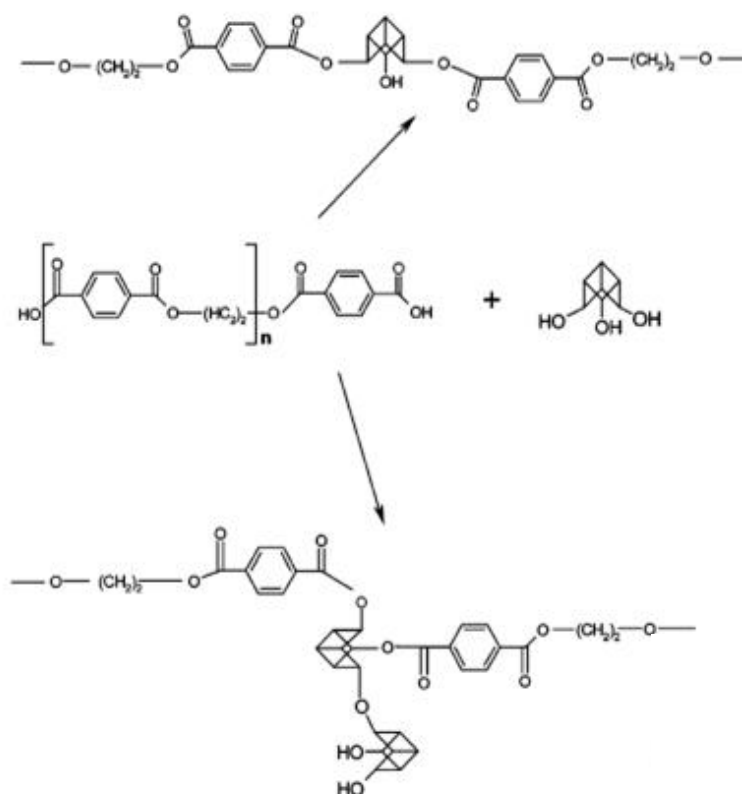


Figure 9.2 Possible structures arising from the reaction between PET structures and open cage trisilanol isobutyl POSS (reprinted from [1]).

9.3 Preparation of samples

The PET was previously dried at 160°C for 2 hours. PET/tspPOSS nanocomposites filled at 0.3, 1, 3, 5 and 7 wt% were prepared mixing by melt compounding using a co-rotating, intermeshing twin screw extruder (Collin Teach-line zk25t) with a the temperature profile, from hopper to die, of 210-250-260-260-255°C and a screw rate of 100 rpm. The extruded materials were dried at 160°C for 2 hours. The specimens for the mechanical tests were produced by injection molding. The films for the oxygen permeability test were produced by compression molding quenching from 210°C to avoid the crystallization of the structure.

8.4 Characterization

Mechanical properties

The mechanical properties of all materials were measured by Galdabini (mod. Sun 2500) dynamometer. Dog-bone shaped specimens produced by injection molding have been subjected to the tensile test (ASTM D638) in order to measure the tensile modulus, with the aid of an extensimeter (1 mm/min tensile rate), and the yield stress and elongation at break (50 mm/min tensile rate).

Rectangular bars (126x12.6x3.2 mm) produced by injection molding have been subjected to the flexural test in order to measure the flexural modulus (1.3 mm/min test rate, 50 mm support span, according to ASTM D790).

DSC

The thermal transitions and the crystallization behavior were examined using a TA Instruments Q200 DSC differential scanning calorimeter working in heat-cool-heat mode, at heating rate of 10°C/min and cooling rate of 5°C/min from 40 to 280°C.

TGA

The thermal behavior was measured by thermogravimetric analysis (TGA) on a TA instruments SDT Q600. Every run was carried out under a 100 mL/min air flow from room temperature to 900°C heating at 20°C/min.

XRD

The presence of crystalline clusters was monitored by X ray diffraction (Bruker D8). The XRD analyses were carried out in reflectance mode with Cu anode material ($K_{\alpha 1} = 1.54056$ nm, $K_{\alpha 2} = 1.54439$ nm). The diffractograms were scanned in a 2θ range from 2.00 to 50.00° at scan rate of $0.03^\circ/\text{s}$. The d -spacings have and the average size of PET crystallites has been calculated by using Equation 4.13 and 4.14 (with $K = 0.9$) respectively.

Oxygen permeability

The barrier properties was investigated by a permeability tester (Extrasolution, MultiPerm), testing 50 cm^2 quenched thin films under $11.2 \text{ mL}/\text{min}$ oxygen gas flow, at 23°C and 50% relative humidity. The constant permeability K , the diffusion coefficient D , the solubility coefficient S have been calculated by using Equation 4.18, 4.19 and 4.20 respectively.

TEM

The morphology was investigated also by high magnification transmission electron microscopy (TEM, Zeiss Leo EM 900). Samples for TEM analyses were cut from ultra-thin specimens using a Leica Ultracut UCT ultramicrotome.

9.5 Results and discussion

9.5.1 Mechanical properties

The variation of the yield stress due to the addition of the filler is not relevant (Figure 9.3a), while the elongation at break increases with the increase of tspPOSS content up to $3 \text{ wt}\%$ and it doesn't change over that value (Figure 9.3b). At low filler content the standard deviation is higher because the specimens fail rather randomly during the propagation of the neck after yield. For PET/tspPOSS at $3 \text{ wt}\%$ and over the failure often happen at complete propagation of the neck along the gauge length of the specimens.

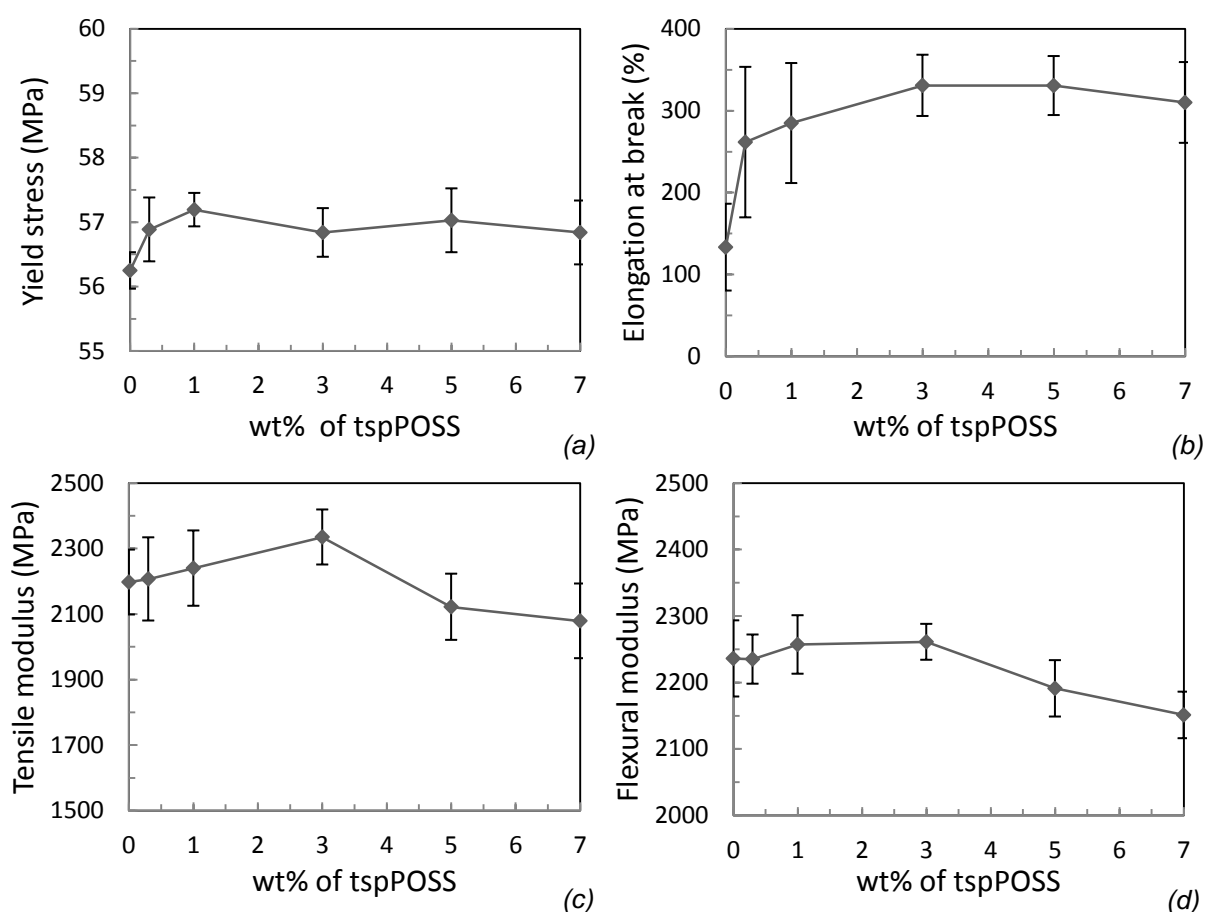


Figure 9.3 Mechanical properties of PET and PET/tspPOSS nanocomposites: yield stress (a), tensile elongation at break (b), tensile modulus (c), flexural modulus (d).

The tensile modulus doesn't change too much by adding the tspPOSS since the variations between the nanocomposites and the unfilled PET have the same order of magnitude, or are lower, than the error bars (Figure 9.3c). Only the difference between the PET/tspPOSS 3 and 5 is relevant and it makes us suppose a presence of an optimum of tensile modulus at low filler content, followed by a decrease at higher contents. The presence of an optimum of a mechanical property related to a narrow range of filler content is common in polymer/POSS nanocomposites [4]. In this case, the optimum value is supposed to be between 1 and 3 wt%. The flexural modulus exhibits a similar trend, over 3 wt% of tspPOSS it decreases (Figure 9.3d). This behavior is usually associated to a coarse size of the dispersed particles [5]. Similarly, although to a greater extent, it has been observed that 1 wt% of dsipOSS and tsiPOSS leads to the best increments of yield stress and modulus, at 5 wt% the properties are lower than neat PET [2].

9.5.2 DSC

Figure 9.4 and Figure 9.5 show the crystallization/melting peaks of the PET/tspPOSS nanocomposites compared with the unfilled PET by DSC analysis. Although usually the filler lead a nucleating activity in the polymer matrix increasing the T_c , the tspPOSS has an opposite effect in the PET. At concentrations more than 1 wt% the T_c decreases of 1-3°C. Moreover the crystallization rate and content are lowered by adding the tspPOSS since the peaks are broader and have a smaller area than the one of the unfilled PET. The rather high decrease of crystalline content is clear comparing the enthalpies of crystallization and melting. In Table 9.1 the crystallization and melting temperatures and enthalpies are listed. It can be assumed that this kind of POSS hinder the nucleating and growing action of the PET crystallites. The T_m doesn't vary by adding the tspPOSS. In a study on PET/POSS nanocomposites it has been observed that small concentrations of filler decrease the T_c by adding dsiPOSS and tsiPOSS due to the copolymerization effect. However at higher concentrations, POSS molecules start to agglomerate and act as nucleating sites, so that the T_c increases although the reaction between POSS and PET occurs [2]. Also in this case the T_m is very close to that of pure PET. In another study the observed decrease in crystallinity content arise from the reduced mobility of the polymer chains induced by the incorporation of tsiPOSS [1] and a similar effect was observed by other authors investigating the crystallization behavior of chain extended PET [6–8]. Also in this case the broadening of the crystallization peak has been meaning a decrease in the crystallization rate. It's interesting to observe that both crystallization and melting peaks of PET/tspPOSS 5 and 7 follow are separated from the other ones.

An high amorphous content of PET is desirable for applications such as blow molding where optical clarity requirement is high.

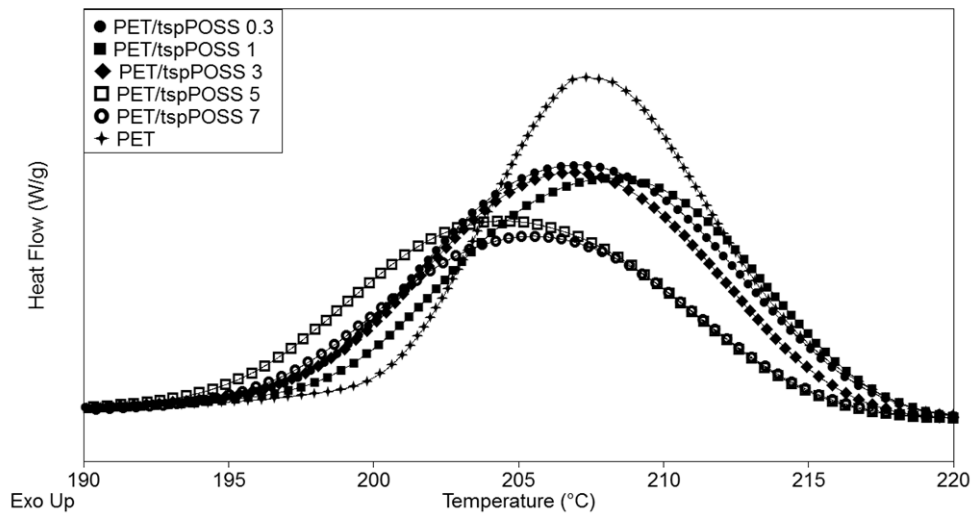


Figure 9.4 Crystallization peaks PET and PET/tspPOSS nanocomposites.

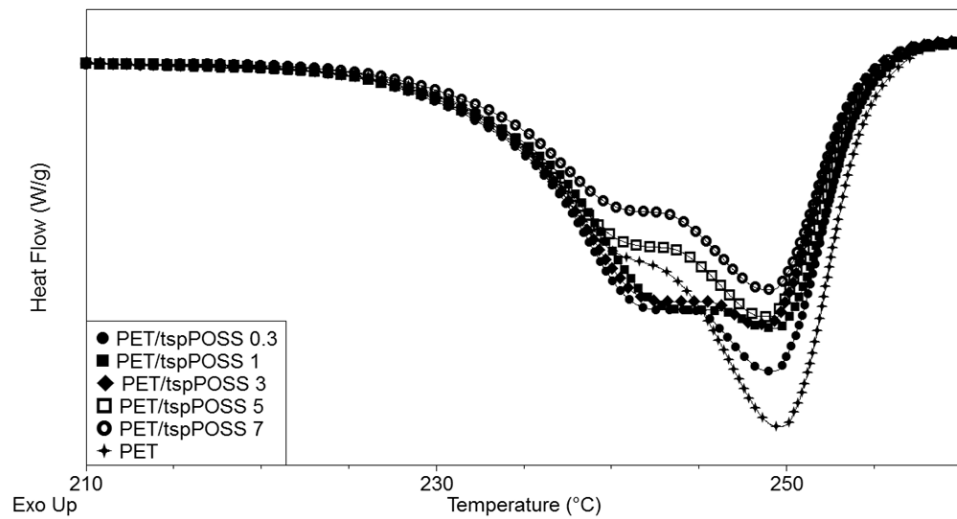


Figure 9.5 Melting peaks of PET and PET/tspPOSS nanocomposites.

Sample	T_c (°C)	ΔH_c (J/g)	T_m (°C)	ΔH_m (J/g)
PET	207.3	48.1	249.5	47.5
PET/tspPOSS 0.3	207.0	45.7	249.1	47.0
PET/tspPOSS 1	208.3	43.6	249.3	45.8
PET/tspPOSS 3	206.5	43.9	248.8	46.1
PET/tspPOSS 5	204.5	39.7	248.7	44.3
PET/tspPOSS 7	205.3	35.6	249.0	39.6

Table 9.1 DSC parameters of PET and PET/tspPOSS nanocomposites: crystallization/melting temperatures (T_c and T_m) and enthalpies (ΔH_c and ΔH_m).

9.5.3 TGA

By TGA analysis under air flow the nanocomposites there aren't relevant differences in the thermal stability respect to the PET (Figure 9.6). The curve of PET/tspPOSS 5 and 7 shift at higher temperature than the low filled nanocomposites, however they have a thermal stability similar to the PET. The TGA parameters are listed in Table 9.2 and reported in function of the filler loading in Figure 9.7. Generally, the nanocomposites exhibit a shorter degradation temperature range $T_{onset2}-T_{onset1}$ and a lower temperature of maximum mass loss rate T_{maxMLR} than PET, meaning a faster degradation process.

The temperature at 5% loss weight $T_{0.05}$ is slight higher than PET because the degradation begin is hindered by the presence of filler. At 3 wt% of tspPOSS the thermal stability gains an improvement since T_{maxMLR} and T_{onset2} increase as the filler content increases. The thermal stability under air flow of tspPOSS is better than the one of PET because the curves of nanocomposites shift to the right at the beginning of the degradation. Once it starts, the process is accelerated by the presence of filler, that is evident at low filler content. This process seems to be in competition with the shield activity of the inorganic clusters at higher filler content. A slight improvement (5–10°C of $T_{0.05}$) of the thermal stability (under nitrogen flow) has been attributed to the reaction between PET and tsi/dsiPOSS [2].

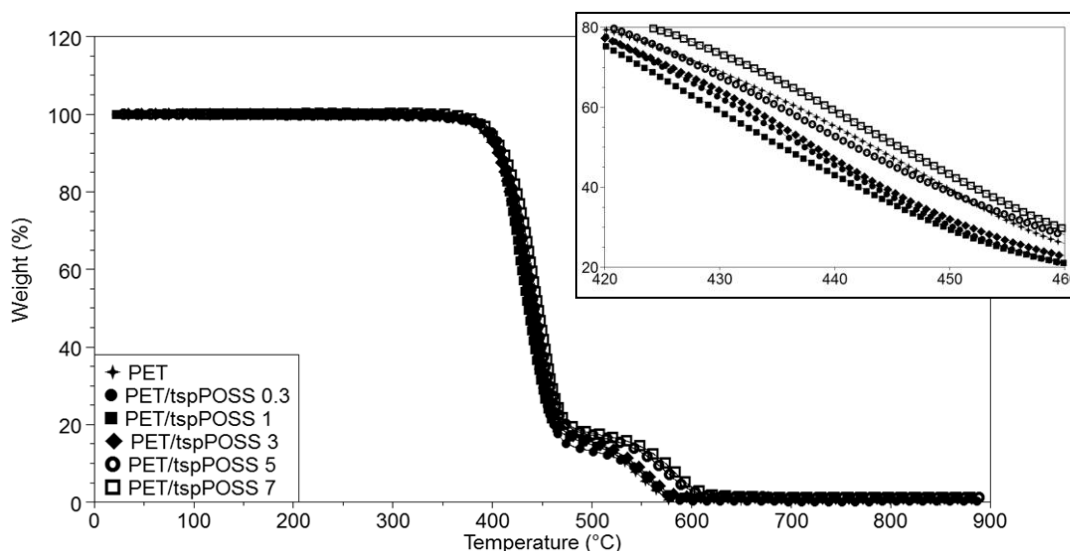


Figure 9.6 TGA under air flow of PET/tspPOSS nanocomposites.

Sample	$T_{\max\text{MLR}}$ (°C)	$T_{0.05}$ (°C)	$T_{\text{onset}1}$ (°C)	$T_{\text{onset}2}$ (°C)
PET	447	392	406	462
PET/tspPOSS 0.3	434	401	406	457
PET/tspPOSS 1	432	399	406	454
PET/tspPOSS 3	437	396	406	456
PET/tspPOSS 5	437	397	408	461
PET/tspPOSS 7	443	398	413	464

Table 9.2 TGA parameters of TPET and PET/tspPOSS nanocomposites: temperatures of start ($T_{\text{onset}1}$) and end ($T_{\text{onset}2}$) of the main degradation, temperature of maximum mass loss rate ($T_{\max\text{MLR}}$), temperature at 5% loss weight ($T_{0.05}$).

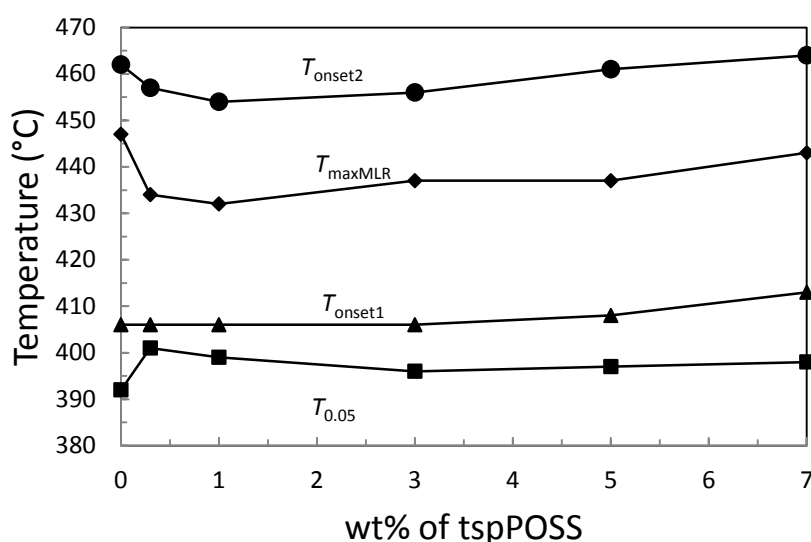


Figure 9.7 TGA parameters of TPET and PET/tspPOSS nanocomposites: temperatures of start ($T_{\text{onset}1}$) and end ($T_{\text{onset}2}$) of the main degradation, temperature of maximum mass loss rate ($T_{\max\text{MLR}}$), temperature at 5% loss weight ($T_{0.05}$).

9.5.4 XRD

In Figure 9.8 the XRD spectra of PET, nanocomposites and as-received tspPOSS are shown, measured on thin films and molded plates respectively. They have been subjected to the XRD analysis to see eventual variations of the average size of the crystalline domains arising by the addition of tspPOSS. The two different XRD analysis have been done because the injection

and compression molding lead different cooling conditions to the sample (cooling rate, pressure). The main diffraction peaks of the tspPOSS are in the 2θ range between $7-9^\circ$ and between $17-20^\circ$. These last peaks are due to the Si-O cage because the Si-to-Si distance is about 0.5 nm, corresponding to a diffraction angle 2θ of 18 nm. The most intense peaks are localized at 7.0° and 7.7° (corresponding to a interplane distance of 12.6 and 11.5 Å respectively). They are very sharp and high compared with the other ones. In the nanocomposites spectra they are not distinguishable since only one broad peak at 7.3° is present, in a middle position between the two main peaks of tspPOSS. It is visible only in the spectrum of nanocomposites with at least 3 wt% of filler and its intensity increases with the increases of POSS content. That means the tspPOSS powder organizes itself in a crystalline structure that is maintained in the nanocomposite.

In a study on PP/POSS fibers the XRD signal of octaphenyl POSS is observed even at 2 wt% [9]. This minimum POSS content that makes observable its diffraction peak depends to the size of functionalizing organic groups. It has been observed that POSS is able to crystallize in nanocomposites even when it is a part of the polymeric chain and there are restrictions on its movement [109]. Hence, the POSS is able to crystallize when it is dispersed physically in PET matrix and there are no chemical linkages to restrict its movement. Moreover, the broad signal of tspPOSS in the nanocomposites means that the crystals are not as perfect as in the as-received tspPOSS.

The peaks due to the polymer crystalline content of the nanocomposites show no difference in the shape if compared with the PET. It is possible to correlate the average size of the crystallites to the full width at half maximum of the peaks (FWHM). The value of D of both plates and films are reported in Table 9.3. The size of crystallites in the nanocomposites are generally slightly higher than the which one in the PET. Comparing with the DSC results the POSS seems to decrease the crystallinity content and increase the crystallites size. The first consideration is strongly evident by comparing the enthalpies, while comparing the crystallites size the variations are lower, but both plates and films exhibit similar results. It is explainable by assuming a decrease of crystallites density in the nanocomposites.

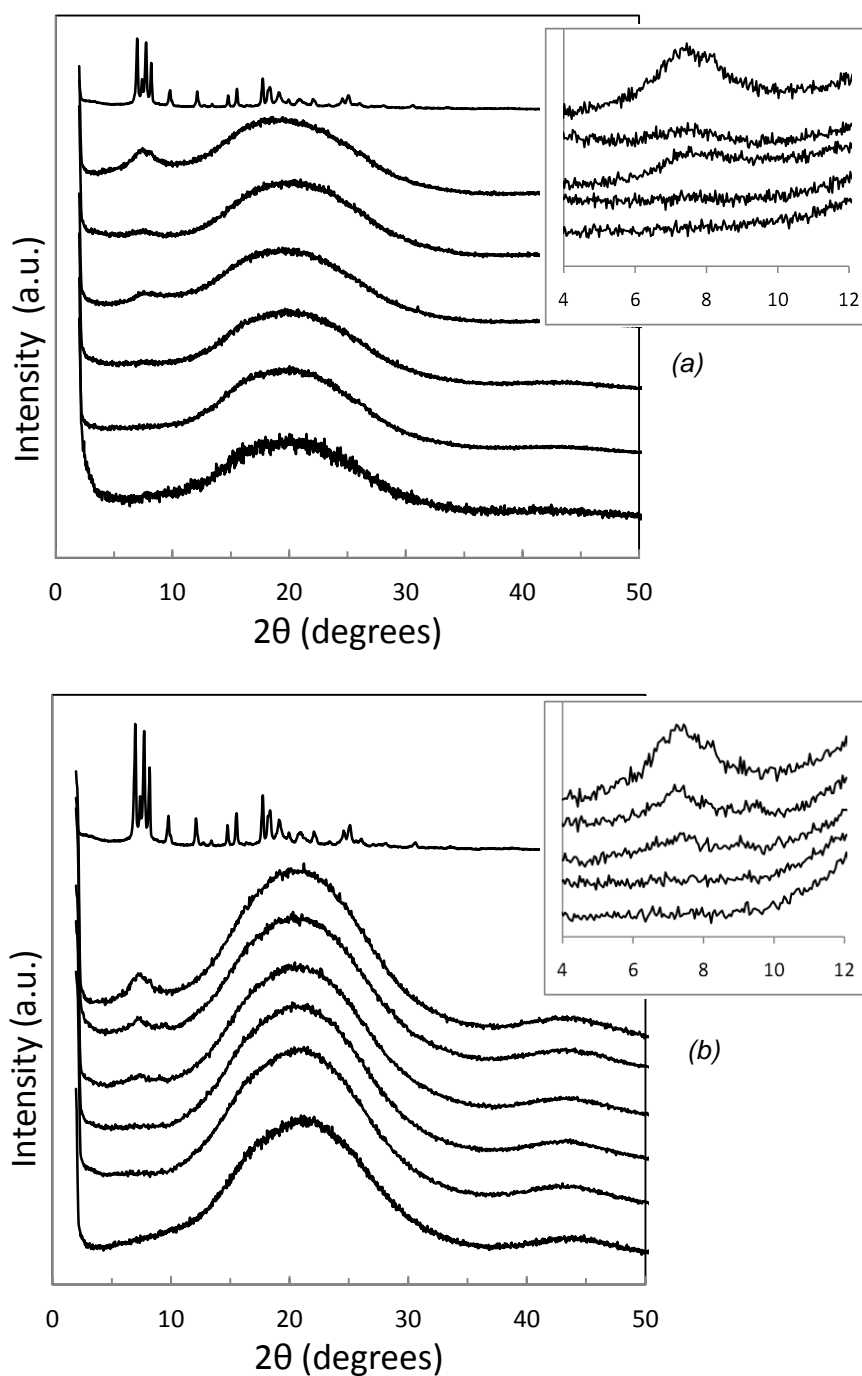


Figure 9.8 XRD spectra of PET, PET/tspPOSS nanocomposites and tspPOSS. The analysis have been done on both thin films (a) and molded samples (b). The magnifice shows the 2θ range of the tspPOSS peak in the nanocomposites.

Sample	D_{plates} (nm)	D_{films} (nm)
PET	7.8	7.7
PET/tspPOSS 0.3	8.3	8.1
PET/tspPOSS 1	8.3	8.3
PET/tspPOSS 3	8.4	7.9
PET/tspPOSS 5	8.3	8.4
PET/tspPOSS 7	8.0	7.7

Table 9.3 Size of polymeric crystallites of PET and PET/tspPOSS nanocomposites calculated for plates (D_{plates}) and films (D_{films}).

9.5.5 Oxygen permeability

The oxygen permeability through thin films has been measured. Permeability constants (K), diffusion coefficients (D) and solubility coefficient (S) are reported in Table 9.4 and showed in Figure 9.8, versus the filler content. The permeability constant, as well as the diffusion coefficient, increase as the filler content increases (Figure 9.9a and 9.9b). It means that the tortuosity path is not so effective to slow down the gas transmission and there is another aspect that promote it. It has been observed that very small particles are able to reduce the gas transmission [11,12], but, if there is a large amount of voids, the permeability of the nanocomposites is higher than the unfilled polymer [13,14]. The creation of voids in a nanocomposite leads to an increase of free volume that takes place in the interface between matrix and filler, as previously seen in Chapter 7. In PC/POSS nanocomposites an increase of diffusivity as the POSS content increase, is associated to the increase of interfacial area [15].

Sample	K ($\text{cm}^3 \mu\text{m m}^{-2} 24\text{h}^{-1} \text{bar}^{-1}$)	D ($10^{-13} \text{m}^2 \text{s}^{-1}$)	S (10^{-2}bar^{-1})
PET	2458	7.63	3.73
PET/tspPOSS 0.3	2389	7.42	3.73
PET/tspPOSS 1	2422	7.51	3.73
PET/tspPOSS 3	2672	8.81	3.40
PET/tspPOSS 5	2793	8.63	3.83
PET/tspPOSS 7	2845	9.76	3.63

Table 9.4 Oxygen transport properties of PET and PET/tspPOSS nanocomposites: permeability constant (K), diffusion coefficient (D), solubility coefficient (S).

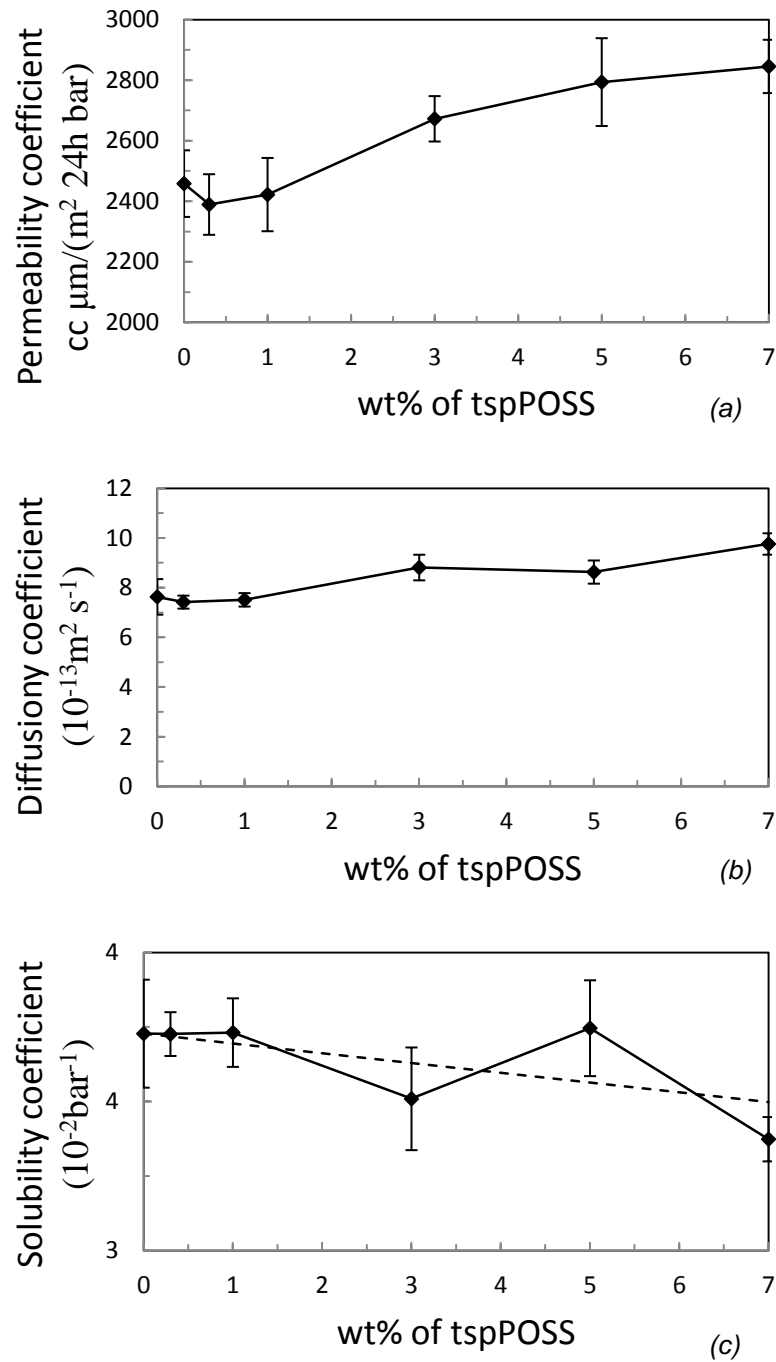


Figure 9.9 Oxygen transport properties of PET and PET/tspPOSS nanocomposites: permeability constant (a), diffusion coefficient (b), solubility coefficient (c). Broken line in Figure 9.8c is the Equation 9.5.

If there are favorable interactions between polymer and filler [16]:

$$S_n = (1 - \phi_f)S_m \quad (9.1)$$

where S_n is the solubility coefficient in the nanocomposite, S_m is the solubility coefficient in the polymer matrix, ϕ_f is the filler volume fraction. The solubility coefficient doesn't depend by the filler content (Figure 9.9c), thus there aren't particular interactions between tspPOSS and oxygen molecules. The similarity between experimental data and Equation 9.5 (solid and broken line respectively) supports this assumption.

9.5.6 TEM

In Figure 9.10 the TEM micrographs of PET/tspPOSS nanocomposites (injection molded plates) with 0.3, 1, 3, 7 wt% of filler, are shown. The which one at 5 wt% hasn't been subjected to TEM because it is supposed it has a middle morphology of the 3 and 7 wt% filled nanocomposites. It is interesting to see if there is any correlation between the particles dispersion or size and the tspPOSS content.

The morphology of all nanocomposites doesn't seems particularly homogeneous, since the size of clusters are polydispersed and they are not uniformly distributed into the matrix, especially in the low loaded nanocomposites. The POSS is present in the form of oriented ellipsoidal clusters along the flow direction (Figure 9.11).

The lighter edge of particle is due to a lower amount of POSS along the electron beam and, for the same reason, the darker region of PET around the particles is due to an higher electrons density (more compacted structure). It has to be taken into account that the particles are oriented even if the sample is not stretched but simply injection molded. Their longer diameter is about double than the shorter one (aspect ratio close to 2, Table 9.5). Their average size generally increases with the filler content as reported in Table 9.5, except for PET/tspPOSS 3 since it is in the middle of the 0.3 and 1 wt% filled nanocomposites. Also the size distribution is narrower for the PET/tspPOSS 3 nanocomposites than the others. It is well known that filler particle size, particle size distribution, and particle shape are known to affect a particulate composite mechanical properties [17–19]. Although quite widely studied, there are still some contradictory reports concerning the effect of particle size [20–22]. On the other hand they have the clusters with the lowest aspect ratio. In another study about PET/POSS nanocomposites the size of the particles in the materials containing 1 and 3 wt% POSS are relatively small, while at 5 wt% the particles are micro-sized [2].

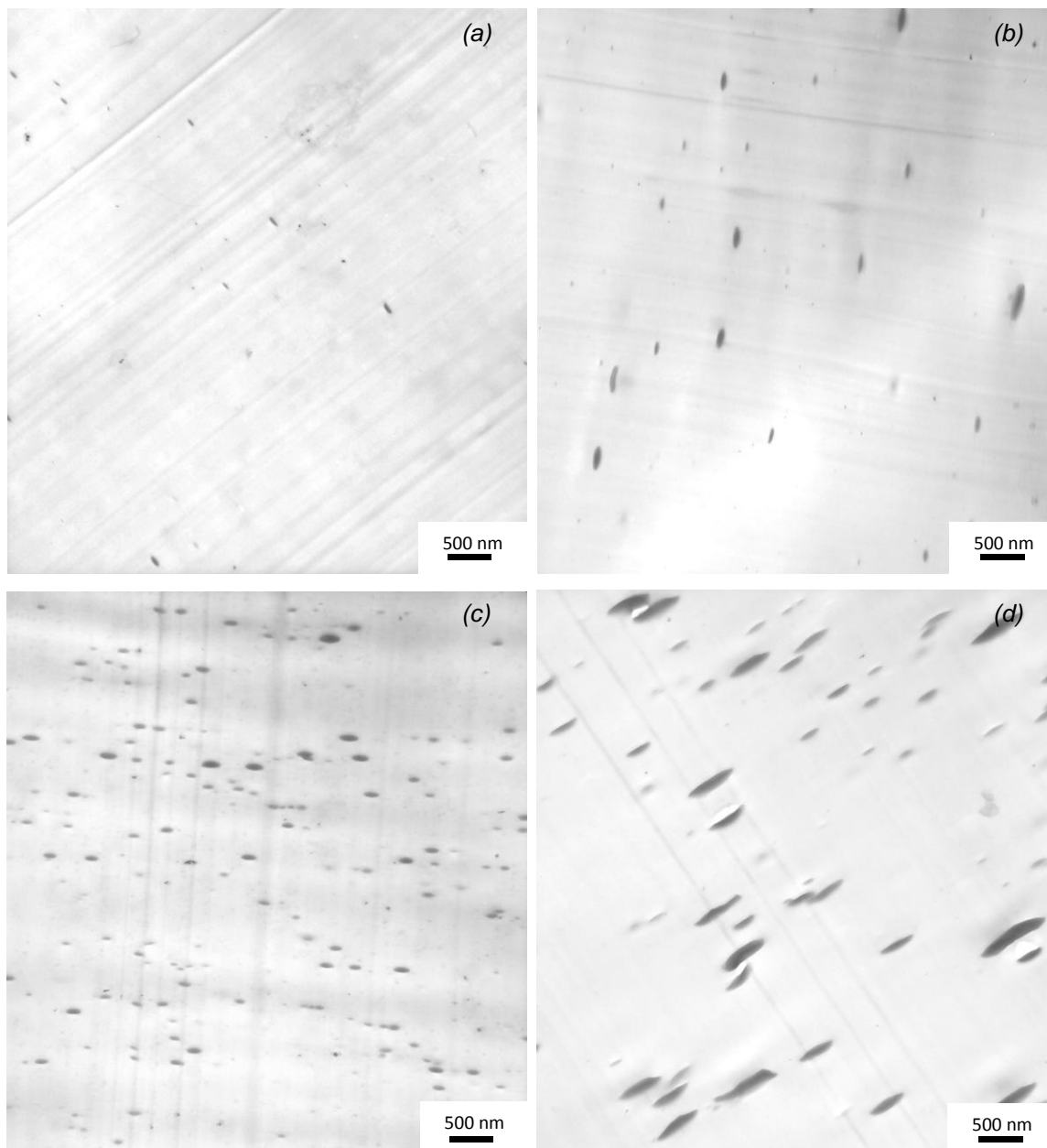


Figure 9.10 TEM micrographs of PET/tspPOSS nanocomposites with 0.3 (a), 1 (b), 3 (c), 7 (d) wt% of filler.

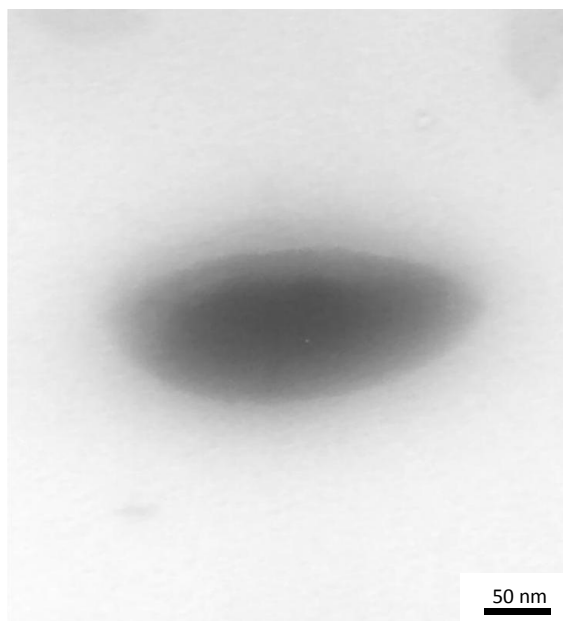


Figure 9.11 Magnification of a tspPOSS cluster in PET/tspPOSS 1 nanocomposites.


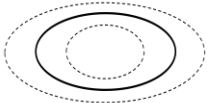
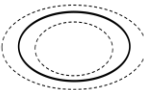
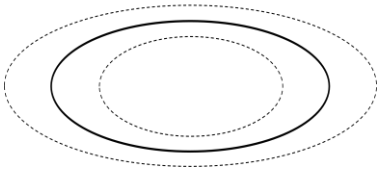
Samples	D_l (nm)	D_s (nm)	D_l/D_s
 PET/tspPOSS 0.3	$\sim 170 \pm 80$	$\sim 70 \pm 20$	2.4
 PET/tspPOSS 1	$\sim 250 \pm 110$	$\sim 100 \pm 30$	2.5
 PET/tspPOSS 3	$\sim 200 \pm 60$	$\sim 90 \pm 20$	2.2
 PET/tspPOSS 7	$\sim 500 \pm 170$	$\sim 170 \pm 40$	2.9

Table 9.5 Average size of ellipsoidal clusters: D_l is the length of the longer diameter, D_s is the length of the shorter diameter, D_l/D_s is the aspect ratio. The ellipsoids on the left are an easy comparison of particles size. The inner and outer lines represent the standard deviation, the line in the middle represents the average value.

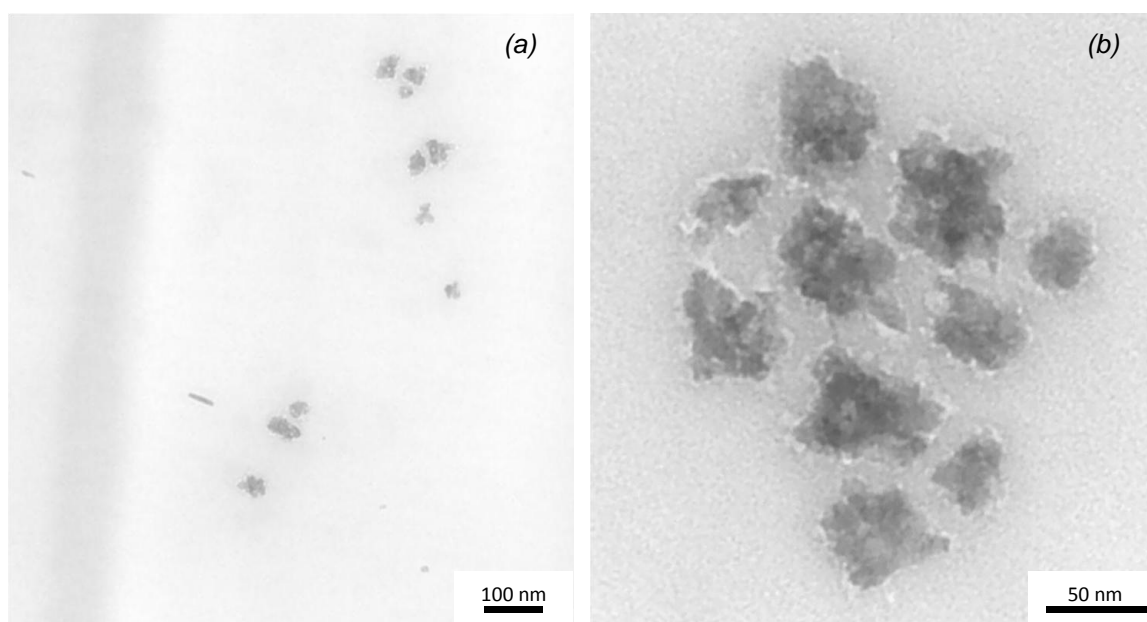


Figure 9.12 Irregular clusters of tspPOSS in PET/tspPOSS 0.3 nanocomposites: isolated clusters (a), groups (b).

A second type of clusters is dispersed into the matrix. Their structure is different from the ellipsoidal clusters previously mentioned (Figure 9.12a). They are mostly dispersed as single clusters but some groups are present as well (Figure 9.12b). Their morphology and shape is very irregular and the interface is lighter than the surrounding matrix suggesting presence of voids. Their relative concentration, respect to the ellipsoidal clusters, is higher in the nanocomposites at low tspPOSS content as it is showed in Figure 9.13.

It is interesting to observe that in some TEM micrographs the matrix portion surrounding these clusters is darker than the rest of the matrix, probably due to a higher density, while the same is not verified for ellipsoidal clusters (Figure 9.14). It suggests that the first kind could promote the crystallization unlike the second one. Different appearance, interfacial morphology, nucleating activity of the this cluster should be due to its different structure. It can be hypothesized that these clusters lose their organic functionalization during the processing, thus their superficial interaction between themselves and between the polymer chains are different if compared with the ellipsoidal clusters. The loss of phenyl group could arise by processing. High shear stress during processing could increase locally the temperature due to a strong friction. These conditions may lead to the degradation of organic parts of filler as well as polymer chains. This explanation could be supported by the higher

density of silica clusters observed in the low loaded nanocomposites assuming they are subjected to higher stress during the processing.

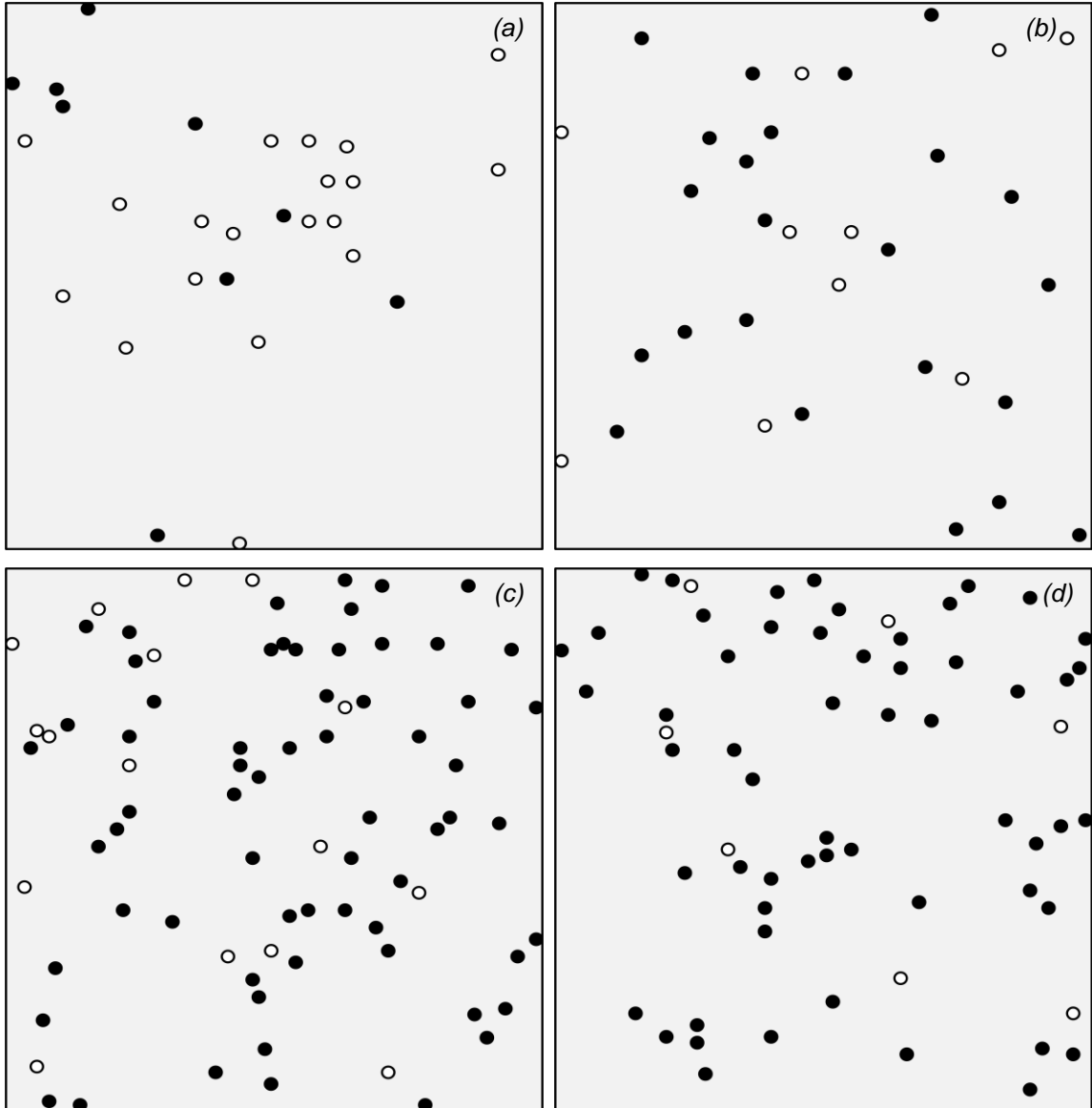


Figure 9.13 Distribution of the two kinds of clusters in Figure 9.9 of the PET/tspPOSS nanocomposites with 0.3 (a), 1 (b), 3 (c), 7 (d) wt% of filler: solid dots indicate the position of ellipsoidal clusters, empty dots indicate the position of irregular clusters.

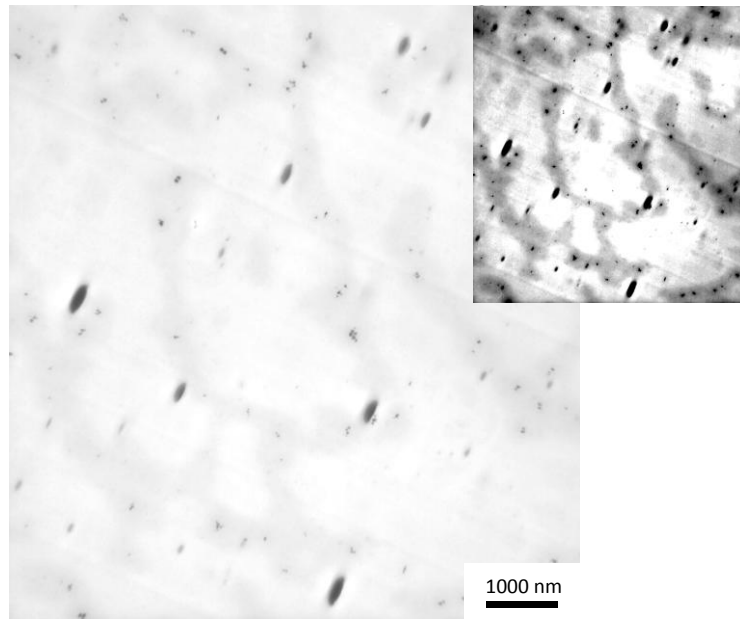


Figure 9.14 TEM micrograph of PET/tspPOSS 1 nanocomposites. It shows an area with high concentration of silica particles. It can be observed the darker color of the matrix surrounding these particles (the small micrograph has been edited to increase the contrast).

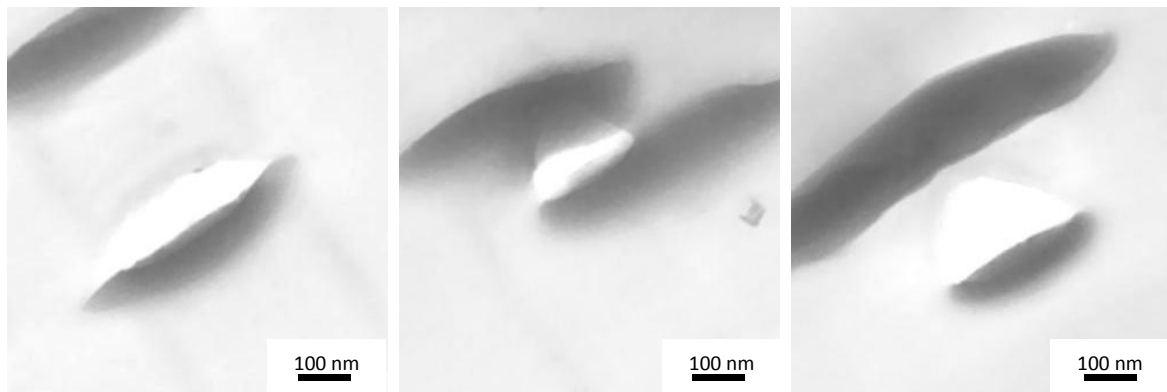


Figure 9.15 Magnifications of the Figure 9.9d of PET/tspPOSS 7 nanocomposites show voids in the interface between the matrix and clusters.

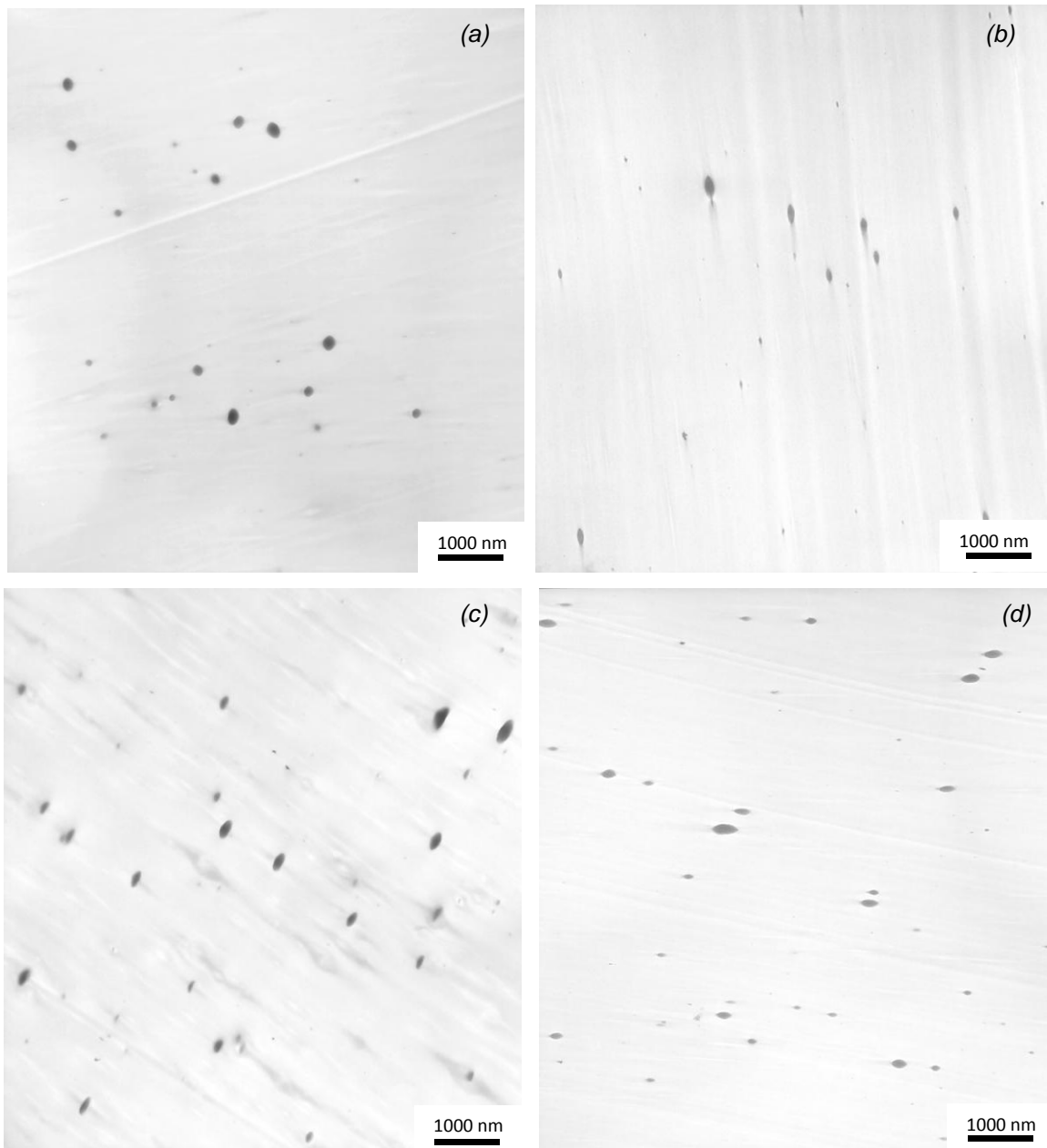


Figure 9.16 TEM micrographs of nanocomposite bottles: neck (a) and stretched sidewall (b) of PET/tspPOSS 1, neck (c) and stretched sidewall (d) of PET/tspPOSS 3.

The interface between matrix and the ellipsoidal filler doesn't exhibit any void except in PET/tspPOSS 7, in particular along one of the two sides of particle parallel to the orientation direction (Figure 9.15). That means it provides a more intense stress concentration due to the big size of clusters.

Figure 9.16 shows the TEM micrograph of the section across the neck and the stretched part of PET/tspPOSS 1 and 3 nanocomposite bottles. In the neck the particles are rather isometric

(Figure 9.16a and 9.16c) while the stretching slightly increases their orientation (Figure 9.16b and 9.16d), but it is not so strong as seen in the molded samples. When the temperature is sufficiently high the tspPOSS acts as a fluid, flowing if a stress is applied. The blow molding involves lower temperature than injection molding and the drawing do not lead a strong stretching of the tspPOSS particles. There are no evidence of slits unlike it has been seen in PET/POSSp nanocomposite bottles (Chapter 7). Thus the compatibility between PET and POSS has been further improved due to the phenyl groups of tspPOSS. Thanks to this morphologies the bottles have a very good optical clarity (Figure 9.17).

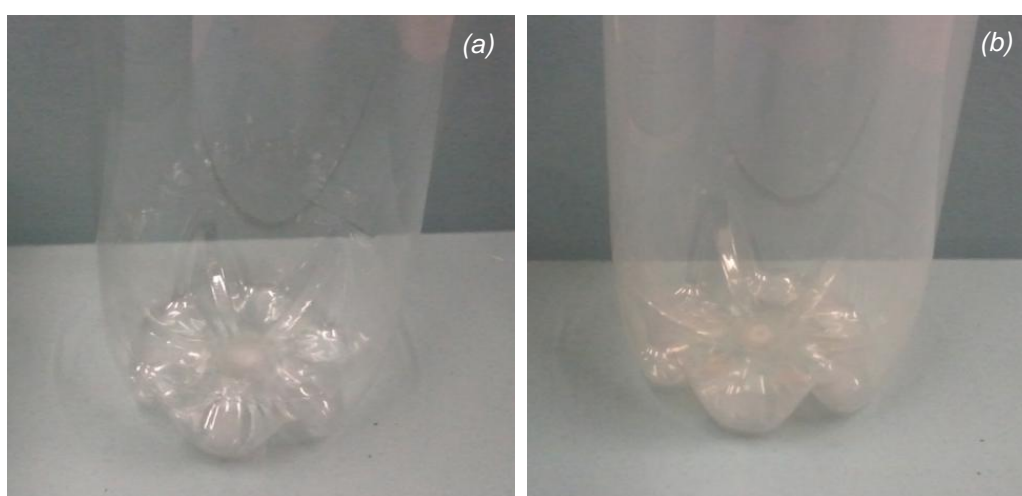


Figure 9.17 Pictures of PET (a) and PET/tspPOSS 3 (b) bottles.

9.5.7 Polarized light

In Figure 9.18 the pictures of 1 mm thickness nanocomposites plates under 90° polarized light are shown. In the PET and PET/tspPOSS 0.3 the optical strain can be observed (Figure 9.18a and 9.18b) unlike the higher loaded nanocomposites. When stress is applied to a polymer, optical strain occurs, causing the double refraction phenomenon- (photoelasticity). The absence of flow lines in the nanocomposites with higher filler content can be attributed to a relaxing of internal stress during the cooling in the mold. Higher is the inorganic content and higher is the temperature achieved after the heating of the material, since the polymers have a higher heat capacity than the inorganic materials (about double). It could explain that following hypothesis: when the material is injected into the mold it still in the molten state for enough time to allow a relaxation of stress.

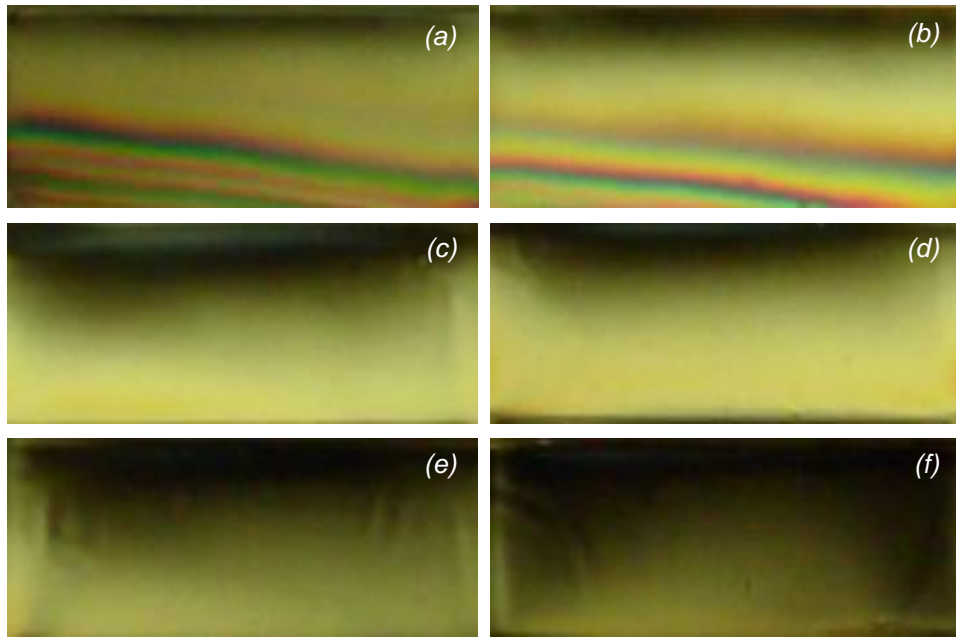


Figure 9.18 Pictures under 90° polarized light of PET (a) and PET/tspPOSS nanocomposites with 0.3 (b), 1 (c), 3 (d), 5 (e), 7 (f) wt% of filler.

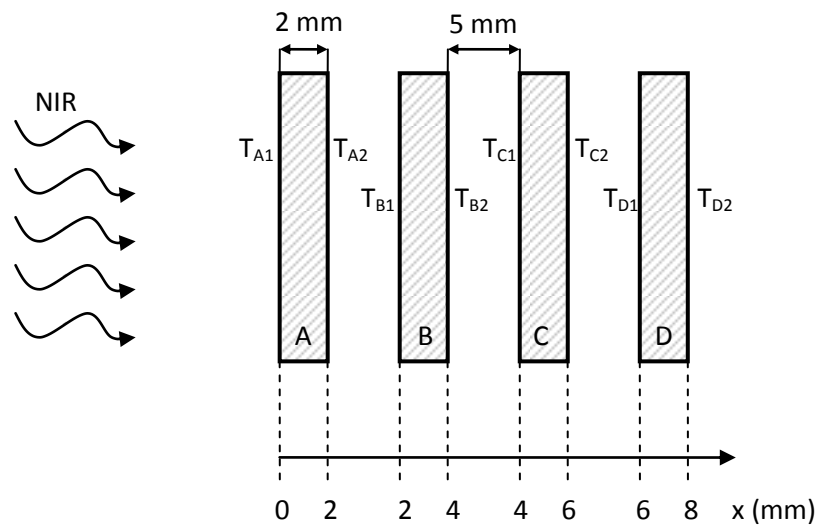


Figure 9.19 Scheme of the measurement system used in the NIR heating test.

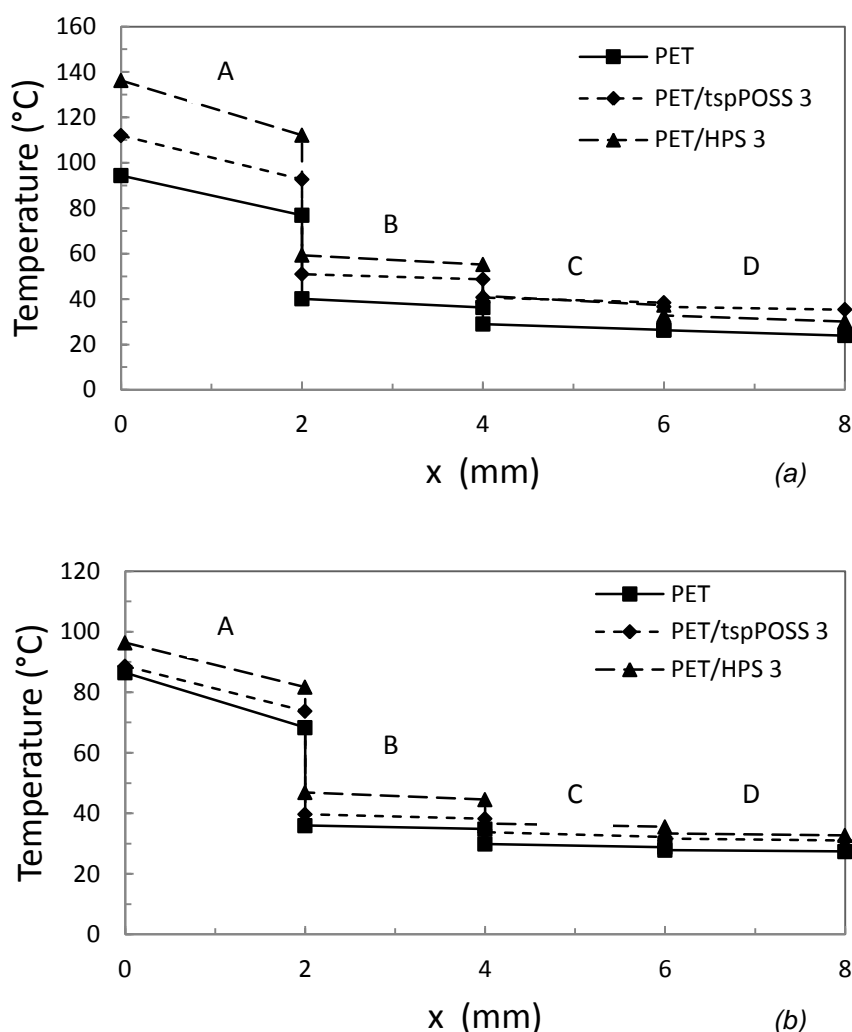


Figure 9.20 Temperatures measured in the surfaces of the plates of the PET compared to the those of nanocomposites, using 50% (a) and 100% (b) lamp power.

9.5.8 Heating test

A heating test by NIR lamps has been carried out in order to verify the heat required to a nanocomposite perform before to be blow molded. The specimens used for this test were 2 mm thickness plates, four of them have been used for one heating, placed according to the scheme in Figure 9.19. The temperature in the two surfaces of each plate, perpendicular to the light direction, has been measured with a thermocamera after a heating of 4 s by NIR lamps. The NIR light (near infrared) has a wavelength range close to the which one of the visible light ($\lambda_{NIR} = 800\text{-}2500$ nm, $\lambda_{VL} = 390\text{-}750$ nm) thus its transmittance through a material is

affected by its transparency. The adopted configuration of plates allows to see if this aspect is relevant by comparing the temperature achieved in the second plate (T_{B1}). Measurements on PET have been compared to those on PET/tspPOSS and PET/MMT (un-modified Dellite HPS) nanocomposites filled at 3 wt%. The optical clarity of PET/MMT plates is very poor if compared with PET and PET/tspPOSS thus a lesser transmitted light is expected (lower T_{B1}). Each heating test has been repeated four times and the average temperature values have been reported in Figure 9.2, using two different lamps powers. The nanocomposites achieve a higher temperature than PET (T_{A1}), specially the MMT filled ones. As mentioned in the previous paragraph the inorganic filler have a lower heat capacity than polymers, thus they require less heat to increase their temperature of 1°C (same volume unit). Nevertheless, the deviations of T_{A1} are too high to considerate that as the reason. Instead it is more plausible to associate the increase of temperature in the nanocomposites surface to the difference in absorbed light since it is affected by the transparency of the material respect to the wavelength. The result of NIR absorption is the heating of the material, since it increases molecular vibrational activity. Probably the PET/tspPOSS nanocomposites have a transparency to the visible light very similar to the one of unfilled PET, while is not so close in the range of NIR light. It could be investigated through UV-NIR spectroscopy. A high scattering intensity of visible light is associated with a turbid appearance of the PET/MMT nanocomposite. The reason is the steeply increasing intensity of scattered light with increasing particle diameter as described by Rayleigh law:

$$\frac{I}{I_0} = \exp - \left[\frac{3\phi_p x r^3}{4\lambda^4} \left(\frac{n_p}{n_m} - 1 \right) \right] \quad (9.2)$$

with intensity I of the transmitted and I_0 of the incident light, radius r of the spherical particles, refractive index n_p of the particles and refractive index n_m of the matrix, λ is the wavelength of the light, ϕ_p the volume fraction of the particles and x the optical path length.

The values of T_{B1} exhibit difference comparable to the difference of T_{A2} . It is assumed that the heating of the B1 surface arise mostly by the conduction trough the 5 mm air gap between plates rather than transmitted light. Nanocomposite preforms allow to consume less energy arising the heating lamps and it is an important industrial advantage.

9.6 Conclusion

The characterization on PET/trisilanol phenyl POSS (tspPOSS) nanocomposites at different filler contents (0.3, 1, 3, 5, 7 wt%) has been carried out in order to obtain bottles with good optical clarity.

The mechanical properties of nanocomposites exhibit a slight increase in tensile and flexural modulus up to 3 wt% of tspPOSS, at higher content they decrease. Assuming a reaction between PET and tspPOSS these values are lower than expected. Instead the elongation at break is very high for all nanocomposites.

DSC showed there is not a nucleating activity of tspPOSS, since it decreases the crystallinity content, the crystallization rate and temperature. The extent of these variations is relatively higher over 3 wt% of filler.

TGA showed a small delay of thermal oxidative degradation by adding tspPOSS, due to its high stability, but it accelerates the process at higher temperature. At 3 wt% of filler and over the shield activity begins to be effective and the thermal stability improves.

The crystalline organization of tspPOSS clusters has been observed by XRD. Calculating the PET crystallites size in two different specimens a slight increase was observed and associated to a lower crystallites density in the nanocomposites than in PET.

The oxygen permeability is maintained up to 1 wt% of filler content, over this value it increases due to an increase of free volume at the interface between PET and tspPOSS clusters. The increase of diffusivity coefficient means that the tortuous path is not so effective to slow down the oxygen transport, while the trend of solubility coefficient makes to suppose there are no interaction between permeants-filler due to the favorable interaction matrix-filler. By TEM micrographs, a dispersion of ellipsoidal clusters in the nanocomposites was observed. Their orientation is affected by the injection molding that gives them the elongated shape. This orientation doesn't occur during the blow molding due to the different temperature. Their size generally increases as the filler content increases but a inverse trend occurred at 3 wt%. A second kind of cluster is present at low filler content and it has a silica appearance. Its presence is hypothesized to be due to the loss of organic functionalization of tspPOSS. Their structural properties differ from those of ellipsoidal clusters since they act as nucleating agents. Highly transparent bottles have been successfully obtained at 3 wt% of filler content showing no presence of delamination phenomena.

Heating test and observation under polarized light confirm that nanocomposites achieve a higher temperature than the unfilled polymer due to the lower transparency than the unfilled PET.

References

- [1] F.C.L. Ciolacu, N.R. Choudhury, N. Dutta, E. Kosior. *Macromolecules* 2007, 40, 265.
- [2] J.K. Kim, K.H. Yoon, D.S. Bang, Y.B. Park, H.U. Kim, Y.H. Bang. *J Appl Polym Sci* 2008, 107, 272.
- [3] E.T. Kopesky, G.H. McKinley, R.E. Cohen. *Polymer* 2006, 47, 299.
- [4] S.K. Lim, E.P. Hong, Y.H. Song, H.J. Choi, I.J. Chin. *J Mater Sci* 2010, 45, 5984.
- [5] M. Sánchez-Soto, D.A. Schiraldi, S. Illescas. *Eur Polym J* 2009, 45, 341.
- [6] K.H. Yoon, M.B. Polk, J.H. Park, B.G. Min, D.A. Schiraldi. *Polym Int.* 2005, 54, 47.
- [7] S.J. Oh, B.C. Kim. *J Polym Sci* 2001, 39, 1027.
- [8] L. Sorrentino, S. Iannace, E. Di Maio, D. Acierno. *J Polym Sci* 2005, 43, 1966.
- [9] B.S. Butola, M. Joshi, S. Kumar. *Fib Polym* 2010, 11, 1137.
- [10] L. Zheng, A.J. Waddon, R.J. Farris, E. Coughlin. *Macromolecules* 2001, 35, 2375.
- [11] V. Alexandros, B. Dimitrios, P. Eleni. *Macromol React Eng* 2007, 1, 488.
- [12] V. Vladimirov, C. Betchev, A. Vassiliou, G. Papageorgiou, D. Bikiaris. *Compos Sci Technol* 2006, 66, 2935.
- [13] G. Monserrat, J. Barsema, R.E. Galindo, D. Cangialosi, J. Garcia-Turiel, W.E. Van Zyl, H. Verweij, D.H.A. Blank. *Polym Eng Sci* 2004, 44, 1240.
- [14] T.C. Merkel, B.D. Freeman, R.J. Spontak, Z. He, I. Pinnau, P. Meakin, A.J. Hill. *Chem Mater* 2003, 15, 109.
- [15] N. Hao, M. Bohning, A. Schonhals. *Macromolecules* 2010, 43, 9417.
- [16] R.M. Barrer. Diffusion and permeation in heterogeneous media. In *Diffusion in Polymers*. J. Crank, G.S. Park editors, Academic Press, London and New York (1968) pp 165-217.
- [17] R. Rethon. *Particulate-filled polymer composites*. Longman Scientific & Technical, New York (1995).
- [18] M.W.L. Wilbrink, A.S. Argon, R.E. Cohen, M. Weinberg. *Polymer* 2001, 42, 10155.
- [19] J. Jancar. *J Mater Sci* 1989, 24, 3947.

[20] S. Ahmed, F.R. Jones. *J Mater Sci* 1990, 25, 4933.

[21] L.E. Nielsen. *Mechanical properties of polymers and composites*, vol. 2, Marcel Dekker, New York (1974).

[22] D.M. Bigg. *Polym Comp* 1987, 8, 115.

Chapter 10

PET/MA-g-EVA/oMMT nanocomposites for flexible packaging application

10.1 Introduction

Concerning PET/PA/oMMT nanocomposites previously described in chapter 5, a selective dispersion of clay into one phase has been observed. It was due to the better chemical affinity between clay and PA rather than clay and PET, independently by the mixing route used [1]. On the basis of where the platelets placed in a ternary nanocomposite, the final properties can be vary in a wide range, since they are strongly dependent by the material morphology. The capability to control the dispersion of the clay allows to tune these properties depending to the application the material is developed for.

This interesting aspect concerning the control on the selective dispersion of clay has been approached by adding organo-functionalized montmorillonite (oMMT) in a impact modified PET ideated for flexible packaging application. The weakness of PET is the very low impact strength. This leads to notches that will cause the failure of the material in a brittle manner, limiting its applicability. This notch-sensitivity is generally higher when clay is added to the PET matrix so its impact modification could be a good route to limit this phenomenon-. It involves the dispersion of small particles of an elastomeric or low-modulus phase into the thermoplastic matrix. The mixing of PET, a polar polymer, with elastomers, that are usually non-polar, leads to a immiscible blend with a coarse dispersed phase. Fine rubber particle size and strong rubber-matrix adhesion are two desiderated aspects to a strong impact strength. A widely used approach to achieve a good morphology is a compatibilization between the two

components. The two main routes involve a functionalized elastomer able to react with the matrix or a third component (e.g. organoclay or polymers) more compatible with the matrix and rubber than themselves. Several studies on impact modified PET, showed that grafting with glycidyl methacrylate (GMA) and maleic anhydride (MA) is an effective method to compatibilize the PET with the low-modulus dispersed phases [2–9].

Because of their opposite effects on mechanical properties of a thermoplastic polymer, and their mutual interaction, rubber and clay are added simultaneously to achieve balanced mechanical properties. With an optimal combination of these it is possible to combine the properties of a rubber toughening polymer (high impact strength) and a polymeric matrix nanocomposite (high Young modulus). The clay added in a blend can play a double role: as reinforcing filler and as refiner of the structure. Concerning the nanocomposite blends, it has been observed that the composition, melt viscosity, and polarity of the components strongly affects the final morphology. The reduction of rubber particle size could occur because an increase of the melt viscosity [10–13] or the barrier activity of platelets [14,15] slow down the coalescence of the droplets, or the organoclay acts as a compatibilizer reducing the interfacial tension [16–19]. The selective localization of clay in one phase rather in the other phase or in the interphase depends also to the mixing sequence. It has been seen that the thermodynamic regulate the migration of clay toward the higher affinity phase [20–22] and the viscosity can affect the preferential localization as well [22–24].

In this study crystallized PET and maleic anhydride grafted ethylene-vinyl acetate copolymer (MA-g-EVA) nanocomposite blends have been produced by melt blending with different PET/MA-g-EVA ratios and clay content (Cloisite 20A, C20A). The EVA dispersed phase acts as an impact modifier of PET since its high VA content (33%) gives a strong elastomeric behavior. The grafting with MA is required for a compatibilization between PET and EVA and eventually between EVA and clay as well. To avoid an embrittlement of the nanocomposite and to eventually obtain a refining activity of the oMMT, the purpose is to constrict the clay inside the rubber domains, by a suitable processing and surfactant. Moreover the crosslinking of EVA should avoid an eventual migration of the platelets.

10.2 Raw materials

Crystallized poly(ethylene terephthalate) (PET) provided by Eastman was VersaTray 12822, with an intrinsic viscosity 0.920-0.980, density 1.40 kg/cm³, melting temperature 250°C. Ethylen-vinyl acetate copolymer (EVA) provided by Celanese was Ateva 3325AC, with 33 wt% of vinyl acetate, melt index 43.0 g/10 min, density 0.952 kg/cm³, melting temperature 60°C. Maleic anhydride (MA) at ≥98% of purity (melting temperature 52-54°C, boiling temperature 200°C) and dicumyl peroxide (DCP) at 98% of purity (melting temperature 39°C) were provided by Sigma Aldrich. Organomodified montmorillonite provided by Southern Clay was Cloisite 20A (C20A), modified with dimethyl dihydrogenated tallow quaternary ammonium (38 wt%), with interlayer distance d_{001} of 24.2 Å (Figure 5.1b). The used raw material structures are showed in Figure 10.1.

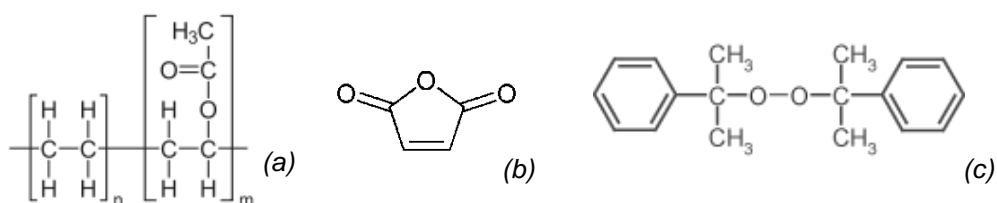


Figure 10.1 Raw materials structures: EVA (a), MA (b), DCP (c).

10.3 Preparation of samples

The EVA was dried under vacuum overnight at 45°C and mixed with 5 wt% of MA, 0.3 wt% of DCP by counter-rotating twin screw extruder (HBI Haake 90) with a temperature profile, from hopper to die, of 45-55-80-80°C and a screw rate of 10 rpm. These amounts of polymer, peroxide and MA have been chosen because a study on MA-g-EVA shows that they produce a good combination of high grafting degree and low gel contents [25]. Moreover, it has been observed DCP leads a low gel content than other kind of peroxides.

After pelletization and drying under vacuum overnight at 45°C the EVA/DCP/MA material was extruded adding a inorganic content of C20A of 1.5, 3, 6, 9 wt% (previously dried under vacuum overnight at 80°C) with a temperature profile of 45-55-80-80°C and a screw rate of 10 rpm. After pelletization and drying under vacuum overnight at 45°C the EVA/MA/C20A nanocomposites were compression molded by press at 175°C (half-life time of DCP is 1.45

min) for 10 minutes to achieve the functionalization (Figure 10.2a) and crosslink [26] (Figure 10.2b) of the polymer. An increase of compatibility between PET and EVA could be achieved by reactive extrusion because of the MA grafted to the EVA chains could react with the hydroxyl and carboxyl end groups of PET [27]. Another advantage of MA grafting is the formation of hydrogen bonding between the maleic anhydride group or carboxylic group and the oxygen groups or hydroxyl groups of the silicates that improve the intercalation degree of non-polar organomodified clay [28].

After pelletization and drying under vacuum overnight at 45°C each MA-g-EVA/C20A nanocomposite were extruded adding PET (previously dried under vacuum overnight at 120°C), using a PET/(MA-g-EVA/C20A) mass ratio of 90/10 and 80/20. The mixing has been carried out by counter-rotating twin screw extruder with a temperature profile of 130-200-250-260°C and a screw rate of 10 rpm. After pelletization and drying under vacuum overnight at 100°C the PET/MA-g-EVA/C20A nanocomposites were injection molded by a press with a temperature profile of 260-275-275°C to produce the specimens for to the mechanical tests.

The neat polymers, the compatibilized and un-compatibilized blends, and the MA-g-EVA/C20A nanocomposites have been molded as well. In Table 10.1 **Errore. L'origine iferimento non è stata trovata.** are listed the developed materials.

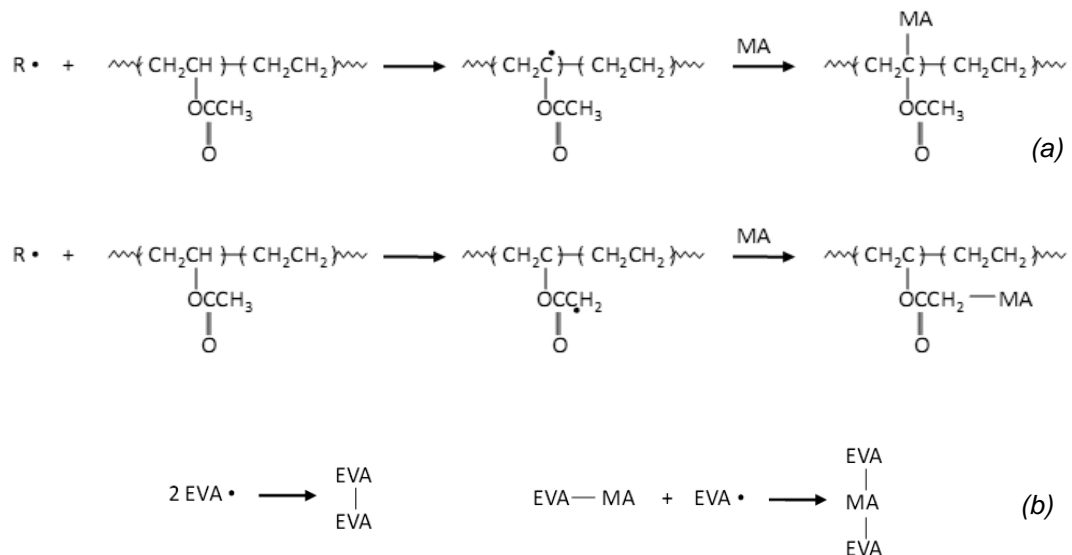


Figure 10.2 Possible mechanisms for the melt functionalization of the EVA copolymer (a) and crosslink reactions of the EVA during melt mixing with DCP and MA (b).

Sample	wt% of PET	wt% of EVA or EVA/MMT	wt% of MMT in EVA
PET	100	0	0
EVA	0	100	0
MA-g-EVA	0	100	0
PET/EVA 80/20	80	20	0
PET/EVA 90/10	90	10	0
PET/MA-g-EVA 80/20	80	20	0
PET/MA-g-EVA 90/10	90	10	0
MA-g-EVA/C20A 1.5 wt%	0	98.5	1.5
MA-g-EVA/C20A 3 wt%	0	97	3
MA-g-EVA/C20A 6 wt%	0	94	6
MA-g-EVA/C20A 9 wt%	0	91	9
PET/MA-g-EVA/C20A 90/10(1.5)	90	10	1.5
PET/MA-g-EVA/C20A 90/10(3)	90	10	3
PET/MA-g-EVA/C20A 90/10(6)	90	10	6
PET/MA-g-EVA/C20A 90/10(9)	90	10	9
PET/MA-g-EVA/C20A 80/20(1.5)	80	20	1.5
PET/MA-g-EVA/C20A 80/20(3)	80	20	3
PET/MA-g-EVA/C20A 80/20(6)	80	20	6
PET/MA-g-EVA/C20A 80/20(9)	80	20	9

Table 10.1 Contents of PET, EVA and MMT in all the produced materials.

10.4 Characterization

Mechanical properties

The mechanical properties of all materials were measured by Instron 5566. Dog-bone shaped specimens produced by injection molding have been subjected to the tensile test in order to measure the tensile modulus, tensile strength, yield stress and elongation at break (50 mm/min tensile rate, according to ADSM D638).

Rectangular bars (125x12.7x3.2 mm) produced by injection molding have been subjected to the flexural test in order to measure the flexural modulus (1.3 mm/min test rate, 50 mm support span, according to ASTM D790).

DSC

The thermal transitions and the crystallization behavior were examined using a TA Instruments Q100 DSC differential scanning calorimeter working in heat-cool-heat mode, at heating and cooling rate of 10°C/min. The run limits used are 20-300°C for PET based materials and 10-100°C for EVA based materials.

TGA

The thermal behavior was measured by thermogravimetric analysis (TGA) on a TA instruments SDT Q600. Every run was carried out under a 100 mL/min air flow from room temperature to 800°C heating at 20°C/min.

XRD

The degree of intercalation and exfoliation of the clay were monitored by X ray diffraction (Philips model X'PERT PRO). The XRD analyses were carried out in reflectance mode with Cu anode material ($K_{\alpha 1} = 1.54056$ nm, $K_{\alpha 2} = 1.54439$ nm). The diffractograms were scanned in a 2θ range from 1.47 to 25.00° at scan rate of 0.0334°/s. The d -spacings have been calculate by using Equation 4.13.

TEM

The level of dispersion was investigated also by high magnification transmission electron microscopy (TEM, JEOL JEM 1200 EXII). Samples for TEM analyses were cut from ultra-thin specimens using a Leica Ultracut UCT ultramicrotome.

10.5 Results and discussion

10.5.1 Mechanical properties

Crosslinking and grafting of EVA with MA the tensile strength and modulus increase but decrease the strain at break as well Figure 10.3. The small differences between the EVA and MA-g-EVA properties means that the crossliking occurred only partially. Moreover the addition of clay improves the modulus and increases the strain at break as well. A similar behaviour has been observed on EVA/OMLS nanocomposites (28 wt% of VA) [29]. The increase of elongation at break with clay content has been explained assuming that the homogeneous and good dispersion of clay leads to a large amount of matrix-clay interphase forms shear zones that stop the development of cracks.

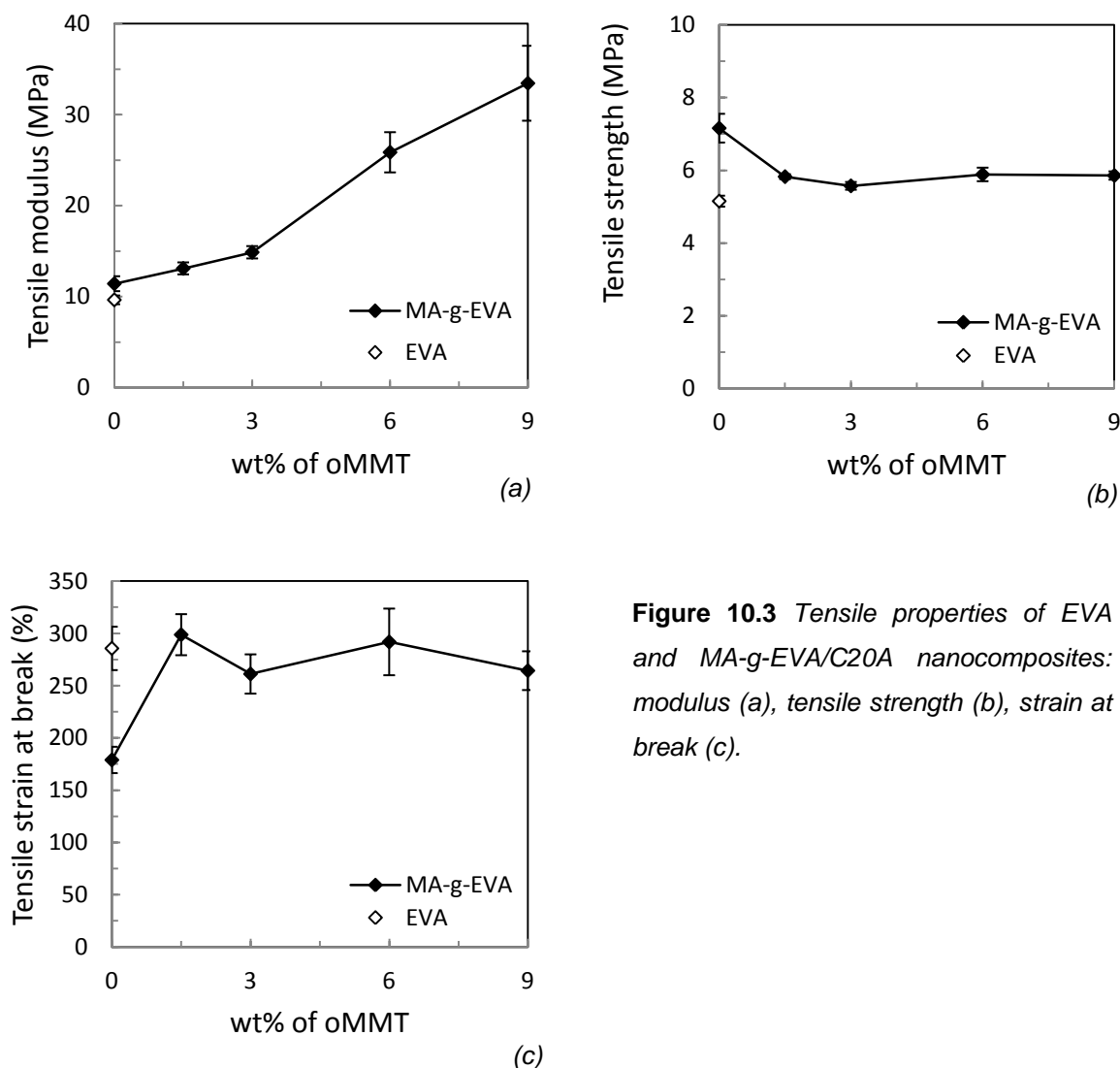


Figure 10.3 Tensile properties of EVA and MA-g-EVA/C20A nanocomposites: modulus (a), tensile strength (b), strain at break (c).

In our case the examined system is slightly different since the grafting with MA has been carried out. Both the increase of the modulus and the strain at break by the increasing of the clay content could be associated to an exfoliation and/or a good intercalation level of the platelets. The dispersion of clay in the MA-g-EVA will be discussed afterwards through XRD and TEM analysis.

Looking at the tensile properties of both PET/EVA and PET/MA-g-EVA blends, the rubber linearly lowers the tensile modulus and the yield stress as expected (Figure 10.4a and Figure 10.4b). An analogue trend has been seen in many studies on impact modified PET [2,3,7,8] according to the rule of mixtures [30]. In our case the PET/MA-g-EVA and PET/EVA blends have a similar value of both the properties since MA-g-EVA and EVA have the same mechanical behavior compared to the stiffer PET.

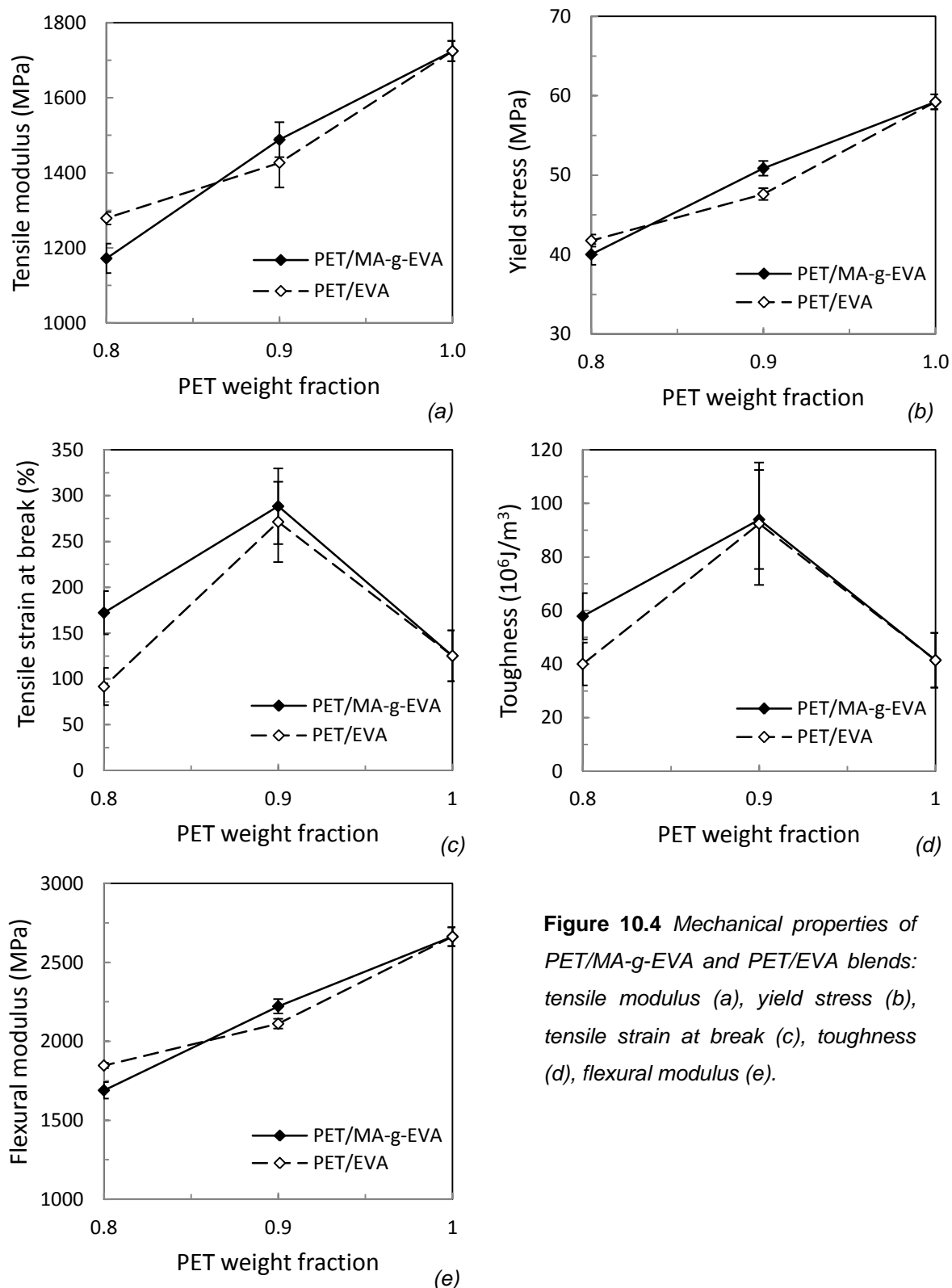


Figure 10.4 Mechanical properties of PET/MA-g-EVA and PET/EVA blends: tensile modulus (a), yield stress (b), tensile strain at break (c), toughness (d), flexural modulus (e).

Unlike the Young modulus, the properties at break usually don't follow the rule of mixture. It has been observed that the strain at break could decrease, by blending PET with a low-modulus polymer, [3] or drop over a certain content [4, 12] due to the coarse size and/or

irregular shape of rubbery domains. In our case an inversion of trend seems to occur at 80 wt% of compatibilized and un-compatibilized EVA in PET.

When the rubbery dispersed phase is compatibilized an improvement of adhesion at interphase and a reduction of particle size are commonly reached leading to an improvement of the properties [31]. The grafting of EVA improves the strain at break of the 80/20 blend (Figure 10.4c) probably due to a refinement of rubber domains and/or to an improvement of the adhesion, that is not relevant in the 90/10 blend.

Calculating the area underneath the curves stress-strain the toughness is determined (Figure 10.4d). It represents the energy of mechanical deformation per unit of volume that material needs to be broken. Considering the 80/20 blend, the influence of MA grafting is hence evidenced from all mechanical properties evaluations, unlike it happens for the 90/10 one. The trend of flexural modulus is in good agreement with the tensile one (Figure 10.4e) and confirms the better enhancement in the compatibilized 80/20 blend.

The presence of clay in PET/MA-g-EVA blends has different effects depending on the ratio of two components. In the 90/10 nanocomposites the tensile modulus doesn't change (Figure 10.5a) and the yield stress is slightly lowered by the addition of clay (Figure 10.5b). For the 80/20 nanocomposites these two trends, assuming they are linear, have a more positive slope. As the benefit of grafting has been seen for the 80/20 blend unlike the 90/10 one, also the addition of clay seems to lead better mechanical properties. These observations can be justified taking into account the double content of clay in the 80/20 nanocomposites. The strain at break of both the two classes of nanocomposites drops over 3 wt% of MMT in MA-g-EVA (Figure 10.5c). The toughness and the flexural modulus reflect the trends of tensile strain at break and tensile modulus respectively, as expected (Figure 10.5d and Figure 10.5e). An increase of the strain at break is associated to a toughening of the material, usually when the clay acts as a compatibilizer that reduces the rubber particle size and/or improves the adhesion at the interphase. Both these characteristics are commonly verified by selective localization of the lamellae in the interphase because they reduce the interfacial tension [16–19]. On the other hand, the refinement due to slowing down of the droplets coalescence is related to a preferential dispersion of the clay in one or both the phases. The two proposed mechanisms are the increase of viscosity by adding the clay [10–13] and the barrier activity of the platelets [14-15]. In our case bigger domains size in the PET/MA-g-EVA/C20A 80/20(6) and 90/10(6) nanocomposites are expected.

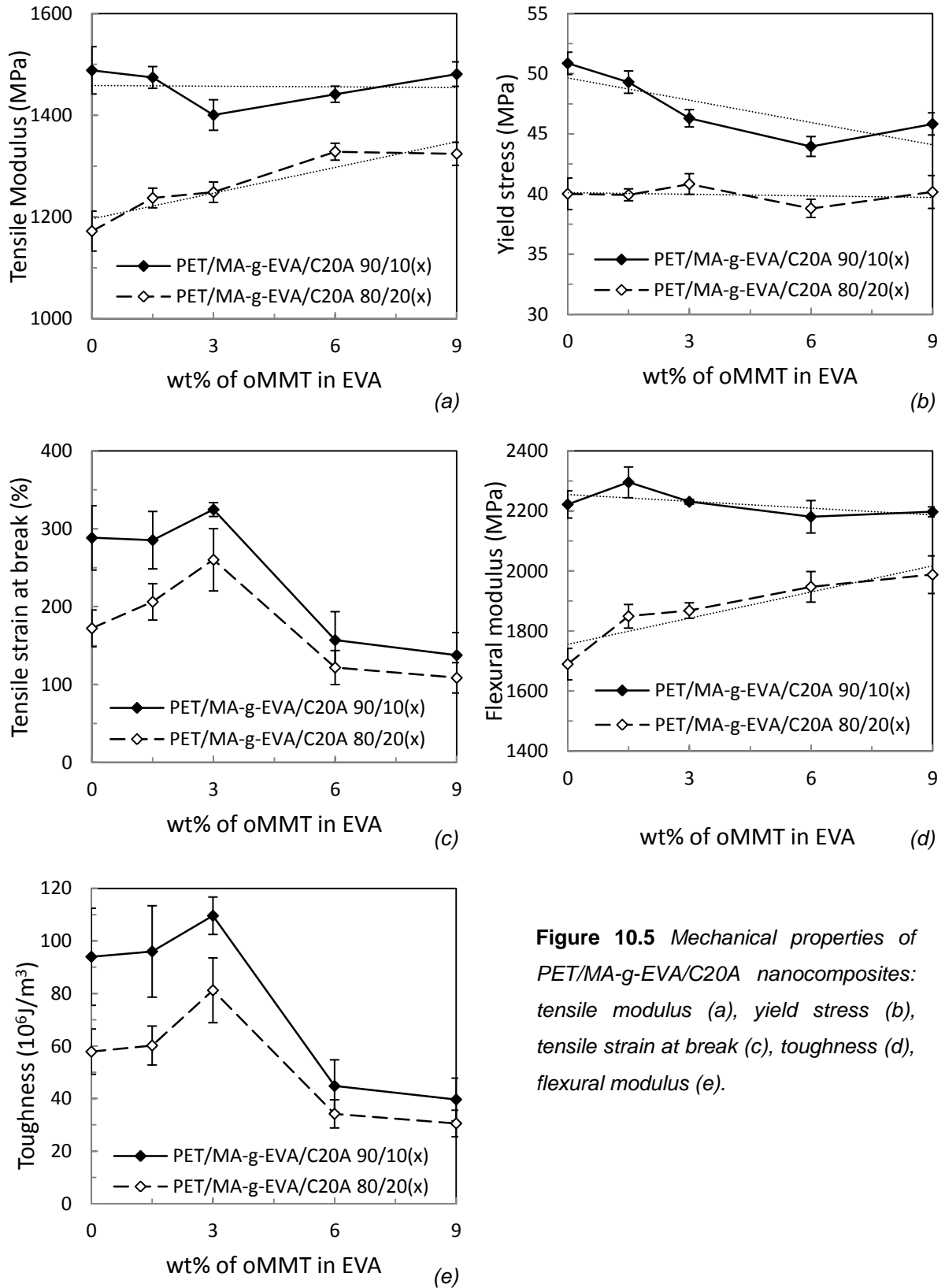


Figure 10.5 Mechanical properties of PET/MA-g-EVA/C20A nanocomposites: tensile modulus (a), yield stress (b), tensile strain at break (c), toughness (d), flexural modulus (e).

10.5.2 TGA

TGA analysis of PET/MA-g-EVA blends compared to the neat PET and MA-g-EVA under air flow are shown in Figure 10.6. The thermo-oxidation of MA-g-EVA occurs in two steps [32]: during the first the elimination of acetic acid is observed with formation of C=C double bonds (300-400°C) and the lost weigh corresponds to the VA content (33%). In the second step the degradation of the backbone occurs (400-500°C).

The thermo-oxidation of PET occurs in two steps as well [33]: the first one is related to the main degradation of the backbone (350-475°C). The second step is the thermo-oxidative degradation of the char formed after the first step (475-600°C).

PET/EVA 90/10 blend has a thermal stability very similar to the neat PET. If the EVA content is higher, as in the PET/EVA 80/20 blend, a faster weigh loss can be seen at the beginning of the main degradation step.

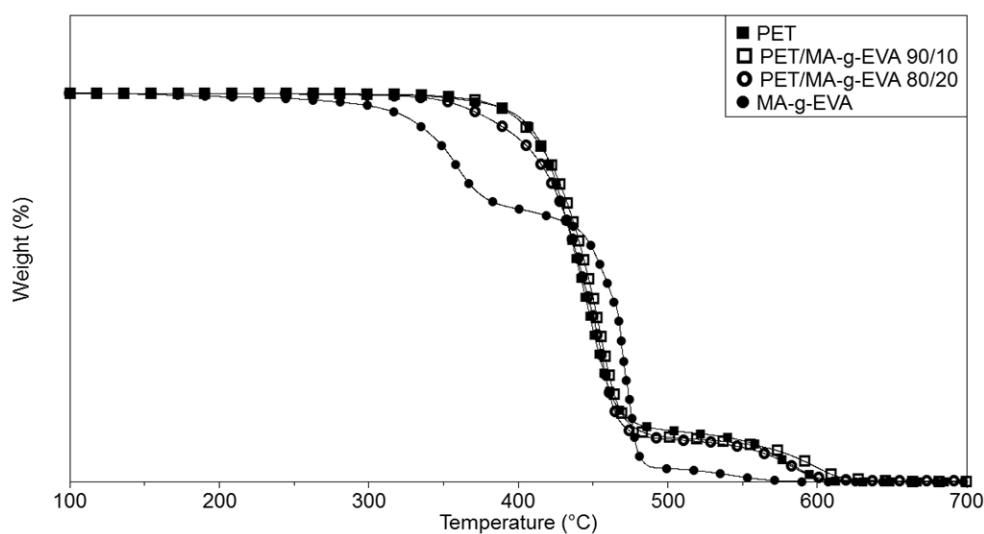


Figure 10.6 TGA under air flow of PET, MA-g-EVA and their blends.

TGA analysis of MA-g-EVA/C20A nanocomposites under air flow are shown in Figure 10.7. As it can be seen, the inorganic residues reflect well the inorganic contents are supposed to be into the matrix.

Concerning the first step of degradation (deacetylation), C20A has not influence on the rate of volatilization as it has been seen in another work [34].

Referring at the main degradation, the starting and the ending temperatures (T_{onset1} , T_{onset2}), the temperature of the maximum of mass loss rate (T_{maxMLR}) are reported in Figure 10.8 at different clay contents. The main degradation is slowed by adding the clay, since its duration (directly proportional to $T_{onset2} - T_{onset1}$) increases with clay content up to 3 wt% of MMT in MA-g-EVA. This enhancement of thermal stability is gradually less effective with increasing of clay content. Moreover also T_{maxMLR} increases up to 3 wt% of MMT in MA-g-EVA and slightly decreases over that value.

The shift of T_{maxMLR} to higher temperature indicates that thermal-oxidation delay is mainly due to the barrier effect promoted by the presence of exfoliated lamellae which collapses upon matrix degradation forming an insulating layer. It slows the diffusion of volatile products as well as diffusion of oxygen from the polymer and the gas phase respectively [35]. A similar inversion of thermal stability, as in our case, has been seen on EVA/12Me-MMT nanocomposites over 6 wt% of MMT due to poor dispersion of lamellae, as verified by XRD [29].

In our case, it is supposed a homogeneous dispersion of the platelets at an exfoliated or intercalated level up to 3 wt% of MMT, with the percolation at an intermediate value between 3 and 6 wt%. Similarly, the Young modulus of MA-g-EVA/C20A nanocomposites exhibited its maximum increase between 3 and 6 wt% of MMT in MA-g-EVA.

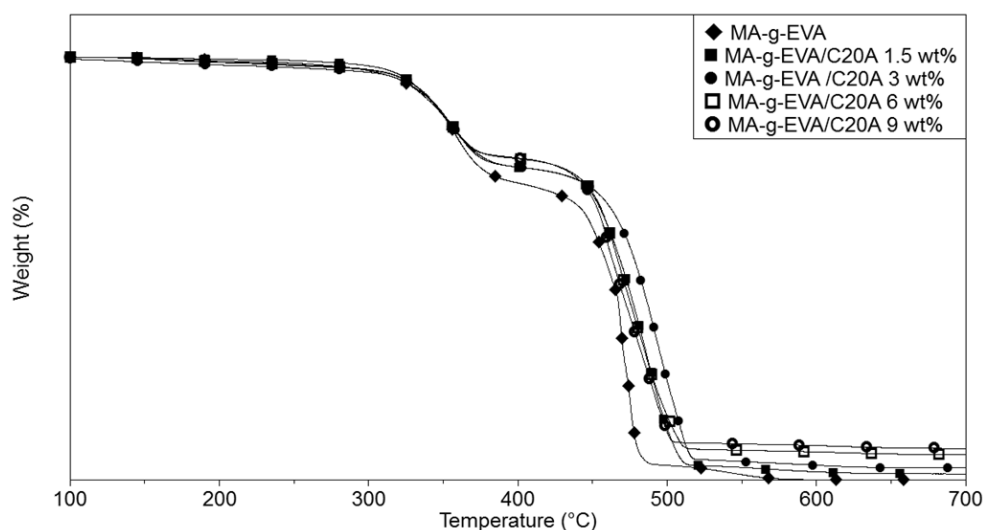


Figure 10.7 TGA under air flow of MA-g-EVA/C20A nanocomposites.

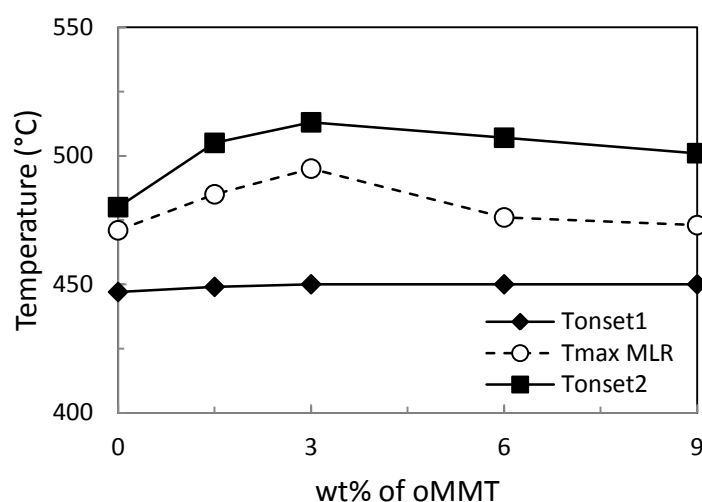


Figure 10.8 TGA parameters of MA-g-EVA/C20A nanocomposites: temperature of starting (T_{onset1}) and ending (T_{onset2}) of the main degradation step, the temperature at the maximum mass loss rate (T_{maxMLR}).

TGA analysis under air flow of PET/MA-g-EVA/C20A nanocomposites with a PET/(MA-g-EVA/C20A) ratio of 90/10 and 80/20 are showed in Figure 10.9. T_{onset1} , T_{onset2} , T_{maxMLR} and $T_{0.05}$ (temperature at 5% weight loss) are reported in Figure 10.10. As it can be seen there aren't significant variations of thermal stability of nanocomposites compared to the blends, even comparing 90/10 nanocomposites with the 90/10 blend they exhibits a decreasing of thermal stability.

This behavior of PET nanocomposites with alkyl-ammonium surfactants modified clay is commonly attributed to the degradation of organic compatibilizer. The Hoffman elimination reaction forms some products [36] accelerating the degradation of matrix in PET/C20A nanocomposites [37]. In the 90/10 nanocomposites this is a competitive and prevailing mechanism affecting the thermal stability, producing the enhancement due to clay.

The effect of clay observed in the 80/20 nanocomposites is better than in the 90/10 ones since the weight-temperature curves are overlapped to the curve of blend (Figure 10.9b) and $T_{0.05}$ do not decrease below T_{onset1} (Figure 10.10b). Similarly to the results of the mechanical properties, the lesser clay content in the 90/10 nanocomposites leads a worse thermal stability than in the 80/20 ones.

In our case an eventual absence of clay into the PET phase and its preferential localization inside the MA-g-EVA domains would explain there isn't any improvement on the thermal stability. Probably the double inorganic content in the 80/20 nanocomposites, forming an insulating char that slows the diffusion of the combustion products, compensates the accelerated degradation due to the Hofmann elimination reaction.

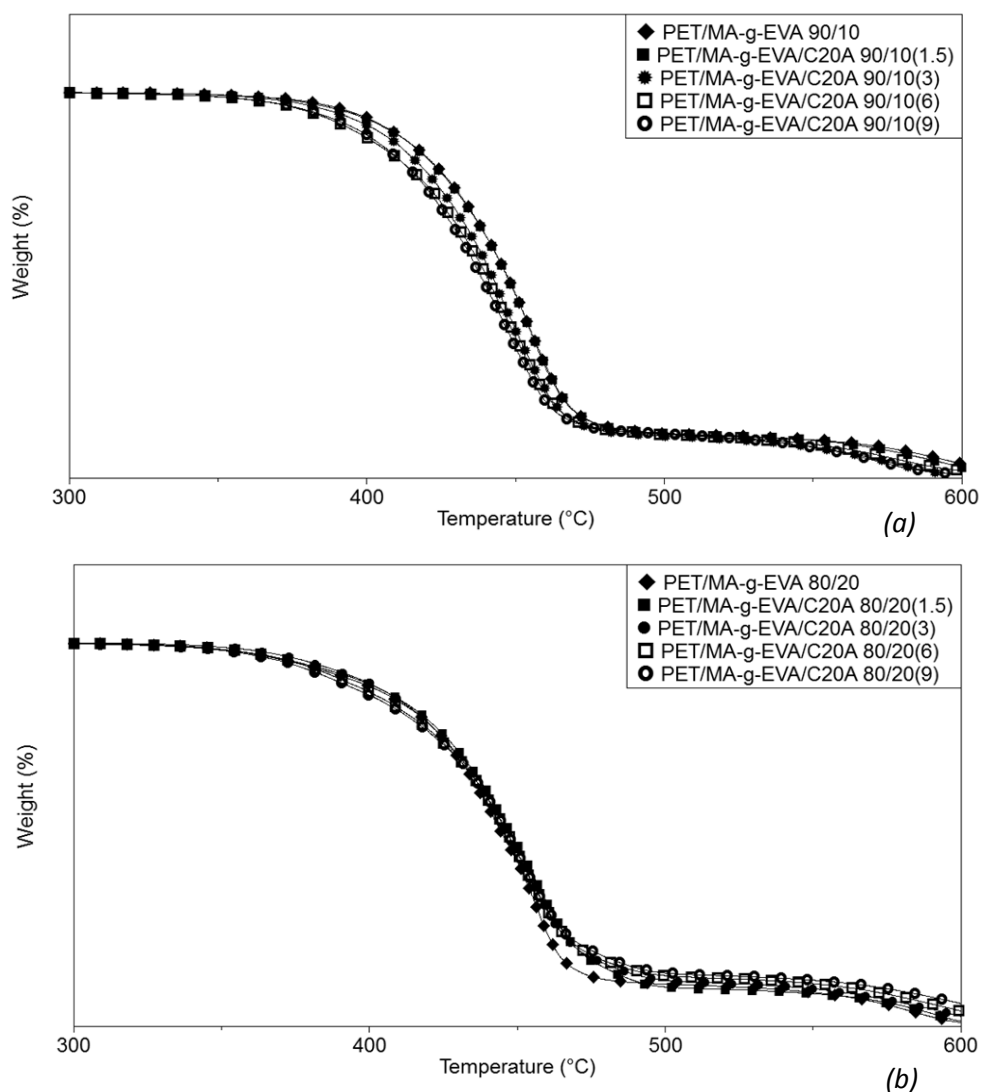


Figure 10.9 TGA under air flow of PET/MA-g-EVA/C20A nanocomposites with a PET/(MA-g-EVA/C20A) ratio of 90/10 (a) and 80/20 (b).

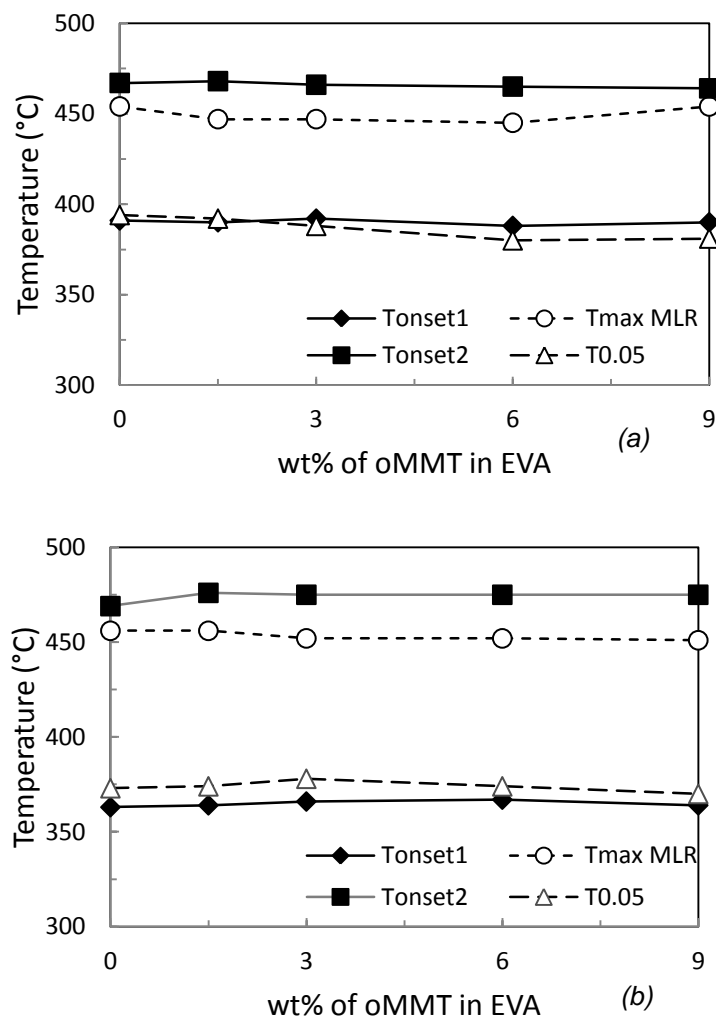


Figure 10.10 TGA parameters of PET/MA-g-EVA/C20A nanocomposites with a PET/(MA-g-EVA/C20A) ratio of 90/10 (a) and 80/20 (b): temperature of starting (T_{onset1}) and ending (T_{onset2}) of the main degradation step, temperature at the maximum mass loss rate (T_{maxMLR}), temperature at 5% weight loss ($T_{0.05}$).

10.5.3 DSC

In Figure 10.11 the crystallization temperature (T_c) and enthalpic (ΔH_c) of MA-g-EVA/C20A nanocomposites compared to the MA-g-EVA and neat EVA are showed. T_c is not affected by crosslinking while the clay increases it of 4°C, independently to its content meaning. It means that heterogeneous nucleation is occurred, as in the most of

polymers/nanofiller systems. The ΔH_c values of polymer with and without clay are similar, meaning a similar extent of crystallinity.

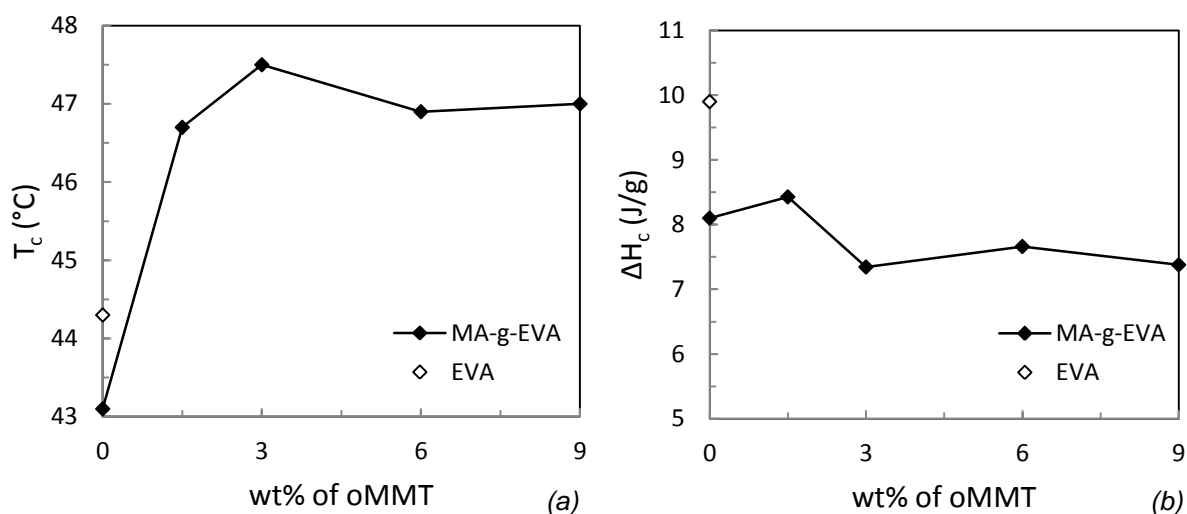


Figure 10.11 DSC parameters of EVA and MA-g-EVA nanocomposites: crystallization temperature and enthalpy, T_c (a) and ΔH_c (b).

In Figure 10.12 the melting and crystallization temperatures (T_m, T_c) and enthalpies ($\Delta H_m, \Delta H_c$) of PET/EVA and PET/MA-g-EVA blends compared to the neat PET are showed. The transition temperatures do not change significantly adding the EVA in the PET (Figure 10.12a and Figure 10.12b). A slight lower T_c of PET/MA-g-EVA 80/20 can be observed. As previously seen the strain at break of this material is much higher than the un-compatible one probably because of a better adhesion between EVA and PET. Usually this is due to the reactions between the functionalized rubber and the matrix, in particular between grafted MA and hydroxyl and carboxyl end groups of PET [26]. For this reason these PET chains has a lower mobility and the crystallization around the rubber domains should be hindered. This is confirmed by the difference in ΔH between PET/MA-g-EVA 80/20 and PET/EVA 80/20, that it is not relevant for 90/10 blends (Figure 10.12c and Figure 10.12d). In many studies about compatibilized blends the enthalpies are lower than the ones of neat matrix [38,39] because some reactions occur in the interphase and the crystallinity content decreases. It agrees with the difference of the elongation at break seen between compatibilized and un-compatible 80/20 blends, unlike the 90/10 ones.

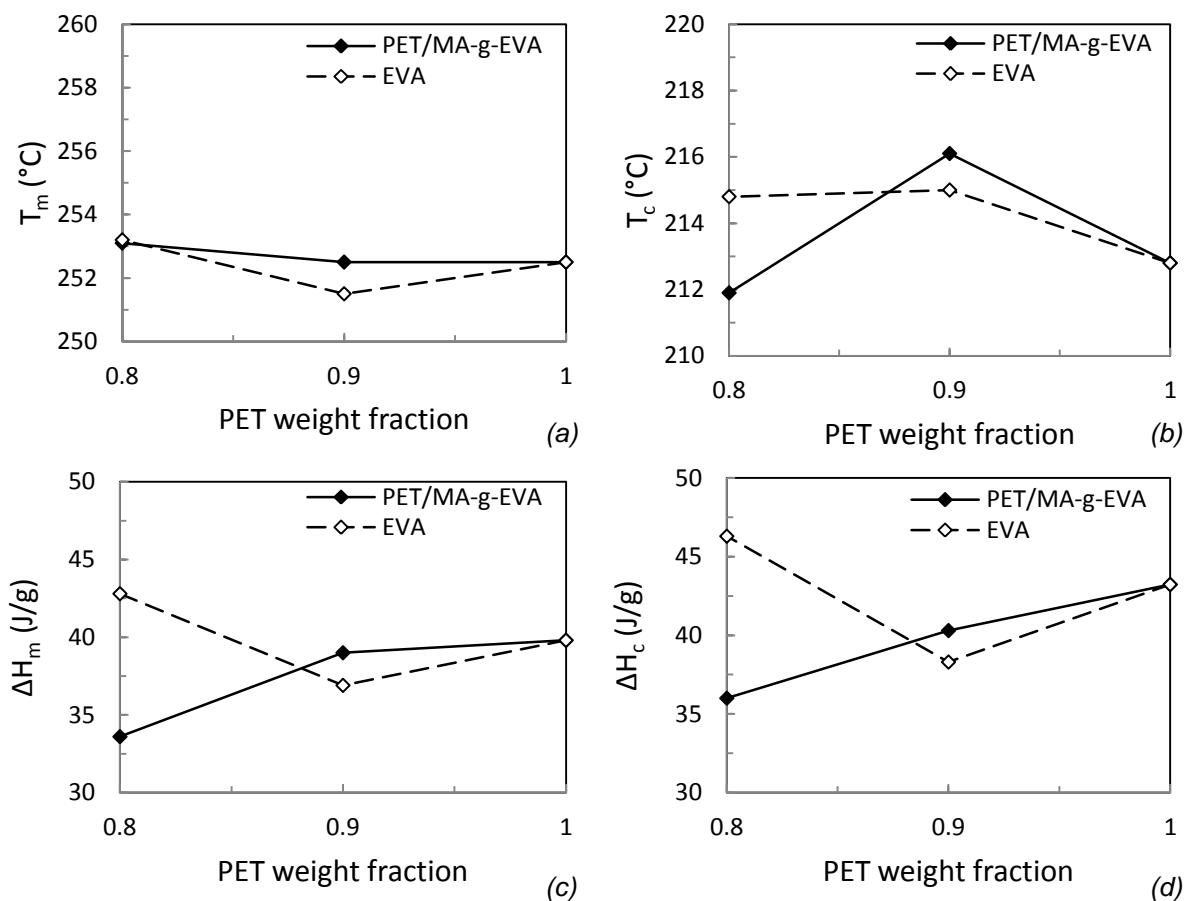


Figure 10.12 DSC parameters of PET/MA-g-EVA and PET/EVA blends: melting and crystallization temperatures, T_m (a) and T_c (b), melting and crystallization enthalpies, ΔH_m (c) and ΔH_c (d).

In Figure 10.13 the melting and crystallization temperatures (T_m, T_c) and enthalpies ($\Delta H_m, \Delta H_c$) of PET/MA-g-EVA/C20A nanocomposites compared to the PET/MA-g-EVA blends are showed. No variations on T_m are seen and T_c increases with increasing of clay only in the 80/20 nanocomposites (Figure 10.13a and Figure 10.13b). They exhibit an increase of enthalpies as well (Figure 10.13c and Figure 10.13b). In PET/OMLS nanocomposites the nucleating activity of clay has been verified by an increasing of T_c (usually T_m is not affected) and enthalpies leading a higher crystallization rate and crystallinity content, and smaller spherulites than neat PET [40].

The heterogeneous nucleation of PET is possible only if the clay is dispersed into the PET matrix or, with a lesser extent, in the interphase between PET and MA-g-EVA, while a complete dispersion inside the rubbery domains is excluded.

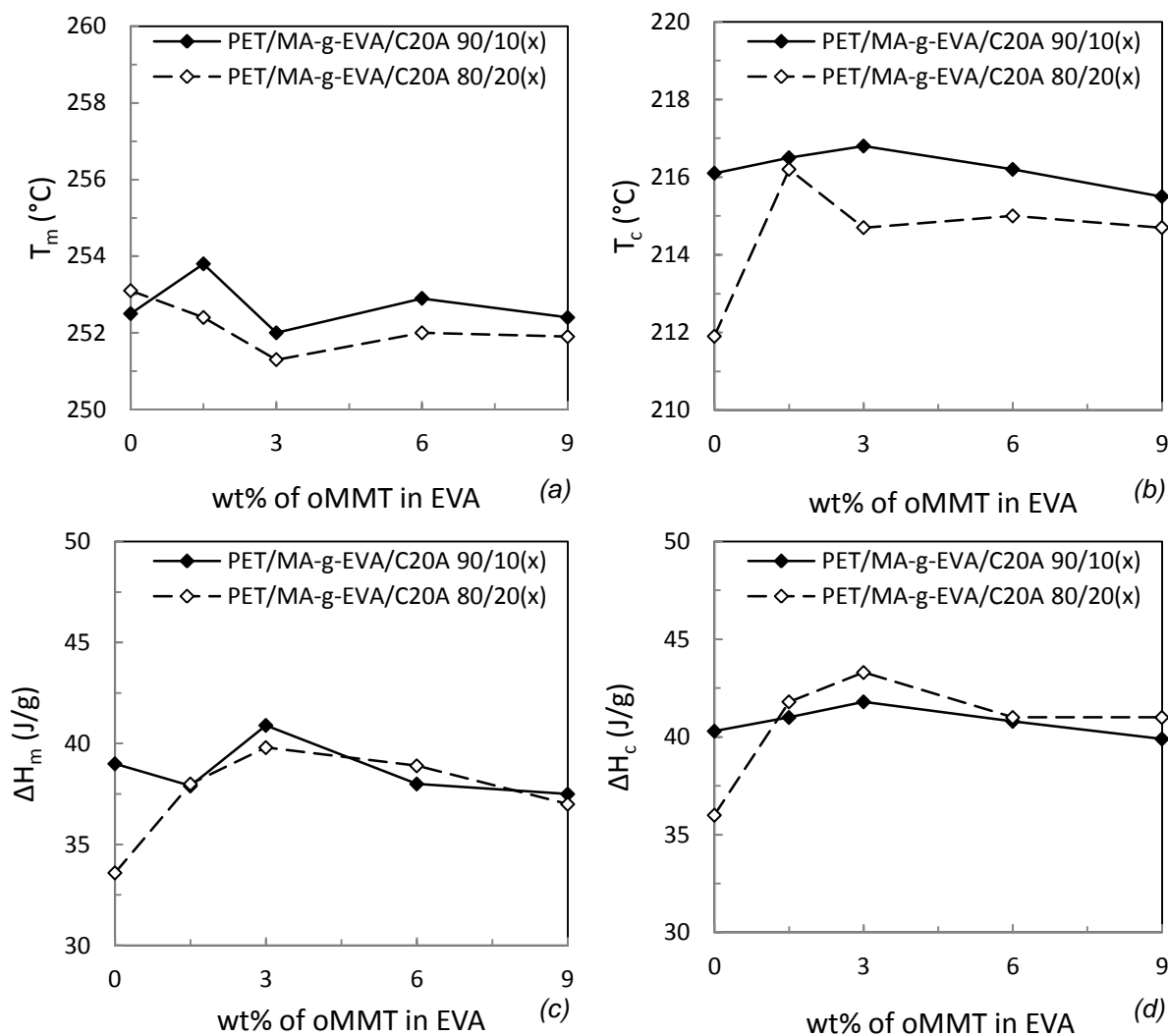


Figure 10.13 DSC parameters of PET/MA-g-EVA/C20 nanocomposites: melting and crystallization temperatures, T_m (a) and T_c (b), melting and crystallization enthalpies, ΔH_m (c) and ΔH_c (d).

10.5.4 TEM

In Figure 10.14 the TEM micrograph shows the dispersion of 3 wt% of MMT into crosslinked EVA. A large extent of exfoliation and some thin stacks of silicate layers mean a good chemical affinity between EVA and non-polar surfactants of C20A. In a previous study on EVA/OMLS nanocomposites both exfoliated and intercalated platelets have been observed. Since the mixing of PET with EVA forms an immiscible blend a biphasic blend is expected. The main factors that affect the morphology of a immiscible blend, and so the continuity of the phases, are the composition and the difference in viscosity between the two components

[41]. In a nanocomposite blend the polarities of the two polymers and of the surfactants has to be taken into account as well.

The TEM micrograph of PET/MA-g-EVA/C20A 80/20(3) nanocomposite shows the two-phase morphology with MA-g-EVA domains dispersed in the PET, as expected (Figure 10.15a). The clay is mostly dispersed in the interphase and only partially in the domains bulk. Moreover the clay is not anymore exfoliated into the EVA phase and exists in the form of exfoliated/intercalated lamellae, tactoid structures and aggregates (Figure 10.15b), despite the homogeneous and good dispersion seen in the binary nanocomposites.

Comparing with the PET/MA-g-EVA/C20A 80/20(6), which exhibits a much lower elongation at break, the preferential localization of clay at the interphase is observed as well (Figure 10.16).

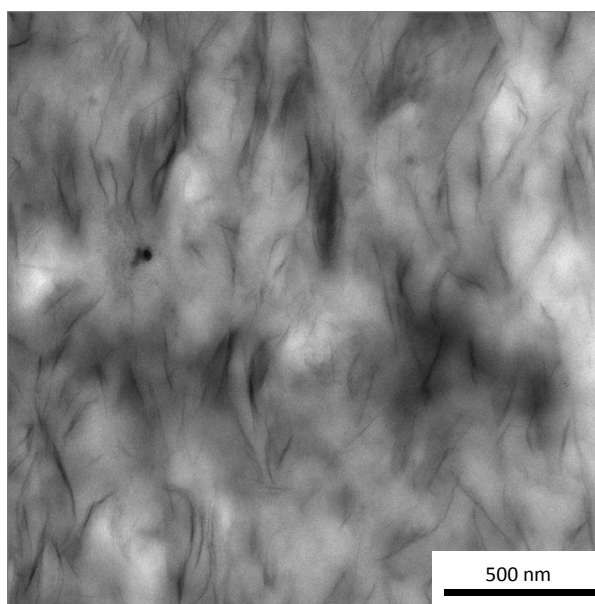


Figure 10.14 TEM micrograph of MA-g-EVA/C20A 3 wt% nanocomposite shows both exfoliated and intercalated platelets.

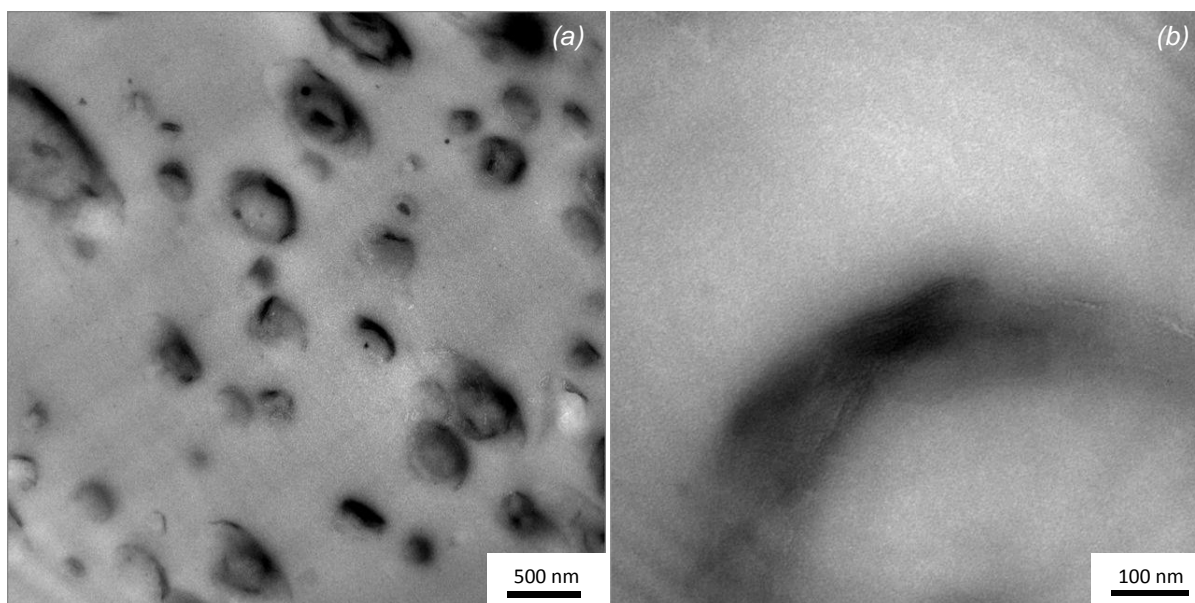


Figure 10.15 TEM micrographs of PET/(MA-g-EVA/C20A) 80/20(3) to show dispersed MA-g-EVA/C20A domains (a) and a higher magnification (b).

The reason of different mechanical properties is probably the coarser size of rubber domains and the reduction of interparticle distance. It is noticeable comparing the two different morphologies in Figure 10.17. The interparticle distance play a key role to affect the mechanical properties of the impact modified polymers [31]. In both the 90/10 and 80/20 nanocomposites it can be supposed the variation of particle size and interparticle distance as the reason of drop of tensile strain at failure.

As is well known, the platelets can take place in the interphase acting as a interfacial compatibilizer when the two polymers have a lower mutual affinity [17]. When the clay take place in the interphase reducing the interfacial tension, a progressive reduction of the domains size occurs by to the increase of its content. Moreover the compatibilization of MA in the 80/20 blend, supported by the comparison of the mechanical properties and crystallization enthalpies, leads a good interphase such that it doesn't need the clay compatibilizing activity. On the basis of these observations, concerning our case, can be excluded that this thermodynamic mechanism is involved.

Similarly, also the refinement of the dispersed domains due to an increase of viscosity should be more effective by increasing the clay content. Thus this mechanism could be excluded as well.

A similar morphology has been observed in MA compatibilized and un-compatibilized PP/PET/clay nanocomposites [42]. It has been observed that the clay is more compatible with PET, due to its polarity, and it has been proposed it segregates in areas where the PET and MA-g-PP are located, thus in the interphase. No refinement of dispersed domains occurred by addition of clay in both the compatibilized and un-compatibilized nanocomposites compared with the respective blends.

The presence of some big stacks of clay can be explained supposing that the partial degradation of the alkyl-ammonium surfactants, due to its poor thermal stability at the PET processing temperature [36], promotes the re-aggregation since the silicate layers are not longer compatibilized and the galleries collapse. The reduction of the d-spacing due to organic modifier degradation has been observed by Delozier et al [43]. For this reason part of the platelets migrates at the interphase being no so much compatibly with the EVA as seen in the binary MA-g-EVA/C20A nanocomposites.

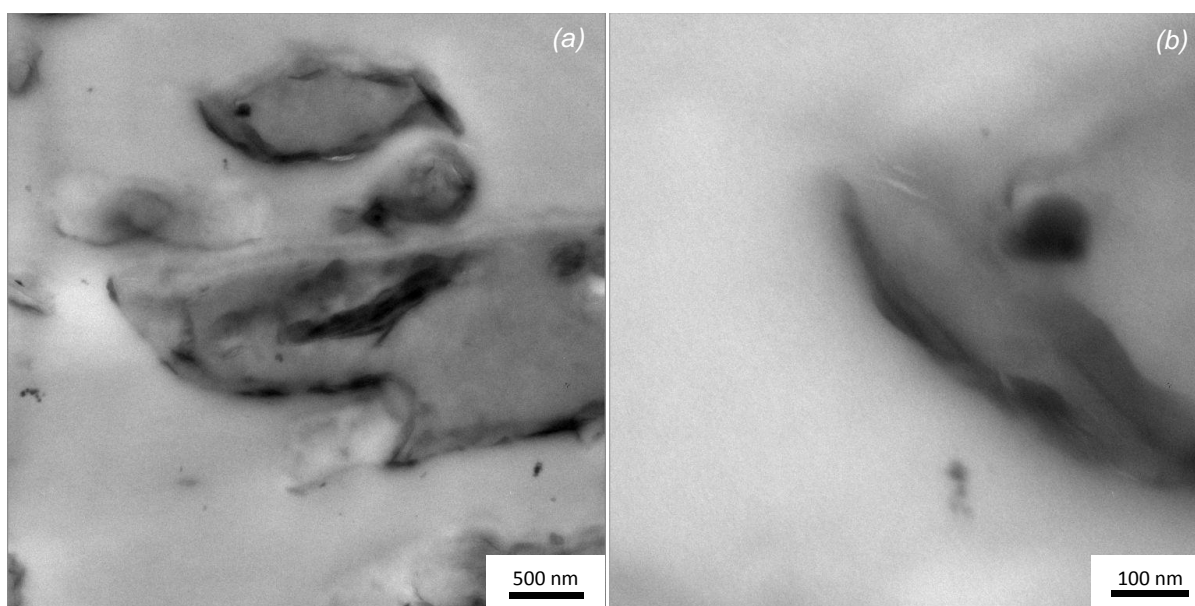


Figure 10.16 TEM micrograph of PET/(MA-g-EVA/C20A) 80/20(6) to show dispersed MA-g-EVA/C20A domains (a) and a higher magnification (b).

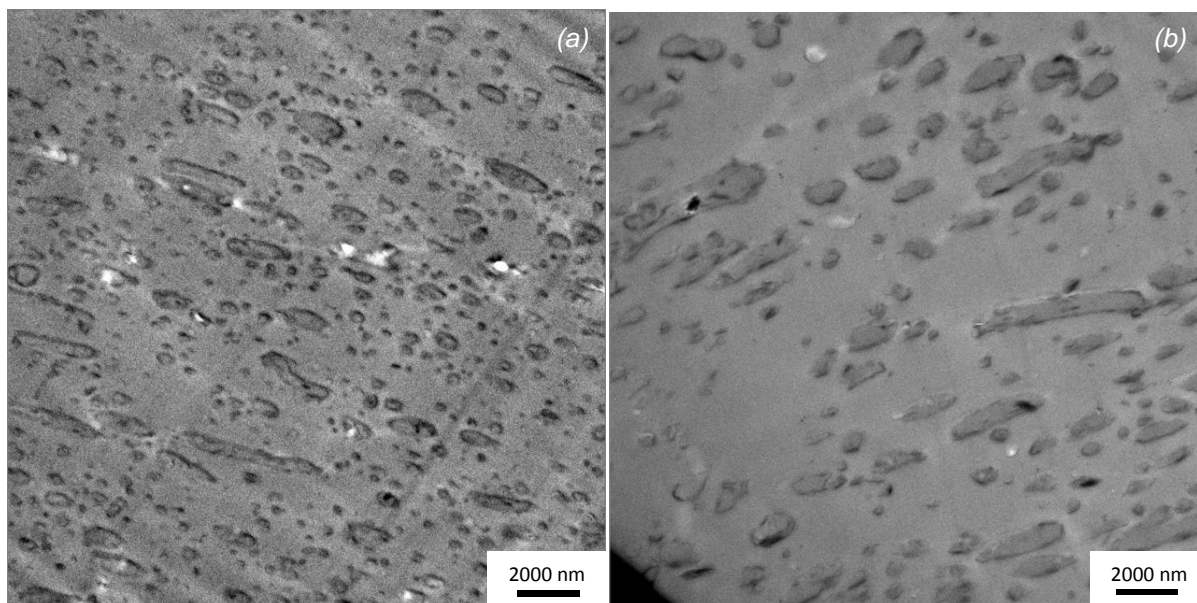


Figure 10.17 TEM micrographs to compare the different size of rubber domains of PET/MA-g-EVA/C20A 80/20(3) (a) and PET/MA-g-EVA/C20A 80/20(6) nanocomposites (b).

10.5.5 XRD

In Figure 10.18 the XRD spectra of the materials previously seen in the TEM paragraph are shown. Comparing the nanocomposite spectra with the C20S one, the shift of the diffraction peaks at a lower angle means an intercalation degree of dispersion of the clay in the matrix that leads an increase of the d -distance between the lamellae. As previously seen the MA-g-EVA/C20A 3 wt% nanocomposite has both intercalated and exfoliated structure, but only the first can be observed by XRD analysis. A similar reduction of the interlayer distance in the ternary nanocomposites with compared to the MA-g-EVA/C20A 3 wt% confirms the hypothesis about re-aggregation of the lamellae.

In Table 10.2 the values of 2θ and the interlayer distance d relative to the first order diffraction peak are listed. When the clay is dispersed in the discontinuous phase having particle size of the same magnitude order of the lamellae a confinement effect of the clay could occur. Since the two ternary nanocomposites exhibit the same interlayer distance, despite they have different MA-g-EVA particle size, also the hypothesis of a partial thermal degradation of the surfactants is plausible as previously mentioned. It is well known that alkyl surfactants have a poor thermal stability if compared to other classes of surfactants, that are more suitable to be dispersed in PET [44]. The thermal degradation of alkyl quaternary

ammonium surfactants begins between 220-250°C, below the processing temperature of PET [45]. These two mechanism that lead a decrease of the interlayer distance have been in other nanocomposite blends [46].

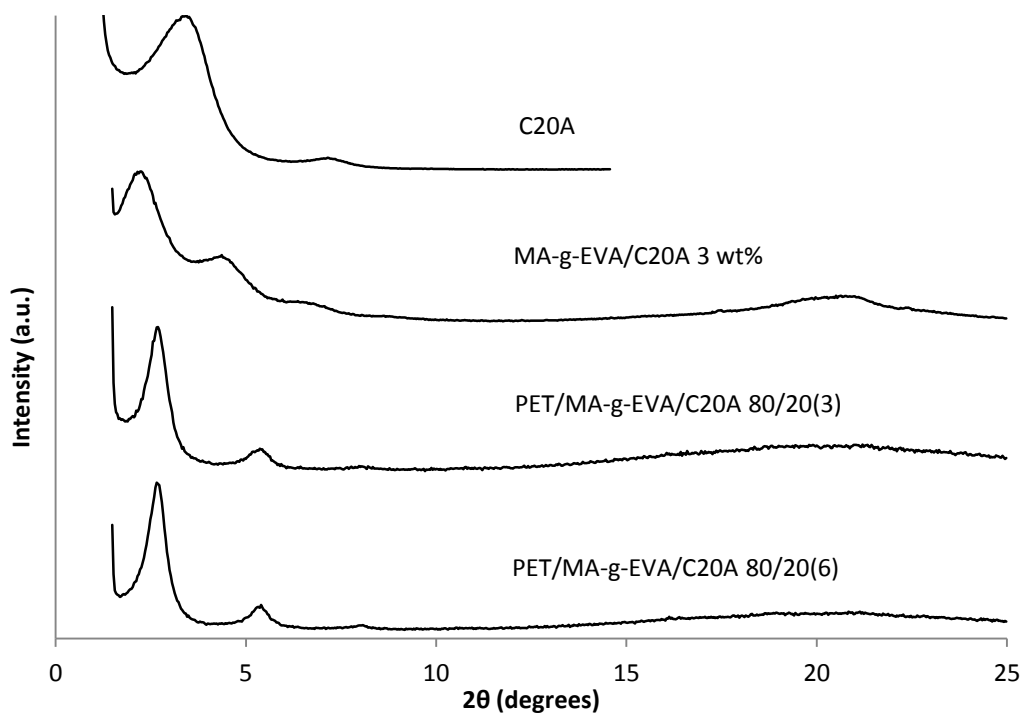


Figure 10.18 XRD spectra of C20A, MA-g-EVA/C20A 3 wt%, PET/MA-g-EVA/C20A 80/20(3) and 80/20(6).

Sample	2θ (degrees)	d_{001} (Å)
C20A	3.40	26.2
MA-g-EVA/C20A 3 wt%	2.20	41.0
PET/MA-g-EVA/C20A 80/20(3)	2.67	33.6
PET/MA-g-EVA/C20A 80/20(6)	2.67	33.6

Table 10.2 Positions of the first order diffraction peak on 2θ axis of XRD spectra and respective interlayer distance d_{001} .

10.6 Conclusion

PET/MA-g-EVA/clay ternary nanocomposites with different MA-g-EVA and clay contents have been produced by melt blending. In order to get balanced mechanical properties, a preferential location of clay has been induced within rubber domains through an appropriate mixing sequence. To distinguish the single effect of the compositional variables on the properties, compatibilized and un-compatibilized PET/MA-g-EVA and PET/EVA blends, MA-g-EVA/clay binary nanocomposites are been produced as well. The materials have been subjected to mechanical, thermal and morphologic analysis.

Through tensile tests and TGA analysis, a higher improvement of the Young modulus and thermal stability in MA-g-EVA/clay nanocomposites than the MA-g-EVA, have been observed. A percolation threshold should be between 3 and 6 wt% of MMT content. The TEM micrographs confirm a homogeneous exfoliation and intercalation of 3 wt% of MMT into the matrix, as expected.

The compatibilization with MA doesn't lead significant improvement of mechanical properties in the PET/MA-g-EVA 90/10 blend, unlike in the 80/20 one. Concerning the latter, tensile tests and DSC analysis show an higher strain at break and a lower crystallinity content than the un-compatibilized blend, meaning an improvement of the PET-EVA adhesion due to the reactions between the grafted MA on the EVA chains and the PET.

Only 80/20 nanocomposites exhibit relevant variations of properties compared the blend due to the addition of clay, unlike the 90/10 ones. Mechanical tests revealed an increase of modulus without compromise the elongation at break at low clay contents. The improved stiffness is due to the heterogeneous nucleation activity of filler. DSC results show that the clay promote the nucleation and increases the crystallinity extent. The lower strain at break exhibited at high clay content is due to the bigger size and higher interparticle distance of the dispersed phase. For this reason, concerning the MA-g-EVA domains size, no compatibilizing effect of clay occur, neither by reducing of interfacial tension, nor by increasing the melt viscosity.

TEM micrographs confirm the two-phase morphology with MA-g-EVA domains dispersed in the PET matrix. The platelets are located mostly in the interphase in form of mixed exfoliated/intercalated lamellae and tactoid structures, unlike the homogeneous exfoliation and intercalation seen in the binary MA-g-EVA/C20A nanocomposites. Presence of mixed

structures and the segregation in the interphase could arise by partial degradation of the alkyl ammonium surfactants during high temperature processing.

XRD analysis confirm the reduction of the interlayer distance between the lamellae probably due to the confinement effect due to the small size of the rubber domains and to the partial degradation of the alkyl ammonium surfactants.

References

- [1] S. Donadi, M. Modesti, A. Lorenzetti, S. Besco. *J Appl Polym Sci* 2011, 122, 3290.
- [2] W. Loyens, G. Groeninckx. *Polymer* 2002, 34, 5679.
- [3] T.L. Carte, A. Moet. *J Appl Polym Sci* 1993, 48, 611.
- [4] N. Chapleau, M.A. Huneault. *J Appl Polym Sci* 2003, 90, 2919.
- [5] N.K. Kalfoglou, D.S. Skafidas, J.K. Kallitsis, J.C. Lambert, L. Van der Stappen. *Polymer* 1995, 36, 4453.
- [6] Y. Pietrasanta, J.J. Robin, N. Torres, B. Boutevin. *Macromol Chem Phys* 1999, 200, 142.
- [7] V. Tanrattanakul, A. Hiltner, E. Baer, W.G. Perkins, F.L. Massey, A. Moet. *Polymer* 1997, 38, 2191.
- [8] K.L. Fung, R.K.Y. Li. *Polym Test* 2005, 24, 863.
- [9] A. Ajji, N. Chapleau. *J Mater Sci* 2002, 37, 3893.
- [10] B.B. Khatua, D.J. Lee, H.Y. Kim, J.K. Kim. *Macromolecules* 2004, 37, 2454.
- [11] Q. Zhang, H. Yang, Q. Fu. *Polymer* 2004, 45, 1913.
- [12] Y.J. Li, H. Shimizu. *Polymer* 2004, 45, 7381.
- [13] S. Mehta, F.M. Mirabella, K. Rufener, A. Bafna. *J Appl Polym Sci* 2004, 92, 928.
- [14] H.S. Lee, P.D. Fasulo, W.R. Rodgers, D.R. Paul. *Polymer* 2005, 46, 11673.
- [15] D. Voulgaris, D. Petridis. *Polymer* 2002, 43, 2213.
- [16] M.Y. Gelfer, H.H. Song, L. Liu, B.S. Hsiao, B. Chu, M. Rafailovich, M. Si, V. Zaitsev. *J Polym Sci* 2003, 41, 44.
- [17] S.S. Ray, S. Pouliot, M. Bousmina, L.A. Utracki. *Polymer* 2004, 45, 8403.
- [18] S.S. Ray, M. Bousmina. *Macromol Rapid Commun* 2005, 26, 450.
- [19] Y. Wang, Q. Zhang, Q. Fu. *Macromol Rapid Commun* 2003, 24, 231.
- [20] E. Manias, M.L. Heidecker, J.Y. Chung, J. Mason. *Polym Prepr* 2007, 138, 1054828.
- [21] C.G. Martins, N.M. Laroocca, D.R. Paul, L.A. Pessan. *Polymer* 2009, 50, 1743.

- [22] A. Dasari, Z.Z. Yu, Y.W. Mai. *Polymer* 2005, 46, 5986.
- [23] X.C. Li, H.M. Park, J.O. Lee, C.S. Ha. *Polym Eng Sci* 2002, 42, 2156.
- [24] Y.M. Wang, J.P. Gao, Y.Q. Ma, U.S. Agarwal. *Compos* 2006, 37, 399.
- [25] B.G. Soares, R.S.C. Colombaretti. *J Appl Polym Sci* 1999, 72, 1799.
- [26] S.J. Kim, B.S. Shin, J.L. Hong, W.J. Cho, C.S. Ha. *Polymer* 2001, 42, 4073.
- [27] P. Bier, D. Rempel. *SPE ANTEC Technic Papers* 1988, 34, 1485.
- [28] X. Li, C.S. Ha. *J Appl Polym Sci* 2003, 87, 1901.
- [29] M. Pramanik, S.K. Srivastava, B.K. Samantaray, A.K. Bhowmick. *J Polym Sci* 2002, 40, 2065.
- [30] A.Y. Coran, R. Patel. *J Appl Polym Sci* 1976, 20, 3005.
- [31] S.H. Wu. *Polymer* 1985, 26, 1855.
- [32] A. Riva, M. Zanetti, M. Braglia, G. Camino, L. Falqui. *Polym Degrad Stab.* 2002, 77, 299.
- [33] A. Vannier, S. Duquesne, S. Bourbigot, A. Castrovinci, G. Camino, R. Delobel. *Polym Degrad Stab* 2008, 93, 818.
- [34] S. Peeterbroeck, M. Alexandre, R. Jerome, P. Dubois. *Polym Degrad Stab* 2005, 90, 288.
- [35] J.W. Gilman, C.L. Jackson, A.B. Morgan, R. Harris, E. Manias, E.P. Giannelis, M. Wuthenow, D. Hilton, S.H. Philips. *Chem Mater* 2000, 12, 1866.
- [36] W. Xie, Z. Gao, W. Pan, D. Hunter, A. Singh, R. Vaia. *Chem Mater* 2001, 13, 2979.
- [37] K. Stoeffler, P.G. Lafleur, J. Denault. *Polym Degrad Stab* 2008, 93, 1332.
- [38] W. Loyens, G. Groeninckx. *Macromol Chem Phys* 2002, 203, 1702.
- [39] A.R. Bhattacharyya, A.K. Ghosh, A. Misra. *Polymer* 2001, 42, 9143.
- [40] C.I.W. Calcagno, C.M. Mariani, S.R. Teixeira, R.S. Mauler. *Polymer* 2007, 48, 966.
- [41] T.K. Kang, Y. Kim, W.K. Lee, H.D. Park, W.J. Cho, C.S. Ha. *J Appl Polym Sci* 1999, 72, 989.
- [42] C.I.W. Calcagno, C.M. Mariani, S.R. Teixeira, R.S. Mauler. *Compos Sci Technol* 2008, 68, 2193.
- [43] D.M. Delozier, R.A. Orwoll, J.F. Cahoon, N.J. Johnston, J.G. Smith, J.W. Connell. *Polymer* 2002, 43, 813.
- [44] M.C. Costache, M.J. Heidecker, E. Manias, C.A. Wilkie. *Polym Advan Technol* 2006, 17, 764.
- [45] W. Xie, Z. Gao, W.P. Pan, D. Hunter, A. Singh, R. Vaia. *Chem Mater* 2001, 13, 2979.

[46] S. Besco, A. Lorenzetti, M. Roso, M. Modesti. Polym Advan Technol 2011, 22, DOI: 10.1002/pat.1641.

Chapter 11

PMMA/oMMT and PC/oMMT nanocomposites: effects of processing parameters

11.1 Introduction

Unlike PET, the lack of processing experience of poly(methyl methacrylate) (PMMA) and polycarbonate (PC) based nanocomposites induced a quick investigation on the influence of the processing parameters on the nanocomposites properties. In particular the purpose of this activity is to find a general processing setting, one for each matrix, to achieve a good particles dispersion avoiding thermal degradation.

The thermodynamic approach to the intercalation of a molten polymer inside a modified layered silicate has been approached through a lattice-based mean field theory by Vaia and Giannelis [1]. They found that the polymer intercalation is determined by an interplay of entropic and enthalpic factors. On the other hand melt processing conditions play a key role in achieving high levels of exfoliation. Indeed, nanocomposites have been formed using a variety of mixing devices. It has been proved that the twin screw extruders is the most effective to disperse the silicate layers [2], especially the co-rotating systems rather than the counter-rotating ones [3]. The optimum processing conditions, considering a fixed matrix-filler system and mixing device, arise by the shear intensity and chains mobility. It has been proposed by Dennis et al. a possible clay delamination paths that involves two phases [4]. The first requires shear intensity to slide the platelets apart to reduce the height of the stacks, the second requires diffusion of polymeric chains into the silicate galleries, thus promoted by residence time, mixing temperature and mixing device. The effects of temperature, shear and

residence time have been described by Modesti et al. [5]. High temperature may help to increase the mobility of the polymer chains but, at the same time, it will reduce the viscosity and thus the mechanical force applied to the nanofillers. Concerning the temperature, the reported results have been relatively contradictory, because this parameter cannot be considered independently of the screw speed and feed rate [6–8]. It is generally admitted that an increase in screw speed leads to a better dispersion [9–14], because a higher shear rate will increase the agglomerates breakup while intercalation. In contrast, long residence times may improve mixing but may also promote thermal degradation. Also high temperature may cause degradation of the organoclay surfactants [15]. Since both PMMA and PC require temperatures above 200°C to be processed, thermal degradation phenomena have to be taken into account. It is well known that the cations of the clays undergo Hofmann degradation in this temperature range [16,17]. It leads to the complete loss of the cation and its replacement with a proton as the counter ion of the clay.

In this activity both filled and unfilled PMMA and PC have been produced using four different processing settings. Melt flow index (MFI) measurements and flexural tests have been done in order to quickly investigate the response of the nanocomposites to the processing parameters. The measurement of MFI is a simple yet very useful way to estimate the chain mobility of polymer materials. By rheological measurements on unfilled polymers it is possible to verify the occurring of thermal degradation phenomena. Moreover the melt viscosity is affected by the dispersion of the oMMT platelets [18]. It has been shown that the typical rheological response in nanocomposites arises from frictional interactions between the silicate layers and not due to the immobilization of confined polymer chains between the silicate layers [19]. Once the percolation threshold has been achieved, the orientation of polymer chains would be retarded since they are confined in narrow spacing between clay particles, resulting in the decrease of melt fluidity. At lower concentration of clay the MFI may be even higher than the neat polymer [20,21].

Flexural test gives a measure of the reinforcing action, indicative about the dispersion of the oMMT. It has been preferred rather than tensile test because it requires rectangular bars that can be molded by compression in a very short time, while the dog-bones specimens would be preferred they are produced by injection molding to have reproducible results. XRD and TEM analysis have not been done, although they give more accurate information about the

dispersion degree of oMMT, because their cost, the time required and they don't give information about an eventual reduction of the matrix molecular weight.

11.2 Raw materials

The poly(methyl methacrylate) (PMMA) provided by Lucite was the Diakon CMG302, the polycarbonate (PC) provided by Dow was Calibre 303-10. As representative kind of filler, the Dellite 72T has been chosen for this activity (Figure 5.1b). It is one of the commonest nanosize clay commercially available and it doesn't add further complexity to the study because its simple chemical structure.

11.3 Preparation of samples

PMMA, PC and D72T were previously dried at 100°C for 3 hours, 120°C for 15 hours, 80°C overnight respectively. PMMA/D72T and PC/D72T nanocomposites filled at 3 wt % were prepared mixing by melt compounding using a co-rotating, intermeshing twin screw extruder (Collin Teach-line zk25t). The fixed filler content it is enough to detect differences in the rheological and mechanical behavior. Four different couple of temperature profiles and screw rate have been used (Table 11.).

Unfilled samples	Filled samples (3wt% of D72T)	Setting	Extruder temperature profile from hopper to die (°C)	Screw rate (rpm)
Neat PMMA	-	-	-	-
PMMA1	PMMA/D72T1	#1	160-220-230-240-240	100
PMMA2	PMMA/D72T2*	#2	160-230-240-260-260	100
PMMA3	PMMA/D72T3	#3	160-190-210-230-220	100
-	PMMA/D72T4	#4	160-220-230-240-240	60
Neat PC	-	-	-	-
PC1	PC/D72T1	#1	210-240-260-270-270	100
PC2	PC/D72T2	#2	210-250-270-290-290	100
PC3	PC/D72T3	#3	210-220-240-260-250	100
-	PC/D72T4	#4	210-240-260-270-270	60

* = It wasn't possible to extrude this sample due to the too low viscosity.

Table 11.1 Produced samples and processing parameters used for them.

The first temperature profile (#1) has been widely used in the literature, the second one (#2) involves high temperatures to lead a higher chains mobility, the third one (#3) involves low temperatures to lead higher shear forces. The last setting (#4) involves the first temperature profile and a lower screw rate to reduce the shear forces and to increase the residence time. The extruded PMMA and PC based materials were dried at 100°C for 3 hours, 120°C for 15 hours respectively. The specimens for the flexural tests were produced by compression molding. The produced samples are listed in Table 11.1. Both unfilled and D72T filled polymers have been extruded and compared to the neat polymers. The unfilled polymers have been extruded using only the first three settings to evaluate the eventual thermal degradation, the fourth setting gives a different residence time and shear forces that it is supposed don't affect too much the properties of the unfilled polymers.

11.4 Characterization

MFI

The melt flow index of the PMMA and PC based materials has been measured according to the ASTM D1238 (230°C, 3800 g and 300°C, 1200 g respectively). Due to the strong thermal degradation at 300°C occurred in the PC/D72T nanocomposites the test parameters used have been set at 260°C and 3800 g.

Flexural test

Rectangular bars (80x12.6x3.2 mm) produced by injection molding have been subjected to the flexural test in order to measure the flexural modulus (1.3 mm/min test rate, 50 mm support span, according to ASTM D790).

11.5 Results

11.5.1 MFI

The normalized MFI values compared to the neat polymers are showed in Figure 11.1. The PMMA2 exhibits a different rheological properties compared with the neat PMMA, while PMMA1 and PMMA3 preserve the same viscosity. It means that the setting #2 involves too

high temperatures that degrades the polymers chain leading in a decrease of viscosity. PMMA/D72T1 and PMMA/D72T3 nanocomposites exhibit a slight lower MFI than neat PMMA, while the MFI of PMMA/D72T4 nanocomposite is higher probably due to the higher residence time that degrades the polymer.

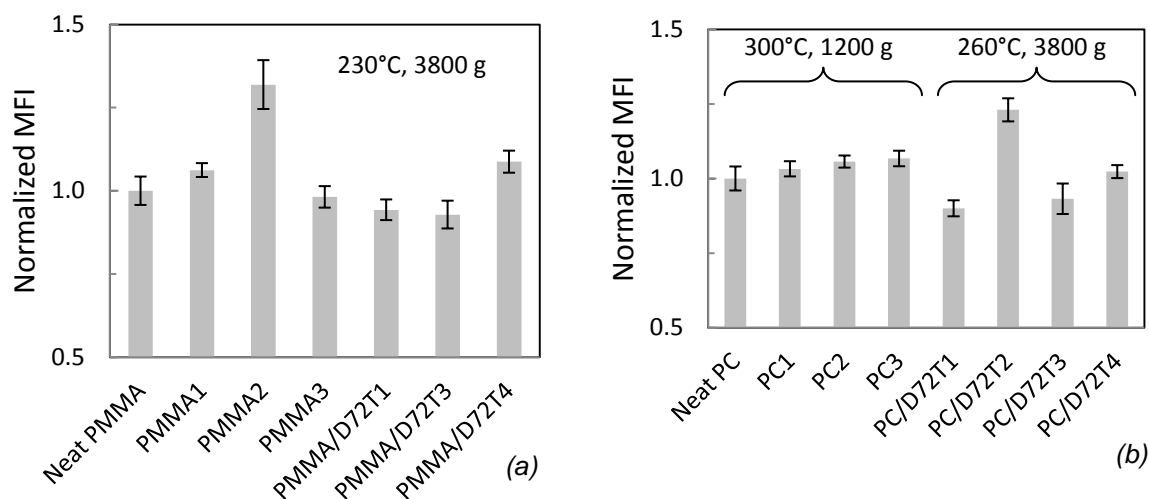


Figure 11.1 Normalized melt flow index of PMMA (a) and PC (b) based materials.

The difference between the MFI of unfilled and filled PC is due to the different test conditions, thus it is not right to compare the MFI of unfilled and filled PC. The viscosity of the extruded PC is slightly lower than neat PC, independently by the processing temperature. PC/D72T2 and PC/D72T4 nanocomposites exhibit the highest MFI than the other nanocomposites, probably because the surfactants partially degrade during the extrusion, while PC/D72T1 and PC/D72T3 nanocomposites have a lower melt viscosity.

11.5.2 Flexural test

The normalized flexural modulus values compared to the neat polymers, are showed in Figure 11.2. There are not strong differences between the three unfilled PMMA. Generally the nanocomposites have a higher modulus as expected, but the PMMA/D27T4 nanocomposite one is comparable to the one of neat PMMA. The extrusion of PC leads a lower modulus than the one of the neat PC, independently by the profile temperature used. PC/D72T1 and PC/D72T4 nanocomposites have higher module than neat PC, unlike the PC/D72T2 and PC/D72T3 ones.

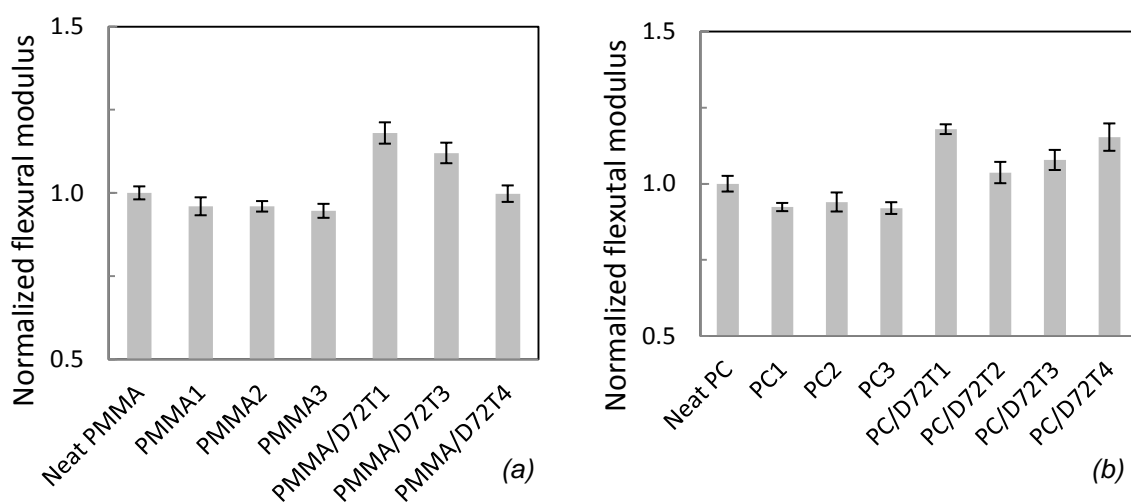


Figure 11.2 Normalized flexural modulus of PMMA (a) and PC (b) based materials.

11.6 Discussion

Figure 11.3 provides an global view about the two previously described properties. As observed in Figure 11.3b, the setting #2 involves temperature too high for PMMA. PMMA2 exhibits high MFI, PMMA/D72T2 nanocomposite has not been extruded. The first of three thermal degradation step of PMMA begins at around 200°C, due to the degradation of weak links in the polymer chain [22]. It has been hypothesized, after XPS measurements, between 200 and 300°C, the degradation of polymer chains terminated with unsaturated groups occurs [23]. The presence of D72T further aggravates the process. The setting #4 results in nanocomposites with low modulus probably due to weak shear forces that leads a poor intercalation degree.

The extruded PC show lower moduli and higher MFI than neat PC (Figure 11.3a), despite the differences are not very high. This polymer is generally sensitive to a variety of chemical processes caused by thermal and oxidative degradation mechanisms at elevated temperatures during melt processing [24–28]. The temperature affects the MFI in the nanocomposites, in PC/D72T2 the degradation is aggravated by the presence of D72T. In addition, it has been seen that a variety of metal ions exist in natural clays, and the degradation products of these constituents may cause various reactions and color formation processes in PC [29,30].

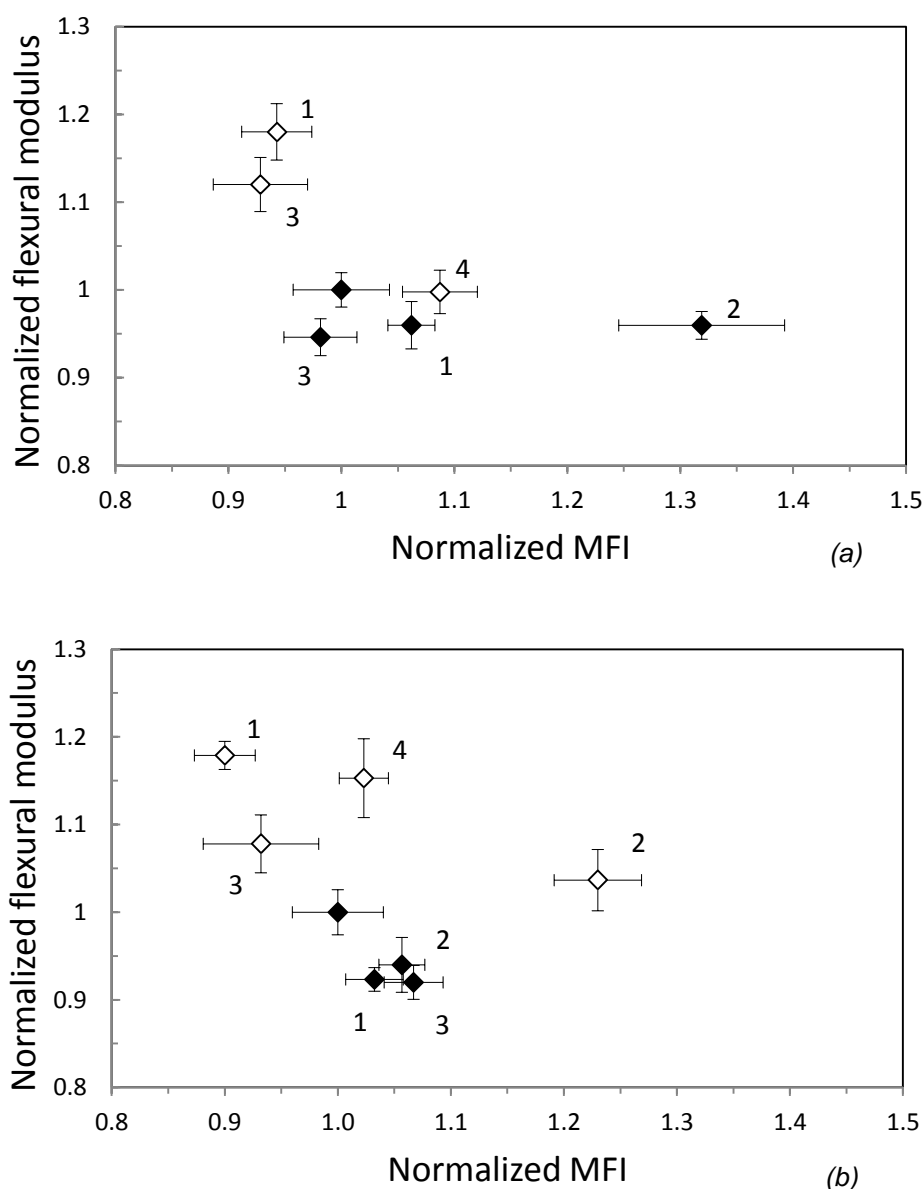


Figure 11.3 Normalized flexural modulus versus normalized melt flow index of unfilled PMMA and PMMA/D72T nanocomposites (a), unfilled PC and PC/D72 nanocomposites (b).

Molecular weight degradation during melt processing produces phenolic end groups and strongly depends on the level of dispersion of the clay [31]. The highest moduli have been achieved using the #1 and #4 setting, rather than the #3. It is expected that higher shear forces are more effective to disperse the oMMT platelets but it has been observed that higher residence time can lead a better exfoliation as well [4]. The higher MFI of PC/D72T4 than the one of PC/D72T3 suggests a higher degradation due to the higher residence time. Some authors supposed that a molecular weight reduction observed in PC/oMMT nanocomposites

may be the result of greater exposure of PC to the platelet surface that causes chain scission [31].

11.7 Conclusion

Unfilled and oMMT-filled PMMA and PC have been extruded by using different processing settings. Melt flow index and flexural modulus have been measured in order to get fast informations about the dispersion degree of the clay. Both polymers are process sensitive since their melt fluidity increase after to be extruded. In particular the PMMA exhibits a higher sensitivity to the temperature. Longer residence time results in a worsening of the mechanical properties of the PMMA/oMMT nanocomposites, while do not affect those of the PC/oMMT nanocomposites. By extruding at very low temperature, close to the melting point of the polymers, thus exercising high shear stress, the materials do not exhibit the highest modulus, meaning that also a good chain mobility is required to achieve a good dispersion.

References

- [1] R.A. Vaia, E.P. Giannelis. *Macromolecules* 1997, 30, 7990.
- [2] T.D. Fornes, P.J. Yoon, H. Keskkula, D.R. Paul. *Polymer* 2001, 42, 9929.
- [3] A.B. Strong. *Plastics: materials and processing*. P. Prentice Hall, 2000.
- [4] Dennis HR, Hunter DL, Chang D, Kim S, White JL, Cho JW, D.R. Paul. *Polymer* 2001, 42, 9513.
- [5] M. Modesti, S. Besco, A. Lorenzetti. Effect of processing conditions on the morphology and properties of polymer nanocomposites. Chapter 17 in *Optimization of polymer nanocomposite properties*. V. Mittal, John Wiley & Sons (2010).
- [6] J.W. Cho, D.R. Paul. *Polymer* 2001, 42, 1083.
- [7] M. Modesti, A. Lorenzetti, D. Bon, S. Besco. *Polym Degrad Stab* 2006, 91, 672.
- [8] M. Tillekeratne, M. Jollands, F. Cser, S.N. Bhattacharya. *Proceedings of Polymer Processing Society 19th Annual Meeting, Melbourne, 2003, CD ROM*.
- [9] L. Incarnato, P. Scarfato, G.M. Russo, L. Di Maio, P. Iannelli, D. Acierno. *Polymer* 2003, 44, 4625.
- [10] M. Kwak, M. Lee, B.K. Lee. *Proceedings SPE ANTEC, San Francisco, 2002, p. 224*.

- [11] M. Modesti, A. Lorenzetti, D. Bon, S. Besco. *Polymer* 2005, 46, 10237.
- [12] W. Lertwimolnun, B. Vergnes. *Polymer* 2005, 46, 3462.
- [13] W. Lertwimolnun, B. Vergnes. *Polym Eng Sci* 2006, 46, 314.
- [14] P. Peltola, E. Välipakka, J. Vuorinen, S. Syrjälä, K. Hanhi. *Polym Eng Sci* 2006, 46, 995.
- [15] P. Médéric, T. Razafinimaro, T. Aubry. *Polym Eng Sci* 2006, 46, DOI: 10.1002/pen.20587.
- [16] W. Xie, Z. Gao, W.P. Pan, R. Vaia, D. Hunter, A. Singh. *Polym Mater Sci Eng* 2000, 83, 284.
- [17] Zhu J, Morgan AB, Lamelas FJ, Wilkie A. *Chem Mater* 2001, 13, 3774.
- [18] S. Bhattacharya, R.K. Gupta, S. Bhattacharya. The rheology of polymeric nanocomposites. In *Polymer nanocomposites handbook*. R.K. Gupta, E. Kennel, K.J. Kim, CRC Press (2010).
- [19] G. Galgali, C. Ramesh, A. Lele. *Macromolecules* 2001, **34**, 852.
- [20] K. Wang, S. Liang, J. Deng, H. Yang, Q. Zhang, Q. Fu, X. Dong, D. Wang, C.C. Han. *Polymer* 2006, 47, 7131.
- [21] W.S. Chow, Z.A. Mohdlshak, J. Karger-Kocsis. *Macrom Mater Eng* 2005, 290, 122.
- [22] T. Kashiwagi, A. Inaba, J.E. Brown, K. Hatada, T. Kitayama, E. Masuda. *Macromolecules* 1986, 19, 2160.
- [23] J. Du, J. Zhu, C.A. Wilkie, J. Wang. *Polym Degrad Stab* 2002, 77, 377.
- [24] L. Lee. *J Polym Sci Part A: Polym Chem* 1964, 2, 2859.
- [25] C. Bailly, M. Daumerie, R. Legras, J.P. Mercier. *Macromol Chem Phys* 1986, 187, 1197.
- [26] I.C. McNeill, A. Rincon. *Polym Degrad Stab* 1993, 39, 13.
- [27] A. Factor. *Angewan Makrole Chem* 1995, 232, 27.
- [28] C. Pulglisi, L. Sturiale, G. Montaudo. *Macromolecules* 1999, 32, 2194.
- [29] R.E. Grim. *Clay mineralogy*. McGraw-Hill, New York, 1968.
- [30] J.M. Sperry, J.J. Peirce. *Water Environ Res* 1993, 71, 316.
- [31] P.J. Yoon, D.L. Hunter, D.R. Paul. *Polymer* 2003, 44, 5341.

Chapter 12

PMMA and PC based nanocomposites: a screening of different fillers

12.1 Introduction

The important feature of POSS to get completely transparent nanocomposites makes interesting them application in other kinds of transparent matrix. The obtainment of reinforced, transparent, PMMA and PC based nanocomposites makes them useful for applications in optical and mechanical fields.

Several studies have been carried out on PMMA/POSS [1,2] and PC/POSS nanocomposites [3–5]. Kopesky et al. [1,2] found that, depending on the tethered versus untethered/blended nature of the POSS in the PMMA and the corresponding state of POSS dispersion, the POSS acts either as a plasticizer (reducing viscosity and thus suggesting an increase in local free volume of the polymer) or as a traditional filler (increasing viscosity and thus suggesting a stiff and/or frictional interaction between the POSS and polymer molecules). Trisilanol phenyl POSS leads a local plasticization effect reducing the overall deformation resistance of the polymer at low temperatures and high-strain rates [3]. Phenetyl POSS increases both tensile modulus and elongation at break below 5 wt% of filler content, over that value leads an embrittlement of the material [4]. Investigation on several kind of POSS showed as the trisilanol phenyl POSS gives the best properties to the nanocomposites and it was the only one that do not compromise the transparency of PC (up to 5wt%) [5].

In this activity we want to verify the optical clarity of PMMA and PC based nanocomposites filled with the same POSS used previously in PET. It is interesting to qualitatively verify if

there is a correlation between the appearance and mechanical properties of nanocomposites, and the solubility of the filler into the matrixes. In order to have a quick response about the suitability of fillers to get interesting materials they have been produced by melt compounding using a plastograph rather than an extruder, keeping a fixed inorganic load. It allows to use a lesser amount of polymer/fillers and a fast processing, thus minimizing wasted material and time. Due to the small amount of samples the mechanical tests have been carried out by tensile tests and dynamic mechanical analysis (DMA) on films rather than on injection molded specimens. In this activity have been used different kinds of POSS and two different nanosized silica particles to prepare PMMA and PC based nanocomposites.

12.2 Raw materials

The poly(methyl methacrylate) (PMMA) provided by Lucite was the Diakon CMG302, the polycarbonate (PC) provided by Dow was Calibre 303-10. Polyhedral oligomeric silsesquioxanes provided by Hybrid Plastics were the glycidyl POSS (gPOSS), trisilanol isobutyl POSS (tsiPOSS), trisilanol phenyl POSS (tspPOSS), polyethylene glycol POSS (pegPOSS), transcyclohexanediol isobutyl POSS (tcdiPOSS), amic acid isobutyl POSS (aaiPOSS), 1,2 propane diol isobutyl POSS (pPOSS) (Figure 7.1b and Figure 8.1). Fumed silica provided by Degussa were Aerosil R202 (AR202) and Aerosil 200 (A200). The first one is hydrophobic, polydimethylsiloxane (PDMS) modified, the second one is hydrophilic, the average particles size are 14 nm and 12 nm respectively (Figure 12.1).

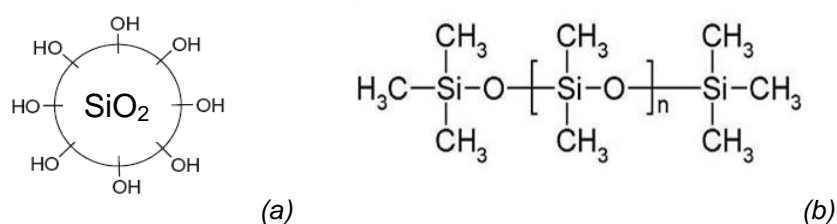


Figure 12.1 Scheme of a hydrophilic silica particle (a) and structure of PDMS (b) used to superficially modify the hydrophobic silica.

12.3 Preparation of samples

PMMA and PC were previously dried at 100°C for 3 hours, 120°C for 15 hours respectively. In the preliminary screening phase PMMA and PC based nanocomposites filled at 3 wt %

with each filler described previously were prepared mixing by melt compounding using a Brabender plastograph. The mixing temperatures used were 200 and 240°C for PMMA and PC based nanocomposites respectively, they have been kept rather low in order to avoid thermal degradation and to have high shear stress during the mixing. The mixing time has been fixed at 5 minutes. The materials have been pelletized and dried at 100°C for 3 hours, 120°C for 15 hours respectively before to be compression molded to get thin films (about 0.1 mm thick). In the second phase PMMA and PC based nanocomposites were prepared mixing by melt compounding using a co-rotating, intermeshing twin screw extruder (Collin Teach-line zk25t). The temperature profile, from hopper to die, was 160-220-230-240-240°C and 210-240-260-270-270°C for PMMA and PC based nanocomposites respectively, the screw rate was 100 rpm. The materials have been dried at 100°C for 3 hours, 120°C for 15 hours respectively before to be injection molded to get tensile dog-bone shaped and flexural bar specimens.

12.4 Characterization

Solubility

The solubility parameters have been calculated through the Hoftyzer-van Krevelen and Hoy methods described in Paragraph 4.2.12. They predict the square of the total solubility parameter as sum of the square of the three contributes (dispersive forces, polar forces, hydrogen bonds). Both the methods have a 10% accuracy thus the average value should be a good compromise.

Mechanical tests

The mechanical properties of all materials were measured by Galdabini (mod. Sun 2500) dynamometer. Rectangular shaped films (90x12.5x0.1 mm) produced by compression molding have been subjected to the tensile test in order to measure the tensile modulus (1.1 mm/min tensile rate).

DMA

Rectangular shaped films (25x6x0.1 mm) produced by compression molding have been subjected to the dynamic mechanical analysis in order to measure the storage modulus versus

temperature (tension mode, 1 Hz frequency, for PMMA: 0-140°C temperature range, 5°C/min heating rate, 15 μm amplitude, for PC: 0-180°C temperature range, 3°C/min heating rate, 17 μm amplitude).

12.5 Results and discussion

12.5.1 Solubility

Similarly to the previous chapter we want to estimate the distance between the solubility parameters of matrixes and fillers. The partial solubility parameters of POSS and PMMA have been calculating by the Hoftzyer-van Krevelen and Hoy methods. Concerning the fumed silica the Hansen solubility parameters (at 25°C) have been used: experimental values for A200 [6] and the PDMS values for AR202 [7]. The contributions of carbonate group to the partial solubility parameters is not assigned by neither Hoftzyer-van Krevelen nor Hoy methods so experimental values have been used for PC [8].

The partial solubility parameters of polymer matrixes, fillers and their average values are reported in Table 12.1, 12.2 and 12.3 respectively. Figure 12.2 shows the bidimensional representation (δ_h - δ_v plot [9]) of the partial solubility parameters of polymer matrixes and fillers. They solubility fields are similar and the fillers can be divided in a soluble and insoluble groups (only AR202 should be soluble in PC and insoluble in PMMA, anyway it is placed close to both the field boundary). Table 12.4 shows the distance R in solubility between polymer matrixes and fillers. R doesn't reflect the distance observable in the plot because is calculated giving a quadruple weight to the dispersive contribute. However, also in this case, R individuates the two soluble/insoluble groups of fillers.

Samples	δ of Hoftzyer-van Krevelen method ($\text{J}^{1/2}/\text{cm}^{3/2}$)				δ of Hoy method ($\text{J}^{1/2}/\text{cm}^{3/2}$)				δ of Hansen method ($\text{J}^{1/2}/\text{cm}^{3/2}$)			
	δ_d	δ_p	δ_h	δ	δ_d	δ_p	δ_h	δ	δ_d	δ_p	δ_h	δ
PMMA	16.5	5.7	9.0	19.7	13.6	9.3	10.3	19.4	-	-	-	-
PC*	-	-	-	-	-	-	-	-	18.3	5.9	6.9	20.4

* = experimental values [8]

Table 12.1 Solubility parameters of polymer matrixes.

Samples	δ of Hoftyzer-van Krevelen method ($J^{1/2}/cm^{3/2}$)				δ of Hoy method ($J^{1/2}/cm^{3/2}$)				δ of Hansen method ($J^{1/2}/cm^{3/2}$)			
	δ_d	δ_p	δ_h	δ	δ_d	δ_p	δ_h	δ	δ_d	δ_p	δ_h	δ
pegPOSS	17.1	10.2	8.7	21.8	16.7	9.9	8.4	21.2	-	-	-	-
tsiPOSS	14.6	2.4	9.9	17.8	16.4	7.8	3.4	18.5	-	-	-	-
tspPOSS	19.8	3.1	10.6	22.6	16.0	10.3	7.0	20.3	-	-	-	-
pPOSS	15.0	1.6	3.2	15.4	16.0	3.0	3.0	16.6	-	-	-	-
tcdiPOSS	14.6	1.5	2.7	14.9	16.0	2.8	2.8	16.5	-	-	-	-
gPOSS	17.1	7.5	7.5	20.1	18.1	8.2	9.4	22.0	-	-	-	-
aaiPOSS	15.2	1.3	1.9	15.3	16.1	3.0	1.5	16.4	-	-	-	-
AR202*	-	-	-	-	-	-	-	-	16.6	1.9	8.0	18.5
A200 [†]	-	-	-	-	-	-	-	-	18.0	10.8	9.0	22.8

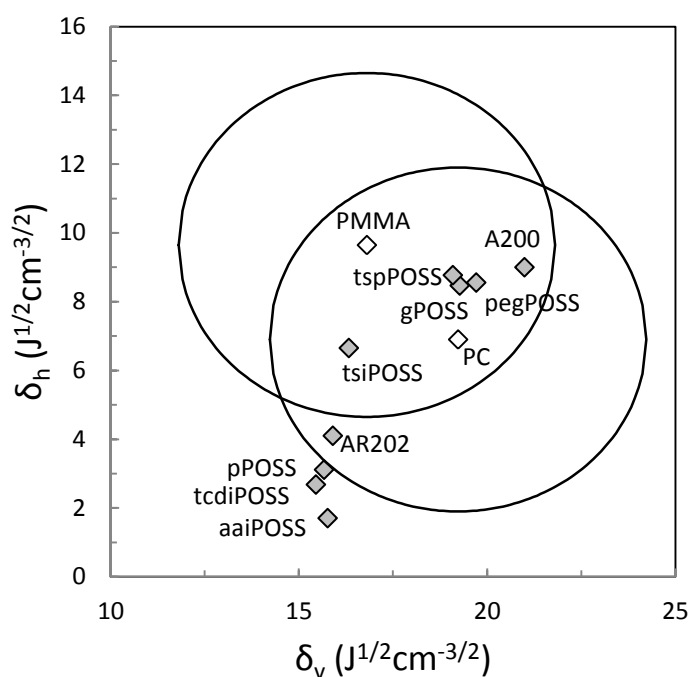
* = from PDMS values [7]

[†] = from experimental values [7]

Table 12.2 Calculated solubility parameters of fillers.

Samples	Average δ ($J^{1/2}/cm^{3/2}$)					Methods
	δ_d	δ_p	δ_h	δ	δ_v	
pegPOSS	16.9	10.1	8.6	21.5	19.7	Hoftyzer-van Krevelen and Hoy
tsiPOSS	15.5	5.1	6.7	18.1	16.3	Hoftyzer-van Krevelen and Hoy
tspPOSS	17.9	6.7	8.8	21.4	19.1	Hoftyzer-van Krevelen and Hoy
pPOSS	15.5	2.3	3.1	16.0	15.7	Hoftyzer-van Krevelen and Hoy
tcdiPOSS	15.3	2.2	2.7	15.7	15.5	Hoftyzer-van Krevelen and Hoy
gPOSS	17.6	7.8	8.5	21.1	19.3	Hoftyzer-van Krevelen and Hoy
aaiPOSS	15.6	2.2	1.7	15.9	15.8	Hoftyzer-van Krevelen and Hoy
AR202	15.9	0.0	4.1	15.5	15.9	Hansen
A200	18.0	10.8	9.0	22.8	21.0	Experimental
PMMA	15.1	7.5	9.7	19.5	16.8	Hoftyzer-van Krevelen and Hoy
PC	18.3	5.9	6.9	20.4	19.2	Experimental

Table 12.3 Average solubility parameters of polymer matrixes and fillers.

Figure 12.2 δ_h - δ_v plot.

Samples	R_{PMMA}	R_{PC}
pegPOSS	4.7	5.3
tsiPOSS	3.9	5.7
tspPOSS	5.7	2.2
pPOSS	8.4	7.7
tcdiPOSS	8.8	8.2
gPOSS	5.2	2.9
aaiPOSS	9.6	8.4
AR202	9.4	8.1
A200	6.8	5.2

Table 12.4 Distance in solubility parameter R between PMMA or PC and fillers.

12.5.2 Tensile test

In Figure 12.3 the tensile modulus of the PMMA and PC based nanocomposites is shown. PMMA based nanocomposites generally exhibit a slight increase of modulus, while only PC/tspPOSS and PC/silica nanocomposites have a modulus similar to the neat polymer, the others exhibit a lower value. The solubility distance R between PC and tspPOSS is the lowest one (2.2), while between PC and silica is higher (5.2 for A200, 8.1 for AR202). Moreover the

tspPOSS has the advantage, compared to the others POSS, to be very thermally stable at the processing temperature (Figure 8.5). The gPOSS leads in the both polymers the worst contribution to the stiffness of material, despite their low R values. This behavior can be attributed to the weak interactions filler-filler of gPOSS since it is in the liquid form at room temperature. It should be dispersed into the nanocomposites in the form of small soft particles. Unlike POSS, silica has a different inorganic structure, more rigid, thus a higher increase of modulus is expected.

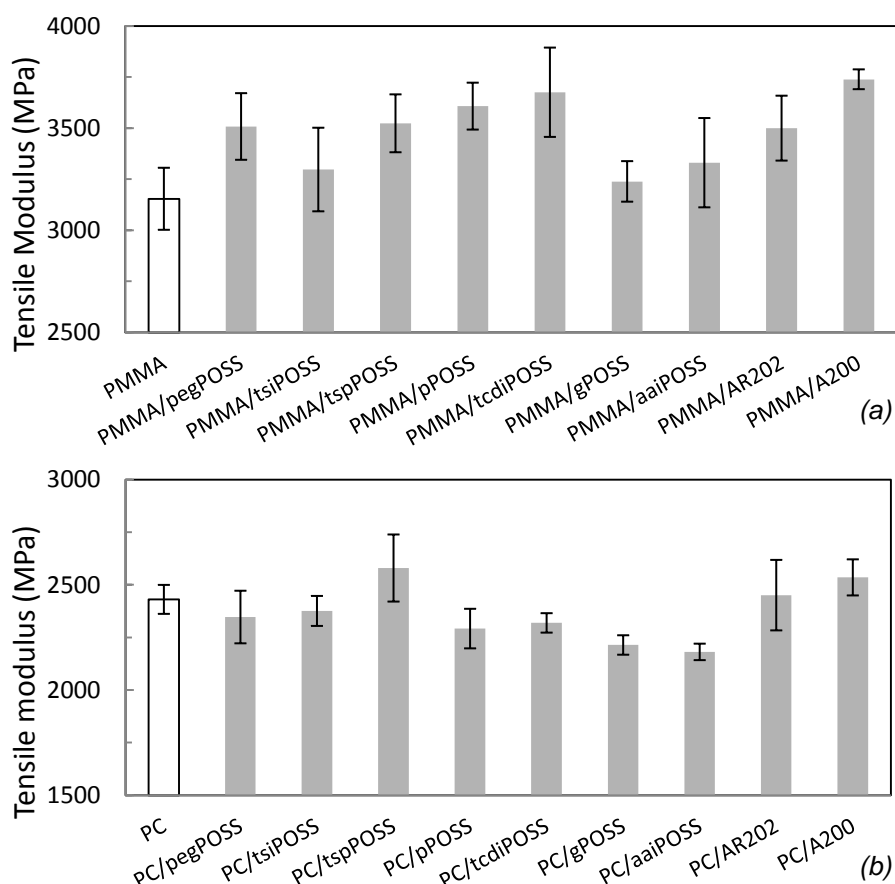


Figure 12.3 Tensile modulus of PMMA (a) and PC (b) based nanocomposites.

12.5.3 DMA

In Figure 12.4 the storage modulus at 25°C of the PMMA and PC based nanocomposites is shown. In the previous paragraph a general enhancement of the tensile modulus has been observed in the PMMA based nanocomposites, while only tspPOSS, AR2002, A200 do not

reduce the stiffness of PC based nanocomposites. Similar consideration can be made concerning the storage modulus.

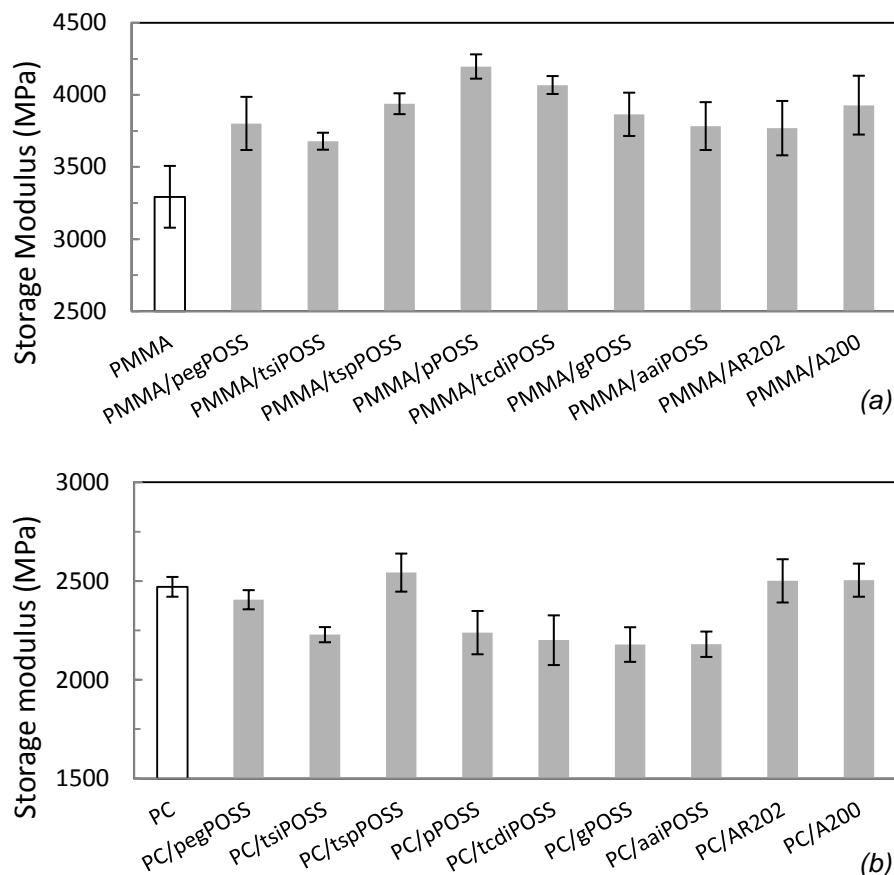


Figure 12.5 Storage modulus of PMMA (a) and PC (b) based nanocomposites.

12.5.4 Optical clarity

Pictures of nanocomposites are shown in Table 12.5. It is interesting to observe that PMMA based nanocomposites are generally more transparent than the PC based ones. It means that the optical properties of PC are more sensitive to the kind of organic functionalization of the fillers. Both tcdiPOSS and aaiPOSS give a light color to PMMA and PC, in particular the PC/aaiPOSS nanocomposites exhibit a brown color. This is not attributed to a thermal degradation of the organic functionalization of fillers because they are thermally stable at the processing temperatures. Moreover the TGA analysis showed that tsiPOSS and pegPOSS are lesser thermally stable in both inert and oxidant atmosphere (Figure 8.4 and 8.5 respectively) but they don't affect the optical clarity of PMMA and just a few the one of PC.

In another study PC/tspPOSS nanocomposites exhibited a transparency similar to that of unfilled PC [5]. They found a slight decrease in transparency was observed as POSS concentrations were increased from 2 to 10 wt%. Has been interesting to observe that the optical transparency of PC was significantly reduced by addition of octaphenyl POSS despite the structural similarities between tspPOSS. According to the authors, the presence of the silanol groups on POSS structures can be postulated to generate particle-polymer interactions (either polar or covalent), which contribute to this enhanced compatibility. The good compatibility between PET and tspPOSS due to the phenyl groups has been seen Chapter 9 thus a good one between PC and tspPOSS was expected since they have a similar polarity [4,12].

Another factor that has to be taken into account is the difference in refractive index between matrix and filler. If the size of dispersed particles is of the same order of magnitude or bigger than the wavelength of the visible light ($\lambda_{VL} = 390\text{-}750$ nm) that is transmitted through the material, then it will be scattered resulting in a opaque material. The refractive index of fillers have been calculated by the method of elemental contribution [13]. It has been proved it is effective to calculate the refractive index of POSS [14] by using the relation:

$$n = \sqrt{\frac{V_m + 2R_m}{V_m - R_m}} \quad (12.1)$$

where n is the volume refractive index, V_m is the molar volume, R_m is the molar refractivity. The values of n are shown in Table 12.6 while PMMA and PC have a refractive index of 1.49 and 1.59 respectively. Except for the tspPOSS all the fillers have a similar value to the one of PMMA thus even the particles are poorly dispersed they should still rather transparent. Concerning the PC, the tspPOSS has the most similar refractive index and the PC/tspPOSS nanocomposite is the only with a good optical clarity, but it is probably due to the fine dispersion of particles. Instead the other PC based nanocomposites exhibit haziness due to the coarse particles size but it is probably affected by the difference in refractive index as well.

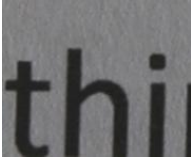
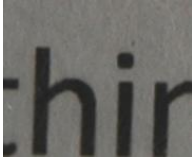
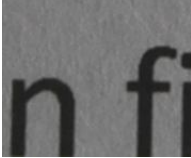
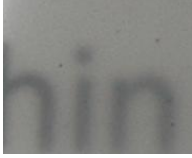
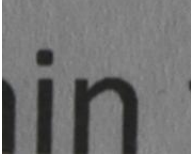

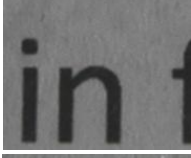

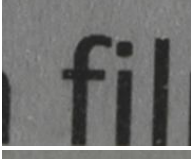
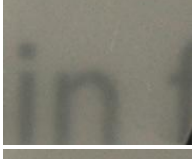
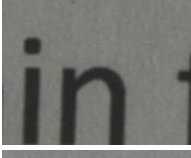

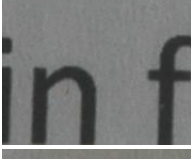
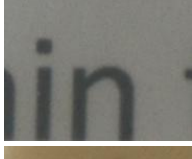
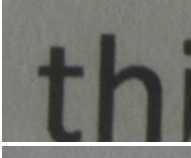

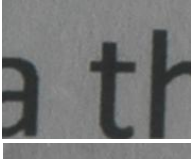
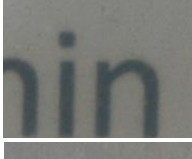
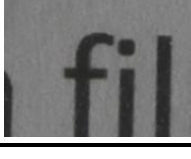
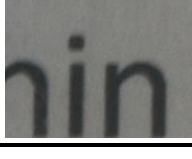
Filler (3 wt%)	PMMA based nanocomposites	PC based nanocomposites
unfilled		
pegPOSS		
tsiPOSS		
tspPOSS		
pPOSS		
tcdiPOSS		
gPOSS		
aaiPOSS		
AR202		
A200		

Table 12.5 Pictures of PMMA and PC based nanocomposites (1 mm thick films).

Filler	n	PMMA based nanocomposites		PC based nanocomposites	
		Transparency	Color	Transparency	Color
pegPOSS	1.46	Good	None	Poor	None
tsiPOSS	1.47	Good	None	Poor	Lght
tspPOSS	1.64	Good	None	Good	None
pPOSS	1.42	Good	None	Poor	None
tcdiPOSS	1.46	Good	Light	Poor	Light
gPOSS	1.48	Good	None	Fair	None
aaiPOSS	1.45	Good	Light	Poor	Brown
AR202	1.45*	Good	None	Fair	None
A200	1.42 [†]	Good	None	Good	None

* = from literature [10]

[†] = from literature [11]

Table 12.6 Qualitative description of optical clarity of PMMA and PC based nanocomposites and refractive index of fillers.

Figure 12.6 offers a qualitative comparison between the optical clarity of the nanocomposites and the solubility of the fillers into the polymer matrix. The correlation is not evident for PMMA based nanocomposites (Figure 12.6a) since they are all almost perfectly transparent. Only the PMMA/tcdiPOSS and PMMA/aaiPOSS nanocomposites appear slightly colored and they related filler take place out from the solubility field of PMMA. The correlation is stronger for PC based nanocomposites (Figure 12.6b). It can be observed that more the difference in solubility is higher and more the related nanocomposites are haze.

A similar comparison has been done concerning the static and dynamic mechanical properties (Figure 12.7). Again, the correlation between optical clarity and tensile moduli of PMMA based nanocomposites is not evident, while is strong for the PC based ones.

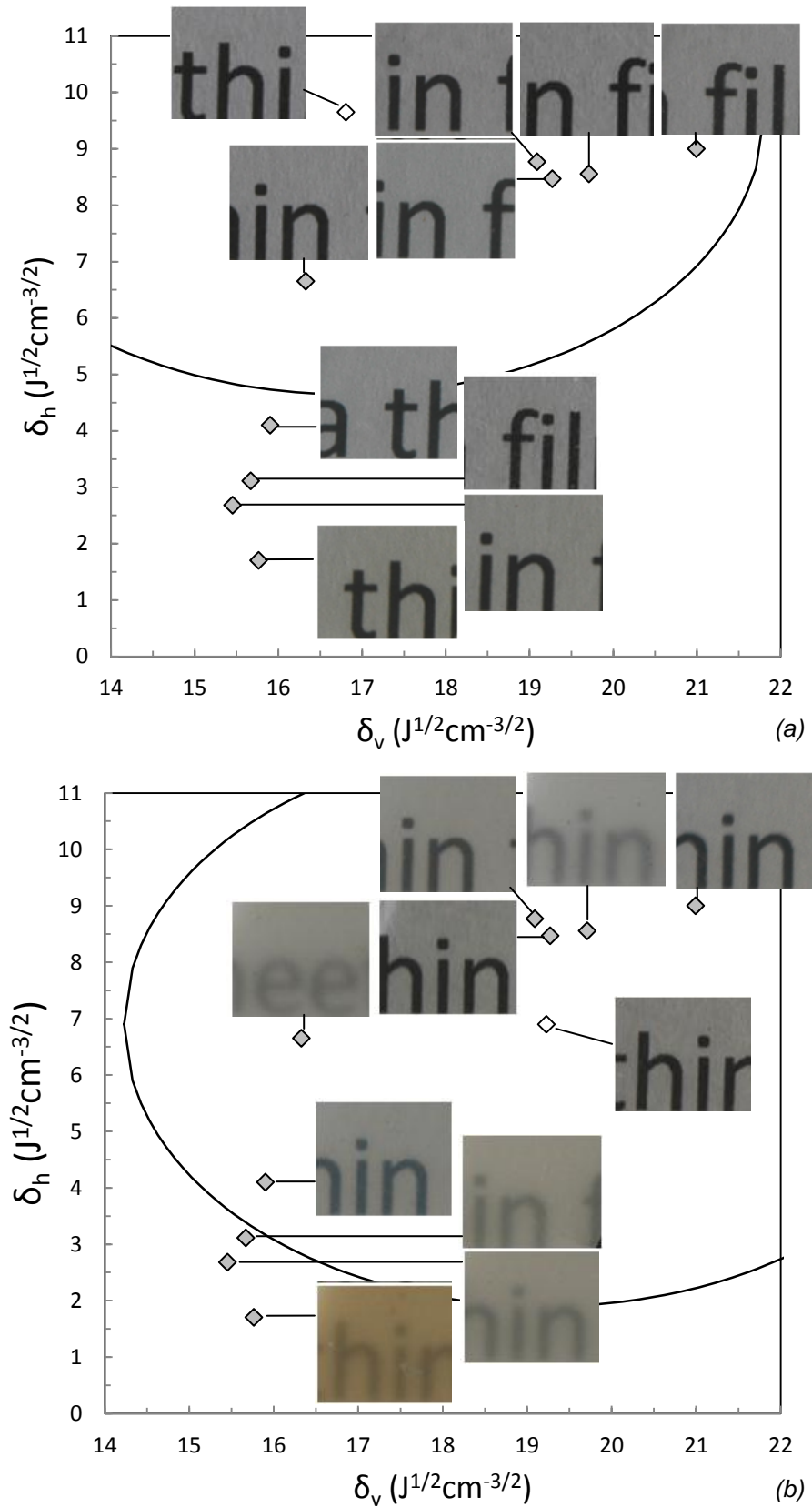


Figure 12.6 Comparison between solubility parameters of fillers and optical quality of the related PMMA (a) and PC (b) based nanocomposites.

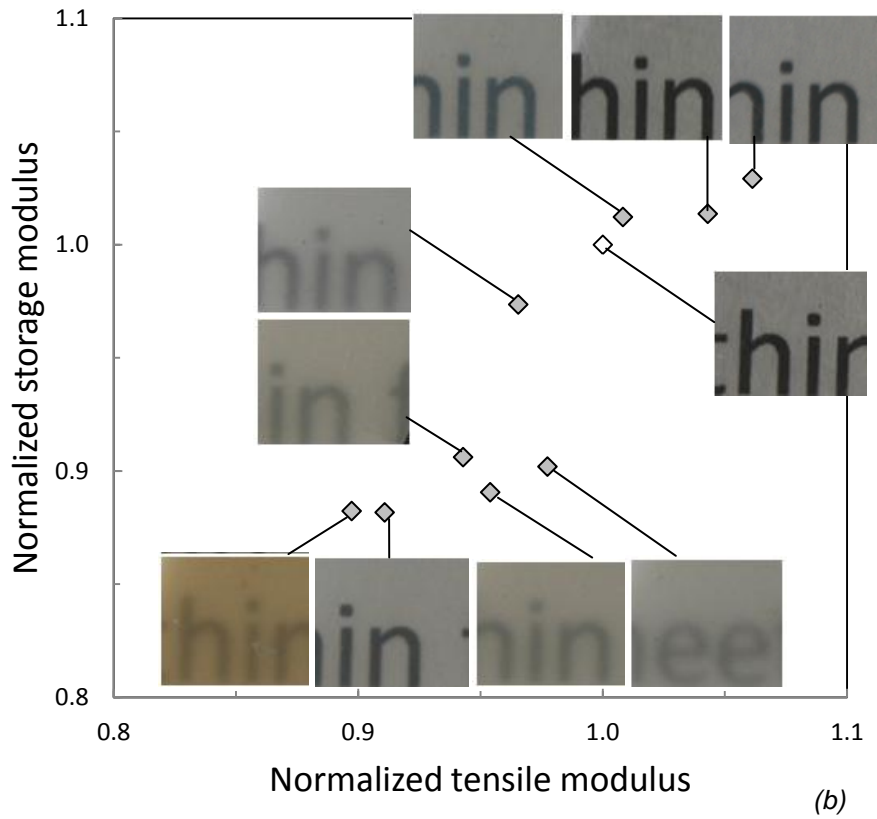
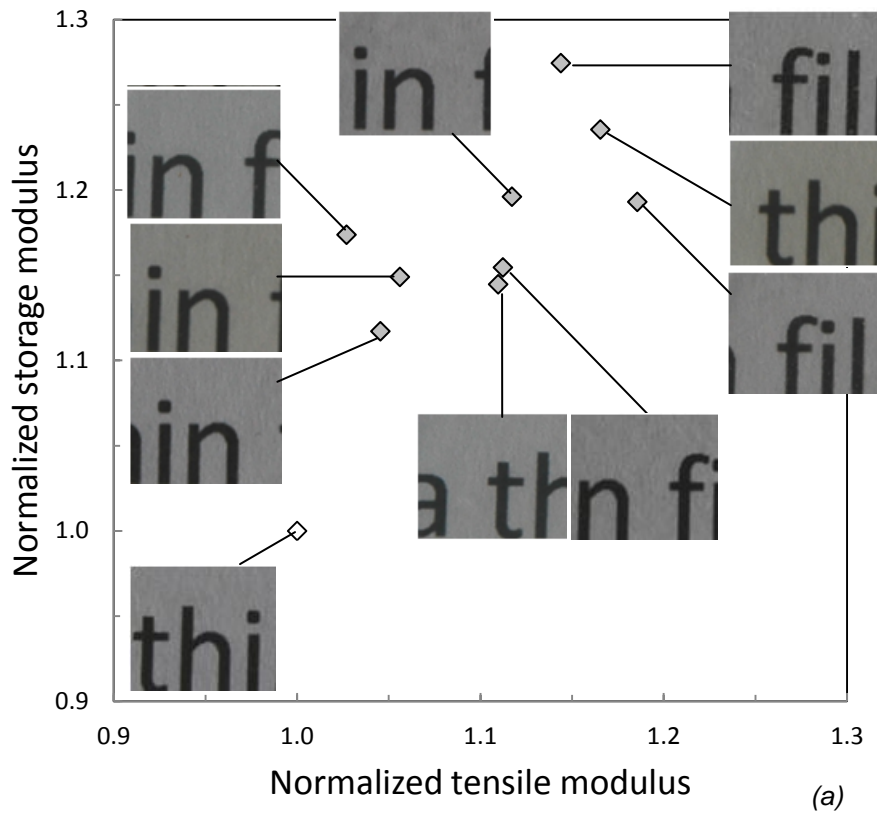


Figure 12.7 Comparison between normalized moduli and optical quality of the PMMA (a) and PC (b) based nanocomposites.

12.6 Conclusion

PMMA and PC based nanocomposites filled with different kind of POSS and nanosize silica have been prepared at 3 wt% of fillers content. Optical clarity, dynamic and static tensile modulus of nanocomposites and fillers solubility have been compared in order to verify the presence of correlation between these aspects.

The two polymers have a similar solubility field but their nanocomposites exhibit very different behavior. Tensile moduli PMMA based nanocomposites generally increase, while the fillers do not affect or reduce those of PC. Concerning the optical clarity PMMA based nanocomposites exhibit a good transparency, while the PC ones are haze or colored. Only the tspPOSS doesn't not affect the good transparency of PC. This behavior is associated to a high difference in refractive index of PC and fillers. If the particles are sufficiently big the refractive index contribution to the scattered light is higher.

A strong correlation of optical clarity with solubility and with tensile moduli has been observed for PC based nanocomposites, in which the differences in appearance are high.

References

- [1] E.T. Kopesky, G.H. McKinley, R.E. Cohen. *Polymer* 2006, 47, 299.
- [2] E.T. Kopesky, T.S. Haddad, G.H. McKinley, R.E. Cohen. *Polymer* 2005, 46, 4743.
- [3] A.D. Mulliken, M.C. Boyce. *J Eng Mater Technol* 2006, 128, 543.
- [4] M. Sánchez-Soto, D.A. Schiraldi, S. Illescas. *Eur Polym J* 2009, 45, 341.
- [5] Y. Zhao, D.A. Schiraldi. *Polymer* 2005, 46, 11640.
- [6] A. Voelkel, K. Adamska, B. Strzemiecka, K. Batko. *Acta Chromat* 2008, 20, 1.
- [7] L.A. Utracki. *Polymer blends handbook*, Vol 1, Springer, 2002.
- [8] C.M. Hansen. *Hansen solubility parameters, A User's Handbook*. CRC, Press, Boca Raton, FL (1999).
- [9] E.B. Bagley, T.P. Nelson, J.M. Scigliniano. *J Paint Technol* 1971, 43, 35.
- [10] T. Hanemann, J. Boehm, P. Henzi, K. Honnef, K. Litfin, E. Ritzhaupt-Kleissl, J. Hausselt. *IEE Proc.-Nanobiotechnol* 2004, 151, 167.
- [11] S.R. Raghavan. *Langmuir* 2000, 16, 7920.

- [12] S. Iyer, A. Abu-Ali, A. Detwiler, D.A. Schiraldi. Transparent polymer-polyhedral oligomeric silsesquioxane composites. In Science and technology of silicones and silicone-modified materials. S.J. Clarson, J.J. Fitzgerald, M.J. Owen, S.D. Smith, M.E. Van Dyke, editors (2007) Chapter 20, p. 313–25.
- [13] R. Weast. Handbook of chemistry and physics. 68th edition. D.R.Lide, R.C. Weast editors, CRC Press (1987).
- [14] H.W. Oviatt. Abstr Papers Amer Chem Soc 2003, 225, U61.

Chapter 13

PMMA/functionalized SiO₂ nanocomposites

13.1 Introduction

PMMA/SiO₂ nanocomposites have been widely investigated in the past. In these last years many researcher functionalized the silica particles in order to better disperse into the matrix. The commonest synthesis route to produce finely dispersed PMMA/SiO₂ nanocomposites involves a first step of particles functionalization with methacryloxypropyltrimethoxy silane (MPS), thanks to the silanol groups in the silica surface, and a second step of radical polymerization of methyl methacrilate (MMA) to create a SiO₂-PMMA core-shell particles. Xu et al. investigated the effect of pH microemulsion and contents of silica, silanol groups and MMA on the particles size and grafting percentage [1]. Yang and al. used two different reactive silane to produced PMMA/SiO₂ nanocomposites with enhanced mechanical and thermal properties [2]. SiO₂-PMMA core-shell particles have been even added to PVC to enhance the mechanical properties. [3]. The control of molecular weight of SiO₂-PMMA macromonomers by addition of a suitable amount of CoBF was successfully carried out by Lu et al. [4]. If this synthesis approach is well performed it is possible to produce particles with controlled size and controlled organic thickness shell. The melt processing approach would greatly expand the commercial opportunities for nanocomposites technology [5, 6] It is cheaper and simpler than in situ polymerization because it involves the use of ordinary compounding devices such as extruders or mixers. Moreover is environmentally friendly since no solvents are required.

The purpose of this activity is to functionalize the silica and to disperse it into the PMMA matrix by melt compounding. One approach is the superficially functionalization with MPS and a second approach is the superficially polymerization of MMA. They differ from the

interaction between matrix and filler. Concerning the first approach, three different methods of functionalization of silica have been adopted in order to compare the easiest and most effective one. The amount of grafted MPS has been observed by TGA analysis and FTIR spectrometry. Moreover, the optical appearance of PMMA/SiO₂ nanocomposites with SiO₂-MPS particles and SiO₂-PMMA core-shell particles has been compared. The resulting mechanical properties of the most interesting materials were compared with the ones of PMMA/SiO₂ nanocomposite (as-received SiO₂ filled) seen in the previous chapter.

13.2 Raw materials

The poly(methyl methacrylate) (PMMA) provided by Lucite was the Diakon CMG302. Hydrophilic fumed silica provided by Degussa was the Aerosil 200, the average particles size are 12 nm. Methyl methacrylate (MMA), methacryloxypropyltrimethoxy silane (MPS), benzoyl peroxide (BPO) for the polymerization and functionalization reactions (Figure 13.1), and ethanol, toluene, acetone as solvents, have been provided by Sigma Aldrich.

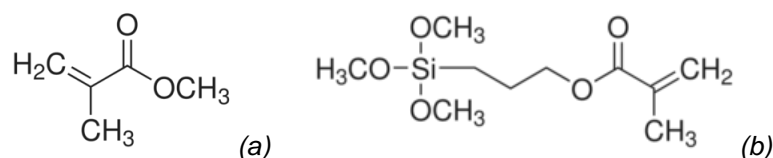


Figure 13.1 Structures of MMA (a), TPM (b).

13.3 Preparation of samples

The first step is the surface functionalization of silica particles with MPS resulting in SiO₂-MPS particles (Figure 13.2). It has been proposed that the MPS can react with hydroxyl groups involving one, two or three methoxy groups eliminating methanol as product of reaction [7]. The ponderal ratio between these components has been fixed at 1:1 according to a similar study [4]. In Table 13.1 the concentration of both hydroxyl groups and MPS are shown, resulting in about 4 MPS/OH molar ratio. The functionalization reaction was conducted in a 500 ml three-necked flask with a stirrer, a termocouple and eventually a condenser and a nitrogen input. The functionalized silica SiO₂-MPS was washed with fresh

acetone for three times and then dried at 80°C overnight. The reaction has been carried out by using three different methods.

1. 5 g of SiO₂, 5 of MPS and 0.1 N of HCl solution were added in 300 mL of ethanol [2]. The mixture was subjected to stirring at room temperature for 24 h. The HCl acts as catalyst: the acid catalysis allows the temporarily transfer of one proton from the acid, reducing the free energy of the transition state of a reaction. The silica surface hydrolyzed completely by HCl, then the silanol groups react with MPS.
2. 5 g of SiO₂ and 5 g of MPS were added in 300 mL of toluene and stirred at 110°C for 12 h under nitrogen flow [4].
3. 5 g of SiO₂ and 5 g of MPS were added in 300 mL of boiling acetone [8]. A solution of 0.6 g of maleic anhydride (MA) and 4 mL of water (0.6 g/4 mL) were added as catalyst. Water leads the opening of maleic anhydride ring, giving maleic acid. The mixture was subjected to stirring at room temperature for 24 h.

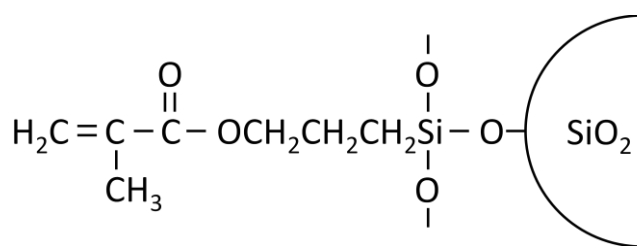


Figure 13.2 SiO₂ surface after functionalization with MPS.

SiO ₂		MPS	
Specific surface area (m ² /g)*	200±25	Molecular weight (g/mol)	248.35
OH surface density (OH/nm ²)†	2.8		
Amount of OH (mol/g)	8.1E-04	Amount of MPS (mol/g)	4.0E-03

* = according to Degussa specification

† = according to TGA/MS ANALYSIS [8].

Table 13.1 Calculations to determine the mole numbers of OH and MPS in solution.

The second step involves a further reaction between the SiO₂-MPS and the MMA resulting in SiO₂-PMMA core-shell particles (Figure 13.3). In this reaction a peroxide (BPO) decomposes into primary free radical and initiates the vinyl group of SiO₂-MPS that undergo radical polymerization. The PMMA chains bonded to the silica surface prevent phase separation

between silica and polymer matrix [2]. The termination by bimolecular reaction shouldn't easily happen due to the low mobility of the SiO₂-MPS particles [3].

In this reaction only the SiO₂-MPS particles produced through the method 2 have been polymerized to produce SiO₂-PMMA core-shell particles: 5 g OF SiO₂-MPS, 50 mL of MMA and 1 g of BPO were added in 300 mL of toluene and stirred at 100°C for 24 h under nitrogen flow (half-life time of BPO at 100°C about 25 minutes) [2]. The resulting solution was cast on a Teflon sheet and dried in oven at 110°C for 3 days.

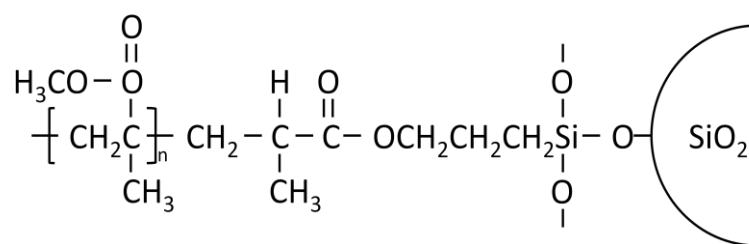


Figure 13.3 SiO₂-MPS surface after polymerization with MMA.

The third step involves the production of PMMA/SiO₂ nanocomposites filled at 3 wt % of inorganic content by melt compounding using a Brabender plastograph. The 3 wt% of inorganic content has been calculated by determining the residue at 800°C running TGA analysis on SiO₂-MPS samples. PMMA was previously dried at 100°C for 3 hours. Neat PMMA and the modified silica were mixed at 200°C for 5 minutes. Another variable in the processing has been introduced in order to achieve a better dispersion of the silica. The SiO₂-MPS particles produced through the method 1 showed in preliminary trials a strong tendency to aggregation after drying. For this reason it has been sonicated for 3 hours in ethanol after washing and compared with the first one.

Sample	Synthesis route
PMMA/ SiO ₂ -MPSe	Method 1
PMMA/SiO ₂ -MPS _t	Method 2
PMMA/SiO ₂ -MPS _a	Method 3
PMMA/SiO ₂ -MPS _{es}	Method 1 + sonication
PMMA/SiO ₂ -PMMA _t	Method 2 + polymerization

Table 13.2 Synthesis conditions of each sample.

The produced samples are shown in Table 13.2. The nanocomposites have been pelletized and dried at 100°C for 3 hours, before to be compression molded to get thin films (about 0.1 mm thick).

13.4 Characterization

FTIR

The Fourier transform infrared spectrometry has been carried out with a Nicolet Nexus 670 apparatus working in transmission mode, scanning in the range of 400-4000 cm⁻¹ (64 scans), on samples in the form of powder englobed in transparent KBr disks.

TGA

The thermal behavior was measured by thermogravimetric analysis (TGA) on a TA instruments SDT Q600. Every run was carried out under a 100 mL/min air flow from room temperature to 800°C heating at 20C°/min. The first part of the analysis was slower than the second one to distinguish the weight loss due to the solvent, MPS, MMA or PMMA.

Mechanical tests

The mechanical properties of all materials were measured by Galdabini (mod. Sun 2500) dynamometer. Rectangular shaped films (90x12.5x0.1 mm) produced by compression molding have been subjected to the tensile test in order to measure the tensile modulus (1.1 mm/min tensile rate).

DMA

Rectangular shaped films (25x6x0.1 mm) produced by compression molding have been subjected to the dynamic mechanical analysis in order to measure the storage modulus versus temperature (tension mode, 1 Hz frequency, 0-140°C temperature range, 5°C/min heating rate, 15 μm amplitude).

13.5 Results and discussion

13.5.1 FTIR

Figure 13.4 shows the FTIR spectra of as-received SiO₂, SiO₂-MPS functionalized through different methods, SiO₂-PMMA_t and MPS. In Table 13.3 and Table 13.4 the peaks position and correspondent vibration modes of SiO₂ and MPS are listed. The presence of the peaks at 1640, 1722 and 2900 cm⁻¹ of C=C, C=O and C-H bonds respectively, in the SiO₂-MPS samples, demonstrates that the silica surface has been successfully functionalized [1, 3, 4]. The intensity of the MPS contribution in the SiO₂-MPSe spectrum is lower than observed for the SiO₂-MPSa and SiO₂-MPSt. It should be attributed to a lower grafting percentage achieved through the first method.

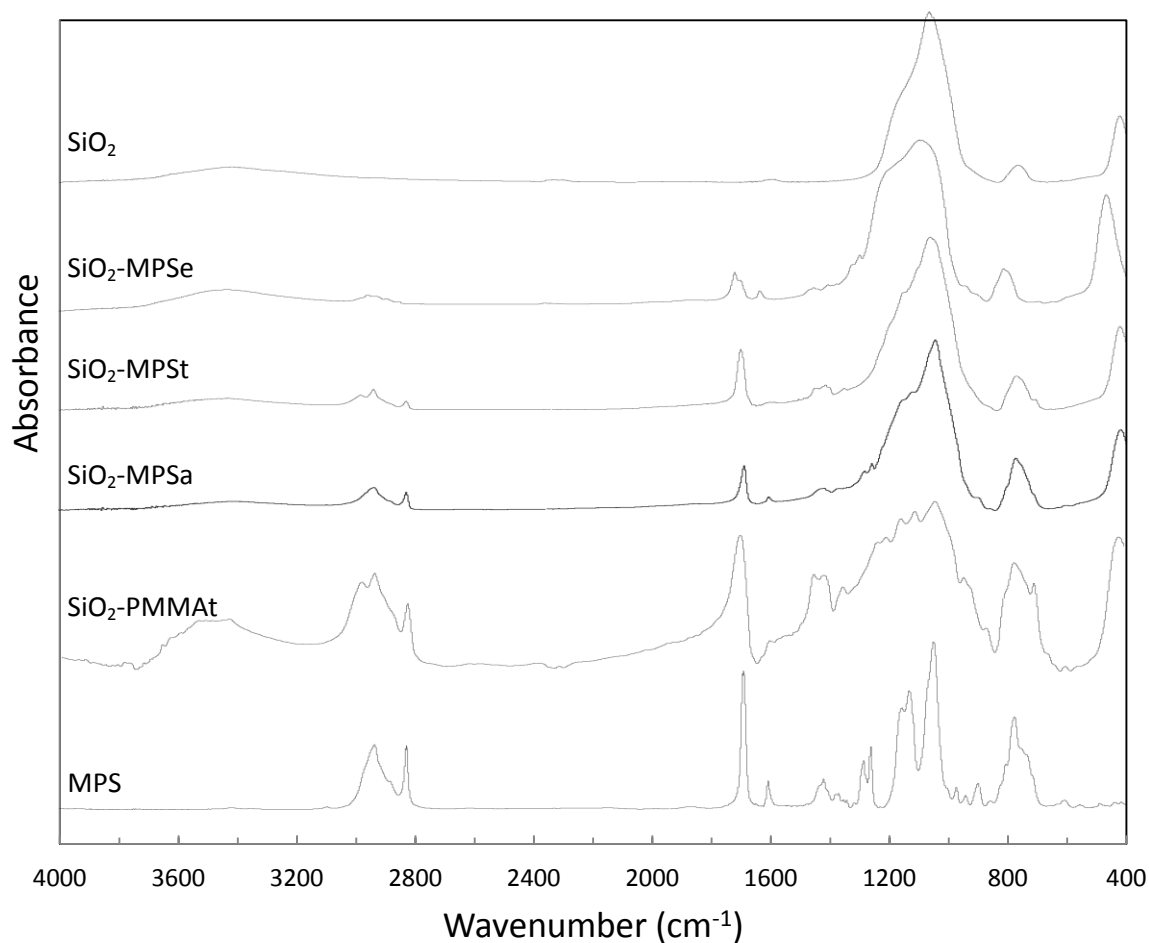


Figure 13.4 FTIR spectra of as-received SiO₂, SiO₂-MPS produced with different method, SiO₂-PMMA_t, and MPS.

Wavenumber (cm ⁻¹)	Vibration modes of SiO ₂
471	Rocking Si-O
809	Bending Si-O
1105	Stretching Si-O
1636	Bending O-H (water)
3300-3600	Stretching free and H-bonded O-H (water, silanols)

Table 13.3 Peaks position of FTIR spectrum of silica.

Wavenumber (cm ⁻¹)	Vibration modes of MPS
820	Bending Si-O
1090	Stretching Si-O
1169	Stretching C-O
1298, 1323	Bending CH ₃
1456	Bending CH ₂
1640	Stretching C=C
1722	Stretching C=O
2843, 2947	Stretching C-H

Table 13.4 Peaks position of FTIR spectrum of MPS.

The SiO₂-PMMA spectrum shows an organic phase rich material because the strong intensity of signals of aliphatic carbons (2800-3000 cm⁻¹ and 1300-1450 cm⁻¹) and ester methacrylate groups (1170 and 1720 cm⁻¹). The C=C peak would be desirable to disappear because means that there is not MMA residue or unreacted vinyl end groups of MPS. In our case a not well defined signal at that wavenumber is present. In literature, FTIR spectra of SiO₂-PMMA exhibit [4] or do not exhibit that peak [3].

13.5.2 TGA

Figure 13.5 shows the TGA curves of as-received SiO₂, SiO₂-MPS functionalized through different methods, SiO₂-PMMA and MPS. Similarly to FTIR spectroscopy, the SiO₂-MPS exhibits a higher residue at 800°C (84.7% versus 77.8% and 79.0% of SiO₂-MPS and SiO₂-MPSa respectively), meaning a lower organic content bonded to the silica surface.

Multiple washing after drying the functionalized silica should be enough to remove all the free MPS that did not react with silica. The temperature range of MPS degradation (90-230°C) is much lower than the one of the SiO₂-MPS samples (250-380°C). That means there are different and stronger bonds involved in the degradation than the ones of MPS.

SiO₂-PMMA_t has 18.9% residue at 800°C. Similar values have been observed by Zhu et al. (20-40%) on SiO₂-PMMA core-shell particles polymerized in aqueous solution [3].

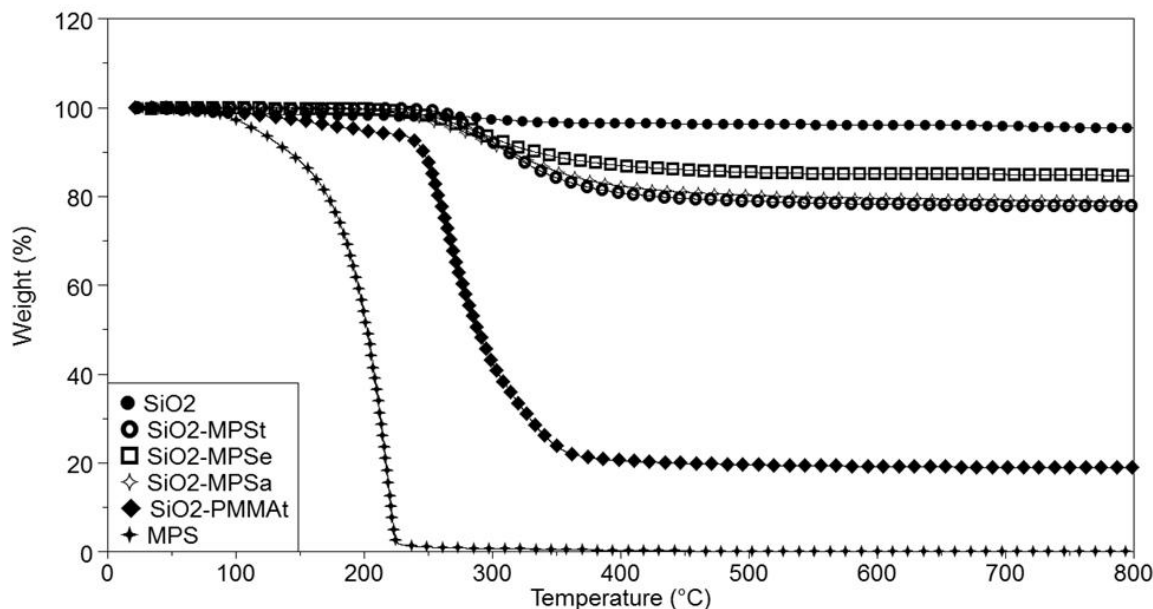


Figure 13.5 TGA curves of as-received SiO₂, SiO₂-MPS produced with different method, SiO₂-PMMA_t, and MPS.

13.5.3 Optical clarity

Table 13.5 shows the optical appearance of nanocomposite 1 mm thick films. The background is black to highlight the silica aggregates. A so bad dispersion of fillers arise from two factors: the drying after functionalization step and the melt compounding by plastograph. The drying is required to remove unreacted MPS and residue solvent but it causes re-aggregation. It has been observed that a wet suspension of silica nanoparticles (12 nm diameter) has aggregates size up to 3.5 μm while the dried suspension has aggregates that achieve 44 μm [10]. The mixing action of the plastograph is not so effectiveness as the one of a twin screw extruder, resulting in weak shear stress that are not enough to re-disperse the silica.

PMMA/SiO₂-MPSe exhibits the coarsest clusters size. The dispersion is strongly improved by sonicating the particles before drying but the clusters still visible. The appearance of PMMA/SiO₂-MPSt is similar to the PMMA/SiO₂-MPSe. In these materials the matrix surrounding the clusters is perfectly transparent probably because the most of the silica forms

big aggregates rather than to be finely dispersed in the PMMA. PMMA/SiO₂-MPSa shows only small and sparse spots and a completely transparent matrix. That could be due to the nanoscale dispersion of silica, except for a little part, that doesn't affect the visible light path transmitted through the material. PMMA/SiO₂-PMMA_t, doesn't exhibits visible silica cluster, unlike the other materials previously described. The appearance is heterogeneous due to the presence of areas with a different transparency degree. Comparing the PMMA/SiO₂-MPSt with PMMA/SiO₂-PMMA_t, a strong enhancement of the size clusters due to the polymerization step can be observed.

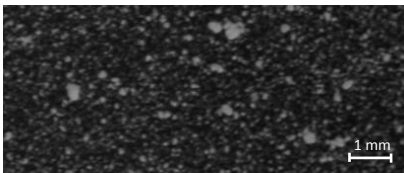
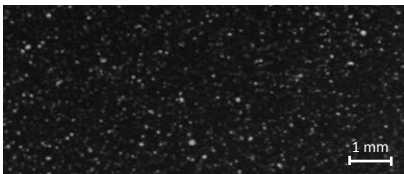
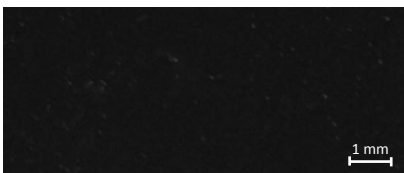
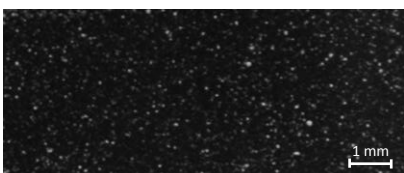
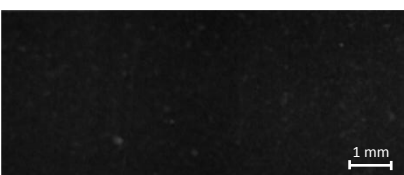
Sample	Silica aggregates on films
PMMA/ SiO ₂ -MPSe	
PMMA/SiO ₂ -MPSt	
PMMA/SiO ₂ -MPSa	
PMMA/SiO ₂ -MPSe _s	
PMMA/SiO ₂ -PMMA _t	

Table 13.5 Optical clarity of PMMA filled SiO₂ nanocomposites (black background).

13.5.4 Mechanical tests

Tensile test and DMA analysis have been carried out to compare these nanocomposites with the PMMA/SiO₂ one seen in the previous chapter (labeled as PMMA/A200). Since PMMA/SiO₂-MPSe, PMMA/SiO₂-MPSt and PMMA/SiO₂-MPSeS exhibited a coarse dispersion of silica aggregates only PMMA/SiO₂-MPSa and PMMA/SiO₂-PMMAAt have been subjected to these tests. In Figure 13.6 the normalized storage and tensile moduli of SiO₂ filled nanocomposites are shown. It can be observed a big difference between the moduli of PMMA/SiO₂-MPSa and PMMA/SiO₂-PMMAAt. The first exhibits a similar behavior to the PMMA/SiO₂ and the tensile modulus has been improved. Functionalizing the silica in acetone the average particles size got slightly bigger but the polymer-filler interface has been improved. These two aspects have an opposite effect on the mechanical properties of the material. Generally they are better as the particles size decreases and the interface adhesion increases [11]. Probably in the PMMA/SiO₂-MPSa nanocomposites these aspects are balanced giving only a moderate increase of stiffness.

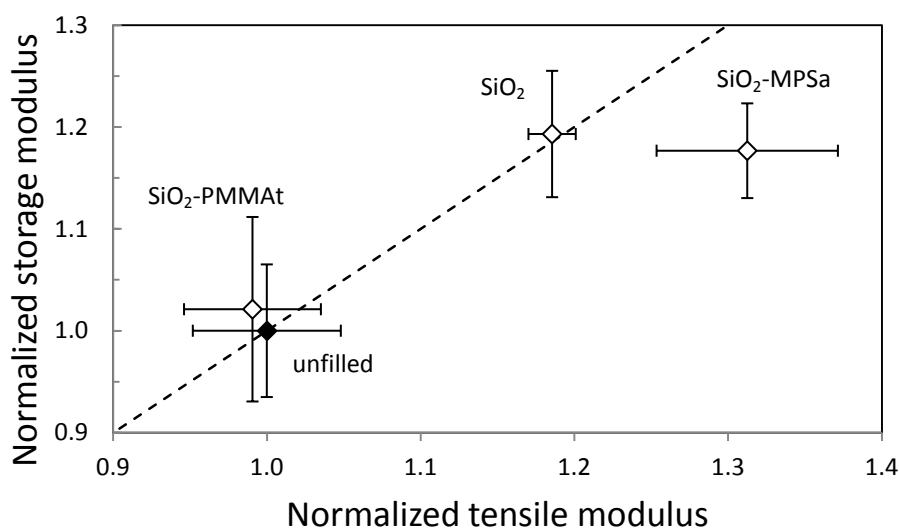


Figure 13.6 Normalized values of storage modulus and tensile modulus of PMMA based nanocomposites. Labels describe the filler.

The PMMA/SiO₂-PMMAAt nanocomposite exhibit the same moduli of neat PMMA. The observed good optical clarity makes to suppose a good dispersion of fillers and a particles size smaller then the PMMA/SiO₂-MPS nanocomposites. A reason to explain the low modulus is

the low molecular weight achieved during the polymerization of MMA. It is constituted by 3 wt% of silica, about 12 wt% of polymerized PMMA by solution and 85 wt% of as-received PMMA. A big difference in molecular weight could affect seriously the mechanical properties since the polymerized PMMA doesn't act just as compatibilizer but is a consistent part of the matrix.

13.6 Conclusion

Compatibilized PMMA/SiO₂ nanocomposites at 3 wt% of inorganic load were produced by melt compounding. SiO₂ has been previously functionalized by three different (using ethanol, toluene, acetone as solvents) method with MPS and grafted with PMMA obtained by polymerization in solution of MMA. Comparing the TGA curves and FTIR spectra of SiO₂-MPS particles, the those produced in acetone and toluene showed a higher organic content than the ones produced in ethanol. After blending with PMMA the nanocomposites exhibited big silica clusters except the ones filled with silica functionalized in acetone and with SiO₂-PMMA core-shell particles. The poor dispersion has been attributed to the re-agglomeration promoted by the drying process carried out after the functionalization step. By tensile test and DMA on films it has been observed an increment of moduli of the PMMA/SiO₂-MPS nanocomposite (through acetone solution) compared with the un-compatibilized PMMA/SiO₂ one, meaning a stronger adhesion of the interface matrix-filler. The PMMA/SiO₂-PMMA nanocomposite exhibit similar moduli values of neat PMMA despite the apparently good dispersion of filler. It is due to the fraction of polymerized PMMA in the matrix that has a lower molecular weight than the as-received PMMA, leading in a lower stiffness of the material.

References

- [1] P. Xu, H. Wang, R. Tong, Q. Du, W. Zhong. *Colloid Polym Sci* 2006, 284, 755.
- [2] F. Yang, G.L. Nelson. *J Appl Polym Sci* 2004, 91, 3844.
- [3] A. Zhu, Z. Shi, A. Cai, F. Zhao, T. Liao. *Polym Test* 2008, 27, 540.
- [4] Z. Lu, J. Wang, Q. Li, L. Chen, S. Chen. *Eur Polym J* 2009, 45, 1072.
- [5] T.D. Fornes, P.J. Yoon, H. Keskkula, D.R. Paul. *Polymer* 2001, 42, 9929.

- [6] J.W. Cho, D.R. Paul. *Polymer* 2001, 42, 1083.
- [7] Y. Hu, S. Zhou, L. Wu. *Polymer* 2009, 50, 3609.
- [8] F. Bauer, H. Ernst, U. Decker, M. Findeisen, H.J. Gläsel, H. Langguth, E. Hartmann, R. Mehnert, K. Peuker. *Macromol Chem Phys* 2000, 201, 2654.
- [9] R. Mueller, H.K. Kammler, K. Wegner, S.E. Pratsinis. *Langmuir* 2003, 19, 160.
- [10] C.N. Suryawanshi, P. Pakdel, D.W. Schaefer. *J Appl Cryst* 2003, 36, 573.
- [11] B.J. Ash, R.W. Siegel, L.S. Schadler. *Macromolecules* 2004, 37, 1358.

Chapter 14

Gas transport in nanocomposites

14.1 Gas permeation in polymers

In 1866 Thomas Graham formulated the solution diffusion process postulating that the permeation process through a polymer involved the dissolution of penetrant, followed by transmission of the dissolved species through the membrane [1]. In 1855 Fick hypothesized that the rate of transfer of diffusing substances through unit area of a section is proportional to the concentration gradient measured normal to the section [2]. Fick's first law of diffusion is:

$$J = -D \frac{\partial C}{\partial x} \quad (14.1)$$

where J is the rate of transfer per unit of section ($\text{mol/m}^2 \text{ s}$), C is the concentration of diffusing substances (mol/m^3), x is the space coordinate normal to the section, D is the diffusion coefficient (m^2/s). Taking into account the mass-balance of an element, assuming the diffusion is restricted to one direction and assuming the diffusion coefficient as constant in every point of the polymer, the Fick's second law of diffusion is [2]

$$\frac{\partial C}{\partial t} = D \frac{\partial^2 C}{\partial x^2} \quad (14.2)$$

In the late 1870's Stefan and Exner demonstrated that gas permeation was proportional to the product of solubility coefficient (S) and Fick's diffusion coefficient (D). Based on the findings of Stefan and Exner, von Wroblewski constructed a quantitative solution to the Graham's solution-diffusion model. The dissolution of gas was based on Henry's law of solubility, where the concentration of the gas in the membrane was directly proportional to the applied gas pressure [1]:

$$C = Sp \quad (14.3)$$

where C is the concentration of the sorbate (mol/m^3), p is the equilibrium vapor pressure of the permeant.

Wroblewski showed that under steady state conditions, and assuming diffusion and solubility coefficients to be independent of concentration, the gas permeation flux can be expressed as [1]:

$$J = -K \frac{\Delta p}{l} \quad (14.4)$$

where K is the permeability coefficient (mol/Pa m s), Δp is the difference between the upstream and downstream pressure, l is the membrane thickness.

14.1.1 Steady state approach

In 1920 Daynes evaluated both diffusion and solubility coefficients by steady-state permeation experiments assuming that D is independent of concentrations (time lag method) [2]:

$$\frac{\partial^2 C}{\partial x^2} = 0 \quad (14.5)$$

Steady state conditions assume that diffusant concentrations remain constant at all points on each side or surface of a membrane. The concentration changes linearly through the membrane and the flux is constant in each section:

$$J = -D \frac{\Delta C}{l} \quad (14.6)$$

If one assumes the diffusion coefficient to be constant [2]:

$$K = DS \quad (14.7)$$

where S is the solubility coefficient ($\text{mol /m}^3\text{Pa}$) and follows Henry's law.

14.1.2 Time-lag method

Assuming a constant diffusion coefficient the amount of diffusant, Q_t , which passes through the sheet in time, t , is given by [2]:

$$\frac{Q_t}{lC_1} = \frac{Dt}{l^2} - \frac{1}{6} - \frac{2}{\pi^2} \sum_{n=1}^{\infty} \frac{(-1)^n}{n^2} \exp\left(\frac{-Dn^2\pi^2 t}{l^2}\right) \quad (14.8)$$

As steady state is approached, $t \rightarrow \infty$, the exponential terms become negligibly small, allowing to plot Q_t versus t : [2]:

$$Q_t = \frac{DC_1}{l} \left(t - \frac{l^2}{6D} \right) \quad (14.9)$$

The extrapolation of the time lag t_0 from the Q_t versus t plot, which correspond to the intercept on the t -axis, allows to calculate D from: [2]:

$$t_0 = \frac{l^2}{6D} \quad (14.10)$$

14.2 Gas permeation in rubbery and glassy polymers

The free volume molecular theory postulates that the movement of gas molecules is dependent upon the available free volume in the polymer matrix, as well as, sufficient energy of the gas molecules to overcome attractive forces between chains [3]. The concept of free volume has been used to qualitatively describe the non-equilibrated nature of the polymer.

In 1960, Fujita proposed the presence of free volume within a polymer. The concept is based on the presence of three components for the specific volume of any polymer. The three components consist of: the occupied volume of the macromolecules; the interstitial free volume and the hole free volume, which is large enough to allow gas transport [4]. The interstitial volume dependence on temperature is essential in defining the differences between the rubbery and glassy state of an amorphous polymer. The glass transition temperature is often defined as the point where the expansion coefficient of the polymer changes. The polymer below its glass transition temperature is treated as a solid and is termed a glassy polymer, whereas the polymer above its glass transition temperature is a rubbery polymer and exhibits viscous liquid like properties.

14.2.1 Free volume

Molecular diffusion through a polymer depends strongly by the amount of free volume [5]. It is constituted by the overall amount of static voids created by inefficient chain packing or transient gaps generated by thermally induced chain rearrangement. The larger and more numerous these preferential pathways to the diffusion are, the faster molecules migrates through a polymer. The fractional free volume is:

$$FFV = \frac{V_{sp} - V_0}{V_{sp}} \quad (14.11)$$

where V_{sp} is the polymer bulk specific volume, V_0 is the volume occupied by polymer chains and can be calculated by [6]:

$$V_0 = 1.3V_w \quad (14.12)$$

where V_w is the van der Waals volume and it can be estimated from group contribution methods.

FFV has been related to diffusion coefficients through the Doolittle equation [5]:

$$D = A \exp\left(\frac{-B}{FFV}\right) \quad (14.13)$$

where B and A are empirical constants.

Concerning the PET, the FFV_a of amorphous phase can be estimated by [5]:

$$FFV_a = \frac{\frac{MW}{\rho_a} - V_0}{\frac{MW}{\rho_a}} \quad (14.14)$$

where MW is the molecular weight, ρ_a is the density of the amorphous phase, calculated by:

$$\rho_a = \frac{\rho - \frac{X_c}{100} \rho_c}{1 - \frac{X_c}{100}} \quad (14.15)$$

where ρ is the measured density, X_c is the crystallinity weight fraction determined by DSC, ρ_c is the density of the crystalline phase (1.440 g/cm³ for PET [7]).

14.2.2 Gas permeation in rubbery polymers

The gas sorption and diffusion in rubbery polymers are defined by Henry's law for solubility and Fick's law for diffusion. The diffusion coefficient is assumed to be concentration independent if Henry's law is applicable [2].

14.2.3 Gas permeation in glassy polymers

Sorption

The failure of Henry's law to explain the higher sorption capability in glassy polymers is explained in terms of the presence of two modes for sorption. The dual sorption model assumes that a polymer consists of a continuous chain matrix, along with microvoids (holes), frozen in the matrix.

These microvoids, present in discrete as well as continuous domains, are caused by the non-equilibrium thermodynamic state of glassy polymers. The dual sorption mechanism is then defined in terms of Henry's law of solubility (dissolution in continuous chain matrix) and Langmuir-type of sorption (sorption in microvoids) and is still the most accepted model by most researchers to explain gas sorption in glassy polymers [3,5,8–12].

The gas concentration in the polymer, for an applied pressure is given as:

$$C = C_D + C_H = k_D + \frac{C'_H b p}{1 + b p} \quad (14.16)$$

where C is the gas concentration, C_D is the gas concentration by normal dissolution, C_H is the gas concentration by hole filling, k_D is the Henry's law of dissolution constant, C'_H is the hole saturation constant, b is the hole affinity constant, and p is the gas pressure. The presence of only two distinct modes is an oversimplification when considering the presence of sorption site size distribution.

Diffusion

The diffusion behavior of glassy polymers has been described adapting the first or second Fick's law for diffusion to the dual transport mode. Several models have been proposed taking into account the Henry and Langmuir modes [13–19].

14.2.4 Gas permeation in semicrystalline polymers

Sorption

Semicrystalline polymers are discussed as materials consisting of two phases, the impermeable crystalline phase and the permeable amorphous matrix. Initial investigations revealed that the gas solubility is directly related to the crystallinity of the polymers. Bitter (1984) describes experiments which confirm the two phase model for a rubber amorphous phase. The solubility is then represented as [20]:

$$S = S_a \phi_a \quad (14.17)$$

where, S_a is the solubility coefficient for pure amorphous polymer, and ϕ_a is the amorphous volume fraction. Later investigation showed negative deviations from the simple two phase model [21] due to the presence of low density crystallites.

Diffusion

The diffusion process in semi-crystalline polymers is studied in terms of a spatial distribution of the impermeable crystalline phase and the permeable amorphous phase, which are cross-linked by tie chains [21]. These tie chains cause reduced mobility for the chains in the amorphous phase. The gas permeate flux through a semicrystalline polymer is given as:

$$J = \frac{\alpha}{\tau} D_a \frac{\partial C}{\partial x} \quad (14.18)$$

where D_a is the diffusivity of gas for a completely amorphous polymer, α is the cross sectional area available to transport, τ is the tortuosity factor accounting for the hindrance to the gas molecules due to the presence of the crystalline phase. The cross-linking effects are accounted for by introducing a chain immobilization factor β , which accounts for the high activation energy required for gas diffusion through such polymers. The diffusion coefficient can be defined as [21]:

$$D = \frac{D_a}{\tau\beta} \quad (14.19)$$

In this model, a penetrant can only diffuse through amorphous material. Therefore, the crystallites create a tortuous pathway for the penetrant by acting as impermeable barriers to diffusion.

The chain segment immobility factor β is given by:

$$\beta = \exp \left[k \left(d - \frac{\sqrt{\phi_L}}{2} \right) \right]^2 \quad (14.20)$$

where k is independent of the penetrant, d is the diameter of the penetrant and $\sqrt{\phi_L}/2$ is approximately equal to the mean unoccupied distance between two chain segments. β is equal to one in glassy polymers and is greater than one in rubbery polymers [21].

14.3 Gas permeation in nanocomposites

In most theoretical treatises the nanocomposite is considered to consist of a permeable phase (polymer matrix) in which non-permeable nanoplatelets are dispersed [22]. There are three main factors that influence the permeability of a nanocomposite: the volume fraction of the nanoplatelets; their orientation relative to the diffusion direction; and their aspect ratio.

It is generally accepted that the transport mechanism within the polymer matrix follows Fick's law, and that the matrix maintains the same properties and characteristics as the neat polymer. Therefore, a decrease of the solubility is expected in the nanocomposite due to the reduced polymer matrix volume, as well as a decrease in diffusion due to a more tortuous path for the diffusing molecules.

The reduction of the diffusion coefficient is higher than that of the solubility coefficient. Indeed, the volume fraction of nanoplatelets is low and, thus, the reduction of the matrix volume is small. The major factor, then, is the tortuosity, which is connected directly to the shape and the degree of dispersion of the nanoplatelets.

Diffusion

Impermeable nanoparticles create a tortuous pathway for the diffusion of gas out of the nanocomposite matrix. This increases the effective path length for diffusion of the gas, thus reducing the diffusion coefficient, thus [23]:

$$D_n = \frac{D_m}{\tau} \quad (14.21)$$

where D_n is the diffusion coefficient in the nanocomposite, D_m is the diffusion coefficient in the polymer matrix, τ is the tortuosity factor.

Sorption

Gas solubility may depend on the concentration of filler particles, as well as their interactions with polymer chains. These are negligible if the filler interacts favorably with the polymer matrix such that it is fully wetted by the polymer chains. In this case [24]:

$$S_n = (1 - \phi_f)S_m \quad (14.22)$$

where S_n is the solubility coefficient in the nanocomposite, S_m is the solubility coefficient in the polymer matrix, ϕ is the filler volume fraction. Otherwise, filler particles can adsorb penetrant molecules [24]:

$$S_n = (1 - \phi_f)S_0 + \phi_f S_f \quad (14.23)$$

where S_f is the sorption onto the surface of a non-porous fillers or into the pore of a porous filler. According with this approach the correlation between the permeability coefficient of the nanocomposites and the which one of the matrix is:

$$\frac{K_n}{K_m} = \frac{D_n S_n}{D_m S_m} = \frac{1 - \phi_f}{\tau} \quad (14.24)$$

14.3.1 Models for permeability of nanocomposites

Low aspect ratio fillers

When the impermeable fillers have spherical shape and they are periodically arrayed, one of the most frequently used examples of models is derived from Maxwell's analysis [25]:

$$\frac{K_n}{K_m} = \frac{1 - \phi_f}{1 + \frac{\phi_f}{2}} \quad (14.25)$$

The limit for its validity is $\phi_f \leq 0.1$ (dilute suspension), because the particles have a tendency to aggregate, which increases with ϕ_f . If the fillers are cylinders oriented parallel to the surface, according with Lord Rayleigh [26]:

$$\frac{K_n}{K_m} = \frac{1 - \phi_f}{1 + \phi_f} \quad (14.26)$$

According to Barrer [24] the permeability of polymers containing impermeable phases is given by:

$$\frac{K_n}{K_m} = (1 - \phi_f)^2 \quad (14.27)$$

These models propose a correlation between the permeability of a nanocomposite and the one of the unfilled matrix that depends only by the volume fraction of the filler. They are shown in Figure 14.1 in the range of dilute regime. Barrer and Rayleigh models have similar trends while Maxwell model has a lower slope.

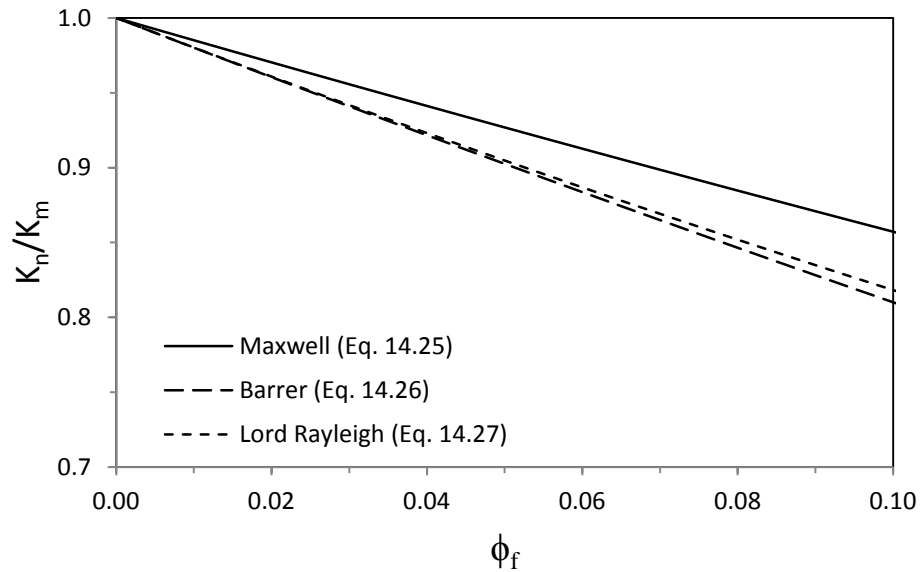


Figure 14.1 Comparison between models that predict the permeability in composites filled with arrays of low aspect ratio particles.

Parallel platelets to the membrane surface (ordered positioning)

The most used model for nanocomposites is given by Nielsen [27], in which each platelet contributes to the enhancement of the diffusion length by $L/2$, thus:

$$\frac{K_n}{K_m} = \frac{1 - \phi_f}{1 + \frac{\alpha}{2} \phi_f} \quad (14.28)$$

where $\alpha = L/W$ is the aspect ratio (Figure 14.2). This relation works in dilute regime.

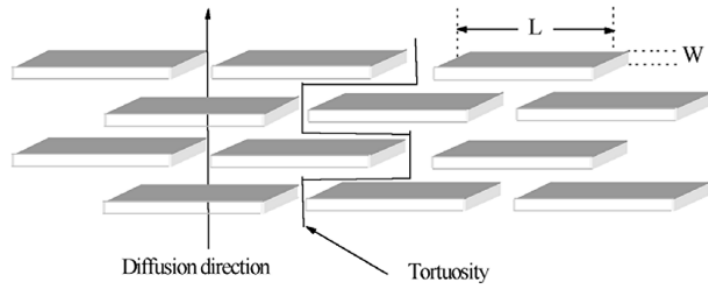


Figure 14.2 Regular arrangement of rectangular platelets oriented parallel to the membrane surface (reprinted from [22]).

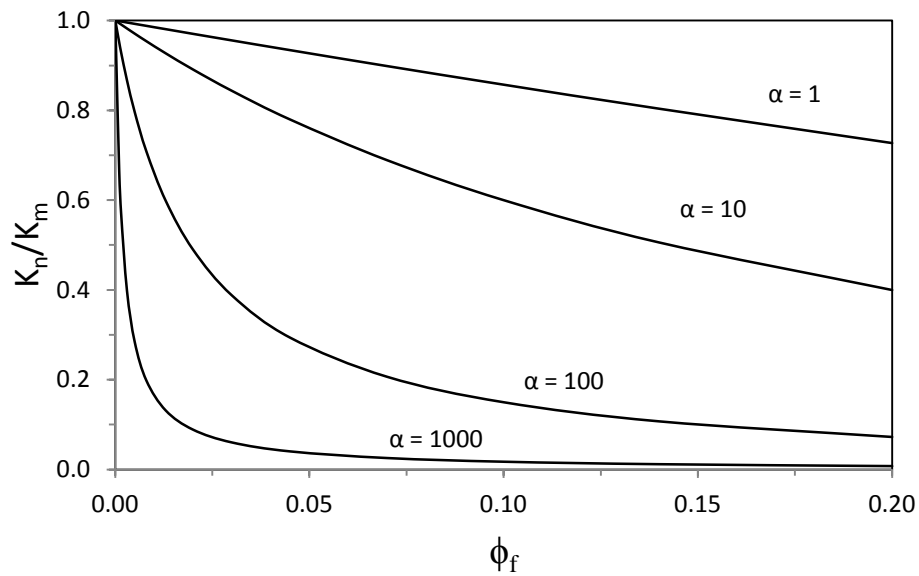


Figure 14.3 Effect of the aspect ratio on the permeability of a composite, according to the Nielsen model (Equation 14.28). Aspect ratio $\alpha=L/W$.

In Figure 14.3 the influence of α in the permeability of nanocomposites is shown (for $\alpha = 1$ the Nielsen relation is equal to the Maxwell relation). Cussler proposed a new relation for the influence of the tortuosity path on the diffusion in a composite [28]:

$$\frac{D_n}{D_m} = \left(1 + \frac{\alpha^2 \phi_f^2}{1 - \phi_f} \right)^{-1} \quad (14.29)$$

assuming that the membrane has flakes $2d$ wide and a thick, separated by a distance b , and extending infinitely into the plane of the page. The gap between flakes is the distance s (Figure 14.4). In this case $\phi_f = 2da/[(d+s)(a+b)]$, $\alpha = d/a$ is the aspect ratio, $\sigma = s/a$ is the slit aspect ratio.

Aris [29] and Wakeham and Mason [30] proposed a more elaborate form of Equation 14.29 introducing new terms:

$$\frac{D_n}{D_m} = \left(1 + \frac{\alpha^2 \phi_f^2}{1 - \phi_f} + \frac{\alpha \phi_f}{\sigma} + \frac{4\alpha \phi_f}{\pi(1 - \phi_f)} \ln \left[\frac{\pi \alpha^2 \phi_f}{\sigma(1 - \phi_f)} \right] \right)^{-1} \quad (14.30)$$

$$\frac{D_n}{D_m} = \left(1 + \frac{\alpha^2 \phi_f^2}{1 - \phi_f} + \frac{\alpha \phi_f}{\sigma} + 2(1 - \phi_f) \ln \left(\frac{1 - \phi_f}{2\sigma \phi_f} \right) \right)^{-1} \quad (14.31)$$

The third term on the right hand side of these two equations are due to the resistance to diffusion of the slits between adjacent flakes in the same horizontal plane. The fourth term is due to the constriction of the permeant to pass through the slits. According to Cussler, the complete form of this equation is [31]:

$$\frac{D_n}{D_m} = \left(1 + \frac{\alpha^2 \phi_f^2}{1 - \phi_f} + \frac{\alpha \phi_f}{\sigma} + \frac{\alpha \phi_f}{2\pi} \ln \left(\frac{2\alpha}{\sigma} \right) \right)^{-1} \quad (14.32)$$

Figure 14.5 compares the Equation 14.30, 14.31, 14.32 (they differ for the fourth term) and the simplified Equation 14.29 for different values of α and σ . If $\alpha = 100$ (Figure 14.5a, 14.5c, 14.5e), as σ increases the models don't differ too much except for the Wakeham-Mason relation, specially for $\phi_f < 0.02$ because the fourth term tends to infinite for $\phi_f \rightarrow 0$. Moreover $D_n/D_m(\phi_f)$ is not a monotonic function, since it has a maximum values. If $\alpha = 10$ (Figure 14.5b, 14.5d, 14.5f), Equation 14.31 is no longer applicable. Equation 14.30 and 14.32 begins to be not applicable at around $\sigma > 1$ and $\sigma = 100$, respectively. In Figure 14.5d and 14.5f the non-monotonic characteristic of Equation 14.30 and 14.32, respectively, is noticeable.

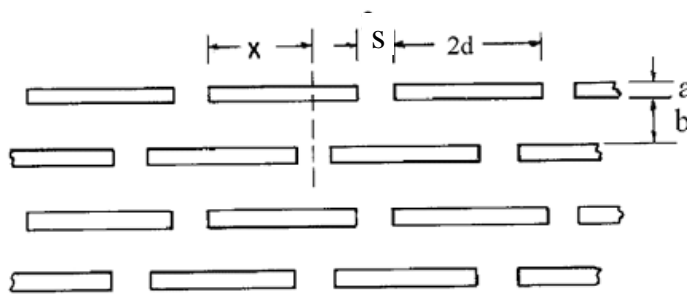


Figure 14.4 Regular arrangement of rectangular platelets and characteristic parameters (reprinted from [22]).

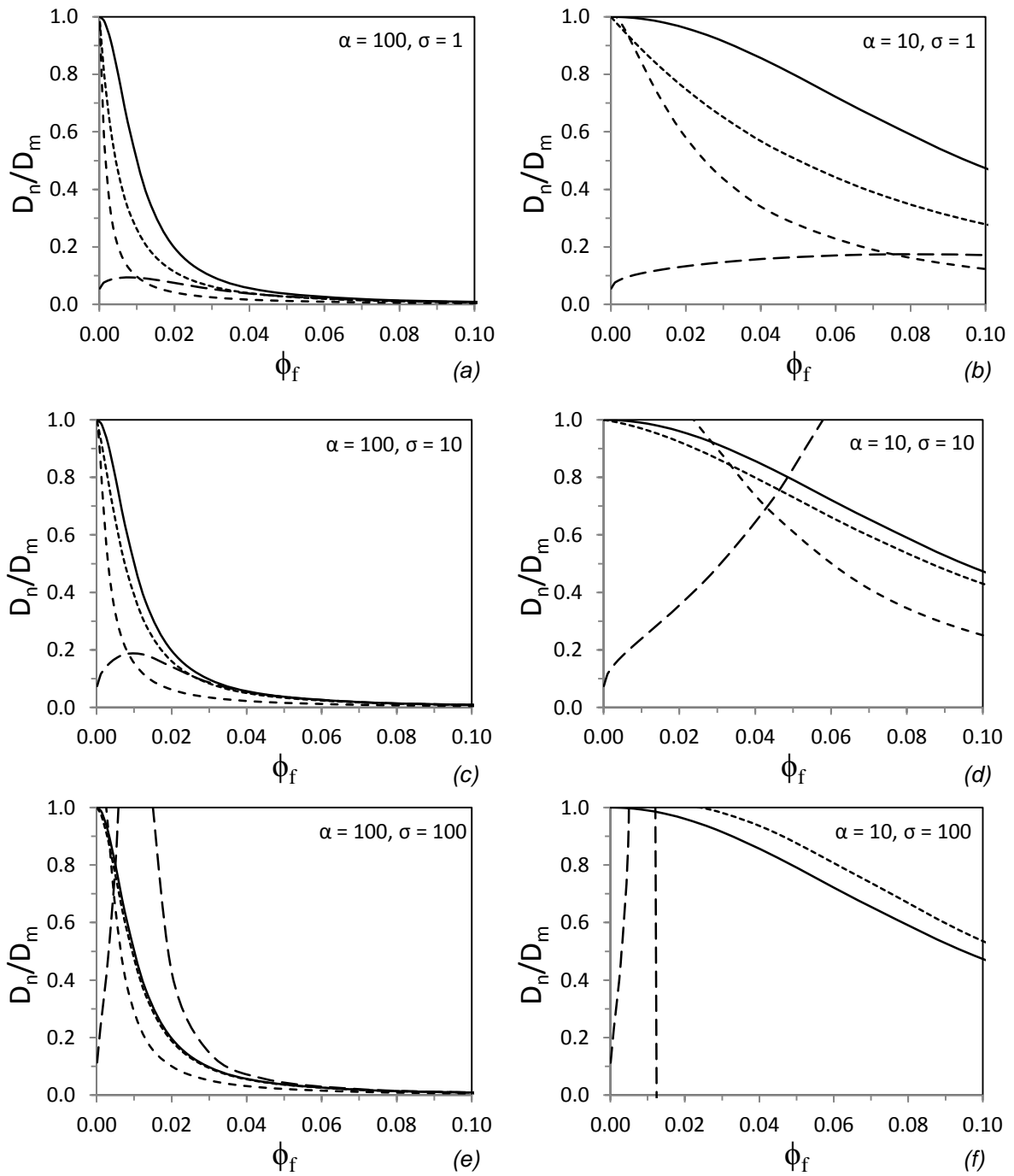


Figure 14.5 Comparison between models that predict the permeability in composites filled with oriented platelets: — simplified Cussler (Eq. 14.29), --- Aris (Eq. 14.30), -- Wakeham-Mason (Eq. 14.31), Cussler (Eq. 14.32). The plots differ for the aspect ratio $\alpha=d/a$ and the slit aspect ratio $\sigma=s/a$.

Parallel platelets to the membrane surface (random positioning)

For random positioning of parallel platelets several models have been proposed. According to Brydges [32]:

$$\frac{D_n}{D_m} = \left(1 + \frac{\alpha^2 \phi_f^2}{1 - \phi_f} \gamma (1 - \gamma) \right)^{-1} \quad (14.33)$$

where $\gamma = x/2d$ is the stacking parameter (from 0 to 0.5), referring to Figure 14.2, with $\alpha = 2d/a > 100$ and $2s \sim \alpha$.

According to Cussler [29]:

$$\frac{D_n}{D_m} = \left(1 + \frac{\mu' \alpha^2 \phi_f^2}{1 - \phi_f} \right)^{-1} \quad (14.34)$$

where μ' is a geometrical factor, by Lape [33]:

$$\frac{K_n}{K_m} = \frac{1 - \phi_f}{\left(1 + \frac{\alpha}{3} \phi_f \right)^2} \quad (14.35)$$

Figure 14.6 compares the Equation 14.33 and 14.35 with the Nielsen relation for different values of α . The Lape relation predicts lower values of K_n/K_m than the Nielsen one, while Brydges relation predicts generally higher values only if α is low (Figure 14.6a).

Random platelets

For non-aligned filled Bharatdwaj [34] modified the Nielsen model by introducing a parameter $S = (3 \cos^2 \theta - 1)/2$:

$$\frac{K_n}{K_m} = \frac{1 - \phi_f}{1 + \alpha \phi_f \frac{1}{3} \left(S + \frac{1}{2} \right)} \quad (14.36)$$

where $S = 1$ for platelets parallel to the surface (Nielsen model), $S = 0$ for random orientations, $S = -1/2$ for platelets perpendicular to the surface.

Maksimov proposed an empirical relation between the permeability in nanocomposites with random platelets (K_n) and platelets parallel to the membrane surface (K_n^{\parallel}) [35]:

$$K_n = \frac{1}{3} [K_n^{\parallel} + 2K_m(1 - \phi_f)] \quad (14.37)$$

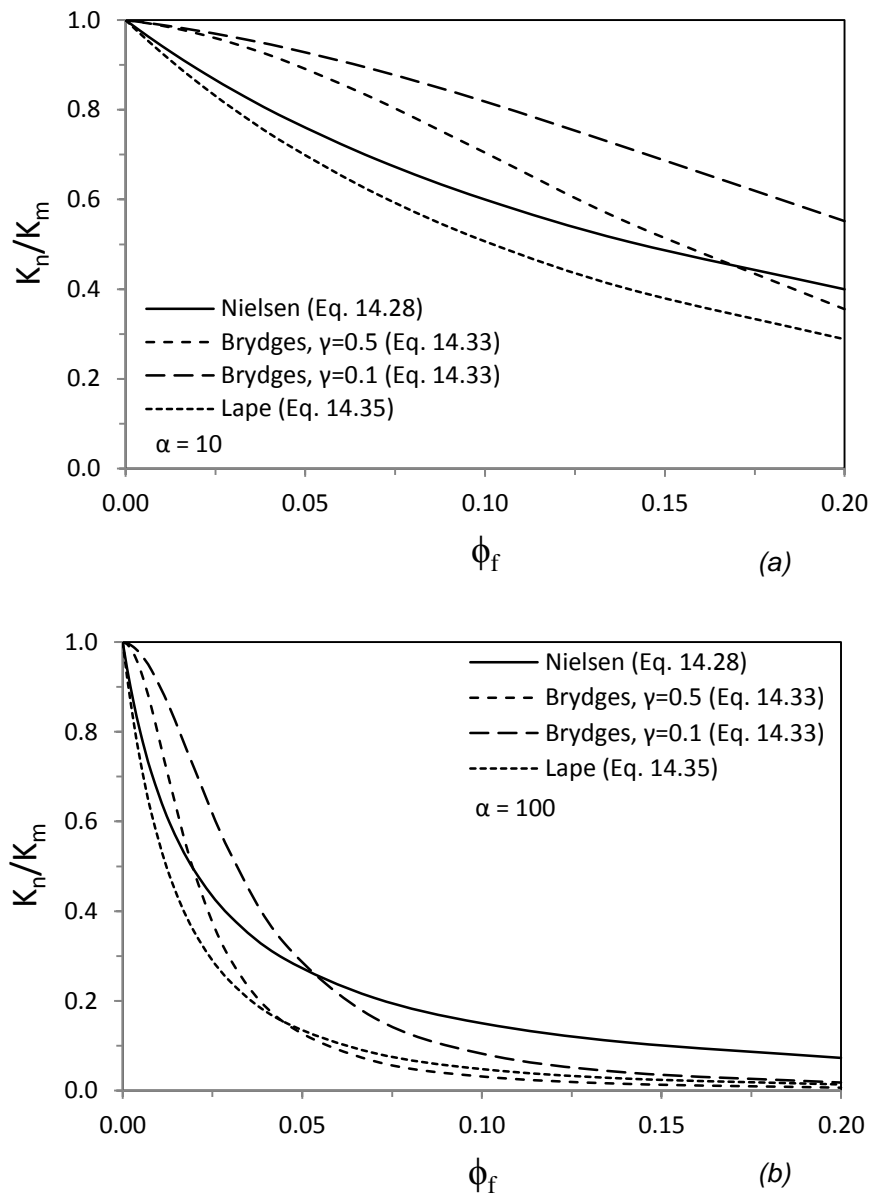


Figure 14.6 Comparison between Nielsen model (ordered positioning) and models for random positioning of parallel platelets. The plots differ for the aspect ratio $\alpha=L/W$.

Figure 14.7 compare the Equation 14.36 and 14.37 for different values of α and θ . When the platelets are parallel to the membrane surface the permeability is minimum. Based on the Nielsen model, the Maksimov relation has a similar trend if compared with the Bharatdwaj relation if $\alpha = 10$ (Figure 14.7a). If $\alpha = 100$ these two relations are rather different (Figure 14.7b).

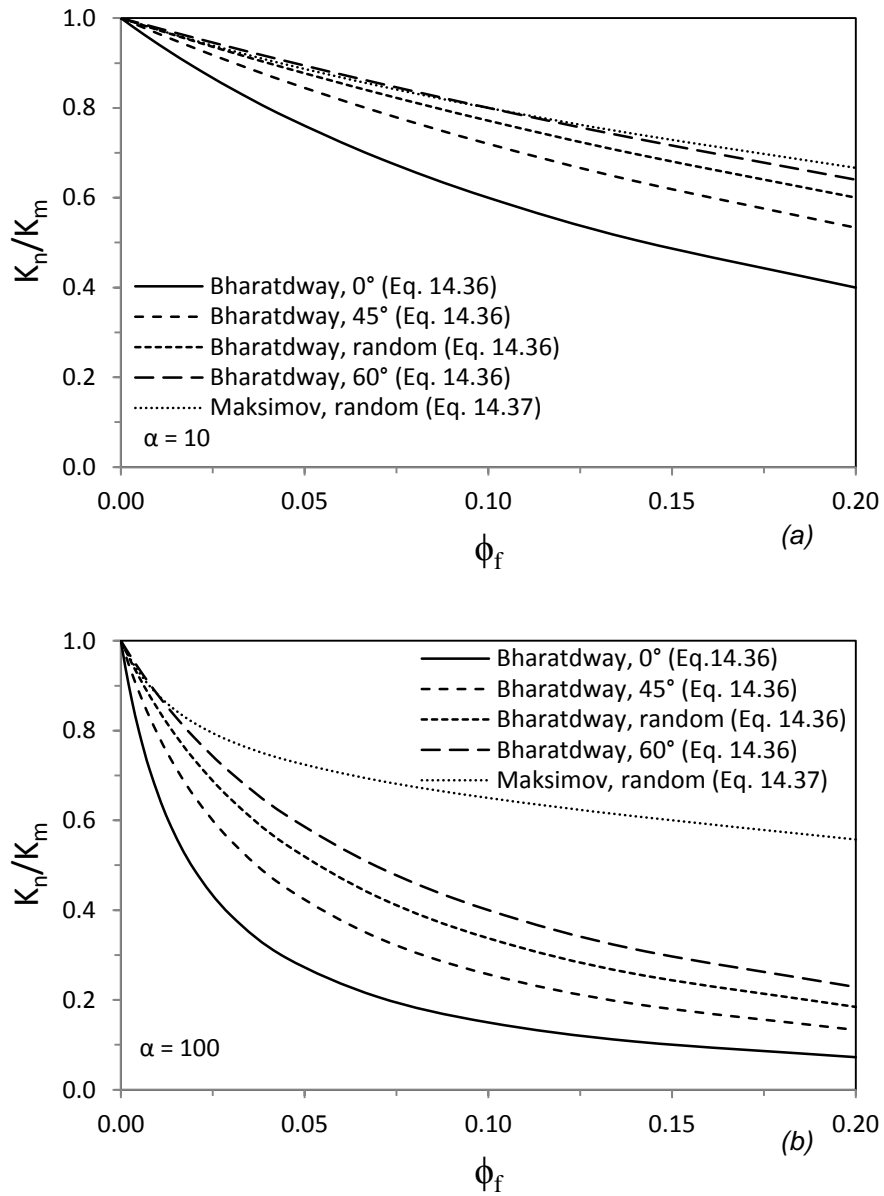


Figure 14.7 Effect of the orientation of platelets. The plots differ for the aspect ratio $\alpha=L/W$.

Parallel disks

If the platelets are circular disks with $\alpha = R/W$, according to Fredrickson and Bicerano [36]:

$$\frac{D_n}{D_m} = \frac{1}{4} \left(\frac{1}{1 + \alpha\phi_f\beta_1} + \frac{1}{1 + \alpha\phi_f\beta_1} \right)^2 \quad (14.38)$$

where $\beta_{1,2} = \pi(2 \pm \sqrt{2})/(4 \ln \alpha)$. It is valid for dilute ($\alpha\phi_f \ll 1$) and semi-dilute regime ($\alpha\phi_f \gg 1$). In their work they adapted the relations previously seen, valid for oriented platelets, to the case of circular disks, obtain the modified Nielsen relation:

$$\frac{D_n}{D_m} = \frac{1}{1 + \frac{\pi\alpha}{\ln \alpha} \phi_f} \quad (14.39)$$

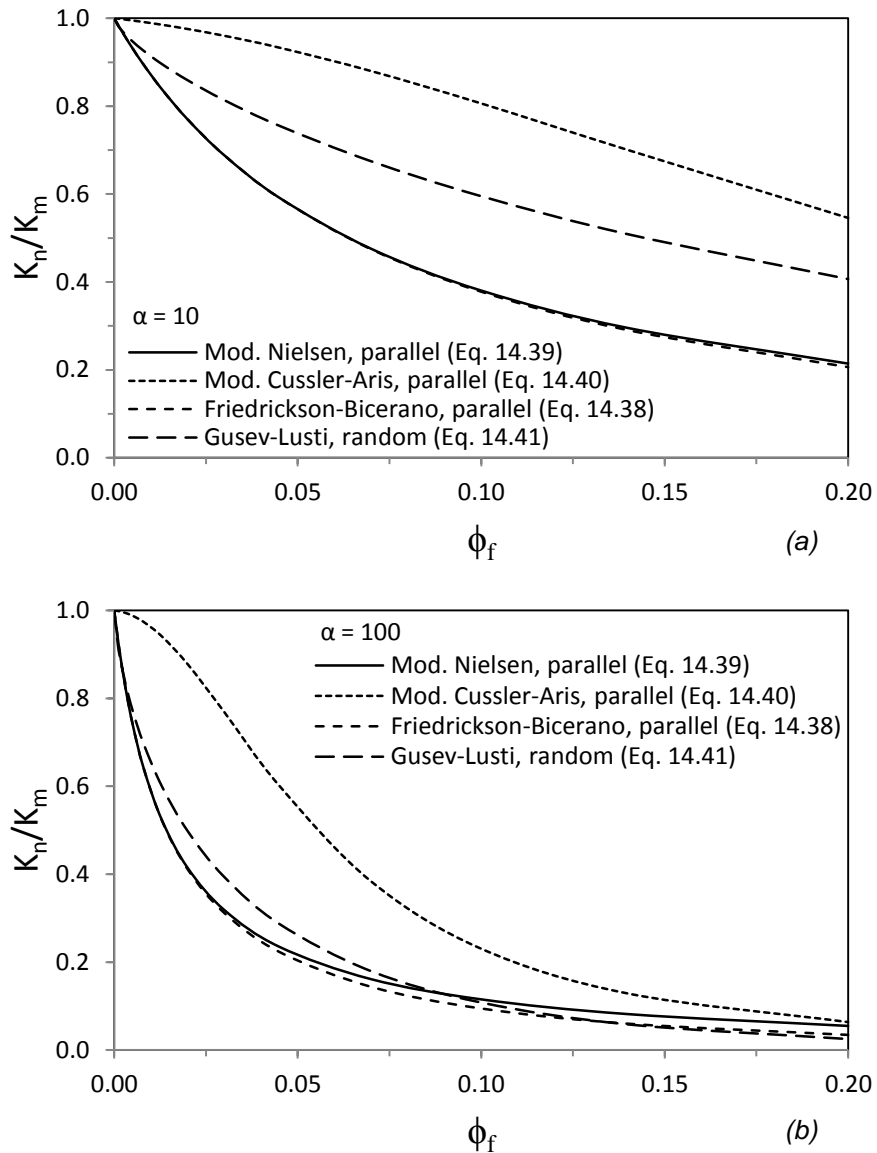


Figure 14.8 Comparison between models for composite filled with parallel or random disks. The plots differ for the aspect ratio $\alpha=R/W$.

and the modified Cussler-Aris relation:

$$\frac{D_n}{D_m} = \frac{1}{1 + \left(\frac{\pi\alpha}{4 \ln \alpha} \phi_f\right)^2} \quad (14.40)$$

Random disks

Gusev and Lusti [37] developed a model performing finite-element analyzes of a random dispersion of disks:

$$\frac{K_n}{K_m} = \frac{1 - \phi_f}{\exp \left[\left(\frac{\alpha \phi_f}{3.47} \right)^{0.71} \right]} \quad (14.41)$$

Figure 14.8 compare the Equation 14.38, 14.39 and 14.40 for parallel disks with the Equation 14.41 for random oriented disks, for different values of α . If $\alpha = 10$ the modified Nielsen and the Fredrickson-Bicerano relations are very similar, while the Gusev-Lusti one (random orientation) predicts a higher permeability as expected (Figure 14.8a). While the modified Cussler-Aris relation predicts a low reduction of permeability, even lower than the Gusev-Lusti one. The same behavior is observable if $\alpha = 100$ (Figure 14.8b).

Other aspects that affect the permeability

Sorrentino et al. introduced a new parameter β' that takes into account the presence of voids in the interfacial region [38]:

$$\frac{K_n}{K_m} = \frac{1 + \beta' \phi_f}{\tau} \quad (14.42)$$

with

$$\beta' = \frac{V_i D_i}{V_f D_m} - \frac{V_i + V_f}{V_f} \quad (14.43)$$

where V_i is the volume of interfaces, V_f is the volume of fillers, D_i is the diffusion coefficient in the interfaces.

Nazarenko et al. modified the Nielsen relation to take into account stacks of layers [39]:

$$\frac{K_n}{K_m} = \frac{1 - \phi_f}{1 + \frac{\alpha}{2N} \phi_f} \quad (14.44)$$

where N is the number of layers in the stack.

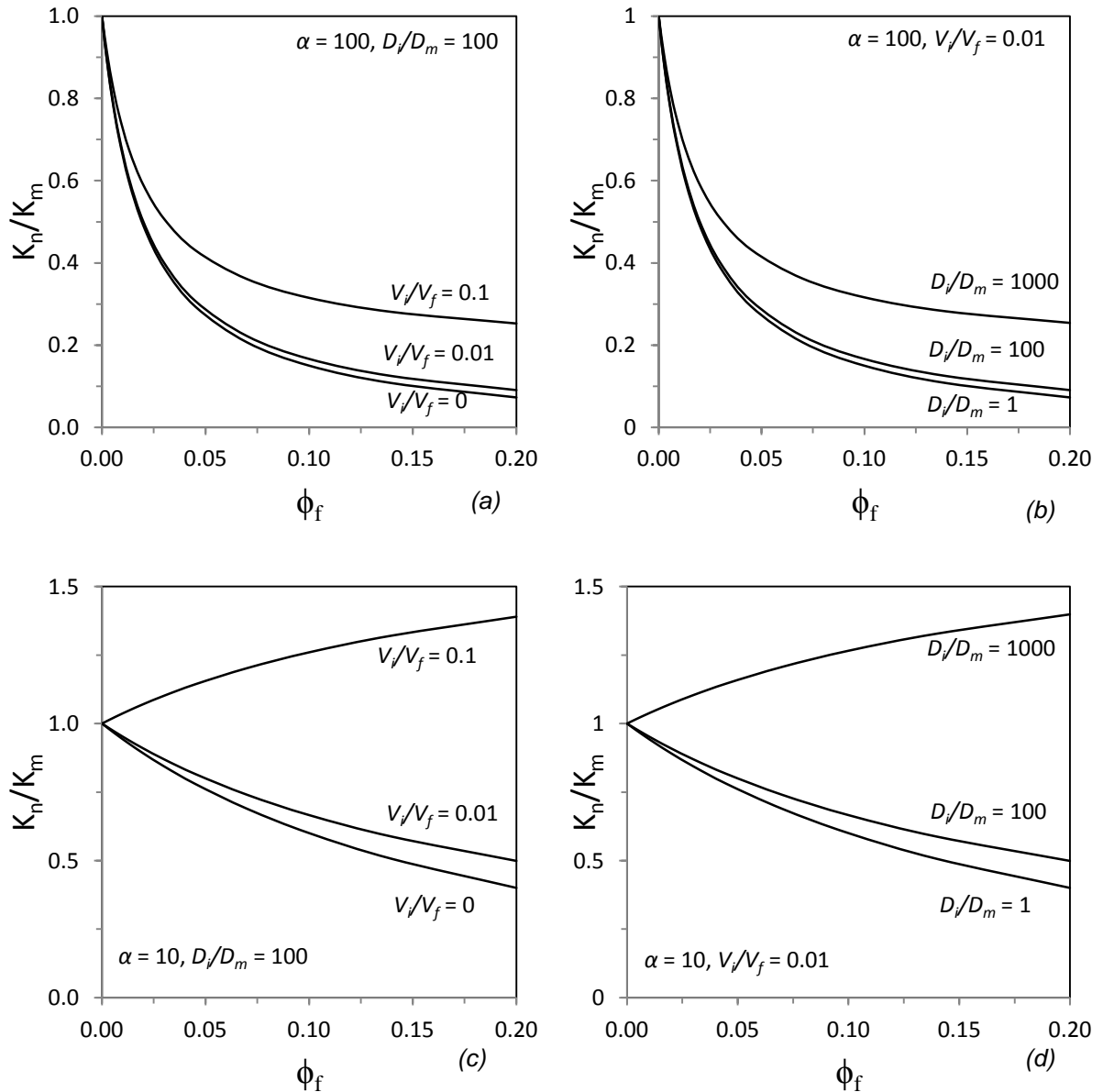


Figure 14.9 Effect of the presence of voids in the interface (Eq. 14.42). The plots differ for the values of α , D_i/D_m and V_i/V_f .

Figure 14.9 shows the influence of α , D_i/D_m and V_i/V_f on Equation 14.43. If $\alpha = 100$ (Figure 14.9a and 14.9b) only couples $D_i/D_m = 100$, $V_i/V_f = 0.1$ and $D_i/D_m = 1000$,

$V_i/V_f = 0.01$ give relevant deviations from the Nielsen model. If one of the two ratios is lower than at least one order of magnitude the deviation is negligible. The same can be observed if $\alpha = 10$ but the deviation is higher, even the K_n/K_m achieves values higher than 1 meaning a higher permeability than the unfilled polymer. Figure 14.10 shows the Equation 14.44 for different values of α and N . As the number of layers increases the reduction of the permeability decreases as expected. This effect is lower as N increases.

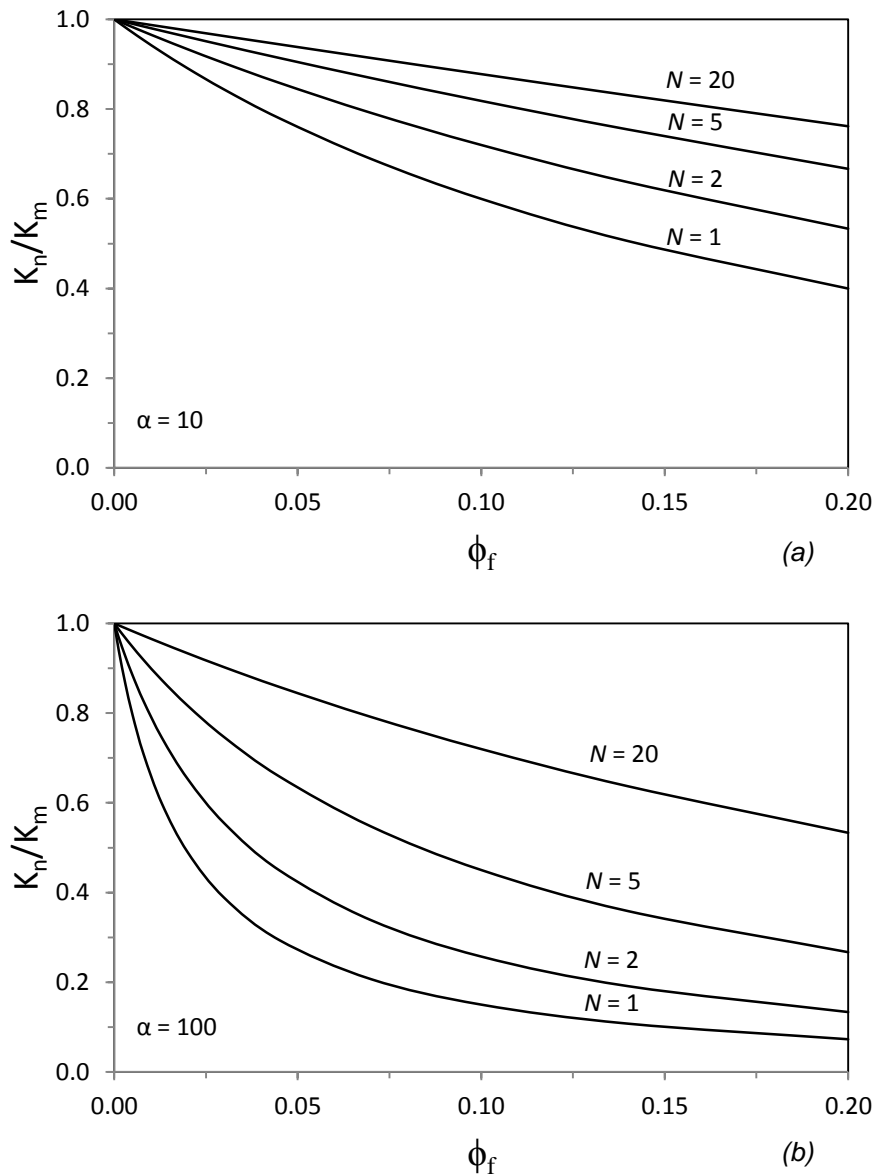


Figure 14.10 Effect of the number of layers in parallel stacks of platelets (Eq. 14.44). The plots differ for the aspect ratio $\alpha=L/W$.

14.3.2 PET/tspPOSS nanocomposites: prediction of permeability

As observed in the Paragraph 9.5.5 the oxygen permeability of PET/tspPOSS nanocomposites get worse as the filler content increases. A lot of nanocomposites system exhibit this behavior, especially if the aspect ratio is close to 1 (isodimensional particles) and it has been associated to the addition of free volume mainly localized at the interface. In PA6/SiO₂ nanocomposites (load 1-5 wt%, 10-20 nm particle size) the permeability is higher than neat PA6 [40]. In PMP/SiO₂ nanocomposites (load 15-40 wt%, 13 nm particle size) the free volume increases because the presence of interface and because the particles affect polymer chain packing [41]. In PP nanocomposites it has been observed that the permeability increases when the SiO₂ particles are not compatibilized, due to the formation of voids around the nanoparticles through which gases could freely permeate [42,43]. In PC/POSS nanocomposites an increase of diffusivity as the POSS content increase, is associated to the increase of interfacial area [44].

Considering a polymer filled with isodimensional particles (e.g. POSS clusters) the following approach can be considered. The material can be seen as an array of equal cubic cells containing a impermeable spherical particle in their middle. In this way it is possible to study the permeation in a single cell and then to extend the results for a multitude of arrayed cells. The elementary cell is shown in Figure 14.11 and it is defined by the side length L and the particles radius R . If a permeant species passes through the cell, from one face to the opposite face, its pathway is p_1 of Figure 14.11 if it doesn't hit the sphere, otherwise it is p_2 . The length of p_1 coincides with L while the length of p_2 depends by the spatial position of the entry point of the permeant in the face (it is maximum when the sphere is hit in the middle). Thus the average pathway \bar{p} through the cell depends by the ratio R/L and $\bar{p} \geq L$ ($\bar{d} = L$ if $R = 0$). It is determined by:

$$\bar{p} = \frac{1}{A} \int_A p \, dA \quad (14.45)$$

where $A = L^2$ is the area of one face.

According with this approach, modeling the membrane as a 3D array of cubic cells, some assumptions can be done:

- the overall pathway through the membrane doesn't depend by the size/number of particles (Figure 14.12a). Thus if $R_1/L_1 = R_2/L_2$ then $\bar{d}_1 = \bar{d}_2$.

- It is not necessary that different layers of a membrane would be aligned each other (Figure 14.12b).
- Every value of ϕ_f defines one value of R/L :

$$\phi_f = \frac{V_f}{V_{tot}} = \frac{V_{sphere}}{V_{cube}} = \frac{4\pi}{3} \left(\frac{R}{L}\right)^3 \quad (14.46)$$

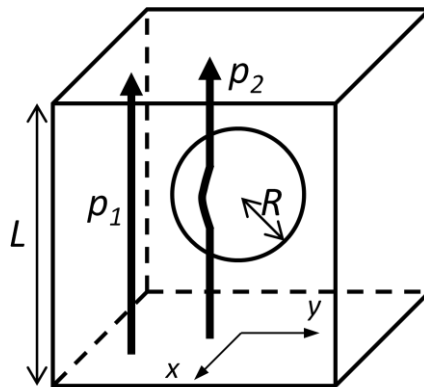


Figure 14.11 Cubic cell filled with a impermeable spherical particle. This scheme has been taken as reference to calculate the tortuosity.

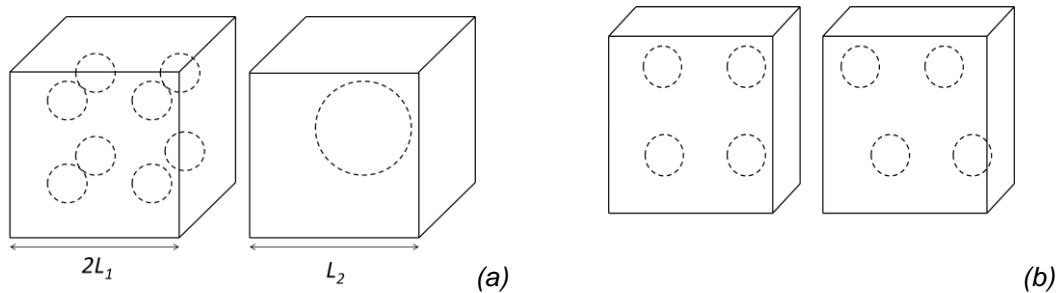


Figure 14.12 Assumption of the model: the permeability doesn't depend by the size and number of particles (a) and by the mismatch of different layers of particles (b).

It can be considered as sum of three contributes to the pathway the permeant goes through: pathways that don't hit the particle (\bar{p}_1 , the average value of p_1 of Figure 14.11), pathways that hit the particle (\bar{p}_2 , the average value of p_2 in Figure 14.11). The latter is sum of a component through the polymer (\bar{p}_{2a}) and a component along the particles surface (\bar{p}_{2b}). A

Cartesian coordinate system as shown in Figure 14.11 (the origin placed in the centre of the bottom face) is considered.

Rigorously, the method to calculate \bar{p} is the following.

$$\begin{aligned}
 \bar{p}_1 &= \frac{1}{L^2} \int_{-\frac{L}{2}}^{\frac{L}{2}} \int_{-\frac{L}{2}}^{\frac{L}{2}} p_1 \, dx \, dy = \frac{1}{L^2} \left[2 \int_0^R 2 \int_{r(y)}^{\frac{L}{2}} L \, dx \, dy + 2 \int_R^{\frac{L}{2}} 2 \int_{r(y)}^{\frac{L}{2}} L \, dx \, dy \right] & (14.47) \\
 &= \frac{1}{L^2} \left[2 \int_0^R 2L \left(\frac{L}{2} - r(y) \right) \, dy + 2 \int_R^{\frac{L}{2}} 2L \left(\frac{L}{2} - r(y) \right) \, dy \right] \\
 &= \frac{1}{L^2} \left[2 \int_0^R 2L \left(\frac{L}{2} - \sqrt{R^2 - y^2} \right) \, dy + 2 \int_R^{\frac{L}{2}} 2L \left(\frac{L}{2} - 0 \right) \, dy \right] \\
 &= \frac{1}{L^2} \left[2 \int_0^R \left(L^2 - 2L\sqrt{R^2 - y^2} \right) \, dy + 2 \int_R^{\frac{L}{2}} L^2 \, dy \right] \\
 &= \frac{1}{L^2} \left[2L^2R - 4L \int_0^R \sqrt{R^2 - y^2} \, dy + 2L^2 \left(\frac{L}{2} - R \right) \right] \\
 &= \frac{1}{L^2} \left[2L^2R - 4L \int_0^{\frac{\pi}{2}} \sqrt{R^2 - R^2 \sin^2 t} \, R \cos t \, dt + L^3 - 2L^2R \right] \\
 &= \frac{1}{L^2} \left[-4LR^2 \int_0^{\frac{\pi}{2}} \cos^2 t \, dt + L^3 \right] = \frac{1}{L^2} \left[-4LR^2 \int_0^{\frac{\pi}{2}} \frac{1 + \cos 2t}{2} \, dt + L^3 \right] \\
 &= \frac{1}{L^2} \left[-4LR^2 \frac{\pi}{4} + L^3 \right] = \frac{1}{L^2} \left[-\pi LR^2 + L^3 \right] = L - \frac{\pi R^2}{L}
 \end{aligned}$$

$$\begin{aligned}
\bar{p}_{2a} &= \frac{1}{L^2} \int_{-\frac{L}{2}}^{\frac{L}{2}} \int_{-\frac{L}{2}}^{\frac{L}{2}} p_{2a} \, dx \, dy & (14.48) \\
&= \frac{2}{L^2} \int_0^R 4 \int_0^{r(y)} \frac{L}{2} - \sqrt{r(y)^2 - x^2} \, dx \, dy \\
&= \frac{2}{L^2} \int_0^R \left(4 \int_0^{r(y)} \frac{L}{2} \, dx - 4 \int_0^{r(y)} \sqrt{r(y)^2 - x^2} \, dx \right) dy \\
&= \frac{2}{L^2} \int_0^R \left(2Lr(y) - 4 \int_0^{\frac{\pi}{2}} \sqrt{r(y)^2 - r(y)^2 \sin^2 t} r(y) \cos t \, dt \right) dy \\
&= \frac{2}{L^2} \int_0^R \left(2Lr(y) - 4r(y)^2 \int_0^{\frac{\pi}{2}} \cos^2 t \, dt \right) dy \\
&= \frac{2}{L^2} \int_0^R \left(2Lr(y) - 4r(y)^2 \int_0^{\frac{\pi}{2}} \frac{1 + \cos 2t}{2} \, dt \right) dy \\
&= \frac{2}{L^2} \int_0^R \left(2Lr(y) - 4r(y)^2 \frac{\pi}{4} \right) dy \\
&= \frac{2}{L^2} \int_0^R 2Lr(y) - \pi r(y)^2 \, dy = \frac{2}{L^2} \int_0^R 2L\sqrt{R^2 - y^2} - \pi(R^2 - y^2) \, dy \\
&= \frac{4}{L} \int_0^R \sqrt{R^2 - y^2} \, dy - \frac{2\pi R^3}{L^2} + \frac{2\pi R^3}{3L^2} \\
&= \frac{4}{L} \int_0^{\frac{\pi}{2}} \sqrt{R^2 - R^2 \sin^2 t} R \cos t \, dt - \frac{4\pi R^3}{3L^2} = \frac{4R^2}{L} \int_0^{\frac{\pi}{2}} \cos^2 t \, dt - \frac{4\pi R^3}{3L^2} \\
&= \frac{4R^2}{L} \int_0^{\frac{\pi}{2}} \frac{1 - \cos 2t}{2} \, dt - \frac{4\pi R^3}{3L^2} = \frac{4R^2}{L} \frac{\pi}{4} - \frac{4\pi R^3}{3L^2} = \frac{\pi R^2}{L} - \frac{4\pi R^3}{3L^2}
\end{aligned}$$

Geometrically p_1 is the volume of the cubic cell without the cylinder with radius r and length L , and p_2 is the volume of this cylinder without the sphere with radius r .

The contribute p_{2b} is the sum of all the spherical surface portions calculated for every x value (the distance from the axis of sphere, as shown in Figure 14.13), that correspond to the grey area (S_2) showed in Figure 14.14. The sum of these contributes (they both have the unit of measure of a volume) has to be divided for the area of the cubic face to obtain the average pathway \bar{p} through the cell.

$$\begin{aligned}
\bar{p}_{2b} &= \frac{1}{L^2} \int_0^R S_2(x) dx = \frac{1}{L^2} \int_0^R [S_{sphere} - 2S_1(x)] dx & (14.49) \\
&= \frac{1}{L^2} \int_0^R [4\pi R^2 - 4\pi R (R - \sqrt{R^2 - x^2})] dx = \frac{4\pi R}{L^2} \int_0^R \sqrt{R^2 - x^2} dx \\
&= \frac{4\pi R}{L^2} \int_0^{\frac{\pi}{2}} \sqrt{R^2 - R^2 \sin^2 t} R \cos t dt = \frac{4\pi R^3}{L^2} \int_0^{\frac{\pi}{2}} \cos^2 t dt \\
&= \frac{4\pi R^3}{L^2} \int_0^{\frac{\pi}{2}} \frac{1 - \cos 2t}{2} dt = \frac{4\pi R^3}{L^2} \frac{\pi}{4} = \frac{\pi^2 R^3}{L^2}
\end{aligned}$$

The total pathway of the cell is:

$$\bar{p} = \bar{p}_1 + \bar{p}_{2a} + \bar{p}_{2b} = L + \frac{R^3}{L^2} \left(\pi^2 - \frac{4\pi}{3} \right) \quad (14.50)$$

Thus the tortuosity and K_n/K_m are:

$$\tau = \frac{\bar{p}}{L} = 1 + \frac{R^3}{L^3} \left(\pi^2 - \frac{4\pi}{3} \right) = 1 + \frac{3\phi_f}{4\pi} \left(\pi^2 - \frac{4\pi}{3} \right) = 1 + \phi_f \left(\frac{3\pi}{4} - 1 \right) \quad (14.51)$$

$$\frac{K_n}{K_m} = \frac{1 - \phi_f}{1 + \phi_f \left(\frac{3\pi}{4} - 1 \right)} \quad (14.52)$$

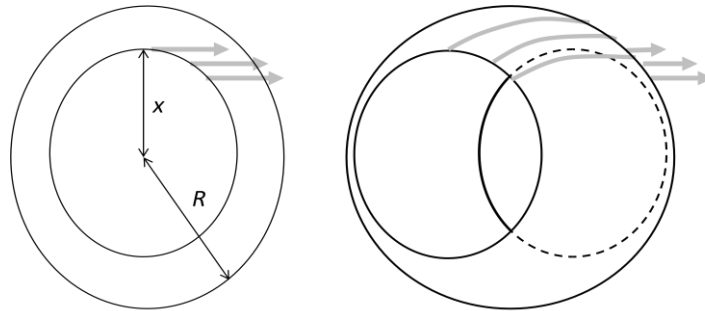


Figure 14.13 Scheme to calculate the pathway along the sphere. The part on the left is the source of permeant. It is constituted by coaxial rings of infinitesimal thickness. The solid surface S_2 on the right is the surface covered by the permeant during its transit (argument of the integral in Equation 14.49).

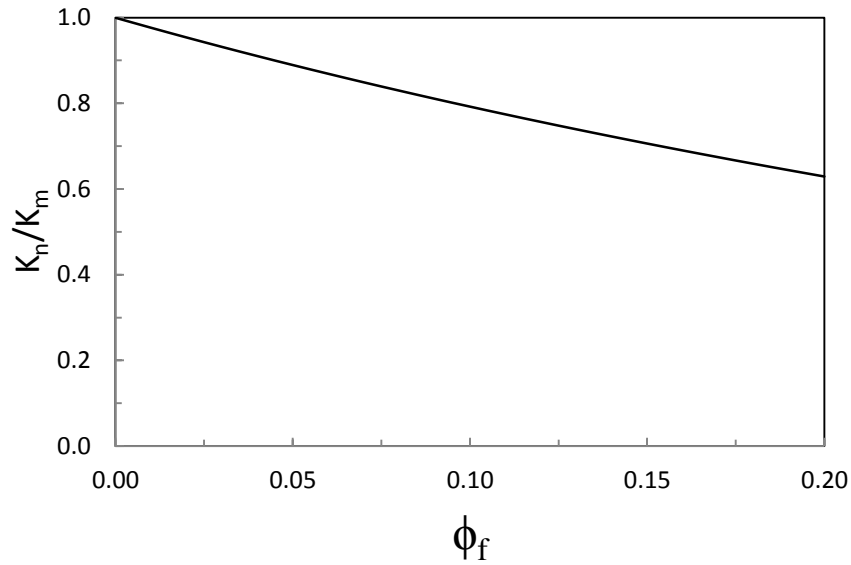


Figure 14.14 Relation proposed in this work for polymers filled with spheres (Equation 14.52).

By using Equation 14.43 it is possible to evaluate the effect of the interface. For this purpose a triphasic model is assumed (Figure 14.15), in which the sphere is surrounded by a void interface. For this model:

$$\beta' = \frac{V_i D_i}{V_f D_m} - \frac{V_i + V_f}{V_f} = (a^3 + 3a^2 + 3a) \left(\frac{D_i}{D_m} - 1 \right) - 1 \quad (14.53)$$

where $a = d/R$. As the interface thickness or the penetrant diffusion coefficient in the interface increase, the permeability of the nanocomposite obviously increases. The value of a is not constant since R can be different for different values of ϕ_f , while d is supposed to be constant because it depends by the interaction between polymer and filler. In our case d and D_i/D_m are unknown. In a recent work Xue et al. utilized 2D material point method (MPM) to study the influence of nanoparticles on the diffusivity of penetrants in model polymer membranes comprised of impenetrable spherical nanoparticles dispersed in a matrix. Diffusion in the nanoparticle-polymer composite membrane was enhanced by the presence of a thin skin of matrix material next to the surface of the nanoparticles with a penetrant diffusion coefficient 100 times that of the bulk matrix [45]. Figure 11.16 shows the effect of the interface thickness on the permeability, holding $D_i/D_m = 100$. L has been fixed because the permeation in the triphasic model is affected by the number/size of particles, unlike the biphasic one. Indeed, if the particles are infinitely small the system can be considerate as a

porous material. To the assumption $L = 700$ nm correspond values of R very close to the real agglomerates size, as shown in Table 14.1, except for the PET/tspPOSS 3. For this sample the model takes into account an average radius of 129 nm, higher than the real size, thus its predicted permeability is lower than the effective value. In this way the fitting of the model can be improved by including the real size of the particle.

It has to be taken into account that PET is a semicrystalline polymer. Every sample has been quenched to reduce as much as possible the crystallinity effect. The crystalline phase is considered as impermeable phase [21] thus contributes to reduce the permeability as spherical fillers do. A further correction in this model can be introduced approaching to the crystallinity using the biphasic model. By DSC analysis on films subjected to the permeability test, the crystallinity content has been measured in different parts of the film. The average values are reported in Table 14.2, using a heat of melting of a PET crystal 140 J/g [46]. The volume fraction has been calculated using a density of the PET crystals of 1.455 g/cm³ dispersed in the amorphous phase with density 1.333 g/cm³ [47]. Combining the contribute of both fillers and crystallinity the prediction is more similar to the experimental values (Figure 14.17). The interface thickness has been fixed at 2 nm.

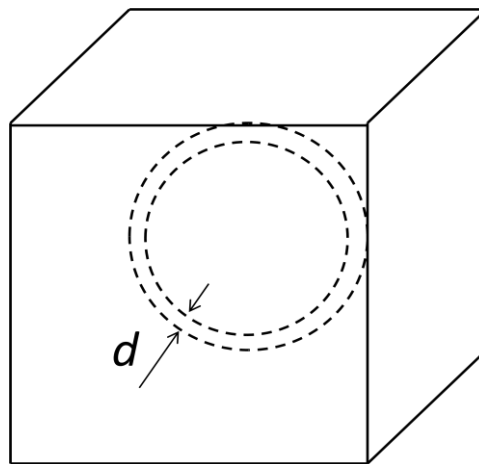


Figure 14.15 Cubic cell filled with a impermeable spherical particle surrounded by a void interface.

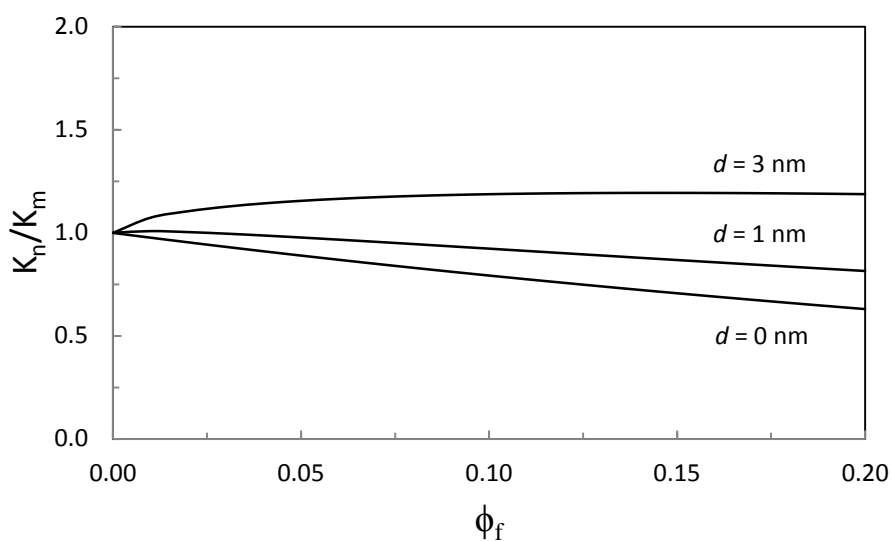


Figure 14.16 Effect of the interface thickness.

Sample	Average diameters of ellipsoidal clusters* (nm)	R of spherical clusters (nm)	R according to the triphasic model (nm)
PET/tspPOSS 0.3	~170-70	~60	60
PET/tspPOSS 1	~250-100	~87	90
PET/tspPOSS 3	~200-90	~72	129
PET/tspPOSS 7	~500-170	~167	171

*= from TEM micrographs

Table 14.1 Clusters size of tspPOSS dispersed in PET (Chapter 9).

Sample	ΔH_m (J/g)	x_c	ϕ_c
PET	4.62	0.033	0.049
PET/tspPOSS 0.3	10.36	0.074	0.068
PET/tspPOSS 1	8.54	0.061	0.056
PET/tspPOSS 3	11.90	0.085	0.078
PET/tspPOSS 7	4.06	0.029	0.027

Table 14.2 Melt enthalpy from DSC analysis (ΔH_m) and crystallinity content: weight fraction (x_c), volume fraction (ϕ_f).

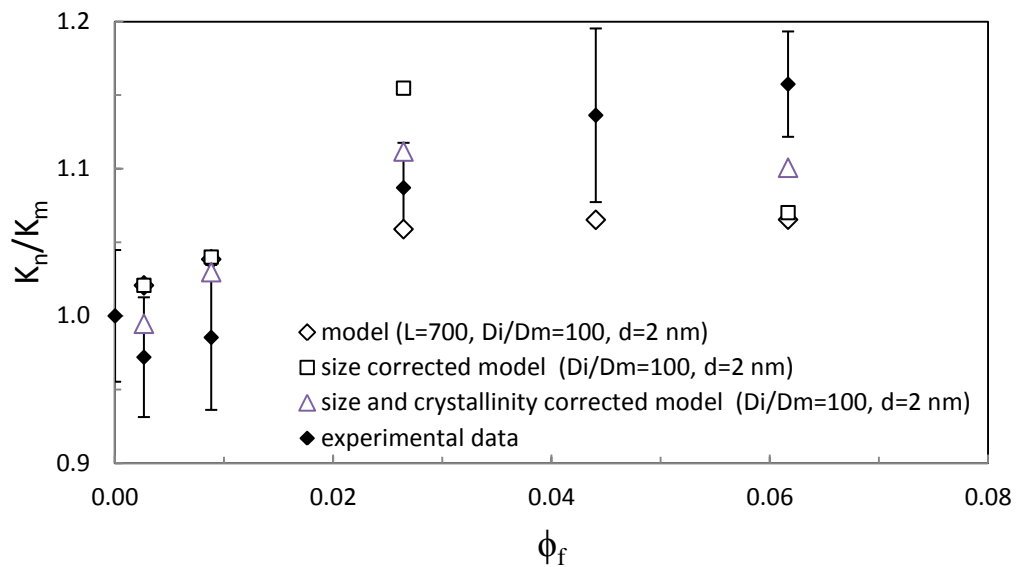


Figure 14.17 Comparison between predicted data by the model presented in this work and experimental data.

References

- [1] V. Stannett. *J Membr Sci.* 1978, 3, 97.
- [2] J. Crank. Methods of measurement. In *Diffusion in Polymers*. J. Crank, G.S. Park, editors, Academic Press, New York (1968) pp 1-39.
- [3] S.A. Stern. *J Membr Sci* 1994, 94, 1.
- [4] R. Kesting, A.K. Fritzsche. *Polymeric gas separation membranes*. John Wiley & Sons, New York (1993).
- [5] K. Ghosal, B.D. Freeman. *Polym Adv Techno.* 1994, 5, 673.
- [6] A. Bondi. *J Phys Chem* 1964, 68, 441.
- [7] D.C. Hoffman, J.K. Caldwell. *Proceedings of specialty polyesters, 1995, Conference Munich.*
- [8] W.R. Vieth. *Membrane systems: analysis and design*. Hanser Publishers, New York (1988).
- [9] W.R. Vieth. *Diffusion in and through polymers: principles and applications*. Hansen Publishers, New York (1991).
- [10] W.J. Koros, G.K. Fleming. *J Membr Sci* 1993, 83, 1.

- [11] W.J. Koros, R.T. Chern. Separation of gaseous mixtures using polymer membranes. In Handbook of Separation Process Technology. R.W. Rousseau, editor, John Wiley & Sons, New York (1987) pp 862-953.
- [12] L.M. Costello, W.J. Koros. *Ind Eng Chem Res.* 1993, 32, 2277.
- [13] D.R. Paul. *J Polym Sci* 1969, 7, 1811.
- [14] J.H. Petropoulos. *J Polym Sci* 1970, 8, 1797.
- [15] J.H. Petropoulos. *Adv Polym Sci* 1985, 64, 93.
- [16] J.H. Petropoulos. *J Polym Sci* 1988, 26, 10090.
- [17] J.H. Petropoulos *J Polym Sci Phys* 1989, 27, 603.
- [18] D.R. Paul, W.J. Koros. *J Polym Sci* 1976, 14, 675.
- [19] R.M. Barrer. *J Membr Sci.* 1984, 18, 25.
- [20] W.R. Vieth, W.F. Wuerth. *J Appl Polym Sci* 1969, 13, 685 .
- [21] A.S. Michaels, W.R. Vieth, J.A. Barrie. *J Appl Phys* 1963, 34, 13.
- [22] G. Choudalakis, A.D. Gotsis. *Eur Polym J* 2009, 45, 967.
- [23] E. Picard, A. Vermogen, J.F. Gerard, E. Espuche. *J Membr Sci* 2007, 292, 133.
- [24] R.M. Barrer. In *Diffusion in polymers*. J. Crank, G.S. Park, editors, Academic Press, London (1968) pp 165-217.
- [25] C. Maxwell. *Treatise on electricity and magnetism*. Oxford Univ Press, London, vol. 1 (1873).
- [26] L. Rayleigh. *Philos Mag* 1892, 34, 481.
- [27] L.E Nielsen. *J Macromol Sci* 1967, A1, 929.
- [28] E.L. Cussler, S.E. Hughes, W.J. Ward, R. Aris. *J Membr Sci* 1988, 38, 161.
- [29] R. Aris. *Arch Ration Mech Anal* 1986, 12, 83.
- [30] W.A. Wakeham, E.A. Mason. *Ind Eng Chem Fundam* 1979, 18, 301.
- [31] E.L. Cussler. *TRI Service Corrosion Conference* 2005.
- [32] W.T. Brydges, S.T. Gulati, G. Baum. *J Mater Sci* 1975, 10, 2044.
- [33] N.K. Lape, E.E. Nuxoll, E.L. Cussler. *J Membr Sci* 2004, 236, 29.
- [34] R.K. Bharatdwaj. *Macromolecules* 2001, 34, 9189.
- [35] R.D. Maksimov, S. Gaidukov, J. Zicans, J. Jansons. *Mech Comp Mat* 2008, 44, 505.
- [36] G.H. Fredrickson, J. Bicerano. *J Chem Phys* 1999, 110, 2181.
- [37] A.A. Gusev, H.R. Lusti. *Adv Mater* 2001, 13, 1641.
- [38] A. Sorrentino, M. Tortora, V. Vittoria. *J Polym Sci* 2006, 44, 265.

- [39] S. Nazarenko, P. Meneghetti, B. Julmon, S. Qutubuddin. *J Polym Sci* 2007, 45, 1733.
- [40] G. Monserrat, J. Barsema, R.E. Galindo, D. Cangialosi, J. Garcia-Turiel, W.E. Van Zyl, H. Verweij, D.H.A. Blank. *Polym Eng Sci* 2004, 44, 1240.
- [41] T.C. Merkel *Chem Mater* 2003, 15, 109.
- [42] V.N. Dournac, R. Alamillo, B.C. Peoples, R. Quijada. *Polymer* 2010, 51, 2918.
- [43] S. Takahashi, D.R. Paul. *Polymer* 2006, 47, 7535.
- [44] N. Hao, M. Bohning, A. Schonhals. *Macromolecules* 2010, 43, 9417.
- [45] L. Xue, O. Boroding, G.D. Smith. *J Membr Sci* 2006, 286, 293.
- [46] A. Mehta, U. Gaur, B. Wunderlich. *J Polym Sci* 1978, 16, 289.
- [47] C.A. Harper. *Handbook of plastics, elastomers, and composites*. McGraw-Hill Professional (2002).

Conclusion

Different research activities have been carried out, generally involving some main phases: the preparation and characterization of polymer nanocomposites, and the industrial trials to obtain the final product. Three transparent polymers have been filled with nanosized fillers in order to improve their mechanical properties: poly(terephthalate) (PET), poly(methyl methacrylate) (PMMA) and polycarbonate (PC). They are important polymers designed to the packaging and automotive applications. Other properties have been evaluated, such as the thermal stability and solubility of fillers, and the gas barrier properties and optical clarity of the nanocomposites.

PET has been initially extruded and compared with the neat PET in order to evaluate the influence of the processing to the polymer properties. By intrinsic viscosity measurements slightly decrease of molecular weight has been observed, while DSC analysis did not show any variation of the glass transition temperature. Indeed the molecular weight is enough high that the extent of its reduction does not significantly affect the mechanical properties.

In a previous activity PET based bottles filled with organomodified montmorillonite (oMMT) have been developed. The occurring of delamination, after the blow molding due to stress concentration, and the brown color of the product, induced us to find new solutions to reinforce the PET. Two alternative fillers were used, i.e. polyhedral oligomeric silsesquioxanes (POSS) with two different organic surfaces. The octaisobutyl POSS (POSSo) is a unreactive molecule surrounded by nonpolar groups, the 1,2-propanediol isobutyl (POSSp) is differentiated by a chain having two hydroxyl groups. PET/POSSo and POSSp nanocomposites have been prepared by melt blending (2 wt% of filler). TEM micrographs show two different morphologies in the bottles: the first exhibit big aggregates dispersed into the matrix that lead many wide slits, making the bottles opaque, the second show no evidence of coarse aggregates, resulting in a few of narrow slits that do not prejudice the transparency. These differences have been attributed to the different affinity of POSSo and POSSp with PET. POSSp is more polar than POSSo, thus it is more finely dispersed and its interface with the matrix has more favorable interactions. It may interact through hydrogen bonds or react with the ester or end groups of the polymer chain. The melt flow index of PET/POSSp

nanocomposites are higher than unfilled PET and PET/POSSo nanocomposites. Moreover, despite the better dispersion and stronger interface of POSSp filled materials, the mechanical properties are not much different to the ones of the matrix. These results induced us to hypothesize the occurring of reactions between POSSp and PET, resulting in a decrease of molecular weight. In order to improve the barrier properties PET/POSSp/oMMT and PET/POSSo/oMMT have been prepared as well (1 wt% of oMMT). XRD analysis showed a slightly better dispersion of oMMT in the PET/POSSo/oMMT nanocomposites. It is associated to the higher viscosity during the processing, compared to the POSSp filled materials, resulting in higher shear stress that break the oMMT stacks.

These are the main differences derived by adding POSS having different compatibility and reactivity. Since these two aspects strongly affect the final properties of the nanocomposites, a screening of different POSS has been performed in a subsequent activity. It has to be noticed that transparent nanocomposites bottles were successfully obtained.

Different POSS typologies have been chosen as suitable reinforcing fillers for PET. To simplify the activity, they have been evaluated on the basis of their thermal stability at the PET processing temperatures and their solubility in this polymer. Moreover, the nanocomposites have been prepared by melt blending in order to compare their optical clarity and their crystallization behavior. The trisilanol phenyl POSS (tspPOSS) resulted the most interesting POSS in terms of thermal stability, solubility, nucleating activity and optical clarity of the nanocomposite.

PET/tspPOSS nanocomposites have been produce by melt blending at different filler content. Bottles filled with 3 wt% of tspPOSS exhibit a good transparence. TEM micrographs show no presence of slits, it has been associated to a strong interface between matrix and filler. The clusters are present mainly in the form of ellipsoidal clusters but some irregular clusters have been observed as well. The stiffness of nanocomposites exhibits a slight increase up to 3 wt% of filler, above this content it decreases. It does not support the occurring of reaction between silanol groups of tsPOSS and the polymer chain, as reported in literature. The thermal stability of the nanocomposites is generally worst than PET, as well as the oxygen permeability, due to an increase of free volume at the interface between PET and tspPOSS clusters. The increase of permeability as the filler content increases has been fitted with a model presented in this work. The conventional models predict a reduction of the permeability thanks to the tortuosity path the permeants has to travel across the film

thickness. The presented model takes into account a diffusion coefficient in the interface higher than the one in the polymer. Its accuracy has been improved by correcting the calculations with the size of POSS clusters and crystallinity content.

Another activity studied toughened PET based nanocomposites for flexible packaging application. The preferential localization of oMMT observed in polymer blend induced us to selectively localize the oMMT in the ethylene vinyl acetate (EVA) domains dispersed in a PET matrix. It has been verified that the platelets of oMMT can kinetically act during the mixing as refiner of the EVA domains, improving the toughness of the material without maintaining a good stiffness. The EVA has been grafted with maleic anhydride (MA-g-EVA) as compatibilizer between the two polymers. Two different PET/MA-g-EVA ratios has been adopted (90/10 and 80/20 w/w), varying the content of oMMT. The selective dispersion should be promoted by using a suitable organomodifier of clay, the presence of MA and the mixing route adopted. Adopting the 80/20 ratio an increase of modulus without compromise the elongation at break at low clay content, occur. The improved stiffness is due to the heterogeneous nucleation activity of filler. It is supported by DSC analysis. The lower strain at break exhibited at high clay content is due to the bigger size and higher interparticle distance of the dispersed phase. It confirms that no compatibilizing effect of clay occurs. Indeed TEM micrographs show the localization of segregated clay lamellae in the interface between PET and MA-g-EVA, despite it is both exfoliated and intercalated into EVA before the mixing with PET. The presence of mixed structures and the segregation in the interphase could arise by partial degradation of the alkyl ammonium surfactants during high temperature processing. XRD analysis revealed a reduction of the interlayer distance between the lamellae, supporting the occurring of thermal degradation of surfactants. This collapse may also be due to a confinement effect due to the small size of EVA domains.

Concerning PMMA and PC based nanocomposites, a preliminary study aimed to optimize the processing parameters, has been performed. Unfilled and oMMT-filled PMMA and PC have been extruded by using different processing settings. Melt flow index and flexural modulus have been measured in order to get fast informations about the dispersion level of the clay and the extent of thermal degradation. It has been seen that both polymers are sensitive to the process, in particular PMMA. Longer residence time results in a worsening of the mechanical properties of the PMMA/oMMT nanocomposites, while do not affect those of the PC/oMMT nanocomposites. By extruding at very low temperature, close to the melting point

of the polymers, thus exercising high shear stress, the materials do not exhibit the highest modulus, meaning that also a good chain mobility is required to achieve a good dispersion.

As previously mentioned, PET/tspPOSS nanocomposites showed a surprising optical clarity that has never been achieved by using oMMT. That turned our interest toward a study on PMMA and PC based nanocomposites filled with different POSS typologies and other similar fillers; i.e. silica nanoparticles. This activity is focused to individuate a qualitative correlation between the solubility of fillers and the mechanical and optical properties of the nanocomposites. It has been observed that the two polymers have a similar solubility field but their nanocomposites exhibit very different features. Tensile moduli PMMA based nanocomposites generally increase, while the fillers do not affect or reduce those of PC. Concerning the optical clarity PMMA based nanocomposites exhibit a good transparency, while the PC ones are haze or colored. It is probably associated, not only to the dimension of inorganic particles but also to the differences in the diffractive index. A strong correlation between optical clarity, solubility and mechanical properties has been observed in particular in PC based nanocomposites.

One of the most interesting materials resulted from this activity are the PMMA/SiO₂ nanocomposites, that exhibit a good compromise of optical clarity and both static and dynamic tensile moduli. They have the advantage to be subjected to a further improvement in terms of dispersion level and interfacial adhesion of silica particles. It is possible by functionalizing the particle surface with a silane (MPS). Another improvement can be done by polymerizing methyl methacrylate (MMA) at the silane ends. These two approaches have been studied in literature involving a multi-step synthesis in solution. In order to make more industrially interesting these material an alternative process has been adopted: it consists in a synthesis in solution followed by an extrusion. Moreover, different methods to functionalize the silica particles with MPS have been compared. FTIR spectroscopy and TGA analysis measured their effectiveness in terms of amount of silane grafted to the silica. These SiO₂-MPS particles were used to prepare PMMA/SiO₂-MPS nanocomposites and to synthesized the SiO₂-PMMA particles. Anyway, the dispersion level in PMMA/SiO₂-MPS nanocomposites is generally very poor, showing big agglomerates. Only one method leads materials with a good optical clarity. Also the SiO₂-PMMA particles were added in PMMA obtaining highly transparent materials. Finally we compared the static and dynamic tensile moduli of PMMA filled with un-modified SiO₂, SiO₂-MPS and SiO₂-PMMA particles. We

found an improvement of stiffness by using the MPS as compatibilizer, while the PMMA-modified particles exhibited a similar mechanical behavior of the neat PMMA. It is probably due to the fraction of polymerized PMMA in the matrix that has a lower molecular weight than the as-received PMMA.

Acknowledgements

I would like to express my gratitude to Prof. Michele Modesti for his support and advice throughout my activity in his research group. Sincere thanks to my co-workers, and friends, Stefano Besco, Denis Hrelja, Alessandra Lorenzetti, Martina Roso and all the people I worked with.

I would like to express my special thank to Prof. Evangelos Manias of Penn State University, and co-workers Charles (Greg) Hogshead and Felipe Salcedo Galan.

Finally, thanks go to my family for their continuous encouragement and support.